

# WCRP REPORT

World Climate Research Programme



ICSU

International Council for Science



## GEWEX Radiative Flux Assessment (RFA) Volume 2: Supplementary Information

A Project of the World Climate Research  
Programme Global Energy and Water Cycle  
Experiment (GEWEX) Radiation Panel

Lead Authors:

**Ehrhard Raschke**

Max-Planck-Institute for Meteorology, Hamburg, and Institute for Meteorology of  
University of Hamburg, Germany

**Stefan Kinne**

Max-Planck-Institute for Meteorology, Hamburg, Germany

**Paul W. Stackhouse**

NASA, Langley Research Center, Hampton, Virginia, USA

December 2012

WCRP Report No. 19/2012

This report consists of two parts:

**Volume 1** contains results, recommendations and conclusions.

**Volume 2** contains various details and supplementary information.

# GEWEX Radiative Flux Assessment (RFA)

## Volume 1: Assessment

<b>Table of Contents for the Entire Report</b>	<b>iii</b>
<b>Foreword</b>	<b>viii</b>
<b>Disclaimer</b>	<b>ix</b>
<b>Executive Summary</b>	<b>xi</b>
Key Findings and Recommendations	xi
Important Findings per Chapter	xiii
Chapter 1: Introduction	xiii
Chapter 2: Incoming Solar Radiation at the TOA	xiii
Chapter 3: Radiation Budget at the TOA	xiv
Chapter 4: Radiation Budget at the Surface	xvi
Chapter 5: In-situ Radiation Flux Measurements at the Surface	xvii
Chapter 6: Comparison with In-Situ Data	xviii
Chapter 7: Vertical Radiative Flux Divergence in the Atmosphere	xix
Chapter 8: Global Mean Radiation Budget	xx
Chapter 9: Radiation Fluxes in Global Modeling for the IPCC-4 <sup>th</sup> AR	xx
<b>List of Contributors</b>	<b>xxiii</b>
<b>List of Acronyms</b>	<b>xxiv</b>

## Chapters of the Report

<b>Chapter 1 – Introduction to the Report</b>	<b>1-8</b>
<b>1.1 Purpose of the Assessment</b>	<b>1</b>
<b>1.2 Radiative Flux Assessment Archive, Data Sets and Parameters</b>	<b>2</b>
<b>1.3 Initial Workshop Towards Assessment</b>	<b>6</b>
<b>1.4 Report Overview</b>	<b>7</b>
<b>Chapter 2 - Incoming Solar Radiation at TOA</b>	<b>9-22</b>
<b>2.1 Solar Irradiance Measurements</b>	<b>9</b>
2.1.1 Total Solar Irradiances	9
2.1.2 Spectral Solar Irradiances	13

<b>2.2</b>	<b>Solar Irradiance Models</b>	<b>16</b>
<b>2.3</b>	<b>Computations of Insolation at TOA</b>	<b>19</b>
<b>2.4</b>	<b>Conclusions and Recommendations</b>	<b>21</b>

## **Chapter 3 – Radiation Budget at the TOA** **23-90**

<b>3.1</b>	<b>Introduction</b>	<b>23</b>
<b>3.2</b>	<b>ERBE vs. CERES Radiation Fluxes</b>	<b>24</b>
3.2.1	Introduction	24
3.2.2	Climatological Annual Regional Averages	25
3.2.3	Temporal Variability	26
3.2.4	Deseasonalized Monthly Time Series	27
3.2.5	Zonal Annual Cycle	28
3.2.6	Seasonal Cycle	29
3.2.7	Summary	30
<b>3.3</b>	<b>Radiation Budget at TOA during ERBE and CERES Period Part I: Climatological Mean and Time Series Comparisons)</b>	<b>31</b>
3.3.1	Introduction	31
3.3.2	Datasets and Analysis Methods	31
3.3.3	ERBE Period Results (February 1985 to January 1989)	32
3.3.4	CERES Period Results (March 2000 to February 2004)	37
3.3.5	ERBE and CERES differences	43
3.3.6	Summary	44
<b>3.4</b>	<b>Radiation Budget at TOA during the ERBE and CERES period. Part II: Annual Mean Cycles</b>	<b>45</b>
3.4.1	Introduction	45
3.4.2	Data Description and Analysis Method	45
3.4.3	Statistical Results	46
3.4.4	Qualitative Results	48
3.4.5	Summary	49
<b>3.5</b>	<b>Anomalies in Datasets of ISCCP, SRB, ERBE &amp; CERES</b>	<b>50</b>
3.5.1	Introduction	50
3.5.2	Errors in Ancillary Data for ISCCP Cloud Retrievals and Radiation computations	50
3.5.3	Time Series of Upward Radiation (ISCCP vs. SRB)	51
3.5.4	Seasonal Average Comparison	57
3.5.5	Comparison with ERBE-ERBS Scanner Data	62
3.5.6	Comparison of ERBE and CERES Flux Fields	65
3.5.7	Some Conclusions and Recommendations	66
<b>3.6</b>	<b>GERB and CERES Monthly Average Comparison for July 2004</b>	<b>69</b>
3.6.1	Background	69
3.6.2	Processing Overview	69
3.6.3	Result and Comparison	71
3.6.4	Summary	74
<b>3.7</b>	<b>Selected Results from ScaRaB</b>	<b>75</b>
3.7.1	Introduction	75

3.7.2	Description of ScaRaB-Instruments	76
3.7.3	The ScaRaB flux products	76
3.7.4	Intercomparison to other data	77
3.7.5	Summary	79
<b>3.8</b>	<b>Diurnal Cycle of TOA Radiation</b>	<b>80</b>
3.8.1	Introduction	80
3.8.2	Outgoing Longwave Radiation	80
3.8.3	Reflected Shortwave Radiation	82
3.8.4	Summary	83
<b>3.9</b>	<b>Required Meridional Energy Transports in the Climate System</b>	<b>84</b>
<b>3.10</b>	<b>ERBE and CERES Data Uncertainty</b>	<b>86</b>
3.10.1	Introduction	86
3.10.2	ERBE Scanner Data Uncertainty	86
3.10.3	CERES Data Uncertainty	87
3.10.4	Summary	87
<b>3.11</b>	<b>Summary of all sections</b>	<b>89-90</b>
 <b>Chapter 4 – Radiation Budget at the Surface</b>		<b>91-134</b>
<b>4.1</b>	<b>Introduction and Overview</b>	<b>91</b>
<b>4.2</b>	<b>Surface Radiation Budget compared with GEWEX-SRB Products</b>	<b>92</b>
4.2.1	Dataset Description	92
4.2.2	Multiyear Regional Comparisons	92
4.2.3	Multiyear Zonal and Global Comparisons	92
4.2.4	Summary	99
<b>4.3</b>	<b>Surface Radiation Budget Product Comparison</b>	<b>100</b>
4.3.1	Datasets and Time Period Covered	100
4.3.2	Annual Mean Time Series	101
4.3.3	Monthly Mean Time Series	105
4.3.4	Conclusions	106
<b>4.4</b>	<b>Annual Cycle of Surface Radiative Fluxes</b>	<b>107</b>
4.4.1	Data Description	107
4.4.2	Analysis Method	108
4.4.3	Qualitative Results	108
4.4.4	Statistical Results	109
4.4.5	Summary	111
<b>4.5</b>	<b>Zonal and regional radiation flux anomalies at the surface (ISCCP/ SRB vs. CERES)</b>	<b>112</b>
4.5.1	Introduction	112
4.5.2	Time Series of Deseasonalised Monthly Zonal Anomalies of ISCCP and SRB	113
4.5.3	Interannual Variation of Effective Surface Albedo and Emission	117
4.5.4	Seasonal CERES maps and difference-maps of ISCCP and SRB to CERES	119
4.5.5	Conclusions and Recommendations	133

<b>Chapter 5 - In-situ Radiation Flux Measurements at Surface</b>	<b>135-157</b>
<b>5.1 Introduction</b>	<b>135</b>
<b>5.2 Measurement Uncertainty Estimates</b>	<b>136</b>
5.2.1 Overview	136
5.2.2 Observations of Interest to this RFA	137
5.2.3 Instruments Utilized	137
5.2.4 Methodologies for Determining Measurement Uncertainty	138
5.2.5 Uncertainties in the Measurement of Total Downward Solar Irradiance	138
5.2.6 Uncertainties in the Downwelling Thermal IR Flux	138
5.2.7 Considerations for Uncertainties in Upwelling Irradiance Observations	139
5.2.8 Time Averaging	140
5.2.9 Long-term Measurement Stability	142
5.2.10 Redundant Measurements as an Uncertainty Assessment Tool	142
5.2.11 Spatial Representativeness	145
5.2.12 Summary of Uncertainties in Ground-Based Surface Observations	146
5.2.13 Conclusions and Recommendations	146
<b>5.3 In Situ Surface Flux Derived Products</b>	<b>149</b>
5.3.1 Available Derived Products	150
5.3.2 Quality and Uncertainty of Derived Products	150
<b>5.4 Long-Term Surface In Situ Time Series Analysis</b>	<b>151</b>
5.4.1 Available Data and Quality	151
5.4.2 Results of Time Series Analyses	152
5.4.3 Methodological Issues	153
<b>5.5 Outstanding Issues and Concerns</b>	<b>155</b>
5.5.1 Calibration Reference Standards	155
5.5.2 Spatial Gaps in Surface Measurements	156
5.5.3 Quality of Widely Deployed Instrumentation	157
5.5.4 Environmental Interference, Especially in Cold Regions	157
5.5.5 Spatial and Temporal Resolution	157
5.5.6 Ancillary Data	158
<b>Chapter 6 – Comparison with In-Situ Data</b>	<b>159-187</b>
<b>6.1 Introduction</b>	<b>159</b>
<b>6.2 Ground-based Reference Data</b>	<b>160</b>
6.2.1 The BSRN network data	160
6.2.2 The GUOR Data	161
6.2.3 The ASRB Data	162
<b>6.3 The Satellite-Based Data Sets</b>	<b>162</b>
<b>6.4 Evaluation Methods</b>	<b>162</b>
<b>6.5 Evaluation against BSRN Data</b>	<b>163</b>
<b>6.6 Evaluation against GUOR Data (GEBA and UOR)</b>	<b>176</b>
<b>6.7 Evaluation against ASRB Data of the Alpine Network</b>	<b>183</b>
<b>6.8 Summary</b>	<b>185</b>
<b>6.9 Conclusions</b>	<b>185</b>

## **Chapter 7 –Radiative Flux Divergence in the Atmosphere 189-208**

<b>7.1</b>	<b>Introduction</b>	<b>189</b>
<b>7.2</b>	<b>Current Understanding (on the basis of ISCCP data)</b>	<b>190</b>
<b>7.3</b>	<b>Influence of Uncertainties in Ancillary Data on Time Series</b>	<b>192</b>
<b>7.4</b>	<b>Inter-annual Variations of Regional Annual Anomalies</b>	<b>195</b>
<b>7.5</b>	<b>Seasonal Variations of Differences of ISCCP &amp; SRB to CERES</b>	<b>198</b>
7.5.1	Solar Divergence	198
7.5.2	Infrared Divergence	201
<b>7.6</b>	<b>Clear-sky and Cloudy-Sky Water Vapor Biases</b>	<b>204</b>
<b>7.7</b>	<b>Conclusions and Recommendations</b>	<b>205-207</b>

## **Chapter 8 – Global Mean Radiation Budget 209-214**

<b>8.1</b>	<b>Introduction</b>	<b>209</b>
<b>8.2</b>	<b>The Global Annual Mean Radiation Budget</b>	<b>210</b>
<b>8.3</b>	<b>Consistency of Global Annual Mean Radiation Budget amongst GEWEX RFA Datasets</b>	<b>212</b>
<b>8.4</b>	<b>Summary and Conclusions</b>	<b>214</b>

## **Chapter 9 – Radiation Fluxes in Global Modeling 215-260**

<b>9.1</b>	<b>Diversity of Results from Model and Climate-Data</b>	<b>215</b>
9.1.1	Introduction	215
9.1.2	The IPCC Median Model	217
9.1.3	Diversity in Modeling	219
9.1.4	The CERES Data Reference	221
9.1.5	Comparing Satellite Based Flux Products	222
9.1.6	Difference of IPCC Median Maps vs. Satellite Reference Data	226
9.1.7	Difference of IPCC Median Maps vs. Satellite Data at the Surface	229
9.1.8	The Atmospheric Greenhouse Effect	232
9.1.9	Summary of Major Findings	238
<b>9.2</b>	<b>Comparisons to GFDL Model Simulations</b>	<b>240</b>
9.2.1	Introduction	240
9.2.2	Differences between CM2.1 and CM2.0 Historical Means	240
9.2.3	Differences in Historical Means of Radiation Fluxes	241
9.2.4	Differences in the Variability of the Radiation Fluxes	244
9.2.5	Summary and Conclusion	246
<b>9.3</b>	<b>Comparison of Reanalysis and Model Surface Radiative Fluxes to in-situ Surface Measurements</b>	<b>247</b>
9.3.1	Introduction	247
9.3.2	Ground-Based Data Description	247
9.3.3	Reanalysis and Model Data Sets	247
9.3.4	Evaluation Methods	248
9.3.5	Comparisons to BSRN Data	248

9.3.6	Comparison to GUOR (GEBA and UOR) data	254
9.3.7	Summary and Conclusions	257-259

**Chapter 10 – All References** **261-273**

## Volume 2: Supplementary Information

<b>Appendix A: Short Description of Data sets</b>	<b>1-80</b>
<b>Appendix B: Radiative Model Comparison</b>	<b>81-93</b>
<b>Appendix C: Supplementary material for Chapters 3.3, 3.4, 3.5, 4.3, 4.5, 7.1 and 9.1</b>	<b>94-211</b>
<b>Appendix D: Lessons learnt by L. Hinkelman and L. Chambers</b>	<b>121-215</b>

## **Appendix A :**

### **Data Product Descriptions and Supporting Detail for Data Error Sources and Estimates**

## A.1: Brief Summary of Long-Term Satellite TOA Flux Data Products

### A.1.1: ERBE/ERBS Nonscanner WFOV Data Set

: T. Wong and B. Wielicki

#### Description of the ERBE/ERBS Broadband Nonscanner WFOV Data

The Earth Radiation Budget Experiment's (ERBE; Barkstrom, 1984) Earth Radiation Budget Satellite (ERBS) Nonscanner WFOV dataset is the only stable long-term climate dataset that is based on broadband flux measurements. The ERBS WFOV instrument is an active cavity radiometer designed to measure broadband hemispheric fluxes. There are two broadband channels in the WFOV instrument. The total channel measures Earth reflected and emitted radiation from the 0.2 to 100  $\mu\text{m}$ . The shortwave channel measures the Earth reflected radiation from 0.2 to 5  $\mu\text{m}$ . The daytime emitted longwave radiation is deduced by subtracting the shortwave data from the total measurement. The longwave radiation at night is obtained from the total channel measurement since there is no reflected sunlight at night.

The basic ERBE Nonscanner (see *Figure 1.1*) processing system contains three main components: calibration, inversion to instantaneous TOA flux, and time-space averaging. First, the ERBE Nonscanner hemispheric flux measurements at satellite altitude are calibrated against both the onboard blackbodies and the sun to determine gains and offsets of the instrument (Luther et al. 1986a, 1986b; Lee et al. 1987). Second, the calibrated satellite altitude (~600 km) flux data are converted to instantaneous TOA flux measurements using the ERBE Nonscanner inversion algorithm (Green and Smith 1991). The ERBE reference TOA altitude is 30 km. Third, the instantaneous TOA flux data are temporally averaged to produce monthly mean datasets using the ERBE time-space averaging algorithm (Brooks and Minnis 1984). The Nonscanner data in the GEWEX-RFA archive is from the latest Edition 3 Revision 1 dataset (Wong et al., 2006) and consists of  $10^\circ \times 10^\circ$  equal-angle grid data that have been averaged over the 72-day precession cycle of the ERBS satellite to avoid problems associated with incomplete diurnal sampling and slow drift of the orbit over time. The ERBS Nonscanner Edition 3 Revision 1 data incorporated algorithms for correcting the subtle but significant effects of satellite altitude change and shortwave instrument drift due to non-uniform exposure to UV radiation (Smith et al., 2002). This dataset covers a 15-year period from 1985 to 1999.

#### Uncertainty Analysis

The major sources of uncertainty for this dataset include those of calibration, angle sampling, spatial sampling, and temporal sampling.

#### Calibration:

The total uncertainty for the WFOV longwave and shortwave is estimated by Green et al. (1990) to be on the order of  $2.5 \text{ Wm}^{-2}$  or 2.5% of SW TOA reflected flux, and 1% of LW TOA emitted flux. For decadal changes and interannual variations as shown in the current paper, however, the more relevant error analysis is for annual mean changes in the tropics and 60S to 60N over the 1985 to 1999 time period. Below we consider the four major error sources (calibration, angle sampling, time sampling, space sampling) and briefly summarize results documenting these uncertainty levels.

The ERBS Nonscanner WFOV calibration stability uncertainty is an order magnitude better than its total uncertainty and is estimated from observations to be on the order of  $0.35 \text{ Wm}^{-2}$ .

<sup>2</sup> over the 1985 to 1999 time period of the Edition 3 Revision 1 ERBS data. Specifically, the total channel ERBS Nonscanner WFOV active cavity radiometer, which controls the ERBS net radiation estimation, has shown stability in solar calibrations of 0.1% or  $0.35 \text{ Wm}^{-2}$  in Earth reflected SW plus emitted LW flux over the 15-year period from November 1984 to September 1999, when compared to other solar constant satellite missions by Lee et al. (2003). This is equivalent to a stability of  $0.2 \text{ Wm}^{-2}$  per decade for Net flux. Note that Net flux trends are controlled by the ERBS Total channel alone, and not by the SW channel. Any calibration changes in the SW channel only affect the relative changes of SW and LW fluxes. The WFOV SW calibration is also determined from solar constant comparisons, and is corrected in the current paper to account for non-uniform transmission loss over the SW filter dome. The filter dome correction has a total change of  $\sim 1\%$  per decade in SW flux, and a 95% confidence uncertainty on the slope of  $0.1\%$  per decade.

### **Spectral Sampling:**

None

### **Spatial Sampling:**

Annual mean spatial sampling errors for the tropical ( $20^{\circ}\text{S}$  to  $20^{\circ}\text{N}$ ) and  $60^{\circ}\text{S}$  to  $60^{\circ}\text{N}$  regions are less than  $0.1 \text{ Wm}^{-2}$ . The estimate is obtained by scaling the results of Green and Smith (1991) for spatial and angular sampling errors with the WFOV ERBS sensor. While the WFOV sees limb to limb on the Earth from the 600 km ERBS orbit altitude, Green and Smith (1991) showed that the equivalent diameter of the WFOV instantaneous observations are  $\sim 1500\text{km}$ . Given ERBS 2700 km typical orbit track separation at the equator, ERBS requires roughly two days to view the entire earth from  $60^{\circ}\text{S}$  to  $60^{\circ}\text{N}$ .

### **Viewing Angle Sampling:**

Since the WFOV sees the entire hemisphere of radiation, it is relatively insensitive to angular sampling errors. Angle sampling sensitivity tests by Green et al. (1990) show that 30% changes in earth's radiation anisotropy from nadir to limb are required to cause global annual WFOV TOA flux changes of  $2 \text{ Wm}^{-2}$  for SW flux and  $1 \text{ Wm}^{-2}$  for LW flux. Angle sampling patterns for the ERBS orbit have not varied over the mission lifetime, unlike drifting NOAA sun-synchronous orbits with changing local times of observation and solar zenith angle from year to year. Even 3% changes in earth's global average anisotropy would be very large for decadal change, so that uncertainty in decadal change for ERBS WFOV due to angle sampling are estimated at less than  $0.2 \text{ Wm}^{-2}$  for SW flux and  $0.1 \text{ Wm}^{-2}$  for LW flux.

### **Time Sampling :**

For time sampling errors, the ERBS spacecraft orbit samples the entire 24 hour diurnal cycle every 72 days, or close to 5 times per year. Sampling studies were carried out using 3-hourly geostationary data subsampled over the tropics at the ERBS orbit times to determine diurnal sampling errors for monthly means. Wielicki et al. (2002a,b) showed that the  $20^{\circ}\text{S}$  to  $20^{\circ}\text{N}$  monthly mean ERBS WFOV SW flux error is  $1.7 \text{ Wm}^{-2}$  and LW flux diurnal sampling error is  $0.4 \text{ Wm}^{-2}$ . They also showed that use of orbit precession cycle means of 36 days for the tropics (72 days for  $60^{\circ}\text{S}$  to  $60^{\circ}\text{N}$ ) dramatically reduce time sampling errors. If the errors were random, annual mean errors would be reduced by a factor of 3.5 (or square root 12 months). This suggests annual tropical mean uncertainties of  $0.5 \text{ Wm}^{-2}$  for SW and  $0.1 \text{ Wm}^{-2}$  for LW flux. In fact, because of the systematic aliasing of ERBS diurnal sampling between 30-day months and the 72-day orbit precession cycle discussed in Wielicki et al. (2002b), the errors are reduced even

further than random noise when averaged over an entire year of 5 precession cycles for the annual mean. A full error simulation of this effect has not been carried out, but the 0.5 and 0.1  $\text{Wm}^{-2}$  time sampling error estimate for annual mean should be considered an upper bound on time sampling error. More realistic values are likely a factor of 1.5 to 2 smaller. A factor of 1.5 is assumed here.

### Gap Filling Methods:

None

### Total Error Summary:

When the four ERBS error sources are combined, the total stability uncertainty (1-sigma) in the 60°N to 60°S and tropical annual mean radiation for the ERBS WFOV 15-year dataset from all three sources combined is on the order of 0.3 to 0.4  $\text{Wm}^{-2}$ . Time sampling uncertainty dominates SW and Net flux stability, while calibration uncertainty dominates LW flux stability.

### References:

- Green, R. N., and G. L. Smith, 1991: Shortwave shape factor inversion of Earth Radiation Budget observation. *J. Atmos. Sci.*, **48**, 390–402.
- Green, R. N., F. B. House, P. W. Stackhouse, X. Wu, S. A. Ackerman, W. L. Smith, and M. J. Johnson, 1990: Intercomparison of scanner and nonscanner measurements for the Earth Radiation Budget Experiment. *J. Geophys. Res.*, **95**, 11 785–11 798.
- Lee, R. B., III, B. R. Barkstrom, and R. D. Cess, 1987: Characteristics of the Earth Radiation Budget Experiment solar monitors. *Appl. Opt.*, **26**, 3090–3096.
- Lee, R. B., III, G. L. Smith, K. A. Bush, J. Paden, D. K. Pandey, R. S. Wilson, and K. J. Priestley, 2003: On-orbit calibrations of the ERBE active-cavity radiometers on the Earth Radiation Budget Satellite (ERBS): 1984–2002. *Proc. SPIE*, **5234**, 433–444.
- Luther, M. R., J. E. Cooper, and G. R. Taylor, 1986a: The Earth Radiation Budget Experiment Nonscanner instruments. *Rev. Geophys.*, **24**, 391–399.
- Luther, M. R., R. B. Lee III, B. R. Barkstrom, J. E. Cooper, R. D. Cess, and C. H. Duncan, 1986b: Solar calibration results from two Earth Radiation Budget Experiment Nonscanner instruments. *Appl. Opt.*, **25**, 540–545.
- Smith, G. L., R. B. Lee III, and J. Paden, 2002: Dome degradation pattern of ERBE wide field-of-view shortwave radiometer. *Proc. SPIE*, **4881**, 369–377.
- Wielicki, B. A., and Coauthors, 2002a: Evidence for large decadal variability in the tropical mean radiative energy budget. *Science*, **295**, 841–844.
- Wielicki, B. A., and Coauthors, 2002b: Response: Changes in tropical clouds and radiation. *Science*, **296**, doi:10.1126/science.296.5576.2095a.
- Wong, T., B. A. Wielicki, R. B. Lee, III, G. L. Smith, K. A. Bush and J. K. Willis, 2006: Reexamination of the Observed Decadal Variability of the Earth Radiation Budget using Altitude-Corrected ERBE/ERBS Nonscanner WFOV Data. *J. Climate*, **19**, 4028–4040.

## **A.1.2: ERBE Scanner Data Set**

T. Wong

### **Description of the ERBE/ERBS Broadband Scanner Data:**

The Earth Radiation Budget Experiment (ERBE; Barkstrom, 1984) scanner instruments were placed on three different satellites: the Earth Radiation Budget Satellite, the NOAA-9 satellite and the NOAA-10 satellite. The data collected from these three spacecrafts were used to produce both the single and multi-satellite ERBE scanner datasets. The ERBE scanner detectors are thermistors designed to measure broadband radiances as the instrument scanned across the earth surface at satellite altitude. There are three broadband channels in the ERBE scanner instrument. The total channel measures Earth reflected and emitted radiation from the 0.2 to 100  $\mu\text{m}$ . The shortwave channel measures the Earth reflected radiation from 0.2 to 5  $\mu\text{m}$ . The longwave channel measures emitted radiation from 5 to 100  $\mu\text{m}$ . The information from the longwave channel, however, is not used to produce scientific data due to the highly non-uniform spectral response characteristics of this sensor. Instead, the daytime emitted longwave radiation is deduced by subtracting the shortwave data from the total measurement. The longwave radiation at night is obtained from the total channel measurement since there is no reflected sunlight at night. The basic ERBE scanner processing system contains three main components: calibration, inversion of radiance measurement to instantaneous TOA flux, and time-space averaging. First, the ERBE scanner footprint radiance measurements at satellite altitude are calibrated inflight against the onboard reference blackbodies which is tied to IPTS68 standard, the Sun through the onboard solar diffuser and the internal incandescent source which is monitored by silicon photodiodes, to determine gains and offsets of the instrument (Barkstrom, 1984). Second, the calibrated ERBE footprint radiance data are converted to instantaneous TOA flux measurements using the ERBE scanner inversion algorithm which includes both the broadband scene identification technique (Wielicki and Green, 1989) and the scene dependent angular distribution model (ADM, Suttles et al. 1988, 1989). Third, the instantaneous footprint TOA fluxes are spatially and temporally averaged to produce a  $2.5^\circ \times 2.5^\circ$  gridded monthly mean datasets using the ERBE time-space averaging algorithm (Brooks et al. 1986). The ERBE scanner data in the GEWEX-RFA archive is from the original release of the ERBE dataset and covers a roughly 5-year period from 1985 to 1989.

### **Uncertainty Analysis:**

The major sources of uncertainty for this dataset include those of calibration, angle sampling, spatial sampling, and temporal sampling. The following uncertainty estimates are taken directly from Table 4 of Wielicki et al (1995).

### **Calibration:**

The monthly average regional 1-sigma calibration uncertainty for the ERBE scanner longwave and shortwave (based on solar incoming of  $348 \text{ Wm}^{-2}$ ) is estimated by to be on the order of  $2.1 \text{ Wm}^{-2}$  for SW TOA reflected flux, and  $2.4 \text{ Wm}^{-2}$  for LW TOA emitted flux. The combined (LW plus SW) 1-sigma uncertainty for net radiation is  $3.2 \text{ Wm}^{-2}$ .

### **Viewing Angle Sampling:**

The monthly average regional 1-sigma angle sampling uncertainty for the ERBE scanner longwave and shortwave (based on solar incoming of  $348 \text{ Wm}^{-2}$ ) is estimated by to be on the

order of  $3.3 \text{ Wm}^{-2}$  for of SW TOA reflected flux, and  $1.6 \text{ Wm}^{-2}$  for LW TOA emitted flux. The combined (LW plus SW) 1-sigma uncertainty for net radiation is  $3.7 \text{ Wm}^{-2}$ .

#### **Time Sampling:**

The monthly average regional 1-sigma time sampling uncertainty for the ERBE scanner longwave and shortwave (based on solar incoming of  $348 \text{ Wm}^{-2}$ ) is estimated by to be on the order of  $3.9 \text{ Wm}^{-2}$  for SW TOA reflected flux, and  $1.3 \text{ Wm}^{-2}$  for LW TOA emitted flux. The combined (LW plus SW) 1-sigma uncertainty for net radiation is  $4.1 \text{ Wm}^{-2}$ .

#### **Spatial Sampling:**

The monthly average regional  $1-\sigma$  spatial sampling uncertainty for the ERBE scanner longwave and shortwave (based on solar incoming of  $348 \text{ Wm}^{-2}$ ) is estimated by to be on the order of  $0.3 \text{ Wm}^{-2}$  for SW TOA reflected flux, and  $0.2 \text{ Wm}^{-2}$  for LW TOA emitted flux. The combined (LW plus SW)  $1-\sigma$  uncertainty for net radiation is  $0.4 \text{ Wm}^{-2}$ .

#### **Gap Filling Methods:**

None

#### **Total Error Summary:**

The monthly average regional  $1-\sigma$  total uncertainty for the ERBE scanner longwave and shortwave (based on solar incoming of  $348 \text{ Wm}^{-2}$ ) is estimated to be on the order of  $5.5 \text{ Wm}^{-2}$  for SW TOA reflected flux, and  $3.2 \text{ Wm}^{-2}$  for LW TOA emitted flux. The combined (LW plus SW)  $1-\sigma$  uncertainty for net radiation is  $6.4 \text{ Wm}^{-2}$ .

#### **References:**

- Barkstrom, B. R., 1984: The Earth Radiation Budget Experiment (ERBE). *Bull. Amer. Meteor. Soc.*, **65**, 1170–1185.
- Brooks, D. R., E. F. Harrison, P. Minnis, J. T. Suttles, and R. S. Kandel, 1986: Development of algorithms for understanding the temporal and spatial variability of the earth's radiation balance. *Rev. Geophys.*, **24**, 422–438.
- Suttles, J. T., and Coauthors, 1988: *Angular Radiation Models for Earth–Atmosphere System*. Vol. I, *Shortwave Radiation*. NASA RP-1184, NASA Langley Research Center, 144 pp.
- Suttles, J. T., and Coauthors, 1989: *Angular Radiation Models for Earth–Atmosphere System*. Vol. II, *Longwave Radiation*. NASA RP-1184, NASA Langley Research Center, 84 pp.
- Wielicki, B. A., and R. N. Green, 1989: Cloud identification for ERBE radiative flux retrieval. *J. Appl. Meteor.*, **28**, 1133–1146.
- Wielicki, B. A., R. D. Cess, M. D. King, D. A. Randall, and E. F. Harrison, 1995: Mission to Planet Earth: Role of Clouds and Radiation in Climate. *Bull. Amer. Meteor. Soc.*, **76**, 2125–2153.

### A.1.3: ScaRaB (Scanner for Radiation Budget)

M. Viollier and R. Kandel

#### Description:

Two models of the ScaRaB radiometer (Scanner for Radiation Budget) have operated in space aboard the Russian satellites Meteor-3-7 (February 1994 to March 1995, Kandel et al., 1998) and Resurs 1-4 (August 1998 to April 1999, Duvel et al., 2001). These missions are the result of a co-operative project between France, Russia and Germany. The satellite orbits were polar, sun-synchronous (10:30) for the satellite “Resurs”, and with a slow precession (24 hours in roughly 200 days) for Meteor.

ScaRaB is a 4-channel cross-track scanning radiometer (details in Monge et al., 1991). The earth scanning angle is  $100^\circ$ . Scanning is obtained by rotation of a cylinder carrying the optics, filters, detector, choppers and analog-digital conversion electronics about an axis parallel to the direction of motion of the spacecraft, within a cylinder mounted on the spacecraft. The four channels (Table 1) include two broad spectral bands from which the reflected SW and emitted LW radiances are derived, and two narrower bands, one corresponding to the infrared atmospheric window, the other to the visible (green to red) portion of the solar spectrum. Both auxiliary channels have been used to study the narrow-to-broad band conversions (Chang and Trishchenko, 2000). The window infrared channel is also particularly useful for the geophysical cross-calibration of the broadband channels (Duvel and Raberanto, 2000).

*Table 1: ScaRaB channels*

Channel no.	Description	Wavelength range	Filter Type
1	Visible (VIS)	0.55 — 0.65 $\mu\text{m}$	Interference
2	Solar (SW)	0.2 — 4 $\mu\text{m}$	Fused silica
3	Total (TW)	0.2 — $>50$ $\mu\text{m}$	Unfiltered
4	IR window (IRW)	10.5 — 12.5 $\mu\text{m}$	Interference

General designs of the ERBE/CERES and ScaRaB scanners are quite different: DC thermistor bolometer for ERBE/CERES, AC pyro-electric detector with 16 Hz frequency chopping against an internal blackbody for ScaRaB; telescope with two mirrors for ERBE/CERES and one for ScaRaB.

#### Calibration:

Radiometric performances were first estimated on the ground (Sirou et al., 2000). In a vacuum chamber, ScaRaB was tested with an actively-controlled-temperature blackbody. These operations established the linearity of response and provided radiometric calibration of the temperature and emissivity of the on-board calibration blackbodies, and calibration of the temperature dependence of detector gains. For the solar ground calibration, the calibration standard was a reference diffuser, illuminated by the Sun. Simultaneously; the incoming solar irradiance was measured by a calibrated pyrheliometer (Mueller et al, 1997). In laboratory, additional tests were carried out with a calibrated integrating sphere. The accuracy of the on-board lamp sources was then estimated to be better than 1.5%. In flight, the temperature of the reference blackbody (emissivity = 0.993) for channel 3 is measured by a platinum resistance thermometric sonde and included in the scientific telemetry. For the SW domain, the calibration system was designed with 3 sets of pre-aged incandescent lamp source (Tremas et al., 1997).

The thermal leak corresponds to the Earth emitted radiation captured by the SW channel (beyond 3.5  $\mu\text{m}$ ). Owing to inter-channel comparisons, it was found to be lower than  $0.8 \text{ Wm}^{-2} \text{ sr}^{-1}$  and corrected as function of the window IR measurements. Daytime radiation in the LW band (nominally 4 to 50  $\mu\text{m}$ ) is determined by appropriately weighted subtraction of the SW signal from the TW signal. Possible differences or variations in SW spectral response of the SW and TW channels can lead to errors in filtered and unfiltered daytime LW radiances, but analysis have indicated that these LW daytime errors are smaller than 0.3 %.

Because of the channel stability (0.1% stability was measured in flight on channel 3), the inter-channel consistency was also evaluated by complementary cross-checking operations. Analysis of very cold bright daytime cloud scenes over tropical convective regimes, for which the TW signal is dominated by SW reflection and the LW component can be estimated independently from the IRW radiance, yields agreement at the 1% level (Duvel and Raberanto, 2000).

Inter-comparisons of ScaRaB and ERBE WFOV were carried out by Bess et al. (1997), and between ScaRaB and CERES by Haeffelin et al., (2001). They are discussed by Smith et al. (2006) who show significant agreements (deviations < 1%).

### **Conversion to fluxes and time integration:**

In order to minimize biases between ERBE and ScaRaB time series, the data processing is based on ERBE algorithms according to published descriptions: Smith et al. (1986), Wielicki and Green (1989) for inversion, and Brooks et al. (1986) for the Monthly Time Space Averaging. However, the LW day-time calculation and the spectral corrections have been adjusted to the ScaRaB spectral characteristics (Viollier et al., 1995). The ScaRaB spectral response is not perfectly flat, and diminishes substantially at wavelengths below 0.4  $\mu\text{m}$ . Using the simulation of reflected SW radiances for 530 cases, a correction for clear and partly cloudy ocean scenes is applied and reduces the spectral filtering errors (rms differences of  $0.83 \text{ Wm}^{-2}\text{sr}^{-1}$  for the 530 cases).

The CERES algorithms (Loeb et al., 2005) cannot be applied due to the lack of imager (such as VIRS or MODIS) aboard the same platform. However, several ways to improve the ERBE-type processing have been studied. Instead of using the LW anisotropic emission factor tabulated for different viewing zenith angles, seasons, latitude band, and scene type, the angular LW correction is parameterized (Stubenrauch et al., 1993) as a function of the atmospheric pseudo-absorptance defined as the normalized difference between the broadband LW radiance (from ScaRaB channels 3 and 2) and the integrated Planck emission at the 11.5  $\mu\text{m}$  brightness temperature derived from the ScaRaB window channel 4. Applications to CERES estimates have shown that this method is efficient at least for the clear-sky scene.

New SW angular corrections have been computed for desert scenes using Meteosat data (Capderou 1998). The two ScaRaB narrow-band radiances have also been used to refine cloud scenes taking into account cloud phase and spatial heterogeneity. This is done by applying the ISCCP algorithms to the ScaRaB narrow-band radiances. General assessment is obtained by comparing ScaRaB data, ScaRaB ISCCP-reprocessed data and real ISCCP data (Stubenrauch et al., 2002).

For the diurnal interpolation, Standfuss et al., (2001) have proposed to use a diurnal climatology of the planetary albedo to improve the reflected solar flux monthly means estimates. The regional diurnal (hourly) albedo climatology is derived for each month from the 5-year data record of ERBS. The choice depends upon the compatibility of the instantaneous observation with the climatological value at observation time: with increasing disagreement between observed and climatological albedo, the use of the climatology for diurnal extrapolation is increasingly restricted.

The data provided to the GEWEX-RFA group correspond to the ERBE-like results. The other versions do not change values of the global means by more than one percent. Kandel and Viollier (2005) have summarized the different estimations of the global and annual means for the Earth as well as for the other planets.

## References:

- Bess, T.D., G.L. Smith, R.N. Green, D.A. Rutan, R.S. Kandel, P. Raberanto, and M. Viollier, 1997 : Intercomparison of Scanning Radiometer for Radiation Budget (ScaRaB) and Earth Radiation Budget Experiment (ERBE) results, Proc. 9th Conf. Atmos. Radiation, Long Beach, California.
- Brooks, D.R., E. H. Harrison, P. Minnis, J. T. Suttles, and R. Kandel, 1986 : Development of Algorithms for Understanding the Temporal and Spatial Variability of the Earth's Radiation Balance, *Rev. Geophys.*, 24, 2, 422-438.
- Capderou, M., 1998 : Determination of the shortwave anisotropic function for clear-sky desert scenes from ScaRaB data. Comparison with models issued from other satellites. *Journal Of Applied Meteorology*, 37 1398-1411
- Chang F.-L., Li Z. and A.P. Trishchenko, 2000 : The dependence of TOA Reflectance Anisotropy on Cloud Properties Inferred from ScaRaB Satellite Data. *J. Appl. Meteor.*, 39, 2480-2493.
- Duvel, J.-Ph., and P. Raberanto, 2000 : A geophysical cross-calibration approach for broadband channels: Application to the ScaRaB experiment, *J. Atmos. Oceanic Technol.* 17, 1609-1717
- Duvel, J. P., S. Bouffiès-Cloch e, and M. Viollier, 2000 : Determination of shortwave Earth reflectances from visible radiance measurements: Error estimate using ScaRaB data, *J. Appl. Meteorol.*, 39, 957– 970.
- Duvel, J. P., M. Viollier, P. Raberanto, R. Kandel, M. Haeffelin, L.A. Pakhomov, V.A. Golovko, J. Mueller, R. Stuhlmann, and the International ScaRaB Scientific Working Group (ISSWG), 2001: The ScaRaB-Resurs Earth Radiation Budget Dataset and first results, *Bull. Am. Metereol. Soc.*, 82, 1397-1408.
- Haeffelin, M., B. Wielicki, J.-Ph. Duvel, K. Priestley, and M. Viollier, 2001 : Intercalibration of CERES and ScaRaB Earth radiation budget datasets using temporally and spatially collocated radiance measurements. *Geophys. Res. Let.* 28(1), 167-170
- Kandel, R., M. Viollier, P. Raberanto, J. P. Duvel, L. A. Pakhomov, V. A. Golovko, A. P. Trishchenko, J. Mueller, E. Raschke, R. Stuhlmann, and the International ScaRaB Scientific Working Group (ISSWG), 1998: The ScaRaB Earth Radiation Budget Dataset, *Bull. Am. Meteorol. Soc.*, 79, 765-783.
- Kandel, R., and M. Viollier, 2005: Planetary Radiation Budgets, *Space Science Rev.*, 120, 1-26.
- Li, Z., and A. Trishchenko, 1999 : A study towards an improved understanding of the relation between visible and SW albedo measurements, *J. Atmos. Oceanic Technol.*, 17, 347– 360.
- Loeb, N. G., S. Kato, K. Loukachine, and Manalo-Smith N., 2005 : Angular Distribution Models for Top-of-Atmosphere Radiative Flux Estimation from the Clouds and the Earth's Radiant Energy System Instrument on the Terra Satellite. Part I: Methodology, *J. Atm. Ocean. Techn.*, 22, 338-351, doi:10.1175/JTECH1712.1.
- Monge, J.L., R.S. Kandel, L.A. Pakhomov, and V.I. Adasko, 1991 : ScaRaB Earth radiation budget scanning radiometer, *Metrologia*, 28, 261-284.
- Mueller, J., R. Stuhlmann, R. Becker, E. Raschke, H. Rinck, P. Burkert, J.L. Monge, F. Sirou, R. Kandel, T. Tr emas, and L.A. Pakhomov, 1997 : Ground Characterization of the Scanner for Radiation Budget (ScaRaB) Flight Model 1, *J. Atmos. Oc. Technol.*, 14, 802-813.

- Sirou F., Dinguirard M., and T. Tremas, 2000 : Ultimate determination of ScaRaB flight model 2 channel gains, *Metrologia* 37 : 469-472.
- Smith, G.L., R.N. Green, E. Raschke, L.M. Avis, J.T. Suttles, B.A. Wielicki, and R. Davies, 1986 : Inversion methods for satellite studies of the earth's radiation budget : development of algorithms for the ERBE mission. *Rev. Geophys.*, 24, 407-421.
- Smith, G. L., Szewczyk, Z. P., Rutan, D. A., and Lee III, R. B., 2006 : Comparison of measurements from satellite radiation budget instruments, *J. Geophys. Res.*, 111, D04101, doi:10.1029/2005JD006307.
- Standfuss C., Viollier M., Kandel R.S and J. Ph. Duvel, 2001 : Regional Diurnal Albedo Climatology and Diurnal Time Extrapolation of Reflected Solar Flux Observations. Application to the ScaRaB record, *Journal of Climate*, 14, 1129-1146.
- Stubenrauch, C., J.-P. Duvel, and R.S. Kandel, 1993 : Determination of longwave anisotropic emission factors from combined broad- and narrow-band radiance measurements, *J. Appl. Meteor.*, 32, 848-856.
- Stubenrauch, C. J., V. Briand and W. B. Rossow, 2002 : The role of clear sky identification in the study of cloud radiative effects: Combined analysis from ISCCP and the Scanner of Radiation Budget (ScaRaB). *J. Appl. Meteor.*, 41, 396-412.
- Tremas T. and M. Dinguirard, 1997: Calibration of ScaRaB FM1 : Methods and first results. *Adv. Space Res.* 19, 1335-1343.
- Trishchenko, A., and Z. Li, 1998 : Use of ScaRaB measurements for validating a GOES-based TOA radiation product. *J. Appl. Meteor.*, 37, 591-605.
- Viollier, M., R. Kandel, and P. Raberanto, 1995 : Inversion and space-time averaging algorithms for ScaRaB (Scanner for Earth Radiation Budget) - Comparison with ERBE. *Annales Geophysicae*, 13, 959-968.
- Wielicki, B. A., and R. N. Green, 1989 : Cloud identification for ERBE radiative flux retrieval. *J. Appl. Meteor.*, 28, 1133-1146.

### A.1.4: CERES Scanner Datasets (CERES-SRBAVG-GEO, CERES-SRBAVG nonGEO, CERES-EBAF, and CERES-ERBE-like)

D. Doelling and T. Wong

#### Dataset Description:

The CERES radiative fluxes are based on broadband radiometer measurements that use precision thermistor-bolometers. The CERES instruments were flown on TRMM, with a 10 km nominal ground footprint, on 46 day precessing orbit and limited to 40° latitude, with a data record from January to August 1998; on Terra with a 20 km nominal footprint on a sun-synchronous 10:30 AM orbit, with the data record beginning in March 2000; and on Aqua with a 20 km nominal footprint on a sun-synchronous 1:30 PM orbit, with the data record beginning in July 2002. The CERES absolute calibration uncertainty is 2% in the SW and 1% in the total channels at the 95% confidence level (Loeb et al., 2008). The CERES instruments rely on onboard lamps and blackbodies for calibration stability (Priestley et al 2002). The Edition2 Rev-1 correction, which was necessary to account for spectral darkening of the transmissive optics on the CERES SW channels, were applied to the SW fluxes in the GEWEX database.

CERES is a 3-channel instrument that measures filtered SW (0.3-5 $\mu$ m), total (0.3-200 $\mu$ m) and IR window (8-12 $\mu$ m) radiances. The CERES spectral response functions are not flat and the filtered radiances are then unfiltered (Loeb et. al 2001). The LW (5-200 $\mu$ m) radiance is taken from the difference of the total and SW radiances. The viewing and solar dependent radiances are then converted to fluxes using CERES ADMs (Loeb et al 2005) for the CERES-SRBAVG-GEO, CERES-SRBAVG-nonGEO and CERES-EBAF dataset and ERBE ADMs (Suttles et al., 1989) for the CERES-ERBE-like dataset. The ADMs are scene dependent and determined from the coincident MODIS pixel level cloud retrievals on both Aqua and Terra and VIRS on TRMM. The CERES ADMs employed the use of the rotating azimuth plane scan mode, which ensures all view and azimuth angles are observed by the CERES instrument.

The CERES footprint fluxes are then spatially averaged into a 1° x 1° equal area nested grid for the CERES-SRBAVG-GEO, CERES-SRBAVG-nonGEO and CERES-EBAF dataset and a 2.5° x 2.5° equal angle grid for the CERES-ERBE-like dataset. For the GEWEX-RFA, the CERES-SRBAVG-GEO, CERES-SRBAVG-nonGEO and CERES-EBAF datasets are further averaged into a 2.5° x 2.5° equal angle grid. In order to derive the monthly mean flux from the CERES observations, the CERES observed fluxes are temporally interpolated in 1-hour increments and then averaged. The CERES-SRBAVG-nonGEO and the CERES-ERBE-like product use the ERBE temporal averaging techniques. The LW the fluxes are linearly interpolated and utilize a half-sine fit over land to take into account land heating. The SW fluxes employ sun-angle dependent diurnal models, which assume linearly changing cloud properties between measurements, similar to ERBE, however there are over 600 CERES scene dependent models compared with 12 for ERBE.

To remove the diurnal sampling bias present in the CERES SRBAVG-nonGEO product, the CERES-SRBAVG-GEO product incorporates 3-hourly geostationary derived broadband fluxes and cloud retrievals to infer the meteorological changes between CERES observations. The geostationary broadband fluxes providing the shape of the diurnal changes are then anchored to the accurate CERES measurements, thus retaining the CERES calibration. The geostationary radiances are first calibrated against MODIS to ensure stability and uniformity across the 2-channel geostationary cloud retrievals produced by the 5 geostationary satellites that are

employed. To remove any remaining systematic biases in the geostationary derived broadband fluxes, the fluxes are normalized against CERES (Doelling et. al. 2006).

The Terra CERES-SRBAVG-nonGEO or GEO products have an annual mean net TOA radiation imbalance on the order of 7.0 and 6.5  $\text{Wm}^{-2}$  respectively and is within in upper end of the uncertainty constraints. In order for the CERES fluxes to be more useful in climate model evaluations, the net flux imbalance was adjusted to the ocean heat storage term of 0.85  $\text{Wm}^{-2}$  in the CERES-EBAF product. A constraint algorithm was used to adjust the TOA fluxes within their range of uncertainties from calibration, unfiltering, ADMs, and temporal averaging (Loeb et al 2008).. The greatest uncertainty was in the instrument calibration. Also clear-sky fluxes were estimated for all  $1^\circ$  regions that did not have a single clear-sky footprint in order to obtain a complete global clear-sky map, which is not the case in the SRBAVG products. These were based on the clear-sky MODIS pixel radiances within a partly cloudy CERES footprint, using clear-sky MODIS-CERES narrowband to broadband regressions (Loeb et al 2008). Loeb et al 2008 provides the most detailed analysis of all CERES instrument and algorithm uncertainties.

Essentially the CERES-ERBE-like products are useful for those comparing fluxes to the original ERBE 1985-1989 product, since the CERES radiances were processed using entirely ERBE algorithms. The CERES-SRBAVG-nonGEO (CERES-only) data are suited to study ADM improvements and conditions during CERES overpasses. The CERES-SRBAVG-GEO (CERES+GEO) product is the most diurnally robust product available and the CERES-EBAF (net adjusted and clear-sky filled) product has adjusted the SRBAVG-GEO fluxes to remove the net imbalance. At [http://eosweb.larc.nasa.gov/PRODOCS/ceres/table\\_ceres.html](http://eosweb.larc.nasa.gov/PRODOCS/ceres/table_ceres.html) are located these original datasets at the NASA Langley Atmospheric Science Data Center (ASDC) and further notes and cautions about these datasets can be obtained in the corresponding Data Quality Summaries.

## References:

- Doelling, D. R., D. F. Keyes, D. F., Young, B. A. Wielicki, and T. Wong, 2006: The newly released 5-year Terra-based monthly CERES radiative flux and cloud product. *12<sup>th</sup> Conference on Atmospheric Radiation*, 10-14 July 2006, Madison, WI, American Meteorological Society, Paper No. 9.4
- Loeb, N.G., K.J. Priestley, D.P. Kratz, E.B. Geier, R.N. Green, B.A. Wielicki, P. O'R. Hinton, and S.K. Nolan, 2001: Determination of unfiltered radiances from the Clouds and the Earth's Radiant Energy System (CERES) instrument. *J. Appl. Meteor.*, **40**, 822-835
- Loeb, N.G., S. Kato, K. Loukachine, and N.M. Smith, 2005: Angular distribution models for top-of-atmosphere radiative flux estimation from the Clouds and the Earth's Radiant Energy System instrument on the Terra Satellite. Part I: Methodology, *J. Atmos. Ocean. Tech.*, **22**, 338-351
- Loeb, L.G., B. A. Wielicki, D. R. Doelling, G. L. Smith, D. F. Keyes, S. Kato, N. M. Manalo-Smith, T. Wong, 2008, Towards Optimal Closure of the Earth's Top-of-Atmosphere Radiation Budget, Submitted *J of Climate*
- Priestley, K.J., B.A. Wielicki, R.N. Green, M.P.A. Haeffelin, R.B. Lee, and N.G. Loeb, 2002: Early radiometric validation results of the CERES Flight Model 1 and 2 instruments onboard NASA's Terra spacecraft, *Adv. Space Res.*, **30**, 2371-2376.
- Suttles, J. T., and Coauthors, 1988: Angular radiation models for Earth-atmosphere system; Vol. I, Shortwave radiation. NASA RP-1184, 144 pp.
- Suttles, J. T., and Coauthors, 1989: Angular radiation models for Earth-atmosphere system; Vol. II, Longwave radiation. NASA RP-1184, 84 pp.

## A.1.5: HIRS OLR Data Set

Hai-Tien Lee and Robert G. Ellingson

### Description of the HIRS OLR Data Set

The HIRS outgoing longwave radiation (OLR) data set is a climate data record (CDR) product that provides monthly mean OLR on  $2.5^{\circ} \times 2.5^{\circ}$  gridded maps with global coverage. The current release Ver02Rev02 (<http://www.ncdc.noaa.gov/cdr/operationalcdrs.html>) hosted at the NOAA National Climate Data Center (NCDC) Climate Data Record program spans from Jan 1979 to Dec 2010 (Lee, 2011). The data set submitted to the GEWEX Radiative Flux Assessment (RFA) project contains HIRS OLR data from Jan 1979 to Sep 2003, which is a subset and is consistent with that released through NCDC. Up to date HIRS OLR data can be obtained via [http://cics.umd.edu/HIRS\\_OLR](http://cics.umd.edu/HIRS_OLR). The HIRS OLR time series can be extended with the operational hyperspectral sounding instruments including IASI and CrIS, and development is in progress (Lee et al., 2010).

### HIRS OLR Algorithm

Ellingson et al. (1989, 1994) developed a multi-spectral regression-based algorithm that can estimate the OLR using radiance observations from the High-resolution Infrared Sounder (HIRS) onboard the operational NOAA TIROS-N series Polar-Orbiting Environmental Satellites (POES) and Eumetsat MetOp satellites. The HIRS OLR regression models are constructed with the radiance and flux simulations using HIRS instrument-specific spectral responses that ensure flux estimation consistency across the satellites. The HIRS OLR regression model performs the narrow-to-broadband conversion and the angular integral simultaneously given radiance observations at a set of frequencies at any observing angle.

### HIRS OLR CDR Production

#### Radiance Calibration

The HIRS instruments are scanning radiometers that have a field of view of 17 km at the nadir (10 km for HIRS/4 instrument onboard NOAA-19 and MetOp-A/B). The HIRS radiance calibration is performed with McMillin method (NOAA POD Users Guide 1998, Appendix M) that incorporates the nonlinear effects of instrument temperature variations in earth-view scans encompassed with calibration scans. This radiance calibration method is applied throughout the time series to achieve radiance data consistency (see Lee et al., 2007 also for subsequent sections hereto).

#### Inter-satellite Calibration

Inter-satellite calibration is performed to eliminate the gross differences between the OLR estimated from different satellites. A set of constant bias adjustments for every satellite was derived, propagated from the reference satellite NOAA-9. This ensures the continuity in the OLR time series derivation.

### HIRS OLR Diurnal Models

Prior to year 2002, the NOAA POSE is operating at two-satellite configuration, nominally at 7:30 and 2:30 equator crossing time, for morning and afternoon satellites, respectively. NOAA-17 is the first to fly on 10:00 (late morning) orbit, followed by MetOp-2 (A). All NOAA POES have precession orbits. The HIRS OLR diurnal models are constructed using composite, inter-satellite calibrated HIRS OLR as observed at different local times from all satellites, at each 2.5°x2.5° grid box and for each month. The monthly mean integral is constrained with these monthly regional diurnal models such that the orbital drift aliasing effects upon the OLR time series can be minimized.

### **Total Error Summary**

The validation and inter-comparison of HIRS OLR data with ERBE-scanner, CERES-scanner, ERBS Non-scanner, and other OLR products have been conducted for numerous times with very consistent results. It is also a continuous effort for HIRS OLR CDR quality assurance purpose.

The HIRS OLR agrees with CERES with accuracy to within 2 Wm<sup>-2</sup> and precession of about 4 Wm<sup>-2</sup> globally. In terms of time series stability, the HIRS OLR CDR, to 95% confidence, has stability comparable to that of the ERBS Non-scanner OLR time series, at about 0.3 Wm<sup>-2</sup> per decade estimated by Wong et al. (2006).

### **References:**

- Ellingson, R. G., R. G., D. J. Yanuk, H.-T. Lee and A. Gruber, 1989: A technique for estimating outgoing longwave radiation from HIRS radiance observations. *J. Atmos. Ocean. Tech.*, **6**, 706-711.
- Ellingson, R. G., H.-T. Lee, D. Yanuk and A. Gruber, 1994: Validation of a technique for estimating outgoing longwave radiation from HIRS radiance observations, *J. Atmos. Ocean. Tech.*, **11**, 357-365.
- Lee, H.-T., R. G. Ellingson, and A. Gruber, 2010: Development of IASI outgoing longwave radiation algorithm. Proceedings of the 2nd IASI International Conference, Annecy, France, January 25-29, 2010.
- Lee, H.-T., A. Gruber, R. G. Ellingson and I. Laszlo, 2007: Development of the HIRS Outgoing Longwave Radiation climate data set. *J. Atmos. Ocean. Tech.*, **24**, 2029–2047.
- Lee, H.-T., 2011: HIRS Outgoing Longwave Radiation Climate Data Record Algorithm Theoretical Basis Document (C-ATBD) (<ftp://ftp.ncdc.noaa.gov/pub/data/sds/cdr/docs/hirs-olr-catbd.pdf>)
- Wong, T., B. A. Wielicki, R. B. Lee III, G. L. Smith, K. A. Bush, and J. K. Willis, 2006: Reexamination of the observed decadal variability of earth radiation budget using altitude corrected ERBE/ERBS nonscanner WFOV data. *J. Climate*, **19**, 4028–4040.

## A.1.6: NASA/GEWEX Surface Radiation Budget (SRB) Data Set (Primary and Quality-Check Algorithms)

P. W. Stackhouse<sup>1</sup>, S. Gupta<sup>2</sup>, S. Cox<sup>2</sup>, T. Zhang<sup>2</sup> and C. Mikovitz<sup>2</sup>

### Introduction

The NASA/GEWEX Surface Radiation Budget (SRB) project at the NASA Langley Research Center (LaRC) has, over the years, submitted multiple datasets of surface and top-of-atmosphere (TOA) shortwave (SW) and longwave (LW) fluxes to the GEWEX Radiative Flux Assessment (RFA) project. Both SW and LW surface fluxes are produced with two sets of algorithms: one set designated as primary (GSW and GLW), and the other as quality-check (QCSW and QCLW). TOA fluxes are produced with primary algorithms only. All except the quality-check SW algorithm derive fluxes on 3-hourly resolution, which are then averaged into daily, monthly, and monthly/3-hourly values. Quality-check SW fluxes are computed on a daily resolution and averaged into monthly values. As per RFA requirement, only monthly averages are submitted to RFA. These datasets are produced originally on a  $1^\circ \times 1^\circ$  global grid and are re-gridded to  $2.5^\circ \times 2.5^\circ$  for submission to RFA. The latest data submitted for the GSW algorithm is designated as Release-2.81 while the latest ones for the other three algorithms are Release-2.5. These datasets cover a period of 22 years (July 1983 – June 2005). Datasets from the older versions of the algorithms are designated as Release-2.0 for GSW and QCLW algorithms and Release-2.1 for the GLW. The older datasets covered a period of about 12 years (July 1983 – October 1995). All datasets are produced using satellite-derived cloud parameters, ozone fields from multiple sources, reanalysis meteorology, and several other ancillary datasets. Surface fluxes from all algorithms are validated with ground-based measurements primarily from the Baseline Surface Radiation Network (BSRN) for the period 1992 onward. Validation for earlier periods is performed using ground data from the Global Energy Balance Archive (GEBA), and other sources.

### Description of Radiation Models

**Primary SW (GSW) Algorithm:** The primary SW algorithm used here is a greatly modified version of the method described originally in Pinker and Laszlo (1992) and follows the steps outlined below. Extensive look-up tables of clear and cloudy sky atmospheric transmissivity and reflectivity over a zero-albedo surface are produced for five SW bands (0.2-0.4, 0.4-0.5, 0.5-0.6, 0.6-0.7, and 0.7-4.0  $\mu\text{m}$ ) for a range of values of column ozone, column water vapor, surface elevation, aerosol or cloud optical depth, aerosol composition, and solar zenith angle using a delta-Eddington method. Next, 3-hourly narrowband visible radiances from satellites are converted to broadband TOA albedo for both clear-sky and cloudy conditions. Surface albedoes in each of the five SW bands are derived and incorporated into the surface albedo model of Briegleb et al. (1986) using five surface types from Matthews et al. (1985). Absolute value of the surface albedo for the scene is determined by scaling the spectral values by the factor required to produce the same broadband TOA albedo implied by the satellite clear-sky composite radiance. Values of TOA albedo computed using this surface albedo and the look-up tables are matched with those derived from satellite radiances by adjusting aerosol and cloud optical depths. Finally, clear- and cloudy-sky fluxes are derived using all of the above information.

**Primary LW (GLW) Algorithm:** The primary LW model is modified version of the delta-two/four-stream combination approximation model outlined originally in Fu et al. (1997). Changes from the original formulation include the use of 2-m temperature and humidity values in the profiles and additional use of surface skin temperature as a separate variable. Cloud properties are assigned within each grid box initially by using information from ISCCP data and adjusted finally by using a maximum-random overlap scheme. Probabilities are computed for each of the 16 configuration combinations of the five ISCCP cloud types. Maximum overlap is assumed within high, middle, and low layers. Random overlap between those main layers is then assumed. Fluxes are computed in 12 spectral bands for each configuration and spectrally integrated. Final flux for the grid box is computed by weighting these fluxes by the probability of each cloud configuration.

**Quality-Check SW (QCSW) Algorithm:** The quality-check SW algorithm consists of physical parameterizations which account for the attenuation of solar radiation in simple terms separately for clear atmosphere and clouds. Surface insolation,  $F_{\text{sfc}}$ , is computed as

$$F_{\text{sfc}} = F_{\text{toa}} T_a T_c, \quad (1)$$

where  $F_{\text{toa}}$  is the TOA insolation,  $T_a$  is the transmittance of the clear atmosphere, and  $T_c$  is the column transmittance attributable to the presence of clouds. All quantities in Eq. 1 refer to broadband SW region approximately 0.2 to 5.0  $\mu\text{m}$ .  $T_a$  and  $T_c$  are computed using simple broadband atmospheric and cloud properties. For a detailed description of the algorithm, the reader is referred to Gupta et al. (2001).

**Quality-Check LW (QCLW) Algorithm:** The quality-check LW algorithm consists of fast parameterizations developed from an accurate narrowband radiative transfer model for computing clear-sky flux and cloud radiative effect in terms of an effective emitting temperature of the lower atmosphere, column water vapor, cloud amount, and cloud-base height. All-sky downward LW flux ( $F_{\text{all}}$ ) is computed as

$$F_{\text{all}} = F_{\text{clr}} + F_{\text{cre}} A_c, \quad (2)$$

where  $F_{\text{clr}}$  is the clear-sky flux,  $F_{\text{cre}}$  is the cloud radiative effect, and  $A_c$  is the fractional cloud amount derived from ISCCP DX data. For a detailed description of the algorithm, the reader is referred to Gupta et al. (1992).

## Model Inputs

Meteorological inputs for this project were obtained from several satellite data archives and data assimilation products. Cloud properties were derived from International Satellite Cloud Climatology Project (ISCCP; Rossow and Schiffer 1999) pixel-level (DX) data and the same method used by ISCCP (Rossow et al. 1996). Other meteorological inputs, namely, the temperature and humidity profiles were taken from GEOS-4 reanalysis product (Bloom et al. 2005) for release-2.5 and -2.81 datasets and from an earlier version, GEOS-2, for Release-2.0 and -2.1, all from the Global Modeling and Assimilation Office (GMAO) at NASA Goddard Space Flight Center (GSFC). For aerosol optical depths, the GSW algorithm started out with initial guess values based on four surface types that were adjusted in the process of matching model-derived and satellite-measured radiances. The QCSW model used monthly climatologies of aerosol optical depths for 10 different species derived from MATCH data (Collins et al. 2001). Corresponding values of single scattering albedo and asymmetry parameter were derived from the OPAC database (Hess et al. 1998).

Column ozone data for the entire length of this dataset were not available from a single source. Bulk of ozone data used came from the Total Ozone Mapping Spectrometer (TOMS) instrument operating a number of platforms starting with Meteor-3 and Nimbus-7 in the early years, followed by ADEOS-3 and EP-TOMS, and OMI on Aura. Since these instruments provided no data for polar night regions, TIROS Operational Vertical Sounder (TOVS) ozone data extracted from ISCCP-D1 files were used to fill the polar night gaps, and even smaller gaps at lower latitudes as needed. Note that the two SW algorithms use the total column ozone as such. The GLW algorithm creates the desired vertical profile by apportioning total column ozone using seasonal climatological ozone profiles available in the literature for each  $10^\circ$  latitude band. The QCLW algorithm takes ozone into account only implicitly. Both LW algorithms use the surface emissivity map developed by Wilber et al. (1999).

TOA insolation computation for Release-2.0 GSW results is made with the same method as used by Pinker and Laszlo (1992) and using a solar constant value of  $1359 \text{ Wm}^{-2}$ . For Release-2.81 results, a method based on the astronomical almanac as outlined by Michalsky (1988) and a solar constant of  $1367 \text{ Wm}^{-2}$  is used. For the Release-2.5 QCSW algorithm, the method described in Gupta et al. (2001) and a solar constant of  $1367 \text{ Wm}^{-2}$  is used.

### **Gap-filling for the Input Data:**

Substantial gaps occur often in all types of input data fields though it is desirable to have derived fluxes available for all grid boxes every 3 hours. A strategy for filling gaps in the input fields is, therefore, essential for producing a long-term global dataset. Gap-filling process may be significantly different depending on the flux algorithm requirements as described below.

**Gap-filling for GSW:** The basic procedure consists of the following steps in the listed order.

1. Fill with the value from the nearest available hour on the same day, or
2. Fill with the value from the nearest grid box with same surface type and latitude on the same day, or
3. Use monthly average value of the variable.

Fields of all input meteorological variables (column water vapor, column ozone, cloud fraction, and ice/snow fraction) are adequately filled by these basic steps. Satellite radiances are not filled directly. In cases of missing radiances, intermediate fields calculated from the radiances (surface albedo, aerosol optical depth, cloud optical depth) are filled instead. The filling procedure generally follows the numbered steps above, with some exceptions made in grid cells that are in polar twilight for the month. Those cells receive no radiance information for that month, as ISCCP does not report visible radiances where the cosine of the solar zenith is below 0.2. In those cases, aerosol optical depth is set at the initial climatological value, surface albedo is set at the reference value for the surface type, and cloud optical depth is set at a value derived from a parameterization for that cell relating cloud fraction to cloud optical depth.

**Gap-filling for Cloud Parameters:** Gaps in all cloud amounts and cloud water paths (liquid or ice) are first filled by linear interpolation or replication from the eight 3-hourly values for the grid box within the same day. If a gap is still left, it is filled with values for the nearest spatial neighbor for the same hour and day. Interpolation in the natural logarithm of cloud optical depth weighted by cloud amount is used to fill that variable. Interpolation in Planck radiance weighted by cloud amount is used to fill gaps in cloud-top temperatures. Occasionally, radiative effects computed for total cloud amounts (VIS-IR or IR-only) and those computed for component

cloud amounts (high, mid, low or water and ice) were found to be significantly different. This situation is resolved by normalizing the combined effect of component clouds with that for the total cloud. No further gap filling was needed for the other three algorithms.

### Validation and Error Statistics:

Surface SW and LW fluxes of this dataset have been extensively validated against corresponding ground-based measurements from large databases from BSRN and GEBA, and smaller databases from the University of Oregon (UOR) and the Alpine Surface Radiation Budget (ASRB) network. As per RFA requirement, validation results presented below are for the latest GEWEX/SRB submissions and only use ground-measured fluxes available from the RFA database. BSRN data used in deriving statistics presented in Table 1 below came from up to 35 sites and cover the period January 1992 to March 2006. GEBA data (Gilgen et al. 1998; Gilgen and Ohmura 1999) were derived from historical databases from hundreds of sites collected over decades. Data from selected 32 sites of the GEBA database were used for deriving the results presented below. ASRB data used here are from 6 sites for January-December 2004. Only three sites from the UOR network are included in the RFA database. These sites are combined with GEBA data to constitute a single dataset and covers the period April 1979 to December 2008. The error statistics presented below provide a realistic assessment of the accuracy of the satellite derived datasets.

**Table A.1.6.1:** Mean bias and root-mean-square (RMS) difference between monthly average GEWEX/SRB surface SW and LW fluxes in comparison with ground-based measurements from various sources as described in the text. Units are  $Wm^{-2}$ .

Flux Algorithm	BSRN		GEBA and UOR		ASRB	
	Bias	RMS	Bias	RMS	Bias	RMS
GSW-2.81	-5.6	23.9	4.6	20.0	-20.7	29.0
QCSW-2.5	0.8	21.5	8.2	22.2	-17.1	28.5
GLW-2.5	-0.8	13.1	---	---	-1.5	9.9
QCLW-2.5	6.1	16.1	---	---	3.7	12.5

### References

- Bloom, S. J., A. da Silva, D. Dee, M. Bosilovich, J-D. Chern, S. Pawson, S. Schubert, M. Sienkiewicz, I. Stajner, M-L. Wu, 2005: Documentation and Validation of the Goddard Earth Observing System (GEOS) Data Assimilation System–Version 4. *NASA/TM–2005-104606*, Vol. 26.
- Briegleb, B. P., P. Minnis, V. Ramanathan and E. Harrison, 1986: Comparison of regional clear sky albedos inferred from satellite observations and model calculations. *J. Climate Appl. Meteor.*, **25**, 214-226.
- Collins, W. D., P. J. Rasch, B. E. Eaton, B. V. Khattatov, and J. –F. Lamarque, 2001: Simulating aerosols using a chemical transport model with assimilation of satellite aerosol retrievals: Methodology for INDOEX. *J. Geophys. Res.*, **106** (D7), 7313-7336.
- Fu, Q., K. N. Liou, M. C. Cribb, T. P. Charlock, and A. Grossman, 1997: Multiple Scattering Parameterization in Thermal Infrared Radiative Transfer. *J. Atmos. Sci.*, **54**, 2799–2812.
- Gilgen, H., and A. Ohmura, (1999): The Global Energy Balance Archive. *Bull. Amer. Meteor.*

- Soc.*, **80**, 831-850.
- Gilgen, H., M. Wild, and A. Ohmura (1998): Means and trends of shortwave irradiance at the surface estimated from GEBA. *J. Climate*, **11**, 2042-2061.
- Gupta, S. K., W. L. Darnell, and A. C. Wilber, 1992: A parameterization for longwave surface radiation from satellite data: Recent improvements. *J. Appl. Meteor.*, **31**, 1361-1367.
- Gupta, S. K., D. P. Kratz, P. W. Stackhouse Jr., and A. C. Wilber, 2001: The Langley Parameterized Shortwave Algorithm (LPSA) for surface radiation budget studies (Version 1.0). *NASA/TP-2001-211272*, 31 pp.
- Hess, M., P. Koepke, and I. Schult (1998): Optical Properties of Aerosols and Clouds: The Software package. *Bull. Amer. Meteor. Soc.*, **79**, 831-844.
- Michalsky, J. J., 1988: The astronomical almanac's algorithm for approximate solar position (1950-2050). *Solar Energy*, **40**, 227-235.
- Pinker, R., and I. Laszlo, 1992: Modeling Surface Solar Irradiance for Satellite Applications on a Global Scale. *J. Appl. Meteor.*, **31**, 194-211.
- Rossow, W. B., A. W. Walker, D. E. Beuschel, and M. D. Roiter, 1996: International Satellite Cloud Climatology Project (ISCCP) documentation of new cloud data sets. *World Climate Research Programme Rep. WMO/TD 737* (World Meteorological Organization, Geneva, Switzerland).
- Rossow, W. B., and R. A. Schiffer, 1999: Advances in understanding clouds from ISCCP. *Bull. Amer. Meteor. Soc.*, **80**, 2261-2288.
- Wilber, A.C., D. P. Kratz, S. K. Gupta, 1999: Surface Emissivity Maps for Use in Satellite Retrievals of Longwave Radiation. *NASA/TP-1999-209362*, 35 pp.

## A.1.7: ISCCP-FD TOA Data Set

W. B. Rossow and Y.- C. Zhang

### Data Product Description

The International Satellite Cloud Climatology Project (ISCCP) produces its Flux product by using its D-series cloud product and other ancillary datasets, hereby called ISCCP-FD (simplified as FD). The product is created by employing the NASA GISS climate Global Circulation Model (GCM) radiative transfer code [with necessary modifications, see *Zhang et al.*, 2004] and a collection of global datasets describing the physical properties of clouds, atmosphere and surface. These input datasets include 3-hrly cloud climatology [ISCCP D1, Rossow and Schiffer, 1999], daily atmospheric profiles of temperature and humidity [National Oceanic and Atmospheric Administration Television InfraRed Observation Satellites (TIROS) Operational Vertical Sounder], daily ozone abundances (Total Ozone Mapping Spectrometer), a climatology of cloud vertical layer distributions from rawinsonde humidity profiles [Wang et al., 2000], a climatology of cloud particle sizes [Han et al., 1994, 1999], a climatology of stratospheric aerosol and water vapor (Stratospheric Aerosol and Gas Experiment-II), a climatology of the diurnal variations of near-surface air temperature [surface weather observations and National Centers for Environmental Prediction (NCEP-1) re-analysis], a climatology of tropospheric aerosols (NASA GISS climate model), and the spectral dependence of land surface albedo and emissivity by land-cover type (NASA GISS climate model). The flux calculation produces the all-sky, clear-sky and overcast, upwelling and downwelling, total shortwave (SW = 0.4 - 5  $\mu\text{m}$  wavelength) and total longwave (LW = 5 - 200  $\mu\text{m}$  wavelength) radiative fluxes at five levels: surface, 680 hPa, 440 hPa, 100 hPa and TOA, at intervals of 3 hours and 280 km (equal-area map equivalent to 2.5 degrees latitude-longitude at the equator) and with coverage for the time period for July 1983 through December 2006 and onwards. The unique feature of the ISCCP-FD product is that it provides, for the first time, a comprehensive determination of the diurnal-to-synoptic scale variations of the vertical profiles of radiative diabatic heating, albeit with crude vertical resolution, but sufficient to represent radiative heating in the lower, middle or upper troposphere and the stratosphere. In order to meet the purposes of different research communities, the ISCCP-FD product is provided in four parallel sub-products, or datasets (with the same resolution): TOA, SRF, PRF and INP (see <http://isccp.giss.nasa.gov/projects/flux.html>); the ISCCP-FD TOA dataset gives the Upwelling and Downwelling SW and LW for all-, clear- and overcast-sky scenes at the Top-of-Atmosphere, defined to be at  $\sim 0$  hPa ( $\sim$ height of 100 km), and a summary of the physical quantities used to calculate them. All 3-hourly TOA data files are ftp-available for the public. The TOA dataset is introduced above and error estimates are given below.

### Error Analysis

The uncertainty of ISCCP-FD TOA fluxes is estimated as 5-10  $\text{W}/\text{m}^2$  for regional, monthly averaged fluxes based on the comparisons with ERBE (1985—1989) and CERES (2000 - 2002). We have also compared the 15-year time-series anomalies between FD TOA and ERBS [*Wielicki et al.*, 2002] for the tropical regions (20° S—20° N), correlation coefficients are  $> 0.73$  for upward SW and LW, and total net fluxes [*Zhang et al.*, 2004].

## References

- Han, Q., W.B. Rossow, and A.A. Lacis (1994), Near-global survey of effective droplet radii in liquid water clouds using ISCCP data, *J. Climate*, 7, No. 4, 465-497.
- Han, Q., W.B. Rossow, J. Chou, K-S. Kuo and R.M. Welch (1999), The effects of aspect ratio and surface roughness on satellite retrievals of ice-cloud properties, *J. Quant. Spectrosc. Radiat. Trans.*, 63, 559-583.
- Rossow, W.B. and R.A. Schiffer, Advances in understanding clouds from ISCCP, *Bull. Amer. Meteor. Soc.*, 80, 2261-2287, 1999.
- Wang, J., W.B. Rossow, and Y.-C. Zhang (2000), Cloud vertical structure and its variations from a 20-year global rawinsonde dataset. *J. Climate*, 13, 3041-3056, doi:10.1175/1520-0442.
- Wielicki, B.A., T. Wong, R.P. Allan, A. Slingo, J.T. Kiehl, B.J.Soden, C.T. Gordon, A.J. Miller, S-K Yang, D.A. Randall, F. Robertson, J. Susskind and H. Jacobowitz (2002), Evidence for large decadal variability in the tropical mean radiative energy budget, *Science*, 295, 841-844.
- Zhang, Y., W. B. Rossow, A. A. Lacis, V. Oinas, and M. I. Mishchenko (2004), Calculation of radiative fluxes from the surface to top of atmosphere based on ISCCP and other global data sets: Refinements of the radiative transfer model and the input data, *J. Geophys. Res.*, 109, D19105, doi:10.1029/2003JD004457.

## A.1.8: FORTH Data Set

I. Vardavas, N. Hatzianastassiou and Ch. Matsoukas

The FORTH top-of-atmosphere (TOA) shortwave (SW) and longwave (LW) radiative fluxes were generated with the FORTH (Foundation for Research and Technology-Hellas) broadband radiative transfer model using ISCCP-D2 and NCEP-NCAR Reanalysis data. The description of the model and input data are given in Appendix A.3.1.5.

### Uncertainty Analysis and Sensitivity of Model Fluxes

A series of sensitivity tests were performed to investigate how much uncertainty is introduced to the model TOA fluxes by uncertainties in the input parameters. Each test calculation covers the entire globe for one month. The results for all-sky outgoing SW fluxes (ASWUP) are summarized in Table 1.

*Table A.1.8.1: Sensitivity test results for outgoing shortwave fluxes at TOA.*

Changed Parameter	OSR difference ( $\text{Wm}^{-2}$ )
Low- $A_c$ +10%	+13.5/-0.3
Middle- $A_c$ +10%	+9.9/-5.4
High- $A_c$ +10%	+12.3/-4.1
Low- $\tau_\lambda^s$ +10%	+5.3/-4.0
Middle- $\tau_\lambda^s$ +10%	+3.8/-4.0
High- $\tau_\lambda^s$ +10%	+5.5/-4.0
Low- $\tau_\lambda^a$ +10%	+0.5/-4.6
Middle- $\tau_\lambda^a$ +10%	-0.2/-4.9
High- $\tau_\lambda^a$ +10%	-0.1/-0.4
$g_c$ +5%	-0.2/-26.0
$W_{\text{H}_2\text{O}}$ +10%	0 /-3.1
$W_{\text{O}_3}$ +10%	0/-5.0
$R_g$ +10%	+84.4/-2.2
ISR +1%	+4.0/+0.1
AOT +10%	+0.3/-4.3
$\omega_{\text{aer}}$ +10%	+6.6/-2.8
$g_{\text{aer}}$ +10%	-0.2/-4.8

A series of sensitivity tests were also performed to investigate how much uncertainty is introduced to the model outgoing longwave fluxes at TOA by uncertainties in the input parameters, in a similar way as was done for the DLR. *Figure 1* shows an example of the results of these sensitivity tests, in which we have increased by 25% the specific humidity in each atmospheric layer for each grid-box. The resulting global increase in the OLR is  $4.1 \text{ Wm}^{-2}$  on

average, with differences ranging from  $\sim -1$  to  $\sim 8 \text{ Wm}^{-2}$ , depending on the initial total water amount in the atmosphere, as well as on cloud amount and temperature.

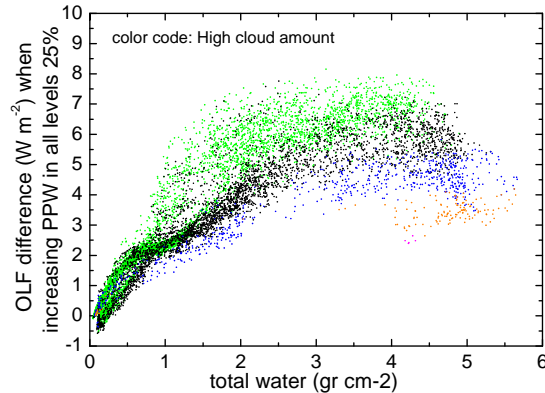


**Figure A.1.8.1:** The change in OLR when precipitable water of the atmosphere is increased by 25% at all levels, as a function of total precipitable water (prior to the increase). The colour coding refers to high cloud cover: green is for high cloud amount ( $AC_{high}$ ) less than 10%, black is for  $10\% < AC_{high} < 30\%$ , blue is for  $30\% < AC_{high} < 50\%$ , orange is for  $50\% < AC_{high} < 70\%$  and magenta is for  $AC_{high} > 70\%$ .

### Evaluation of Model Fluxes

The model OSR and OLR fluxes have been validated through comparison with corresponding extensive satellite measurements from the Earth Radiation Budget Experiment (ERBE) S4 scanner satellite data (1985-1989). Similar comparisons have been also performed against corresponding ERBE S-10 data as well either over the globe or specific zones such as the tropical ( $30^{\circ}\text{S}$ - $30^{\circ}\text{N}$ , see Hatzianastassiou et al., 1999; 2001; 2004; Fotiadi et al., 2005; Hatzidimitriou et al., 2004). *Figure A.1.8.2* below shows the scatter plot comparisons between model-computed OSR, and ERBE-S4 scanner data for the months of January (a), and July (b), at the pixel level and monthly mean term, for the 5-year period from January 1985 through December 1989. The about 40,000 pixel data pairs reveal a good agreement, with a bias equal to about  $4.0 \text{ Wm}^{-2}$ , indicating an overall model overestimation of OSR fluxes, with a small scatter (rms differences equal to 11 and  $14 \text{ Wm}^{-2}$  for January and July, respectively) and high correlation coefficients (0.981 and 0.985). The slopes of the best fitted lines are  $0.89 \pm 0.0008$  for January and  $0.88 \pm 0.0009$  for July, indicating good agreement with the 1 to 1 line. Scatter plots comparing the model OLR fluxes and the ERBE values for the entire globe, and for the months of January (a), and July (b) are shown in *Figures 3a and 3b*. The red lines indicate the least-squares linear fit result, while the dashed line is the inclination 1 line, shown for comparison. The correlation coefficients between model and ERBE fluxes are 0.99 for both January and July, while the slopes of the best fitted lines are  $0.944 \pm 0.002$  for the former and  $0.945 \pm 0.001$  for the latter, indicating good agreement. Also given below are the biases (in  $\text{Wm}^{-2}$ ) between the average model-computed and Earth Radiation Budget Experiment (ERBE) all-sky OSR and OLR fluxes for January and July. At pixel level, the differences are of the order of  $5\text{-}10 \text{ Wm}^{-2}$ , although the discrepancy is higher over the Arctic and the Antarctic with the most probable sources for the discrepancies between model and ERBE being the ISCCP-D2 cloud cover,  $A_c$ , data used by the model and surface albedo,  $R_g$ . At pixel level, the differences between model and ERBE OLR fluxes range within  $\pm 10 \text{ Wm}^{-2}$ , with the model OLR fluxes being generally underestimated. The cause of this underestimation is related to discrepancies in cloud top temperature, skin temperature, and water vapour, particularly in the upper troposphere.

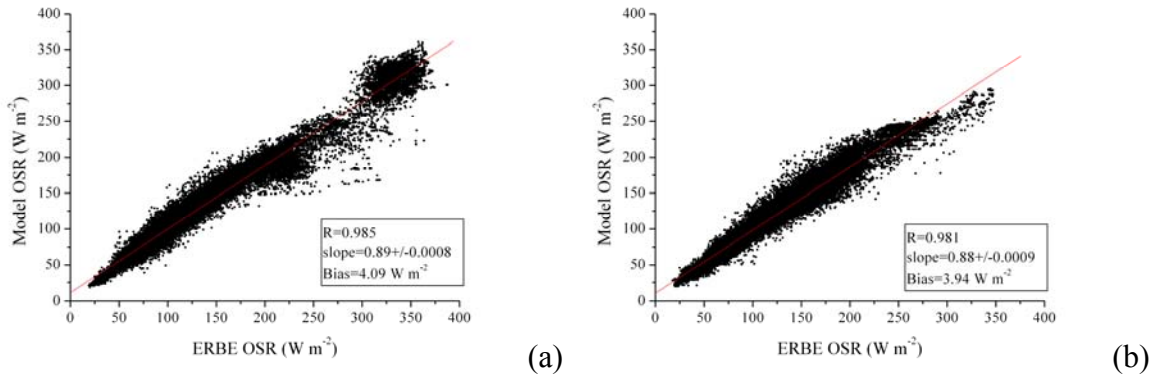


**Figure A.1.8.2:** Scatter plot comparison between model-computed and Earth Radiation Budget Experiment (ERBE) pixel data of monthly average OSR for January and July, over the 5-year (1985-1989) period.

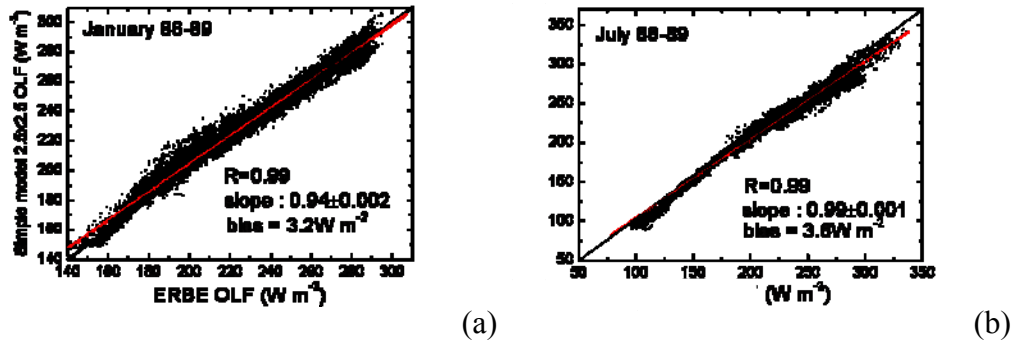


**Figure A.1.8.3:** Scatter plot comparison between model-computed and Earth Radiation Budget Experiment (ERBE) pixel data of monthly average OLR for January and July, over the period 1986-1989.

## References:

- Fotiadi, A., Hatzianastassiou, N., Matsoukas, C., Pavlakis, K. G., Drakakis, E., Hatzidimitriou and Vardavas, I.: Analysis of the decrease in the tropical mean outgoing shortwave radiation at the top of atmosphere for the period 1984-2000, *Atmos. Chem. Phys.*, 5, 1721-1730, 2005, Sref-ID: 1680-7324/acp/2005-5-1721, 2005.
- Hatzianastassiou, N. and Vardavas, I.: Shortwave radiation budget of the Northern Hemisphere using International Satellite Cloud Climatology Project and NCEP/NCAR climatological data, *J. Geophys. Res.*, 104, 24 401-24 421, 1999.
- Hatzianastassiou, N. and I. Vardavas: Shortwave radiation budget of the Southern Hemisphere using ISCCP C2 and NCEP/NCAR climatological data, *J. Climate*, 14, 4319-4329, 2001.
- Hatzianastassiou, N., Fotiadi, A., Matsoukas, C., Drakakis, E., Pavlakis, K. G., Hatzidimitriou and Vardavas, I., 2004: Long-term global distribution of Earth's shortwave radiation budget at the top of atmosphere, *Atmos. Chem. Phys.*, 4, 1217-1235.
- Hatzidimitriou, D., I. Vardavas, K.G. Pavlakis, N. Hatzianastassiou, C. Matsoukas, and E. Drakakis, 2004: On the decadal increase in the tropical mean outgoing longwave radiation for the period 1984-2000, *Atmos. Chem. Phys.*, 4, 1419-1425.

## A.1.9: University of Maryland Shortwave Radiation Budget (V3.3)

R. T. Pinker

### A.1.9.1: Description of Retrieval Framework

#### A.1.9.1.1: Inference scheme

The University of Maryland/Shortwave Radiation Budget (UMD/SRB) model (V3.3) as implemented in support of the RFA activity uses satellite information on TOA reflectivity and cloud amount to infer fluxes at both TOA and the surface. The TOA reflectivity,  $y$  is a function of atmospheric parameters, surface parameters and sun-earth geometry expressed as:

$$y = f(\mathbf{x}) \quad (\text{A.1.9.1})$$

where  $\mathbf{x}$  is a vector denoting all the parameters determining the TOA reflectivity. In the UMD/SRB model, the cloud optical depth, aerosol optical depth and surface albedo are the parameters that need to be inferred first from the satellite observations and ancillary data on the state of the atmosphere and the surface. Once retrieved, equation (A.1.9.1) is used again in a forward way to compute atmospheric transmissivity, reflectivity, and, subsequently, the corresponding fluxes at both boundaries of the atmosphere.

Under the assumption of a Lambertian surface, the total reflectivity (planetary reflectivity) and transmittance are expressed as:

$$R_{tot} = R_{10} + \frac{(T_{11}\alpha_{10} + T_{10}\alpha_{00})T_{00}}{1 - \alpha_{00}R_{00}} \quad (\text{A.1.9.2})$$

$$T_{tot} = T_{11} + \frac{T_{10} + T_{11}\alpha_{10}R_{00}}{1 - \alpha_{00}R_{00}} \quad (\text{A.1.9.3})$$

where  $T$  is transmittance;  $R$  is reflectance; subscript “1” refers to the direct component; subscript “0” refers to the diffuse component; and  $\alpha$  is the surface albedo.

The UMD/SRB model infers the shortwave radiative (SW) fluxes in 5 broadband intervals (0.2-0.4, 0.4-0.5, 0.5-0.6, 0.6-0.7, and 0.7-4.0  $\mu\text{m}$ ). Output parameters include direct and diffuse surface downwelling and upwelling fluxes as well as TOA upwelling fluxes.

#### A.1.9.1.2: Look-Up-Table (LUT) Approach

The LUTs contain spectral values of the optical functions for discrete values of solar zenith angle, amount of water vapor, ozone, aerosol, and cloud optical depth. For V3.3 the LUTs are computed for a plane-parallel, vertically inhomogeneous scattering and absorbing atmosphere using the delta-Eddington approximation of radiative transfer (Joseph et al., 1976). The model accounts for (1) absorption by ozone and water vapor; (2) Rayleigh scattering; (3) multiple scattering and absorption by aerosols and cloud droplets; and (4) multiple reflections between the atmosphere and surface. It has five or six layers, depending on the aerosol profile considered and whether a cloud is present.

### **A.1.9.1.3: Retrieval of radiative fluxes**

If the surface albedo is known, the optical functions for clear and cloudy conditions are determined by matching the broadband TOA albedoes derived from the instantaneous clear and cloudy radiances of the satellite data, respectively, with TOA albedoes from the model calculation. The algorithm assumes that the atmospheric state such as the amount of water vapor ozone are known, but that the surface albedo and aerosol optical depth need to be determined from the satellite radiances. The retrieval methodology is implemented in two steps. First, utilized is information on the average clear sky radiance which is either provided (like in the case of the ISCCP data) or can be generated from available satellite observations to derive the surface albedo, assuming that information on the average properties of aerosols is known. Surface type information is also needed to select the appropriate narrow-to-broadband transformations and the anisotropic coefficients (that are surface type dependent). Version 3.3 uses vegetation type information from Matthews (1985) and surface spectral albedo models of Briegleb et al. (1986). Once the surface albedo is retrieved, it is kept constant for the entire period represented by the clear sky composite. In step two, assuming now a known surface albedo, one can go back to each individual clear sky observation and retrieve an estimate of aerosol optical depth by adjusting it till the best match is obtained between the measured and calculated TOA albedo. In a similar manner, cloud optical depth is derived from each cloudy pixel. The optical functions obtained are then used along with the surface albedos in equations (A.1.9.2) and (A.1.9.3) to compute the fluxes for clear and cloudy conditions at both the TOA and the surface.

The computed instantaneous fluxes are first scaled by the 3-hourly average of the cosine of the solar zenith angle to get the mean flux for the 3-hourly time interval and then integrated numerically for the daylight hours and divided by 24 to obtain a daily average. Because of the finite number of observations available per day, the total daily flux obtained from numerical integration of the instantaneous fluxes is potentially inaccurate. Therefore, the daily total fluxes are adjusted by the ratio of the TOA incoming flux as obtained by an analytical integration to that computed from the numerical integration. To account for missing days in the monthly averages, first, an average TOA and surface albedo and an average transmittance are computed from the daily average flux. The monthly mean TOA downward flux computed analytically is then multiplied by the average TOA albedo to yield the monthly mean of the TOA upward flux. Similarly, the product of the analytical TOA shortwave downward flux and the average transmittance gives the monthly mean of the surface downward flux. The monthly mean of the surface upward flux is then obtained by multiplying the monthly mean surface downward flux by the average surface albedo. The above procedure assumes that the days with observations are representative of the entire month.

In Version 3.3, solar-earth geometry is adopted from the International Astronomical Union's SOFA (Standards of Fundamental Astronomy) software collection to replace the Spencer's formulas used in previous versions of the UMD/SRB model. Computation of the mean cosine of the solar zenith angle for 3-hourly intervals and daily mean TOA downwelling shortwave flux are restricted to prevent possible unrealistic values of the cosine of the solar zenith angle from being included in the average.

### **A.1.9.2: Description of specific procedures**

To match the model-derived broadband TOA reflectance, the satellite-measured narrowband radiance needs to be transformed into a broadband quantity by applying narrow-to-broadband conversions and correction for bidirectional effects. All the ISCCP D1 visible

radiances from the various satellites have been normalized to an absolute reference measurement, which is the visible channel of AVHRR on NOAA-9, thus the narrow-to-broadband transformation is based on this channel. The conversion coefficients used in Version 3.3 for various surface types are listed in Table A.1.9.1

**Table A.1.9.1:** *Narrow-to-broadband conversion coefficients (Version 3.3)*

	<b>Water</b>	<b>Vegetation</b>	<b>Desert</b>	<b>Snow/Ice</b>	<b>Cloud</b>
Slope	0.902	0.779	0.804	0.760	0.780
Offset	0.01426	0.06831	0.02819	0.0083	0.05004

In Version 3.3, four surface types (ocean, land, desert, and snow) are implemented when generating the LUTs and cloud is assumed to be an overcast cloud with optical depth equal 10. Bidirectional corrections are based on ERBE.

The surface albedo is determined from the narrowband clear-sky composite radiance, which is based on radiances for typical clear-sky conditions over about a month from the ISCCP data. An alternative approach is to use a seven-day running mean of clear sky composites and follow similar procedures as when the clear sky composite is used. We have run V3.3 with both options. The advantage of one over the other is, as yet, not clear. The version with the running mean clear sky reflectance was submitted to the RFA archive. The iterative procedure to derive surface albedo is as follows: 1) apply narrow-to-broadband transformation and bi-directional reflection correction to obtain a clear-sky composite TOA albedo; 2) assume climatological aerosol optical properties and use observed amount of water vapor and ozone to calculate optical functions. Initial information on optical depth, single scattering albedo and scattering asymmetry factor is needed for the retrieval of the surface albedo from a clear sky composite (provided with the ISCCP-D1 data). Information on surface type is used to select the spectral dependence of a reference surface albedo model. The Liu (Liu et al., 2005; Liu et al., 2008; Liu and Pinker, 2008) aerosol “climatology” gives monthly mean, regionally resolved aerosol information on a 2°x2.5° grid. Parameters include extinction coefficient, single scattering albedos and asymmetry factor for the five wavelength bands listed above. These optical functions combined with the first-guess surface albedos (for land and ocean are from Briegleb et al. (1986) and for snow are from Wiscombe and Warren (1980)) give satellite estimates of the TOA albedoes. To get a better first guess for snow-free surfaces, a scaling factor based on the seasonal broadband albedos from Mathews (1985) is initially applied to the above reference albedoes. The calculated TOA albedo is then compared to the one obtained from the clear-sky composite radiance. If there is no agreement, the spectral values of the modeled surface albedo are adjusted and a second iteration is applied until a match is achieved. The final retrieved surface albedo is the one for which the calculated TOA albedo matches the satellite measured TOA albedo.

The original scheme to derive radiative fluxes from satellite observations has been modified so that it can incorporate new information on aerosol properties at global scale. By incorporating new information on aerosol properties, it is possible to improve surface total and diffuse shortwave fluxes. Details can be found in Liu and Pinker (2008).

### **Improvement in aerosol representation – aerosol optical depth**

The following sources of information have been used to combine information from independent sources to characterize monthly mean clear-sky daytime aerosol optical depth ( $\tau$ ): simulations from the Global Ozone Chemistry Aerosol Radiation and Transport (GOCART) (Chin et al., 2002) model; retrievals from the Moderate Resolution Imaging Spectroradiometer

(MODIS) instrument on the Terra satellite; and measurements from the Aerosol Robotic Network (AERONET). Leading empirical orthogonal functions (EOFs) were used to represent the significant variation signals from model and satellite results; the EOFs were fitted to the ground observations to propagate the AERONET information at global scale. The methodology was implemented with a 2-year time record when collocated data from all three sources are available. Details are presented in Liu et al. (2005).

### **Improvement in aerosol representation - ( $\varpi_0$ ) and ( $g$ ).**

The estimates of aerosol optical depth at 0.55  $\mu\text{m}$  based on the spatial and temporal variation patterns of model and satellite data and regulated by the AEROSOL ROBOTIC NETWORK (AERONET) measurements as described in (Liu et al., 2005) have been supplemented with information on the large scale distribution of the single scattering albedo ( $\varpi_0$ ) and the asymmetry parameter ( $g$ ). Data from the Global Ozone Chemistry Aerosol Radiation and Transport (GOCART) model, Moderate Resolution Imaging Spectro-radiometer (MODIS) retrievals, and AERONET measurements/retrievals are used. The single scattering albedo is generated by extending  $\varpi_0$  at 0.55  $\mu\text{m}$  from GOCART to the entire shortwave (SW) spectrum using spectral dependence derived from available AERONET retrievals. The asymmetry parameter over the solar spectrum is derived from the MODIS Ångström wavelength exponent, utilizing an empirical relationship based on AERONET almucantar observations. The normalized extinction coefficient is estimated from the MODIS Ångström wavelength exponent. Sensitivity tests for  $\varpi_0$  and  $g$  have been performed to assess effects on surface downward SW fluxes. For an assumed global average  $\tau_{0.55\mu\text{m}}$  of 0.15, a perturbation of 0.05 and 0.1 in  $\varpi_0$  and  $g$  results in flux changes of about 2.0 and 1.5  $\text{Wm}^{-2}$ , respectively. A comparison between the empirically derived aerosol intensive optical properties with estimates based on the GOCART model has been performed as detailed in Liu et al. (2008).

### **Surface elevation correction**

The surface elevation effect is addressed by assuming that the atmosphere over the elevated area is the upper part of a model atmosphere with its lower portion ‘cut out’. The ‘cut out’ part of the atmosphere has thickness extended from zero to mountain level. Based on this two-layer model, the reflectance and transmittance ( $R$  and  $T$ ) corresponding to the atmosphere above mountains are computed by modifying the total  $R/T$ , from the original LUT using ‘adding method’. The  $R/T$  functions for the lower layer are pre-calculated for five standard atmospheres (tropical, mid-latitude summer, mid-latitude winter, subarctic summer, and subarctic winter), for 11 elevations from 0.0 km to 10.0 km using the SBDART model. No aerosols or clouds are assumed in the lower part of the atmosphere. Since the water vapor absorption is pressure dependent, the same amount of water vapor in the upper layer will be less absorptive than that in the lower layer where gas pressure is higher. This effect is also taken into account by scaling the water vapor amount following a scaling approximation developed by Chou (1986).

### **Evaluation of V3.3**

Evaluation has been undertaken against ground observations both on daily and monthly time scales. Ground truth from SURFRAD, BSRN, and ARM measurement sites and buoy

observations has been used. The results indicate that the rms error on monthly time scale is about 5% of the mean value. An independent evaluation is conducted in the RFA framework (as discussed in this report.)

### References:

- Briegleb, B., P. Minnis, V. Ramanathan, and E. Harrison, 1986: Comparison of regional clear-sky albedos inferred from satellite observations and model computations, *J. Appl. Meteorol.*, **25**, 214–226.
- Chou, M.-D., 1986: Atmospheric solar heating rate in the water vapor bands. *J. Climate Appl. Meteor.*, **25**, 1532-1542.
- Liu, H., Pinker, R. T., and Holben, B. N., 2005: A global view of aerosols from merged transport models, satellite, and ground observations. *J. Geophys. Res.*, Vol. 110, No. D10, D10S15, doi:10.1029/2004JD004695.
- Liu, H. Q., and Pinker, R. T., 2008: Radiative fluxes from satellites: Focus on aerosols *J. Geophys. Res.*, Vol. 113, No. D8, D08208.
- Liu, H. Q., Pinker, R. T., Chin, M., and L. Remer, 2008: Synthesis of information on aerosol optical properties. *J. Geophys. Res.*, Vol. 113, No. D7, D07206.
- Matthews, E., 1985: Atlas of archived vegetation, land-use and seasonal albedo data sets, NASA-TM-86199, NASA, Washington, D. C.
- Wiscombe, W., and S. Warren, 1980: A model for the spectral albedo of snow, I, Pure snow, *J. Atmos. Sci.*, **37**, 2712–2733.

## A.1.10 ERA-40 Reanalysis Data Set

J.-J. Morcrette

### Data Product Description:

ERA-40 was the re-analysis of 40 plus years of meteorological data carried out in the mid-00s by the European Centre for Medium-Range Weather Forecasts (ECMWF). Within a meteorological analysis, a large number of satellite data related to temperature, humidity, ozone, winds are ingested together with more conventional meteorological measurements provided by radiosoundings, synoptic observations, aircraft and ship observations. During the analysis process, these observational data are compared to first guess values (model-simulated observations in the geometry and at the time of the observations) provided by a short (12-hour) forecast by the meteorological model initialized with the previous analysis. The 3D variational analysis method (Andersson et al., 1998) operational at ECMWF between January 1996 and November 1997 was then used within ERA-40 to produce the increments for all analysis variables (temperature, humidity, winds, ozone, surface temperature and moisture) that minimized the distance between the observations and the first guess values.

ERA-40 provides analyses with a six hourly frequency throughout the period September 1957 to August 2002 with a horizontal grid-spacing close to 125 km and 60 levels on the vertical between the surface and 0.1 hPa (see Products/index in the Reference section below). Using the temperature, humidity, surface temperature provided by the analysis, cloud fields and other surface conditions produced by the model parametrizations together with the climatological aerosols, radiative heating rates and fluxes were then computed with the radiation schemes operational at the time. A description of the physical parametrizations (convection, planetary boundary layer and cloud schemes) used in ERA-40 is given in Gregory et al. (2000). More specifically, details of the radiation parametrizations can be found in Morcrette (2002a).

ERA-40 radiative fluxes can be made available with the horizontal grid-spacing close to 125 km, at the top-of-the-atmosphere and at the surface, for the downward and upward, short-wave and long-wave, clear-sky and total radiation (see link in the Reference section below), or are available on a  $[2.5 \text{ deg}]^2$  grid from the GEWEX RFA site.

In addition to the assessments of re-analysis products carried out when and just after the re-analysis was performed (see Publications in the Reference section below), studies by Morcrette (2002b), Allan et al. (2004) and Markovic et al. (2009) have specifically evaluated the adequacy of the ERA-40 radiation fluxes for various applications. The potential user of ERA-40 radiative fluxes is encouraged to familiarize themselves with what a re-analysis can provide by reading Uppala et al. (2005).

### Error Analysis

No error estimate valid over the whole period covered by ERA-40 is available as the variations in the number of observations (no satellite data pre-1978, introduction of various satellite systems between 1979 and 2002) directly affect the final analysis (see Data\_Services / section 3 in the Reference section below). However, Allan et al. (2004) assessed the clouds, water vapour and radiation over the period 1979-2001, reporting that:

- Clear-sky outgoing long-wave radiation (OLR) is well simulated with monthly mean errors smaller than  $10 \text{ Wm}^{-2}$  related to ERBE;
- Errors in clear-sky absorbed short-wave radiation (ASR) are generally between 10 and  $20 \text{ Wm}^{-2}$  on a monthly basis, with larger errors over Sahara;

- ERA-40 overestimates cloudy OLR by up to  $15 \text{ Wm}^{-2}$  in the tropics;
- ERA-40 underestimates cloudy ASR in the tropics by up to  $30 \text{ Wm}^{-2}$  and overestimates it in the extratropics by similar amounts. As outside stratocumulus areas (where a large underestimation of the cloud cover is present), ERA-40 cloud fraction appears reasonable compared to ISCCP, the errors in radiation have been linked to errors in the amount of condensed water in clouds and/or cloud optical properties (Chevallier et al., 2003).

### References:

- <http://www.ecmwf.int/research/era/ERA-40/Products/index.html>  
<http://www.ecmwf.int/publications/library/do/references/list/192>  
[http://www.ecmwf.int/research/era/ERA-40/Data\\_Services/](http://www.ecmwf.int/research/era/ERA-40/Data_Services/)  
[http://www.ecmwf.int/research/era/ERA-40/Data\\_Services/section3.html#rb](http://www.ecmwf.int/research/era/ERA-40/Data_Services/section3.html#rb)
- Allan, R.P., M.A. Ringer, J.A. Pamment, and A. Slingo, 2004: Simulation of the Earth's radiation budget by the European Centre for Medium-Range Weather Forecasts 40-year reanalysis (ERA40), *J. Geophys. Res.*, 109, D18107, doi:10.1029/2004JD004816.
- Andersson, E., et al., 1998: The ECMWF implementation of three-dimensional variational assimilation (3D-Var). III: Experimental results. *Quart. J. Roy. Meteor. Soc.*, 124, 1831-1860.
- Chevallier, F., G. Kelly, A.J. Simmons, S. Uppala and A. Hernandez, 2003: High clouds over oceans in the ECMWF 15-year and 45-year re-analyses. ERA-40 Project Report Series No. 11. <http://www.ecmwf.int/publications/library/do/references/show?id=86043>
- Gregory, D., J.-J. Morcrette, C. Jakob, and A.C.M. Beljaars, and T. Stockdale, 2000: Revision of convection, radiation, and cloud schemes in the ECMWF integrated forecasting system. *Quart. J. Roy. Meteor. Soc.*, 126A, 1685-1710.
- Markovic, M., C.G. Jones, K. Winger, and D. Paquin, 2009: The surface radiation budget over North America: Gridded data assessment and evaluation of regional climate models. *Int. J. Climatol.*, 29, 2226-2240, doi: 10.1002/joc.1860.
- Morcrette, J.-J., 2002a: Assessment of the ECMWF model cloudiness and surface radiation fields at the ARM-SGP site. *Mon. Wea. Rev.*, 130, 257-277.
- Morcrette, J.-J., 2002b: The surface downward longwave radiation in the ECMWF forecast system. *J. Climate*, 15, 1875-1892.
- Uppala, S.M., et al., 2005: The ERA-40 re-analysis. *Quart. J. R. Meteorol. Soc.*, 131, 2961-3012. doi:10.1256/qj.04.176.

## A.1.11: NCEP/-DOE AMIP-II Reanalysis (R-2)

S.-K. Yang

### Data Product Description:

The NCEP/-DOE AMIP-II Reanalysis (Kanamitsu, et al, 2002), often designated R-2, is an update of NCEP/NCAR Reanalysis (R-1) (Kalnay, et al, 1996), the first major reanalysis project carried out in the mid-'90s. The objective of reanalysis projects is to eliminate artificial "climate jumps" caused by the episodic changes of the operational data assimilation systems. By using a frozen system reanalyzing meteorological data retrospectively, the outcome is a long data series, unified in output structure and format, suitable for studying climate variations and other applications. The projects of this scale are of tremendous undertakings. During and after the main production phase of R-1, a number of human and system errors were discovered, but couldn't be corrected due to resource issues. For most of studies, these errors would cause minor consequences; still, they may affect some other important studies. Subsequently, the Atmospheric Model Inter-comparison Project of Department of Energy provided the resources for an updated production, thus R-2.

R-2 covers the satellite period, from 1979 to the present, and expected to continue up to June 2011. It fixed known problems of R-1, with minor system updates. The basic structure includes the NMC global model (Kanamitsu, 1989), and Spectral Statistical Interpolation (SSI), a three-dimensional variational analysis scheme of Parrish and Derber (1992). The model uses spectral truncation of T62, approx.  $2^\circ \times 2^\circ$  lat/lon for horizontal resolution, and 28 vertical layers. The output variables and file formats, in BRIB and BIFR, are similar to R-1. The R-2 update from R-1 includes: For computing the radiation fluxes, the shortwave radiation algorithm and parameterization of Chou (1992) and Chou and Lee (1992), replaces R-1's Lacis and Hansen (1974). An improved desert albedo of Briegleb et al. (1996) is prescribed. The Longwave algorithm of Schwarzkopf and Fels (1991) (SF) are maintained, which incorporates the effects of water vapor e-type continuum, water-carbon dioxide overlap, and Voigt line shape, etc. The reanalysis uses fixed 350 ppmv for carbon dioxide concentration throughout the period, an increase of 20ppmv from R-1. An improved ozone climatology of Rosenfield et al (1987) is adopted. Sea surface temperature is from the optimal interpolation reanalysis by Reynolds and Smith (1994). The emissivity of 1 is used for the whole globe.

Between R-1 and R-2, minor differences are found in the primary analysis variables such as free atmospheric geopotential height and winds in the Northern Hemisphere extratropics, while significant improvements upon R-1 are made in land surface parameters and land-ocean fluxes.

### Error Analysis:

One of the significant shortcomings that prompted NCEP to change the shortwave radiation transfer algorithm for R-2 was the excessive surface insolation found in R-1. The general consensus from Kiehl and Trenberth (1997) indicates that the correct magnitude of surface insolation about 49% of the solar constant over the annual mean. With the new algorithm of Chou (1992) and refined cloud algorithm, R-2 substantially improved the ratio, to ~55%, as compared to 60% of R-1.

Using the surface albedo of Briegleb et al. (1996) greatly enhances the accuracy, especially over the Sahara. The new albedo algorithm handles direct and diffuse components separately, and divides the solar spectra into visible and near-infrared bands. The treatment successfully brightens the Sahara from 0.3 (in Albedo unit) in R-1 to beyond 0.4 in R-2, which is

in good agreement with the estimate from Staylor and Wilbur (1990). Ocean surface albedo of R-2 is also remarkably reduced to 0.06~0.07 from 0.15 of R-1, which substantially reduced the global annual mean planetary albedo to 0.31 from 0.34 of R-1. The corresponding reflected shortwave radiation at the top of the atmosphere was reduced to ~105 W/m<sup>2</sup> from 115 W/m<sup>2</sup>, which compares well with 103 W/m<sup>2</sup> measured by Earth Radiation Budget Experiment (ERBE; Barkstrom et al., 1989).

Improvement in shortwave radiation, however, is somewhat offset by the increase of outgoing longwave radiation. R-1 is in very good agreement with ERBE (Yang, et al, 1999); with the annual global mean of 237 and 234 Wm<sup>-2</sup>, for R-1 and ERBE, respectively. R-2, at 242 W/m<sup>2</sup>, is about 3% higher than ERBE. The overestimation is more severe over the tropics, where R-2 can be 15~20 Wm<sup>-2</sup> larger than ERBE and R-1. Much of the difference can be traced to the dryer humidity in the upper troposphere in R-2, which OLR is sensitive to (Yang, et al. 2000).

### References:

- Briegleb, B. P., P. Minnis, V. Ramanathan, and E. Harrison, 1996: Comparison of radiational clear-sky albedos inferred from satellite observations and model computations. *J. Climate Appl. Meteor.*, **25**, 214–226.
- Chou, M.-D., 1992: A solar radiation model for use in climate studies. *J. Atmos. Sci.*, **49**, 762–772.
- , and K.-T. Lee, 1996: Parameterizations for the absorption of solar radiation by water vapor and ozone. *J. Atmos. Sci.*, **53**, 1203–1208.
- Kanamitsu, M., 1989; Description of the NMC global data assimilation and forecast system. *Wea. Forecasting*, **4**, 334-342.
- Kanamitsu, M., W. Ebisuzaki, J. Woollen, S-K. Yang, J. J. Hnilo, M. Fiorino, and G. L. Potter, 2002: NCEP–DOE AMIP-II Reanalysis (R-2). *Bull. Amer. Meteor. Soc.*, **83**:1631–1643
- Kalnay, E., and co-authors, 1996: The NCEP/NCAR 40-year Reanalysis Project, *Bull. Amer. Meteor. Soc.*, **77**, 437-471
- Kiehl, J. T., and K. E. Trenberth, 1997: Earth’s annual global mean energy budget. *Bull. Amer. Meteor. Soc.*, **78**, 197–208.
- Lacis, A. A., and J. E. Hansen, 1974: A parameterization for the absorption of solar radiation in the earth’s atmosphere. *J. Atmos. Sci.* **31**, 118-133.
- Parrish, D. F. and J. C. Derber, 1992: The National Meteorological Center’s spectral statistical interpolation analysis system. *Mon. Wea. Rev.*, **120**, 1747-1763.
- Payne, R., 1972: Albedo of the Sea Surface, *J. Atmos. Sci.*, **V29**, pp 959-970.
- Reynolds, R. W., and T. M. Smith, 1994: Improved global sea surface temperature analyses using optimum interpolation. *J. Climate*, **7**, 9292-948.
- Rosenfield, J. E., M. R. Schoeberl, and M. A. Geller, 1987: A computation of the stratospheric diabatic circulation using an accurate radiative transfer model. *J. Atmos. Sci.*, **44**, 859–876.
- Schwarzoph, M.D., and S. B. Fels, 1991: The simplified exchange method revisited: An accurate, rapid method for computation of infrared cooling rates and fluxes. *J. Geophys. Res.*, **96**, 9075-9096
- Staylor, W.F. and A. C. Wilber, 1990: Global surface albedos estimated from ERBE data, Preprints, Seventh Conf. on Atmospheric Radiation, San Francisco, CA, Amer. Meteor. Soc., 231-236.
- Yang, S.-K., Y.-T. Hou, A. J. Miller, and K. A. Campana, 1999: Evaluation of the Earth Radiation Budget in NCEP-NCAR Reanalysis with ERBE, *J. of Climate*, **12**, 477-493.

## A.1.12: IPCC-4AR statistical data

S. Kinne

The IPCC-AR4 statistical data (average, median, and standard deviation) files in the GEWEX-RFA archive contain processed data produced specifically for this Assessment. The files consist of monthly global radiative flux maps based on the output of 15 global models that was contributed to the IPCC 4<sup>th</sup> assessment. The data considered covered the last 20 years (1980-1999) of the simulation run with the greenhouse gas concentrations observed over the 20th century (experiment 20C3M). The original data is available through the IPCC portal (<http://www-pcmdi.llnl.gov/ipcc/ipcc.php>).

The 15 models provided a total of 21 data sets because some models provided data for different model configurations (e.g., different resolution in the atmospheric model or different ocean models.) Background information on the 21 IPCC model data is listed in *Table 1*.

**Table A.1.12.1:** Information regarding the 21 IPCC-AR4 model data sets used to produce the statistical data files. Indicated are the 3-letter labels, as will appear in data presentations, the institute providing the data, and the name of the atmospheric model with its spectral (T..) or lat/lon (..x..) degree spatial resolution and its number of vertical levels (L..), when available.

Label	Institution	Location	Atmospheric model
<b>BCC</b>	Bjerknes Center for Climate	Bergen, Norway	Arpege V3, T63/L31
<b>CCc</b>	Canadian Climate Center	Victoria, Canada	AGCM3, T63/L31
<b>CCC</b>	Canadian Climate Center	Victoria, Canada	AGCM3, T47/L31
<b>CCs</b>	Center for Climate Sys Res.	Tokyo, Japan	AGCM, T106/L56
<b>CCS</b>	Center for Climate Sys Res.	Tokyo, Japan	AGCM, T42/L20
<b>CNR</b>	CNRS Meteo-France	Toulouse, France	Arpege V3, T42L45
<b>CSI</b>	CSIRO Atmosph. Research	Melbourne, Australia	CSIROmk3, T63L18
<b>DMN</b>	Institute for Numerical Math	Moscow, Russia	INMcm3, 4x5 L21
<b>GFD</b>	NOAA, GFDL	Princeton, USA	GFDLcm2, T45L24
<b>GI1</b>	Godd. Inst. for Space Studies	New York, USA	GISS-ER* 4x5 L20 run1
<b>GI2</b>	Godd. Inst. for Space Studies	New York, USA	GISS-ER* 4x5 L20 run2
<b>GI3</b>	Godd. Inst. for Space Studies	New York, USA	GISS-EH* 4x5 L20 run1
<b>GIS</b>	Godd. Inst. for Space Studies	New York, USA	GISS AOM, 4x3 L12
<b>IAP</b>	Inst. For Atmospheric Physics	Beijing, China	GAMIL
<b>IPS</b>	Inst. Pierre Simon Laplace	Paris, France	IPSL-CM4 v1
<b>MPI</b>	Max-Planck-Institute	Hamburg, Germany	ECHAM5, T63L32
<b>MRI</b>	Meteorological Res.Institute	Tsukuba, Japan	cGCM2.3.2 T42L30
<b>NCA</b>	Nat. Center for Atmos. Res.	Boulder, USA	CAM3 T85L26
<b>PCM</b>	Nat. Center for Atmos. Res	Boulder, USA	CCM3.6.6 T42L18
<b>UBO</b>	University of Bonn	Bonn, Germany	ECHAM4
<b>UKM</b>	UK Met Office	Exeter, England	HADcm3 2.5x3.75

\* GISS ER uses a lower resolution ocean model (4x5 L13) than GISS EH (2x2 L16).

When combining the data sets, at most two of the four GISS (GI...) versions listed in *Table A.1.12.1* were allowed, in order to avoid a bias toward that model. Thus, at most 19 different model output results were considered for each parameter. Global maps were created from the average, median, and standard deviations for each parameter and each month at every individual grid box. For the statistical analysis, the different spatial resolutions of the model output were harmonized to a common 1°x1° latitude-longitude grid. However, before submitting

maps of these three statistical properties to the RFA database, all data were spatially averaged to the RFA standard  $2.5^{\circ} \times 2.5^{\circ}$  latitude-longitude resolution. Following the suggested naming conventions, median data are listed under the prefix of “IPCC-MEDIAN\_EdAR,” averages under the prefix “IPCC-AVERAGE\_EdAR,” and “IPCC-STDDEV\_EdAR4” is the prefix for the standard deviation, which characterizes for the local variability.

The IPCC data files in the archive cover most standard RFA flux parameters. More specifically, for both clear-sky (C...) and all-sky (A...) conditions, statistical properties are provided for the downward solar fluxes (CSWDN, ASWDN) at ToA and surface, for the solar surface and the planetary albedo (CALB, AALB), for the IR upward flux (CLWUP, ALWUP) at surface and ToA (or OLR), and for the IR downward flux at the surface (CLWDN, ALWDN). Output from all 19 models was used in computing statistics for only a few parameters because not all models provided data for all standard RFA flux parameters, especially for cloud-free conditions. Still, at least 16 models contributed to the statistics for all-sky conditions and at least 14 models contributed for clear-sky conditions. The differences in ensemble mixtures weaken links among the same statistics for different flux parameters (e.g., loss of additivity), especially for median maps. Still, statistical benefits were considered more important, so that all available model data (but never more than two from the same modeling tree) were always included.

## **A.2.1: Supplement to Error Analysis of Surface In-Situ Measurement Data Products as presented in Chapter 5.1**

E. Dutton, C. Long (with contributions from J. Gröbner)

### **A.2.1.1: Uncertainty in downwelling total solar irradiance observations**

#### **A.2.1.1.1: Single Pyranometer**

Un-shaded, upward-facing pyranometers are widely used for total downwelling solar irradiance observations because of their simplicity and operational robustness. A reasonably complete evaluation of the measurement uncertainty in a WMO Class 1 model pyranometer (Eppley PSP) was provided by Myers 1989 with updates Myers et al 2002, using the formal error-source summing method. Using the error sources identified, Myers,1989 derived a pyranometer uncertainty of  $\pm 2.8\%$  for instantaneous total irradiance. Other analyses of thermopile pyranometers have suggested 95% range of uncertainties as high as  $\pm 5\%$ , (Philipona, 2002 and others) although even higher values suggested by Philipona are considered extreme. Even higher errors,  $> 8\%$ , can occur when using various non-thermal based detectors based on manufactures own claims. Although a detailed analysis for other makes of pyranometers (done independently of the manufacturer) are not as readily available, results similar to Meyers' are expected due to similarities in the instrument designs. It is primarily due to basic inherent errors in pyranometers (cosine and offsets) that the BSRN was led to adopt a potentially more accurate approach that combines (sums) the individually observed downwelling direct and offset-error-free diffuse solar components. In this case, the error in the resulting total solar irradiance is does not have a dominant cosine response error with the errors that remain within each component discussed in the following. Another advantage of the component method that has become apparent after its adoption by the BSRN and others is the relative ease by which the dome thermal cooling or offset error can be addressed which further complicates and contributes to many thermopile pyranometer measurements, e.g., Bush et al 2000, Haeffelin et al 2001, Dutton et al 2001, and Philipona 2002.

#### **A.2.1.1.2: Components Summation Method**

##### **A.2.1.1.2.1: Direct solar radiation**

The measurement of direct solar irradiance has received much attention over the past century, particularly the last five decades, primarily because of its close association to the efforts in the determination extraterrestrial solar irradiance at the top of the Earth's atmosphere (ETR) and the fundamental nature on the observation methodology. The emphasis on this measurement was not just on determination in the uncertainty of the ETR solar, but also on the initial establishment of the absolute reference solar irradiance calibration scale. Those efforts on this measurement, and the fact that it is a basically geometrically simple observation with virtually all the energy in a collimated beam perpendicular to the receiver surface, has led to higher and better documented measurement accuracy than for other surface irradiance quantities. Under ideal outdoor conditions accuracies of close to 0.3% are claimed for the reference measurement of direct solar beam, Fröhlich, 1991. This accuracy is degraded slightly, to  $\sim 0.45\%$  when transferring the reference calibration to operational instruments, Michalsky et al 2011.

Nonetheless, the routine continuous, all-weather measurement instrumentation used for operational measurements does not achieve this level of accuracy when considering the additional random measurement error. The uncertainty in the operational direct-beam solar measurements used in this assessment is given in the next two sub-sections.

#### A.2.1.1.2.2: Uncertainties in the calibration reference standard

The direct solar irradiance calibration reference standard utilized by BSRN and other measurement programs prescribing the WMO/CIMO recommendations is the World Radiation Reference (WRR) maintained by the World Radiation Center in Davos Switzerland, Fröhlich. The WRR is determined by the consensus measurement level of 6 to 7 self-calibrating (after characterization) electrical-substitution ambient-temperature active cavity radiometers. The stated uncertainty in the WRR is 0.3% at the nominal measurement level of  $1000 \text{ Wm}^{-2}$ . This level of consensus agreement was achieved after nearly a  $\frac{3}{4}$  of century of efforts within the solar measurement community. The WRR scale is routinely transferred to participating institutions from around the world that possess cavity radiometers once every 5 years (since 1975) during the International Pyrheliometer Comparisons (IPC) held in Davos, Switzerland. The WRR has been maintained for over 30 years with a precision of better than 0.01% with transfer to IPC participants having a precision of better than 0.1%. Further information on the WRR and the IPCs is available at (<http://www.pmodwrc.ch/pmod.php?topic=wrc>).

The accuracy of any direct beam solar cavity, including windowed cavities, what has been brought into agreement with the WRR is considered to be accurate to within 0.45%. Multiple instruments can be maintained within an organization such that the stability of each can be checked between the IPCs. More recent advances in spaceborne absolute cavity radiometers (Kopp et al., 2005)) and their comparison with other sensors on the WRR scale suggest that the absolute uncertainty in the WRR is 0.35% (C. Fröhlich personal comm). This discrepancy is under study and is discussed in the preceding Chapter 3. Halthore et al., 1997; Kato et al., 1997; and others, have showed agreement to within 0.4% was achieved when radiative transfer models are compared to a cavity radiometer when adequate atmospheric information is available.

#### A.2.1.1.2.3: Operational pyrheliometers

The routine operation of un-windowed cavity radiometers capable of replicating the accuracy of the WRR have not been widely deployed for the observations used in this RFA because of practical limitations. Therefore, routine measurements of direct solar irradiance were typically made with less accurate pyrheliometers with their mean absolute calibration level transferred from the WRR. The additional uncertainty in the process of transferring the WRR calibrations to the pyrheliometers as well as to their actual performance in the field needs to be considered.

Two different models pyrheliometers are used widely by the sites reporting results for this assessment, the Eppley Laboratories Normal Incidence Pyrheliometer (NIP) and the Kipp and Zonen CH-1 pyrheliometer. Evaluations of these instruments early in the history of the BSRN project concluded that their uncertainty was not sufficient to match the desired capabilities of the cavity radiometers. However, a thorough evaluation of the pyrheliometers actual operational uncertainty in routine use was not pursued until recently ( Michalsky et al 2011). Comparisons conducted by BSRN (WCRP, 1991) suggested the spread between two specific pyrheliometers could be as much as 2.4%, although a sample group of 21 instruments were used to indicate that a

95% range of -1.3% to 1.1% could be achieved when the data were closely checked for proper instrument operation, such as with example results shown in *Figure A.2.1.1*.

In another approach using the error-source summing methodology, Myers (1988) found an uncertainty in Eppley pyrliometer to be 1.99%. However, the primary error sources identified (Myers, 1989) came from solar tracking and thermopile temperature sensitivity, which can now be shown to be substantial less with more modern trackers and instruments selected for better thermal sensitivity. Halthore et al 1997 estimated that the typical pyrliometer had an accuracy of 1% and showed that highly sophisticated physical model calculations of the quantity agreed to direct observations within that uncertainty. Others (e.g., Michalsky et al 2005) have found similar results under ideal or near-ideal clear sky conditions. However, there could be significant undocumented uncertainty under all-sky all-meteorological conditions where that unwindowed reference cavity radiometer is unable to operate because of its sensitivity to strong air currents and interference from precipitation. Also, conditions of high variability and forward scattering due to moving broken clouds will complicate evaluation of measurement uncertainties due to differences in the time constants and fields-of-view of the instrumentation. In addition, the impacts of partial tracking failure or minor optical window contamination are very difficult to quantify, particularly their net effects in a continuous operational data set. Including these potential error-sources in the error-summing methodologies would produce extremely large measurement uncertainties. The actual error in these cases is unknown because the frequency of occurrence of those conditions, and hence the total uncertainty, is indeterminate.

#### A.2.1.1.2.4: Improved instrumentation

Thermally stabilized and windowed cavity radiometers have been developed and suggest good promise for providing more accurate direct beam measurement at sites where they can be supported financially and logistically (Michalsky et al., 2011). Also, as of 2010, new models of commercially available pyrliometers have been introduced and will need to be evaluated for future use by the scientific community. One such evaluation was undertaken by BSRN with facilitating support from the US National Renewable Energy Laboratory in Golden Colorado.

This evaluation, called the Variable Conditions Pyrliometer Comparison (VCPC) includes a triplicate sample of current and older commercial pyrliometers compared to triplicate windowed and unwindowed direct-beam cavity radiometers, which should provide more definitive information on the overall uncertainty of current and past operational direct beam observations but still with error-free solar tracking, which is being maintained during VCPC. Michalsky et al., 2011 have provided initial results from the VCPC and confirm an improved level of 95% spread uncertainties with newest available commercial pyrliometers but which do not impact the analysis in this assessment.

#### A.2.1.1.3: Diffuse solar irradiance

Diffuse solar irradiance is best measured, as recommended by BSRN, by a thermal-offset-free or corrected, level, upward-facing pyranometer that is blocked from the direct solar beam by a small tracking shade-disk device. These shaded pyranometers are subject to fewer sources of uncertainty than unshaded ones because of the lack of strong directional component in the observed field, although, the diffuse field can have some directional dependence due to unevenly distributed clouds and aerosols as well as the zenith angle dependence of Rayleigh scattering. Although not isentropic, the typical mean incident angle for diffuse sky solar radiation is about 45 degrees and pyranometers can be well characterized for that case. The uncertainty in the

diffuse measurement comes from several sources starting with the primary calibration reference standard. Because there was, and is, not a recognized specific reference standard for diffuse solar irradiance measurement, various transfer standards that translate the WRR irradiance levels to 2 pi steradian fov instruments have been devised and widely utilized. A common and direct way to accomplish this under steady clear sky conditions is by making simultaneous observations with both the WRR direct beam instrument and the pyranometer while alternately shading and unshading the pyranometer with a small shade disk, subtending the same angle as the pyrheliometer fov, on a schedule designed to allow for the time responses of both instruments. The pyranometer calibration is then that needed to equate its response to the difference between being shaded and unshaded to the separately measured direct beam. The details of this can be tedious and varied but when done with the solar zenith angle near 45 degrees the sensitivity of the pyranometer at the typical diffuse incident angle is determined. In this case, the effects of the glass dome thermal offsets are essentially canceled. The uncertainty in the resulting diffuse irradiance measurements has recently been determined by intercomparison of largely independent (except for connection to the WRR) measures of diffuse and compared to realistic physical computations of expected values (Michalsky et al., 2006). In a follow-up paper, Michalsky et al 2007 recommend a methodology for the establishment of base diffuse reference standard. However, this methodology has not yet been widely implemented and measurements used elsewhere in this comparison can only be indirectly related to that recommendation and result. With those results, it appears that diffuse solar irradiance under clear and cloudy sky, with the possible exception of extreme directional diffuse or precipitation cases, can be measured to within better than  $3 \text{ W m}^{-2}$  (6% for typical Rayleigh sky) 95% of the time. Prior to this there was a range of uncertainties in reported diffuse measurements that can sometimes depend on undocumented aspects of the measurement program and the proliferation of thermal offset errors in this measurement.

#### **A.2.1.1.4: Effects of the pyranometer body-dome temperature differentials (thermal offset)**

The extent of thermally induced offsets due to dome temperature differentials have not always been fully recognized or accounted for. Contributing to this problem were production instrument designs that had strayed away from earlier remedial concepts designed to minimize these errors. In addition, instrument ventilation systems sometimes can aggravate the problem. This can result in diffuse errors exceeding those that would have been estimated by manufacturers and formal uncertainty analysis. Errors as large as 40% to 50% in diffuse were possible, particularly when skies were clear and the irradiance values low (Bush et al 2000, Dutton et al. 2001, Haeffelin et al., 2001). Correction methodologies were developed (Dutton et al., 2001; and Younkin and Long, 2004) and affected data provided for this assessment have been reprocessed at their origin to eliminate or substantially reduce this error. Michalsky et al., 2006, 2007 have shown that the corrected diffuse solar data have an uncertainty of near 4 to 6  $\text{W m}^{-2}$  when corrected using methods described by Dutton et al or Younkin and Long, with somewhat better accuracies using the Younkin and Long correction. It was also recognized that diffuse observations acquired by black and white (segmented detector) and certain newer pyranometers are inherently less susceptible to the offset error.

## A.2.1.2: Uncertainty in downwelling thermal IR (Pyrgeometer) observations

### A.2.1.2.1: Background

Attempts to compare, standardize, expand, and significantly improve in situ broadband measurements surface IR irradiance were begun by the BSRN and others around 1990. Prior to that the time, estimates in the uncertainty of the best maintained surface IR irradiance observations could not be substantiated at better than  $\pm 30 \text{ Wm}^{-2}$ . The earliest demonstration that modern pyrgeometers do provide observations that are in agreement to within about  $5 \text{ Wm}^{-2}$  of relatively complete and rigorous radiative transfer theory over a wide range of conditions were given by Dutton (1993), and Miskolczi (1994). This result was confirmed with model comparisons to spectrally integrated observations reported by Ellingson and Wiscombe (1996).

A pyrgeometer round-robin comparison, Philipona et al., 1996, first established that a consensus calibration reference level appeared to exist among number of international calibration laboratories and could be further used and maintained to advance the state of the IR measurement capability. The inter-laboratory agreement established by Philipona et al., 1996 showed that a clear consensus pyrgeometer calibration level existed among 6 of the 13 participating independent laboratories with the remaining 7 indicating no other particular agreement between them. The narrow spread in the consensus agreement,  $\sim 1.5\%$ , also provided strong evidence that the consensus level could be indicative of the proximity to absolute values.

The next step in developing an international IR calibration reference was the construction and utilization of a self-calibrating, sky-scanning, IR radiance, radiometer, Philipona et al (2001). Direct comparisons between that instrument's observations and a group of pyrgeometers calibrated to agree with the initial 6-laboratory round-robin consensus showed agreement to within the 1% to 2% , Philipona et al (2001) and Marty et al (2003), In 2005, the WMO Committee on Instruments and Methods of Observations (CIMO), which sanctions the WRR scale for solar measurements, established an interim international IR calibration traceable reference standard (World Infrared interim Standard Group, WISG) based on the aforementioned IR work. CIMO continues to refine and further substantiate the absolute level of this reference standard as well perpetuate and propagate it within the international community. This WISG is perpetuated by the WRC is currently believed to be accurate to within about  $3 \text{ Wm}^{-2}$ , Gröbner, 2008.

Given proper operation of instrumentation and transfer of the reference standard calibration, this level of accuracy can be expected to be most readily achieved in the field at night or in the solar shaded configuration because the solar component increases the uncertainty due to variations in pyrgeometers' spectral characteristics and a small component of thermal IR in solar radiation.

The additional uncertainty in solar shaded daytime IR measurements has been estimated to be about  $2\text{-}3 \text{ Wm}^{-2}$ , Philipona et al 2001. Multiple pyrgeometer calibration and data reductions methodologies have been developed from the fundamental heat budget formulation for the thermal sensing detector at the core of the instrument. The calibration and data reduction methods are inter-related in that the calibration process provides the opportunity to fit the multivariate instrument output to a calibration source's known blackbody irradiance to produce coefficients for the heat budget based data reduction equation. Most widely used during the era covered by this assessment is the equation developed by Albrecht and Cox (1977) that is a mathematical simplification to the complete solution of the instrument heat budget by dropping the smallest terms.. Solutions using the more complete heat budget expression were proposed by Philipona (1998), Fairall et al (1998), and Reda (2002) and are beginning to be used more widely with some

improvement in instrument precision, as demonstrated by Philipona et al 2001. The details of application of these methods are not within the context of this report, however, application of the new expressions has minor impact on operational pyrgeometer mean results, as seen in the following.

To assess each of the three currently most widely used pyrgeometer data calibration/reduction expressions [Albrecht, Philipona (PMOD), and Reda (NREL)] each was used to reproduce the WISG scale. The results are given in *Figure A2.1.2* and summarized in *Figure A.2.1.3* (Provided by J. Gröbner/WRC.). These figures show the standard deviations for 50 different instruments with each using each of the three methods to derive incident IR irradiance as compared to the value obtained by the WISG. It is seen that even though the more sophisticated equations produce slightly smaller range of results, the differences of the means are negligible. Field deployments of pyrgeometers are transitioning to the more complete expressions as calibration centers start supplying the required calibration coefficients. It has, however, been noted that the more complete expressions do better capture short term fluctuations, particularly in daytime.

During 1990's when the in situ surface observations used here were being expanded, only one commercially available pyrgeometer (Eppley Labs PIR) had a demonstrated ability to make IR observations at the level of accuracy described above. Subsequently, the Kipp & Zonen CG4 pyrgeometer has demonstrated similar qualities and is in wide use currently. However, as a result, a majority of the IR data collected by BSRN and available at the archive for this assessment have derived from the Eppley instruments using the Albrecht method with calibrations supplied by Eppley Laboratory. Unfortunately, a specific value of the coefficient for the dome correction term in the Albrecht method was not supplied by Eppley and some contributors have used a generic value of 4.0 as once recommended by Eppley.

However, Albrecht dome-coefficient values closer to 3.0 to 3.5 are now known to be more typical with the approximate range being from 2.0 to 4.5 from instrument to instrument. A bias in this coefficient leads to IR irradiance errors with the sign depending on dome and case temperature differences. A positive bias in the coefficient leads to a positive bias in the irradiance if the dome temperature is less than the case (or body) temperature, which is typical for unheated ventilator installations. For example, pyrgeometer calibrations performed by NOAA/CMDL(ESRL) assigned dome coefficients prior to 1 Nov 2010 that were biased high by about 0.5, which accounts for some, if not all, of the mean bias of about +4 W m<sup>-2</sup> seen in *Figure 5.1.5* (Chapter 5).

#### **A.2.1.2.2: Indoor vs. outdoor IR calibrations**

Investigations are underway into outdoor vs. indoor calibrations of pyrgeometers. Indoor calibrations are conducted relative to laboratory black-body irradiance whereas those outdoors are using an integrated spectrum substantially different from a black body due to the semitransparent portions of the atmospheric IR spectrum. Outdoor calibration methods utilize either a hybrid of laboratory and outdoor determined coefficients or a direct transfer from reference instruments to field instruments. The differences are expected to be within existing uncertainty stated above because much of the earlier work involved comparing laboratory calibrated pyrgeometers with absolute sky-scanning radiometer outdoors where the overall agreement was within about 3 Wm<sup>-2</sup> (Philipona et al, 2001 and Marty et al 2003) when restricted to nighttime. It can be expected that the more complete calibration solutions of Philipona or Reda would be preferred in sunlight, particularly if the instrument is not operated with the tracking solar shade device, although most observations utilized in this RFA were solar-shaded.

### **A.2.1.2.3: Uncertainty from pyrgeometer dome spectral characteristics**

The amount of energy in the surface radiation budget to be accounted for by this measurement is from entire spectral range over which atmospheric constituents or earth's surface are emitting, as viewed from just above (typically ~2-4 m but a height of 30 m or more is recommended) the earth's surface. As with solar instruments, uncertainty in the measurement includes that amount of energy from the source of interest that falls outside the actual spectral sensitivity range of the particular instrument. Simple calculations of the Planck curve provide the upper limits to the amount of energy outside the nominal spectral cutoffs of the filters. In the range of -70C to +40C less than  $0.5 \text{ Wm}^{-2}$  comes from wavelengths shorter than 3.5 micrometers.

For wavelengths longer than the nominal pyrgeometer longwave cutoff of 50 micrometers, there is between  $7 \text{ Wm}^{-2}$  (9%) and  $15 \text{ Wm}^{-2}$  (2.7%) for -70C and 40C respectively, with actual ambient amounts less depending on water vapor and cloud emission. Since most pyrgeometer calibrations are performed over a range of temperatures and single mid-range value corresponding to near 0C is typically used, and considering that most currently available data calibrated ultimately to a black body reference, the calibrated final value accounts for fixed amount of the roughly 4% of the energy being beyond 50 micrometers. This translates to  $-4 \text{ Wm}^{-2}$  and  $+7 \text{ Wm}^{-2}$  error for extreme target temperatures of -70C and +40C respectively, and  $0 \text{ Wm}^{-2}$  error at 0C for this error source.

However, since emission from the filter dome itself beyond 50 um does reach the instrument detector the error is reduced depending on the difference of the dome and effective sky temperature. For example, if the respective temperatures are 30C and 0C then the net error equals about  $2 \text{ Wm}^{-2}$  and is partially compensated in the laboratory calibration by forcing agreement to the black body. The error is always positive for a target cooler than the dome.

### **A.2.1.2.4: Uncertainty due to pyrgeometer temperature measurement**

All methods of reducing pyrgeometer observations depend on the 4<sup>th</sup> power of the measured instrument temperatures. Most pyrgeometers use /YSI-44031 thermistor based temperature sensors with a specified absolute interchangeability of 0.1C but with an order of magnitude better long-term precision over the full range of the measurement. The interchangeability bias in a particular pyrgeometer thermistor would tend to be removed by the calibration process where there agreement with reference irradiances is achieved through least squares regression or similar processes. The maximum pyrgeometer irradiance error for a  $\pm 0.02\text{C}$  relative error at 27C ambient would be  $\pm 1.0 \text{ Wm}^{-2}$ .

### **A.2.1.3: Data sampling and recording**

The typical thermopile radiometers under fixed illumination produce unamplified signals that are steady to around 1 part in 10,000. However, the need for amplification and the transfer of that signal to the data logger introduce sources for noise that should be filtered or averaged out. Also, when exposed to an atmospheric signal, a substantial amount of variability can occur in a few seconds that is not of interest for most applications in climate or meteorology. Since temporally complete integrated irradiant energy is the desired quantity, both noise reduction and high-speed continuous sampling is desirable. To help address this, integrating voltage measurement methods are used (typically integrating over one AC power line cycle) for each sample effectively averaging over the finite individual sampling times. Thirteen or more bits of

A/D resolution are used over the sample integration time; typically multiples of  $1/50^{\text{th}}$  or  $1/60^{\text{th}}$  of a second (one AC powerline cycle) are satisfactory for removing any AC power induced noise. However, that level of noise reduction does not assure all forms of electromagnetic interference, such as RFI, will be removed and vigilance of the observing system is required to avoid undesirable observing conditions. Although somewhat arbitrary, this minimum retrievable time resolution has widely been determined to be one minute, as is the case in the BSRN specifications. Unpublished studies done for BSRN (B. Forgan personnel communication) have shown that one-minute averages of 1 Hz samples do adequately (to within  $1-2 \text{ Wm}^{-2}$ ) capture the true one-minute integral (or average) of typically varying clear-sky surface irradiance signals even though only being sampled for  $1/50^{\text{th}}$  to  $1/60^{\text{th}}$  of the time during that minute. This sampling does not as completely capture the true minute average for the case of the potentially highly varying direct solar beam in broken cloud cases. In those cases both the response time of the radiometer and the sampling rate are not adequate to maintain the stated uncertainty in the one minute average. The true rate of beam variations are not well documented because the lack of better than 1-sec e-folding time response of typically available pyrhemometers. However, with the purpose of the average of 1-Hz samples being representative of a 1-minute integral, this slower time response behaves as a component of the integrating process by averaging over the high frequency natural variability. A quantification of just how well a 1-second time-response instrument captures much higher frequency variability is a subject for further investigation. To preserve some information on the within-minute variability, BSRN recommends that the standard deviations of the one-minute averages also be computed and saved.

### References (for Appendices A.2.1):

- Albrecht, B. And S. Cox, 1977: Procedures for improving pyrgeometer performance. *J. Appl. Meteor.* **16**, 188-197.
- Bush, B.C., F.P.J.Valero, A.S. Simpson, and L.Bigone, 2000: Characterization of thermal effects in pyranometers: A data correction algorithm for improved measurement of surface insolation, *J. Atmos. Oceanic Technol.* **17**, 249-264.
- Dutton, E.G., J.J. Michalsky, T. Stoffel, B.W. Forgan, J. Hickey, D.W. Nelson, T.L. Alberta, and I. Reda, 2001: Measurement of broadband diffuse solar irradiance using current commercial instrumentation with a correction for thermal offset errors. *J. Atmos. Oceanic Tech.* **18**, 297-314.
- Fairall, C.W., P.O.G. Persson, E.F. Bradley, R.E. Payne, S.P. Anderson, 1998: A new look at calibration and use of Eppley precision infrared radiometers. Part I: Theory and application. *J. Atmos. Oceanic Tech.* **15**, 1229-1242.
- Fröhlich, C., 1991: History of solar radiometry and the World Radiation Reference. *Metrologia*, **3**, 111-115.
- Haeffelin, M., S. Kato, A.M. Smith, C.K. Rutledge, T.P. Charlock, and J.R. Mahan, 2001: Determination of the thermal offset of the Eppley precision spectral pyranometer. *Appl. Opt.* **40**, 47
- ers, D. R. (1988). Uncertainty Analysis for Thermopile and Pyranometer and Pyrhemometer Calibrations Performed by SERI SERI/TR 215-3294. Golden, CO, Solar Energy Research Institute.
- Myers [http://www.sciencedirect.com/science?\\_ob=ArticleURL&\\_udi=B7572-4808MGX-2K&\\_user=2640392&\\_coverDate=12%2F31%2F1989&\\_rdoc=1&\\_fmt=high&\\_orig=search&\\_origin=search&\\_sort=d&\\_docanchor=&\\_view=c&\\_searchStrId=1459855833&\\_rerunOrigin=google&\\_acct=C000058412&\\_version=1&\\_urlVersion=0&\\_userid=2640392&md5=da0766270fc8733c988a35f334cf53d7&searchtype=a](http://www.sciencedirect.com/science?_ob=ArticleURL&_udi=B7572-4808MGX-2K&_user=2640392&_coverDate=12%2F31%2F1989&_rdoc=1&_fmt=high&_orig=search&_origin=search&_sort=d&_docanchor=&_view=c&_searchStrId=1459855833&_rerunOrigin=google&_acct=C000058412&_version=1&_urlVersion=0&_userid=2640392&md5=da0766270fc8733c988a35f334cf53d7&searchtype=a) - implicit0
- D.R., K.A. Emery, and T.L. Stoffel, 1989: Uncertainty estimates for global solar irradiance measurements used to evaluate PV device performance. *Solar Cells* **27**, Issues 1-4, 455-464.

- Myers, D.R., I. Reda, S Wilcox, A Andreas, 2004: - Optical radiation measurements for photovoltaic applications: instrumentation uncertainty Proceedings of SPIE's 49th Annual Meeting, Denver, Colorado, August 2-6 2004.
- Philipona, R., et al., 1998: The BSRN pyrgeometer round-robin calibration experiment. *J. Atmos. Ocean. Tech.* **15**, 687-696.
- Philipona, R., et al., 2001: Atmospheric longwave irradiance uncertainty: Pyrgeometers compared to an absolute sky-scanning radiometer, atmospheric emitted radiance interferometer and radiative transfer model. *J. Geophys. Res.* **106**, 28,129-28,141.
- Philipona R, 2002: [Underestimation of solar global and diffuse radiation measured at Earth's surface](#) : *J. Geophys. Res.* **107**, **D22** Article Number: 4654
- Reda, I. et al., 2002: Pyrgeometer calibration at the National Renewable Energy Laboratory (NREL) *J. Atmos Solar-Terres Phys.* **64**, 1623-1629.
- WCRP, 1991: Radiation and Climate: Second workshop on implementation of the Baseline Surface Radiation Network. Davos, Switzerland 6-9 August 1991. World Climate Research Program Report-64, WMO/TD No. 453, 26pp.
- Younkin K and CN Long. 2004. "Improved Correction of IR Loss in Diffuse Shortwave Measurements: An ARM Value Added Product." Atmospheric Radiation Measurement Program Technical Report, ARM TR-009. Available via <http://www.arm.gov.2-484>.
- Halothore, R. N., S. E. Schwartz, J. J. Michalsky, G. P. Anderson, R. A. Ferrare, B. N. Holben, H. Ten Brink. 1997: Comparison of model estimated and measured direct-normal solar irradiance, *J. Geophys. Res.*, 102, 29,991- 20,002.
- Kopp, G., G. Lawrence, and G. Rottman, 2005: The Total Irradiance Monitor (TIM): Science Results, *Solar Physics*, **230**, 1, 129-140.
- Kato, S., T. P. Ackerman, E. E. Clothiaux, J. H. Mather, G. G. Mace, M. L. Wesely, F. Murcray, and J. Michalsky (1997), Uncertainties in modeled and measured clear-sky surface shortwave irradiances, *J. Geophys. Res.*, 102(D22), 25,881–25,898.
- Marty, C., et al., 2003: Longwave irradiance uncertainty under arctic atmospheres: Comparisons between measured and modeled downward longwave fluxes. *J. Geophys. Res.*, VOL. 108, NO. D12, 4358, doi:10.1029/2002JD002937.
- Michalsky, J.J, et al 2010: An extensive comparison of commercial pyrheliometers under a wide range of routine observing conditions, *J. Tech.*, Submitted.
- Michalsky, J. J., et al., Toward the development of a diffuse horizontal shortwave irradiance working standard, *J. Geophys. Res.*, 110, D06107, doi:10.1029/2004JD005265, 2005.
- Michalsky J. J., C. Gueymard, P. Kiedron, L. J. B. McArthur, R. Philipona, T. Stoffel (2007), A proposed working standard for the measurement of diffuse horizontal shortwave irradiance, *J. Geophys. Res.*, **112**, D16112, doi:10.1029/2007JD008651.
- Myers, D.R., I Reda, S Wilcox, T Stoffel - Uncertainty Analysis for Broadband Solar Radiometric Instrumentation Calibrations and Measurements: World Renewable Energy Congress, 2004.

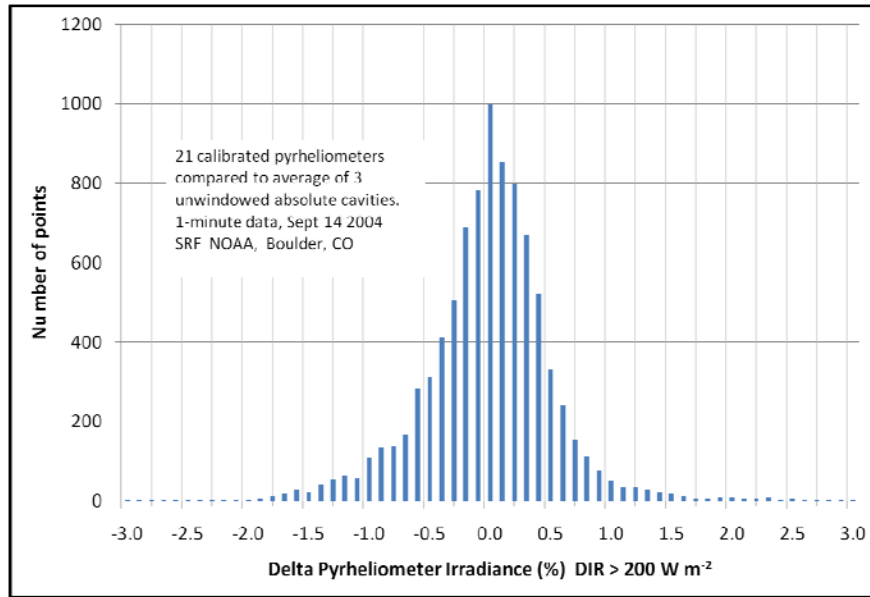


**Figure A.2.1.1:** Differences between solar irradiances measured by 21 test pyrheliometers and that measured by an average of 3 unwindowed active cavity radiometers.

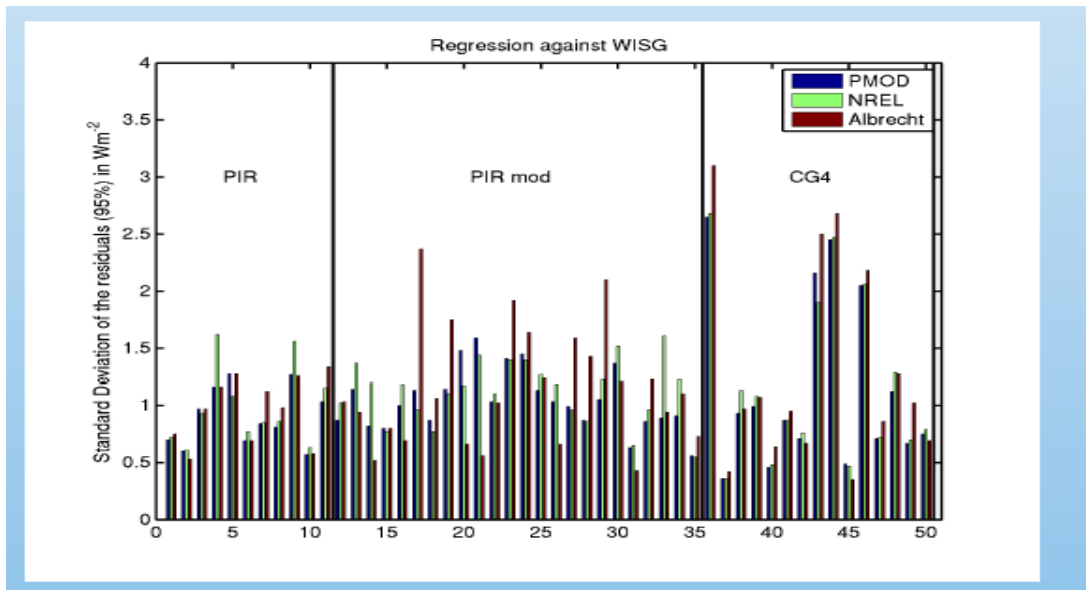


**Figure A.2.1.2:** Standard deviations of the differences from a WISG reference for a number of pyrometers (abscissa) when each is operated with three different instrument transfer (calibration) expressions identified as PMOD, NREL, and Albrecht in the text

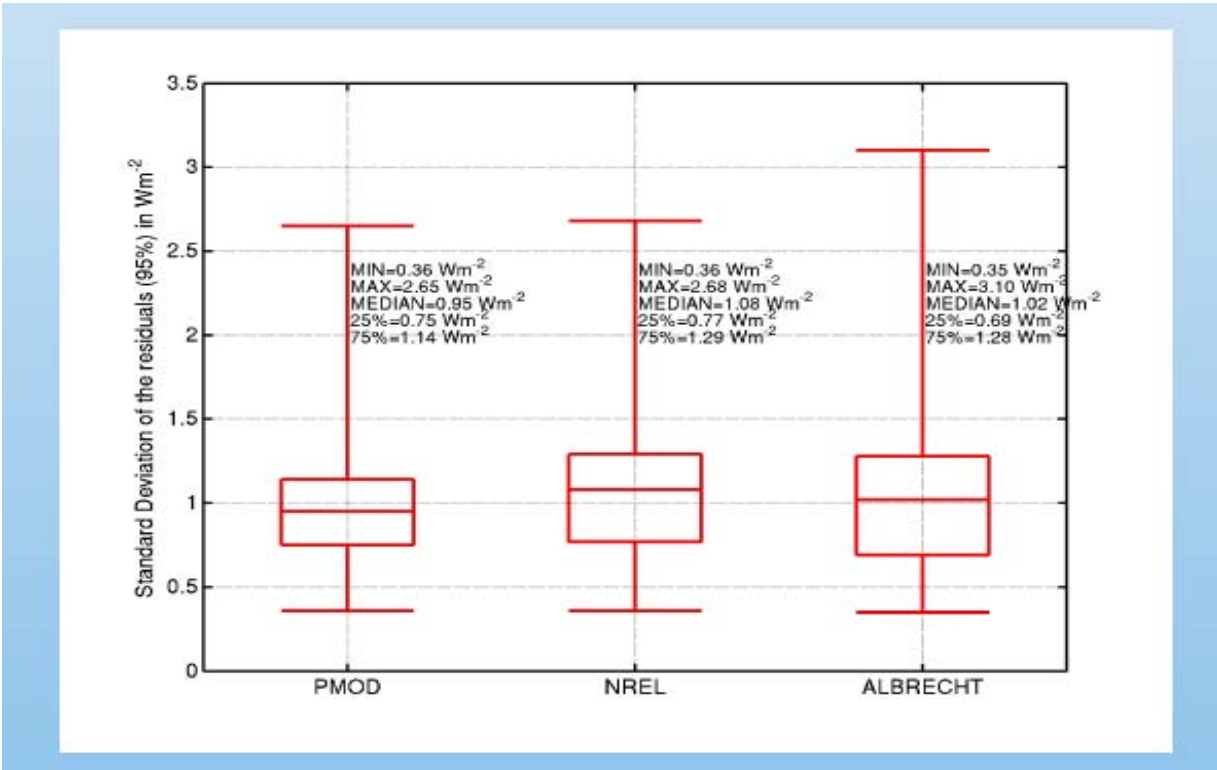


*Figure A.2.1.3: Box-&-Whisker plot summary of the results show in Figure A2.1.1*

## A.2.2: Brief Summary of Surface In-Situ Measurement Data Products

E. G. Dutton, C. Long, D. Rutan, R. Philipona, M. Wild, G. König-Langlo, F. Vignola

Note: if using any of the data described below be sure to comply with the data use policy as described at each original data set location as given.

### A.2.2.1: Global Energy Balance Archive

The [Global Energy Balance Archive \(GEBA\)](#) is a database developed and maintained at ETH Zürich for worldwide instrumentally measured energy fluxes at the Earth's surface (Ohmura et al 1989, Gilgen et al. 1998, Wild et al. 2011). GEBA's mission is to provide a comprehensive source of information on the global distribution of surface energy fluxes. GEBA currently undergoes major revisions and updates both technically and data content wise to meet these goals (Wild et al. 2011). Data sources for GEBA include data reports from national weather services, data from various research networks (e.g., BSRN, ARM, SURFRAD), data published in peer reviewed publications and by the World Radiation Data Centre in St Petersburg, Russia, as well as data obtained through personal communication. Data in GEBA are stored with a temporal resolution of monthly means.

As of this assessment, GEBA contains more than 2000 sites with 450,000 monthly means of various energy flux components. The most widely measured and stored surface energy flux component is the downward surface solar radiation. Many sites started to measure this quantity in the late 1950s during the International Geophysical Year (IGY), or in the early 1960s. The longest record of downward surface solar radiation in GEBA extends back to the early 1920s (Stockholm site). The data in GEBA undergo a number of quality checks to assure homogeneity (Gilgen et al. 1998). Accuracy of the surface solar radiation data in GEBA were estimated in Gilgen et al. (1998) at 2% for annual means.

The GEBA dataset is widely used in the international community to:

- detect long term variations in the radiative forcing at the Earth surface both in the solar spectrum (“global dimming/brightening”) and in the thermal spectrum (“surface greenhouse forcing”)
- evaluate global and regional climate models as well as re-analyses in their ability to reproduce surface energy exchanges
- evaluate satellite derived products of surface fluxes
- determine atmospheric column absorption by combining the surface observations from GEBA with collocated satellite observations of top of atmosphere fluxes
- provide information for solar energy applications and solar power plants.

A list of GEBA sites for which data is included in the GEWEX Radiative Flux Assessment archive is provided in *Table A.2.2.1*.

**Table A.2.2.1. GEBA sites with geographical information.**

No.	Code	Lat (°)	Lon (°)	Elev (m)	Location
1	KIR	67.8500	20.2333	505	Kiruna, Sweden
2	SOD	67.3667	26.6500	178	Sodankyla, Finland
3	RKJ	64.1333	-21.9000	52	Reykjavik, Iceland
4	JOK	60.8167	23.5000	104	Jokioinen, Finland
5	MLH	55.3667	-7.3333	25	Malin Head, Ireland
6	HAM	53.6500	10.1167	49	Hamburg, Germany
7	POT	52.3833	13.1000	33	Potsdam, Germany
8	WAR	52.2667	20.9833	130	Warszawa, Poland
9	WAG	51.9667	5.6500	10	Wageningen, Netherlands
10	UCL	50.8000	4.3500	105	Uccle, Belgium
11	HRA	50.2500	15.8500	241	Hradec Kralove, Czech Republic
12	WRZ	49.7667	9.9667	275	Würzburg, Germany
13	ZAK	49.2833	19.9667	857	Zakopane, Poland
14	ULB	47.8500	106.7500	1264	Ulan-Bator, Mongolia
15	DVG	46.8167	9.8500	2670	Davos, Switzerland
16	SIO	46.2167	7.3333	480	Sion, Switzerland
17	LMG	46.1667	8.7833	380	Locarno-Monti, Switzerland
18	BRD	44.8333	-0.7000	49	Bordeaux, France
19	URM	43.7833	87.6167	918	Urumqi, China
20	SAP	43.0500	141.3333	17	Sapporo, Japan
21	SHN	41.7333	123.4500	43	Shenyang, China
22	BRN	40.6500	17.9500	15	Brindisi, Italy
23	LZH	36.0500	103.8833	1517	Lanzhou, China
24	FUK	33.5833	130.3833	3	Fukuoka, Japan
25	KAG	31.5667	130.5500	4	Kagoshima, Japan
26	NAH	26.2333	127.6833	35	Naha, Japan
27	AHM	23.0667	72.6333	55	Ahmadabad, India
28	CLC	22.6500	88.4500	4	Calcutta, India
29	NAN	-17.7500	177.4500	16	Nandi, Fiji
30	VAL	-33.0333	-71.4833	70	Valparaiso (USM), Chile

**References for A.2.2.1:**

- Ohmura, A., H. Gilgen, and M. Wild, 1989: Global Energy Balance Archive GEBA, World Climate Program - Water Project A7, Report 1: Introduction. *Zürcher Geografische Schriften* Nr. 34, Verlag der Fachvereine, Zürich, 62pp.
- Gilgen, H., M. Wild, and A. Ohmura, 1998: Means and trends of shortwave irradiance at the surface estimated from Global Energy Balance Archive data. *J. Climate*, **11**, 2042-2061.
- Wild, M. et al. (2011) The new GEBA version 2011 (in preparation.)

**A.2.2.2: Baseline Surface Radiation Network (BSRN)****A.2.2.2.1: Introduction**

The objective of the BSRN is to provide in situ observations of short- and long-wave surface radiation fluxes of the best possible quality currently available from geoclimatically representative sites for climate research applications. The observed surface radiation fluxes are high sampling-rate observations (typically 1-hz samples averaged over one minute) obtained

from a small number of stations within different climate zones of the globe. At many of these sites collocated surface and upper air meteorological data and other supporting observations are also available. Throughout the BSRN network, the measurements are meant to be time-continuous. However, gaps of various lengths occur for various operational reasons and can impact subsequent averaging summaries of the data such as those used in this assessment. An evaluation of the impact of these gaps on various averaging strategies was given by Roesch et al 2011.

The acquired BSRN data can be used to:

- monitor the background of the short- and long-wave irradiance as well as changes of the components in regions least influenced by human activities, with the best methods currently available;
- provide datasets for validation and evaluation of satellite-based measurements of surface radiative fluxes; and
- produce high-quality observational datasets for the comparisons with climate model (GCM) results and for the development of local radiation climatologies.

From [http://www.bsrn.awi.de/fileadmin/user\\_upload/Home/Publications/McArthur.pdf](http://www.bsrn.awi.de/fileadmin/user_upload/Home/Publications/McArthur.pdf) the BSRN operations manual can be accessed (*McArthur L.J.B.*, 2004). It offers detailed information on how these BSRN measurements are made. All the BSRN measurements are centrally archived in the World Radiation Monitoring Center (WRMC) that was founded in 1992 at ETH Zürich, Switzerland. In 2008, it was moved to the Alfred-Wegener-Institute (AWI), Bremerhaven, Germany (see: <http://www.bsrn.awi.de/>).

#### **A.2.2.2.2: Data Quality Assurance**

Within the BSRN there is a station scientist for each site who is responsible for the quality of the data submitted to WRMC. For this reason, the station scientists are required to check their data carefully prior to the submission. Nevertheless, each submitted file is visually checked by the WRMC staff before entering the archive. Additionally, any dataset with recognized quality problems is excluded from the archive and resubmitted – carrying a higher version number - if the problems could be solved. A process for identifying and flagging data of questionable quality was applied to the BSRN data utilized in this assessment as described by Roesch et al., 2011 and summarized later.

#### **A.2.2.2.3: Description of the BSRN-Based Data Sets**

Products derived from BSRN archived data ([http://eosweb.larc.nasa.gov/GEWEX-RFA/ground\\_measurements/time\\_series.html](http://eosweb.larc.nasa.gov/GEWEX-RFA/ground_measurements/time_series.html)) were computed for use in the RFA and have file names that start with “BSRN”. While the WRMC contains the original data from all existing BSRN stations in full time resolution, the RFA products are averages, both 15-minute and one-month, from 35 BSRN sites – see Table A2.2.2 covering the time up to 2005. The RFA product generation for monthly averages follows the “method 7” in Roesch et al., 2011 and basically fills missing data from a monthly mean diurnal cycle.

**Table A.2.2.2:** BSRN sites with geographical information. Networks to which individual sites belong are listed in parentheses. When sites are not maintained by organizations within the country of operation, the nationality of the maintaining institution is listed in brackets.

No.	Code	Lat (°)	Lon (°)	Elev. (m)	Location
01	NYA	78.9333	11.9500	11	Ny Ålesund, Spitsbergen [Germany]
02	BAR	71.3167	-156.6000	8	Barrow, Alaska, USA
03	LER	60.1333	-1.1833	84	Lerwick, Shetland Islands, Great Britain
04	TOR	58.2667	26.4667	70	Toravere, Tartu Observatory, Estonia
05	LIN	52.2167	14.1167	125	Lindenberg, Offenbach am Main, Germany
06	CAM	50.2167	-5.3167	88	Camborne, Cornwall, Great Britain
07	REG	50.2000	-104.7167	587	Regina, Saskatchewan, Canada
08	FPE	48.3167	-105.1000	634	Fort Peck, Montana, USA
09	PAY	46.8167	6.9500	491	Payerne, Vaud Canton, Switzerland
10	CAR	44.0500	5.0333	100	Carpentras, France
11	PSU	40.7167	-77.9333	376	Rock Springs, Pennsylvania, USA
12	BOS	40.1333	-105.2333	1689	Boulder, Colorado, USA
13	BON	40.0667	-88.3667	213	Bondville, Illinois, USA
14	BOU	40.0500	-105.0000	1577	Boulder, Colorado, USA
15	CLH	36.9000	-75.7167	34	Chesapeake Light Station, Virginia, USA
16	DRA	36.6500	-116.0167	1007	Desert Rock, Nevada, USA
17	E13	36.6000	-97.5000	318	SGP Extended Facility 13, Oklahoma, USA
18	BIL	36.6000	-97.5167	318	Billings, Oklahoma, USA
19	TAT	36.0500	140.1333	25	Tateno, Tsukuba City, Japan
20	GCR	34.2500	-89.8667	98	Goodwin Creek, Mississippi, USA
21	BER	32.3000	-64.7667	30	Bermuda [USA]
22	SBO	30.8667	34.7667	500	Sede Boqer (Sde Boker Kibbutz), Israel
23	SOV	24.9167	46.4167	650	Solar Village, Riyadh, Saudi Arabia
24	TAM	22.7833	5.5167	1385	Tamanrasset, Tamanrasset Province, Algeria
25	KWA	8.7167	167.7333	10	Kwajalein, Marshall Islands [USA]
26	ILO	8.5333	4.5667	350	Ilorin, Kwara State, Nigeria [USA]
27	NAU	-0.5167	166.9167	7	Nauru Island [USA]
28	MAN	-2.0500	147.4333	6	Momote, Manus Is., Papua New Guinea [USA]
29	ASP	-23.7900	133.8833	547	Alice Springs, Northern Territory, Australia
30	FLO	-27.5333	-48.5167	11	Florianopolis, Santa Catarina, Brazil
31	DAA	-30.6667	24.0000	1287	De Aar, Northern Cape, South Africa
32	LAU	-45.0000	169.6833	350	Lauder, Otago Region, New Zealand
33	SYO	-69.0000	39.5833	18	Syowa, Antarctica [Japan]
34	GVN	-70.6500	-8.2500	42	Georg von Neumayer, Antarctica [Germany]
35	SPO	-89.9830	-24.7990	2800	South Pole, Antarctica [USA]

The 15-min averages are first computed from the 1-min data for each month. Computation of a single bin (monthly 15-minute average) requires at least 20% valid data. Minute values that are outside the limits listed in *Table A.2.2.3* are treated as missing. For shortwave radiation fluxes, values below  $0 \text{ Wm}^{-2}$  during night (solar zenith angle  $>93$ ) were set to  $0 \text{ Wm}^{-2}$ , although a better practice is to set all night-time values 0.0 to eliminate any instrument induced night bias as well as properly fill any missing night values in daily or longer averages. However, since most night-time values are very close to zero or slightly negative as typically reported from the BSRN instruments due to thermal effects on instruments glass dome, the approach of zeroing the negative values does effectively remove most the night-time bias and thereby reducing the associated bias that would have been incorporated in the daily and monthly average had no night-time adjustments been made. The monthly mean is then computed by averaging the 96 bins ( $96 \times 15 \text{ min} = 24 \text{ h}$ ) that have been produced for each month. The monthly mean is valid only if all bins are filled (include at least 20% of possible observations). Performing computation of the

monthly mean diurnal cycle benefits from the typical diurnal cycle of shortwave fluxes, allowing more accurate estimates for incomplete observations.

**Table A.2.2.3:** Limits used for filtering the high time resolution data before deriving the averaged RFA radiation products. Values outside the indicated intervals were treated as missing prior to forming the monthly averages.  $S_o$  is the solar constant adjusted for Earth-Sun distance.  $\mu$  is the cosine of the solar zenith angle.

Parameter	Lower bound	Upper bound
Global	$-4 \text{ Wm}^{-2}$	$1.5 S_o \cdot \mu^{1.2} + 100 \text{ Wm}^{-2}$
Diffuse	$-4 \text{ Wm}^{-2}$	$0.95 S_o \cdot \mu^{1.2} + 100 \text{ Wm}^{-2}$
Direct	$-4 \text{ Wm}^{-2}$	$S_o \cdot \mu^{1.2}$
Reflected	$-4 \text{ Wm}^{-2}$	$1.2 S_o \cdot \mu^{1.2} + 50 \text{ Wm}^{-2}$
Long-wave down	$40 \text{ Wm}^{-2}$	$700 \text{ Wm}^{-2}$
Long-wave up	$40 \text{ Wm}^{-2}$	$900 \text{ Wm}^{-2}$

## References:

Roesch, A et al. 2011: Assessment of BSRN radiation records for the computation of monthly means” Atmos. Meas. Tech., 4, 339-354, 2011  
[www.atmos-meas-tech.net/4/339/2011/](http://www.atmos-meas-tech.net/4/339/2011/) doi:10.5194/amt-4-339-2011.

### A.2.2.3: CERES/ARM Validation Experiment (CAVE) data sets

#### A.2.2.3.1: Description

The CERES/ARM Validation Experiment (CAVE) data are a collection of radiometric observations at the Earth's surface collected at 24 locations around the globe. The data, which come from a variety of projects and nations, were originally placed in a database for validation of radiation transfer model estimates of surface broadband fluxes calculated by the Surface and Atmospheric Radiation Budget (SARB) group, which is part of the NASA's Clouds and the Earth's Radiant Energy System (CERES) project. At any given surface site, a maximum of seven variables is possible as listed below in Table A2.2.4, though many sites do not include all seven observations.

Initial data are downloaded from the various data sources. Generally these data are 60-second averages of 1-Hz observations. These are then averaged to 15 minutes (minute 0 to minute 14, minute 15 to minute 29, etc.) for a month resulting in 2976 numbers over a 31-day month. We require 7 minutes for a valid 15-minute average where 1-minute data is available, and 6 minutes (two time steps) for the SURFRAD data, which was originally supplied as 3-minute averages. There is no data gap filling at this level of averaging. Quality control of the original data consisted primarily of a series of simple threshold tests requiring each value to be within physically reasonable limits as determined by the data provider and secondarily by CAVE processing. All data in the GEWEX RFA archive are for the year 2004. The CAVE database began collecting data in 1998 to coincide with the launch of CERES PFM on the TRMM satellite and continues today. The entire CAVE data time series can be found at: <http://www-cave.larc.nasa.gov/cave>

**Table A.2.2.4:** GEWEX RFA variable name definitions for the CAVE surface flux data set.

Variable Name	Description	Instrument	Units
ALWDN	All Sky long wave down	Shaded pyrgeometer	Wm <sup>-2</sup>
ALWUP	All sky long wave up	Pyrgeometer	Wm <sup>-2</sup>
ASWDHEM	All sky shortwave down hemispheric	Pyranometer	Wm <sup>-2</sup>
ASWUP	All sky shortwave up	Pyranometer	Wm <sup>-2</sup>
ASWDIR	All sky shortwave direct normal	Pyrheliometer	Wm <sup>-2</sup>
ASWDIF	All sky shortwave diffuse	Shaded pyranometer	Wm <sup>-2</sup>
ASWDN	All sky shortwave down	Component sum (1+2)	Wm <sup>-2</sup>

**Table A.2.2.5:** Measurement locations in the GEWEX RFA CAVE surface flux data set.

Surface Site Location	3 Letter Identifier	Reference Number	Original Data Web Access
Alice Springs, Australia	ASP	(2)	<a href="http://www.bsrn.awi.de/">http://www.bsrn.awi.de/</a>
Barrow, Alaska, USA	BAR	(3)	<a href="http://www.bsrn.awi.de/">http://www.bsrn.awi.de/</a>
Bermuda Island	BER	(3)	<a href="http://www.bsrn.awi.de/">http://www.bsrn.awi.de/</a>
Bondville, Illinois, USA	BON	(4)	<a href="http://www.srrb.noaa.gov/">http://www.srrb.noaa.gov/</a>
Table Mountain, Colorado	BOS	(4)	<a href="http://www.srrb.noaa.gov/">http://www.srrb.noaa.gov/</a>
Boulder Tower, Colorado	BOU	(2)	<a href="http://www.bsrn.awi.de/">http://www.bsrn.awi.de/</a>
Ches Light Tower, USA	CLH	(2)	<a href="http://cove.larc.nasa.gov/">http://cove.larc.nasa.gov/</a>
De Aar, South Africa	DAA	(2)	<a href="http://www.bsrn.awi.de/">http://www.bsrn.awi.de/</a>
Desert Rock, Nevada, USA	DRA	(4)	<a href="http://www.srrb.noaa.gov/">http://www.srrb.noaa.gov/</a>
Lamont, Oklahoma, USA	E13	(1)	<a href="http://www.arm.gov/">http://www.arm.gov/</a>
Billing, Oklahoma, USA	BIL	(1)	<a href="http://www.arm.gov/">http://www.arm.gov/</a>
Fort Peck, Montana, USA	FPE	(4)	<a href="http://www.srrb.noaa.gov/">http://www.srrb.noaa.gov/</a>
Goodwin Creek, Mississippi, USA	GCR	(4)	<a href="http://www.srrb.noaa.gov/">http://www.srrb.noaa.gov/</a>
G. von Neumayer, Antarctica	GVN	(2)	<a href="http://www.bsrn.awi.de/">http://www.bsrn.awi.de/</a>
Kwajalein Island	KWA	(4)	<a href="http://www.bsrn.awi.de/">http://www.bsrn.awi.de/</a>
Lauder, New Zealand	LAU	(2)	<a href="http://www.bsrn.awi.de/">http://www.bsrn.awi.de/</a>
Manus Island	MAN	(1)	<a href="http://www.arm.gov/">http://www.arm.gov/</a>
Nv Alesund, Norway	NYA	(2)	<a href="http://www.bsrn.awi.de/">http://www.bsrn.awi.de/</a>
Paverne, Switzerland	PAY	(2)	<a href="http://www.bsrn.awi.de/">http://www.bsrn.awi.de/</a>
Rock Springs, Pennsylvania, USA	PSU	(4)	<a href="http://www.srrb.noaa.gov/">http://www.srrb.noaa.gov/</a>
Samoa, Island	SAM	(4)	<a href="http://www.esrl.noaa.gov/gmd/">http://www.esrl.noaa.gov/gmd/</a>
Sede Boqer, Israel	SBO	(2)	<a href="http://www.bsrn.awi.de/">http://www.bsrn.awi.de/</a>
South Pole, Antarctica	SPO	(2)	<a href="http://www.bsrn.awi.de/">http://www.bsrn.awi.de/</a>
Tateno, Japan	TAT	(2)	<a href="http://www.bsrn.awi.de/">http://www.bsrn.awi.de/</a>

Each individual file in the GEWEX-RFA archive contains 15-minute averages for one variable for one year of data. *Table A2.2.5* lists each surface site's unique 3-letter identifying name, it's location on the globe and a web site where the original 1 minute data may be accessed.

#### A.2.2.4: Radiative Flux Analysis data and products

The Radiative Flux Analysis is a methodology designed to analyze the time series of surface broadband shortwave (SW) and longwave (LW) irradiance time series to identify periods of clear (i.e., cloudless) skies. Functions are fit to the detected clear-sky data, then fit coefficients are interpolated for cloudy periods and continuous clear-sky SW and LW estimates are calculated. The measured and clear-sky values are then used to infer various cloud macro-physical properties as described below.

A note on the definition of “clear-sky” here: in any determination of whether there are clouds present, some inherent definition of what is and is not a cloud is used. Always some amount of condensed water, either liquid or ice, is allowed under the “clear-sky” classification, otherwise the “cloud cover” would be “overcast” for every square meter of Earth because inevitably there is at least one tiny ice particle and/or liquefied aerosol somewhere in the column. As determined in DuPont et al. (2008), for the SW-based daylight total sky cover the Long and Ackerman (2000) method of clear-sky detection generally allows up to a visible optical depth of about 0.15 to be classified as “clear-sky,” usually as sub-visual cirrus. This “definition” of clear-sky effectively matches that of sky imager retrievals and human sky observations, as shown in Long et al. (2006). Because the broadband downwelling LW is virtually insensitive to high, cold cloud emissions through the intervening atmosphere, “LW effective” clear-sky can contain cirrus of even larger optical depths. Similarly, the “LW effective” sky cover retrievals represent primarily low and mid-level cloud amounts, and rarely includes high clouds.

##### A.2.2.4.1: General

These results are from the Radiative Flux Analysis based on the clear-sky detection and fitting techniques described in Long and Ackerman (2000), Long and Gaustad (2004), Long (2004, 2005), Long et al., (2006), Long and Turner (2008), Barnard and Long (2004), and Barnard et al. (2008). Whereas the original SW Flux Analysis code dealt only with the SW portion of the surface radiative energy budget, this updated code now also includes the LW. This effort is for some variables a work-in-progress, and not all of the methodologies have undergone peer review.

##### Calculated variables that are considered "solid":

Estimates of clear-sky downwelling GlobalSW, DifSW, DirSW; SW fractional sky cover; cloud optical depth for sky cover > 0.95; effective cloud transmissivity; clear-sky downwelling LW, and clear-sky broadband effective emissivity.

##### Calculated variables that are considered "good":

LW sky cover, clear-sky upwelling SW, Cloud radiating temperature

##### Some calculated variables "not yet proven":

Clear-sky upwelling LW, Cloud height estimates

All data, prior to processing through the Radiative Flux Analysis codes, were first quality screened using the QCRad methodology. The QCRad methodology tests all SW and LW data for occurrences that lie outside climatologically-derived expected ranges, as described in Long and Shi (2008).

#### A.2.2.4.2: Notes

The cloud optical depth estimates are based on a technique by Barnard and Long (2004) and Barnard et al. (2008). This technique, an empirically derived relationship adapted from the Delta-Eddington approximation and based on the results of Min and Harrison (1996), is officially only valid for overcast skies (sky cover  $> 0.95$ ) of liquid water clouds. Thus the current output includes cloud optical depth only for sky cover  $> 0.95$  for now. Initial comparisons conducted as part of the ARM CLOUD project (Turner et al., 2006) suggest that the Min and Harrison technique itself tends to overestimate the cloud optical depth for thinner clouds ( $\tau < 5$ ), thus so does the original Barnard and Long (2004) technique. However, a later adaptation of the methodology (Barnard et al., 2008) solved the "thin cloud" problem. Finally, these are "effective" optical depths in that they assume a single uniform liquid cloud layer with an effective radius of 10 microns and an asymmetry parameter of 0.87.

The estimated clear-sky downwelling LW is derived from a technique based on Brutsaert (1975). Unlike the Brutsaert formulation, we use the known clear-sky periods and the corresponding measured clear-sky downwelling LW to calculate lapse rate coefficients (Long and Turner, 2008). We then interpolate these calculated lapse rate coefficients for cloudy periods, similar to the SW technique. Comparisons show that about 85% of the estimated clear-sky LW falls within  $5 \text{ Wm}^{-2}$  of the corresponding clear-sky measured LW (Long, 2004). The uncertainty for cloudy periods, using comparisons to the best model calculations possible, indicates an agreement similar to that above. There is a known "problem", however, in that the only information available for LW estimation is surface measurements. For those times of abrupt major changes in temperature or humidity profiles significantly differing from the "LW effective" clear-sky data the lapse rate coefficients were determined from, such as cold front passages, the clear-sky LW estimates will exhibit greater error. Fortunately, these conditions occur infrequently.

The LW effective sky cover is from a technique developed by Dürr and Philipona (2004), but with some differences. Dürr and Philipona use a climatologically derived and applied formulation for clear-sky effective broadband LW emissivity, whereas those here are derived from surrounding clear-sky data. In addition, Dürr and Philipona use a calculation of downwelling LW standard deviation for the hour preceding the time of interest in their sky cover prediction, where the Radiative Flux Analysis uses a running 21-minute standard deviation centered on the time of interest. The variable is deemed as the "effective LW sky cover" in that the downwelling LW at the surface is insensitive to high and thin clouds, thus the sky cover is essentially most representative of the amount of low and mid-level cloudiness (Long, 2004; Long and Turner, 2008). The original Dürr and Philipona retrieval is in Oktas, so the inherent uncertainty is at least 1/8 of sky cover. The Radiative Flux Analysis uses an 11-minute running mean to smooth the results. For the clear-sky upwelling SW, there are identified problems associated with guesstimating upwelling SW measurements using only detected clear-sky measurements, and then interpolating fit coefficients as is done for the downwelling SW (Long, 2005). For instance, when it snows, it's cloudy, thus the "fit" is way off until the next "clear enough" day for fitting after the snow event. This introduces a large error during the period, and for times of snow melt. Data show that the bi-directional reflectance function also changes over time depending on the surface characteristics. Thus, the current procedure for estimating clear-sky upwelling SW is to look through the data and take a daily average for all data from 1100 through 1300 local standard time. This captures, at least on a daily basis, the major changes in surface albedo such as those from snow accumulation or snow melt. A second pass through the data then uses the "daily noon average" as a constant, and determines a function for any data that

include at least 25% of the total SW produced by the direct component (i.e. significant direct sunlight producing the bi-directional nature of the albedo dependence) using the cosine of the solar zenith angle as the independent variable. Again, these fit coefficients are interpolated for days when insufficient data are available for fitting. The function is then multiplied times the estimated clear-sky SWdn to produce a continuous estimate of clear-sky SWup. Examination of these results for over 10 years of cases from the ARM SGP and NSA sites suggest this technique does fairly well eliminate the problem of it always being cloudy when it snows, and does a better job than just multiplying the measured albedo (SWup/SWdn which often behaves erratically through time depending on whether the direct sun is blocked by cloud or not) times the clear-sky SWdn.

The clear-sky upwelling LW uses the same detected SW and "LW effective" clear-sky data to empirically derive fit coefficients that are again interpolated for cloudy periods (Long, 2005). In this case, since the upwelling LW is tied to the total surface energy exchange including latent and sensible heat, the independent variables used are the downwelling LW, the net SW, 2 meter relative humidity, and wind speed. These last are used as surrogates to help account for the unknown relative changes in surface sensible and latent heat exchange. Comparisons show that over 90% of the estimations agree with detected clear-sky LWup measurements within  $5 \text{ Wm}^{-2}$ . Though estimation of the accuracy of the interpolated values has yet to be investigated, visual inspection indicates that the results appear reasonable. The one exception so far has been for the ARM Barrow site, where the proximity to the near-by ocean, with periods of the open ocean leads that can significantly impact the lower atmosphere. This then decouples the upwelling LW from the local surface conditions and the assumptions that the primary driver of the clear-sky upwelling LW are tied to the clear-sky downwelling LW. Thus in these cases, and with changing wind directions determining whether the local conditions fall under drier continental or moister oceanic conditions, the upwelling clear-sky LW technique has significantly larger uncertainty for the Barrow site. Investigations at other polar sites that are not located on the sea coast do not exhibit these problems.

The cloud field radiating temperature and height estimates are "work in progress," using the measured and clear-sky estimated LWdn, the LW effective sky cover amount, and Independent Pixel Approximation arguments to estimate the LW effective radiating ("cloud") temperature. The uncertainty in this estimation is largely driven by the uncertainty associated with the LW effective sky cover. The value generated assumes a single layer of cloudiness covering the "LW sky cover" portion of the sky, and with uniform radiating properties. Thus this value is best described as an "effective cloud field radiating temperature" with all the assumptions that the word "effective" usually implies. In addition, given a good cloud radiating temperature estimate, one must then figure out how to reasonably translate that temperature to a cloud height. I use here the difference between the estimated cloud field radiating temperature and the ambient air temperature, and a simple 10-degree-C-per-km lapse rate to estimate the effective cloud field radiating height. Note that the imaginary "radiating surface" relates approximately to about one optical depth into the cloud, and so is NOT located at the same height as the cloud physical boundary as would be determined by a lidar or cloud radar. Also, this is an estimate as if all cloudiness were in a single uniform layer. Again, this is a work in progress. Use these at your own risk for now.

#### A.2.2.4.3: Uncertainties

Both the measured and retrieved variables include some degree of uncertainty. *Table A.2.2.6* below lists estimates of the uncertainty for each radiative Flux Analysis variable where possible, and the source of information for the estimate.

#### A.2.2.4.4: Monthly diurnal and monthly average files

There has been considerable discussion with reference to producing monthly averages and what to do about missing data as part of the surface RFA effort. Somehow trying to manufacture numbers to "fill in" for missing data has always made me nervous. For this data set, I have chosen not to attempt any "filling in", but only to use the data available, with a minimum limit in order to produce an average.

*Table A.2.2.6: Estimated uncertainties of variables included in the Radiative Flux Analysis*

Variable	Est. 95% Uncertainty	Information Source
Downwelling Total SW	6% or 10 Wm <sup>-2</sup>	Stoffel, 2005, ARM-TR
Downwelling Diffuse SW	3% or 4 Wm <sup>-2</sup>	Stoffel, 2005, ARM-TR
Downwelling Direct SW	6% or 20 Wm <sup>-2</sup>	Stoffel, 2005, ARM-TR
Clear-sky Total, Diffuse, Direct SW	RMSE(2X Meas. Uncert.)	Long and Ackerman, 2000
Upwelling SW	6% or 10 Wm <sup>-2</sup>	Stoffel, 2005, ARM-TR
Clear-sky Upwelling SW	RMSE(2X Meas. Uncert.)	Long, 2005
Downwelling LW	2.5% or 4 Wm <sup>-2</sup>	Stoffel, 2005, ARM-TR
Clear-sky Downwelling LW	4-5 Wm <sup>-2</sup>	Long and Turner, 2008
Upwelling LW	2.5% or 4 Wm <sup>-2</sup>	Stoffel, 2005, ARM-TR
Clear-sky Upwelling LW	Unknown	
Daylight Fractional Sky Cover	10%	Long et al., 2006
LW Effective Sky Cover	1-2 Oktas	Durr and Philipona, 2004
Cloud Visible Optical Depth	10%	Barnard & Long, 2004; Barnard et al., 2008
Effective Cloud Transmissivity	10%	Estimated from above Total and Clear-sky SW
Cloud Radiating Temperature	Unknown	
Cloud Radiating Height	Unknown	

For the monthly diurnal cycle files, all available data were collected into 15-minute bins, and then if there is at least half of the possible data available, an arithmetic average is taken of the values in the 15-minute bin. Once a month's diurnal cycle is produced, then again if there is at least half the possible data, then a monthly average for that value is produced. This is about the simplest way of averaging without "filling in", while at the same time mitigating the problem of WHEN (i.e. what solar elevation angles) especially solar variables are missing that is inherent in using just a straight arithmetic average of all available data to produce a monthly average.

The choice of "if half the data are available" is arbitrary. In all cases for the monthly diurnal and average files, the actual number of data used in a given average is provided so that those who want a tighter restriction can screen for it. In the case of the monthly diurnal files, a corresponding file is provided that lists the number of data used. For example, the monthly diurnal file for Barrow, Alaska (bar\_diurmnth.asc) includes all the average values themselves, while the corresponding "number of data" file (bar\_diurmnth.ndt) includes the data counts. For the monthly average files, both the average values, and the number of data counts are all in the same file. Thus again, those who want to screen more tightly for whether to use a particular average value can do so with the information provided.

All files (monthly diurnal and monthly average, 2004 and 2005 15-minute) are provided in ASCII format, with each row of data time stamped at the beginning of the row followed by the variables. Variables are in columns, with a "header row" describing the variable in that column. Descriptions of the header abbreviations are given below. The years 2004 and 2005 15-minute files are provided in daily files, i.e. one day of data per file, with each site's files tar bundled.

### A.2.2.4.5: Output file header description

YYYYMM	year and month of year (used in monthly average and diurnal files)
hhmm	hour and minute (used in monthly diurnal files, based on LST)
Zdate	date in YYYYMMDD format, based on GMT
Ztim	time in hhmm format, based on GMT
Ldate	date in YYYYMMDD format, based on LST
Ltim	time in hhmm format, based on LST
CosZ	Cosine of the solar zenith angle
AU	earth-sun distance in AUs
SWdn	best estimate downwelling SW from sum or global pyranometer ( $Wm^{-2}$ )
CSWdn	estimated clear-sky downwelling SW ( $Wm^{-2}$ )
LWdn	downwelling LW from pyrgeometer ( $Wm^{-2}$ )
CLWdn	estimated clear-sky downwelling LW ( $Wm^{-2}$ )
SWup	upwelling SW from pyranometer ( $Wm^{-2}$ )
CSWup	estimated clear-sky upwelling SW ( $Wm^{-2}$ )
LWup	upwelling LW from pyrgeometer ( $Wm^{-2}$ )
CLWup	estimated clear-sky upwelling LW ( $Wm^{-2}$ )
DifSW	measured downwelling diffuse SW ( $Wm^{-2}$ )
CDifSW	estimated clear-sky downwelling diffuse SW ( $Wm^{-2}$ )
DirSW	measured downwelling direct SW ( $Wm^{-2}$ )
CDirSW	estimated clear-sky downwelling direct SW ( $Wm^{-2}$ )
LWScv	estimated LW effective fractional sky cover
SWScv	estimated SW (total) fractional sky cover
CldTau	estimated effective visible cloud optical depth
CldTrn	estimated effective SW cloud transmissivity (SWdn/CSWdn ratio)
CldTmp	estimated effective cloud radiating temperature (K)
CldHgt	estimated effective cloud height (km)
Tair	air temperature (K)
VPrs	vapor pressure (mb)
RH	Relative Humidity (%)
RHfac	RH-based adjustment to $E_c$ to account for haze formation
$E_c$	effective clear-sky LW emissivity using $T_a$
Wspd	Wind speed (m/s)
Wdir	Wind Direction (degrees from North) WARNING: these are arithmetic averages,
Aprs	Air pressure, usually in mb, but sometimes in hPa
LWlw	(2004 15-minute files) Contribution to CLWup from CLWdn variable ( $Wm^{-2}$ )
SWlw	(2004 15-minute files) Contribution to CLWup from SWnet variable ( $Wm^{-2}$ )
RHlw	(2004 15-minute files) Contribution to CLWup from RH variable ( $Wm^{-2}$ )
Wslw	(2004 15-minute files) Contribution to CLWup from Wspd variable ( $Wm^{-2}$ )
NSWClr	(monthly average and diurnal files) number of SW (i.e. totally) clear-sky data detected
NAIIClr	(monthly average and diurnal files) number of SW plus LW (i.e. "LW Effective") clear-sky data detected
ClrF	(2004 15-minute files) number of SW plus LW clear-sky detected
PossN	(2004 15-minute files) number of time stamped lines in input file, so possible number in each individual average
NPoss	(monthly average and diurnal files) possible number of data
Minnum	(monthly average and diurnal files) minimum number required to produce an average

In all the files provided for the RFA, variable names are mostly standardized. The following is a listing of the common column header abbreviations, and a description of the variable so labeled: In the monthly average files, the count of number of data used in a particular average is labeled with an "N" in front of the variable header abbreviation. For example, for SWdn, the number of data is labeled "NSWdn".

For the monthly diurnal files, a separate file with the same stem, but extension ".ndt" gives the number of data counts with the same header abbreviation as for the variable itself in the monthly diurnal data file. For example, the column abbreviation "SWdn" is in both the monthly diurnal ".asc" and ".ndt" files. There may be other columns of data if the provider used the option to include up to 20 extra variables. Hopefully the column header abbreviations in this case are self-explanatory as to what the variables are...if not, contact me for more info (chuck.long@pnl.gov).

#### References for A2.2.4.5:

- Barnard, J. C., and C. N. Long, (2004): A Simple Empirical Equation to Calculate Cloud Optical Thickness Using Shortwave Broadband Measurement, *JAM*, 43, 1057-1066.
- Barnard, J. C., C. N. Long, E. I. Kassianov, S. A. McFarlane, J. M. Comstock, M. Freer, and G. M. McFarquhar (2008): Development and Evaluation of a Simple Algorithm to Find Cloud Optical Depth with Emphasis on Thin Ice Clouds, *OASJ*, 2, 46-55, doi: 10.2174/1874282300802010046.
- Brutsaert, W., (1975): On a Derivable Formula for Longwave Radiation from Clear Skies, *Water Resour. Res.*, 11(3), 742– 744.
- Dupont J.C., M. Haeffelin, and C.N. Long (2008): Evaluation of cloudless-sky periods detected by shortwave and longwave algorithms using lidar measurements, *GRL* 35(10), doi:10.1029/2008GL033658.
- Dürr B. and R. Philipona, (2004): Automatic cloud amount detection by surface longwave downward radiation measurements, *JGR*, 109, D05201, doi:10.1029/2003JD004182.
- Long, C. N. and T. P. Ackerman, (2000): Identification of Clear Skies from Broadband Pyranometer Measurements and Calculation of Downwelling Shortwave Cloud Effects, *JGR*, 105, No. D12, 15609-15626.
- Long, C. N. and K. L. Gaustad, (2004): The Shortwave (SW) Clear-Sky Detection and Fitting Algorithm: Algorithm Operational Details and Explanations, Atmospheric Radiation Measurement Program Technical Report, ARM TR-004, Available via <http://www.arm.gov>.
- Long, C. N., (2004): The Next Generation Flux Analysis: Adding Clear-sky LW and LW Cloud Effects, Cloud Optical Depths, and Improved Sky Cover Estimates, 14th ARM Science Team Meeting Proceedings, Albuquerque, New Mexico, March 22-26, 2004.
- Long, C. N., (2005): On the Estimation of Clear-Sky Upwelling SW and LW, 15th ARM Science Team Meeting Proceedings, Daytona Beach, Florida, March 14-18, 2005.
- Long, C. N., T. P. Ackerman, K. L. Gaustad, and J. N. S. Cole, (2006): Estimation of fractional sky cover from broadband shortwave radiometer measurements, *JGR*, 111, D11204, doi:10.1029/2005JD006475.
- Long, C. N., and Y. Shi, (2008): An Automated Quality Assessment and Control Algorithm for Surface Radiation Measurements, *OASJ*, 2, 23-37, doi: 10.2174/1874282300802010023.
- Long, C. N., and D. D. Turner, (2008): A Method for Continuous Estimation of Clear-Sky Downwelling Longwave Radiative Flux Developed Using ARM Surface Measurements, *JGR*, 113, D18206, doi:10.1029/2008JD009936.
- Min, Q., Harrison, L. C., (1996): Cloud Properties Derived from Surface MFRSR Measurements and Comparison with GOES Results at the ARM SGP Site, *Geophysical Research Letters*, Vol. 23, pp. 1641-1644.
- Turner, D.D., A.M. Vogelmann, R.T. Austin, J.C. Barnard, K. Cady-Pereira, J.C. Chiu, S.A. Clough, C. Flynn, M. M. Khaiyer, J. Liljegren, K. Johnson, B. Lin, C. Long, A. Marshak, S. Y. Matrosov, S.A. McFarlane, M. Miller, Q. Min, P. Minnis, W. O'Hirok, Z. Wang, and W. Wiscombe, (2006): Thin Liquid Water Clouds: Their Importance and Our Challenge, *BAMS*, 88, No.2, 177-190, DOI:10.1175/BAMS-88-2-177.

## A2.2.5: Alpine Surface Radiation Budget (ASRB) Regional Network

### A.2.2.5.1: Description

The Alpine Surface Radiation Budget (ASRB) project was initiated in 1994 to investigate the altitude dependence of the surface radiation budget over the Alps with a particular focus on accurate measurements of the longwave downward radiation (Marty et al., 2002). Broadband short- and longwave radiation fluxes are continuously measured within this network at ten stations between 370 and 3580 m a.s.l. in the Swiss Alps. New calibration techniques, modified pyrgeometers, and an adequate ventilation and heating system decreased the uncertainty for longwave radiation measurements even under harsh alpine weather conditions to about  $\pm 3 \text{ Wm}^{-2}$ . This corresponds to about 1% uncertainty on daily means. On the shortwave radiation measurements the uncertainty on daily means is about 2%.

In recent years the ASRB network has become increasingly important to detect decadal changes of the radiation fluxes in relation with increasing anthropogenic greenhouse gases (Philipona et al., 2004) and the subsequent enhancement through the water vapor feedback (Philipona et al., 2005).

Data are supplied for the GEWEX-RFA by MeteoSwiss for six sites listed below in *Table A2.2.7*. Four of the sites are high altitude locations. The station Payerne makes the connection between the alpine measurements to the Swiss “Mittelland” plateau and to the extended international BSRN radiation measurements. The station Locarno-Monti represents together with Cimetta the southern part of the Alps. All ASRB stations are located at MeteoSwiss automatic network sites (ANETZ) or at complementary network sites (ENET), where surface air temperature, humidity, and atmospheric pressure and wind are measured.

*Table A.2.2.7: ASRB site information*

Site Location,	3 Letter Name,	Altitude,	Lat/Long
Cimetta,	CIM,	1670 m,	8.48° / 46.12°
Davos,	DAV,	1610 m	9.51° / 46.49°
Jungfrau-joch	JFJ	3580 m	7.59° / 46.33°
Locarno-Monti	LOM	370 m	8.47° / 46.10°
Payerne	PYR	490 m	6.57° / 46.49°
Weissfluhjoch	WFJ	2690 m	9.49° / 46.50°

Original data have temporal resolution of 2 minutes (120-second averages of 1-Hz observations). The data are quality checked and flagged. The 2-minute averages were subsequently replicated to 1-minute resolution for the purpose of calculating 15-minute averages. Consequently a minimum of eight values was required for a 15-minute average to be included in these time series. There was no filling of data gaps. Three variables are available for the year 2004 and are listed below. Original data can be obtained from [Rolf.Philipona@meteoswiss.ch](mailto:Rolf.Philipona@meteoswiss.ch).

### References for A2.2.5

- Marty, C., R. Philipona, C. Fröhlich, and A. Ohmura, 2002: Altitude dependence of surface radiation fluxes and cloud forcing in the Alps: results from the alpine surface radiation budget network, *Theor. Appl. Climatol.*, 72, 137-155.
- Philipona, R., B. Dürr, C. Marty, A. Ohmura, and M. Wild, 2004: Radiative forcing - measured at Earth's surface - corroborates the increasing greenhouse effect, *Geophys. Res. Lett.*, 31, L03202, doi:10.1029/2003GL018765.

Philipona, R., B. Dürr, A. Ohmura, and C. Ruckstuhl, 2005: Anthropogenic greenhouse forcing and strong water vapor feedback increase temperature in Europe, *Geophys. Res. Lett.*, 32, L19809, doi:10.1029/2005GL023624.

#### A.2.2.6: University of Oregon Solar Monitoring Regional Network

Solar radiation data from three sites in the University of Oregon Solar Radiation Monitoring Laboratory Network (UO SRML) with long term data were contributed the GEWEX database. The sites were Burns, Eugene, and Hermiston, Oregon as described in *Table A2.2.8*. The solar monitoring equipment and other sensors at the sites along with site latitude, longitude, and altitude are listed in the *Table A2.2.9*.

*Table A.2.2.8: University of Oregon Solar Monitoring Network Sites*

Site in Oregon USA	Lat	Long	Elev. (m ASL)
Eugene	44.05N	123.07W	150
Burns (prior to April 1982)	43.58N	119.05W	1295
Burns (after April 1982)	43.52N	119.02W	1265
Hermiston	45.82N	119.28W	180

At the Eugene station, the original data were collected on strip charts and digitized. This equipment was replaced by a data logger that recorded data on a punched paper tape. In 1979, data loggers that digitized were developed and installed at all three stations. These data loggers were based on an SKD 8085 computer board and had “pod” with capacitors that were charged by the incoming signals. When a preset charge was reached, the capacitor discharge and sent a pulse to the data logger. These pulses were counted and every five minutes the totals were stored. Every hour, the 5 minute data were placed on a cassette tape. The instantaneous signals were also sent to charts for backup records and hourly records were also printed out on a printer. The accuracy of these shop built data loggers is about 0.1%.

The chart records were traced out on a bit pad when the cassette records and the printer tape records were not available. Data collection started in 1979 in Burns and Hermiston. The first several months of hourly records at the Hermiston site consist of digitized chart records. The accuracy of digitized data is about 2% at full scale on clear days and about 5% on the toughest days to digitize with intermittent sun. In 1995, the data loggers developed at the UO were replaced by the Campbell Scientific CR10 data loggers. (The Campbell data loggers were installed on June 27, 1995, for Burns, August 31, 1995, for Eugene, and June 29, 1995, for Hermiston). In Eugene, some data as early as April 1995 was obtained using a Campbell data logger. Instruments were calibrated at Eppley Labs, NOAA, NREL, and in the field. The National Renewable Energy Laboratory (NREL) has calibrated some of the station instruments and the reference instruments over the years. The station instruments were calibrated in the field using side by side comparisons.

Originally, the calibrations with the pyranometers were done at solar noon. Later calibration values were determined when the solar zenith angle was 45° to be consistent with the NREL calibration values. All the data given to GEWEX was adjusted to the 45° zenith angle calibration. Clear day noon-time values were used to confirm the calibrations. Calibrations were determined by examining the long-term trends over several years.

*Table A.2.2.9: Data collected at the University of Oregon Solar Monitoring sites.***Site: Eugene**

<b>Data type</b>	<b>Instrument</b>	<b>Data interval</b>	<b>Period of record</b>
<b>Solar radiation data:</b>			
Global	Eppley PSP	hourly	1975-1995
		5 min.	1995-present
	Ascension Technology RSP	5 min.	2000-present
Direct normal	Eppley NIP	hourly	1977-1995
		5 min.	1995-present
	Ascension Technology RSP	5 min.	2000-present
Diffuse	[Calculated]	hourly	1977-1995
		5 min.	1995-present
	Eppley PSP with shade disk	5 min.	1997-present
	Ascension Technology RSP	5 min.	2000-present
	Schenk Star pyranometer with shade disk	5 min.	2000-present
Tilted south 30°	Schenk Star pyranometer	hourly	1982-1985
	Eppley PSP	hourly	1985-1995
		5 min.	1995-present
Tilted south 45°	Eppley PSP	hourly	1983-1995
		5 min.	1995-present
Tilted south 60°	Eppley PSP	hourly	1977-1995
		5 min.	1995-1998
Tilted south 90°	Schenk Star pyranometer	hourly	1981-1984
	Eppley PSP	hourly	1984-1995
		5 min.	1995-present
Tilted north 90°	Eppley PSP	hourly	1988-1995
		5 min.	1995-present
Ground reflected	Eppley PSP	5 min.	1998-present
<b>Spectral data</b>			
UV spectrum	Eppley TUVR	hourly	1994-1995
		5 min.	1995-present
Multifilterer radiometer	YES MFR-7	2.5 min.	1997-1998
		1 min.	1998-present
Beam RG695	Eppley NIP	hourly	1988-1995
		5 min.	1995-present
Beam RG630	Eppley NIP	hourly	1989-1995
		5 min.	1995-1999
Beam OG570	Eppley NIP	hourly	1989-1995
		5 min.	1995-1999
<b>Meteorological data:</b>			
Temperature		hourly	1977-1995
		5 min.	1995-present
Wind speed	R.M. Young	hourly	1984-1995
		5 min.	1995-present
Relative humidity	Campbell Scientific	hourly	1982-1995
		5 min.	1995-present

This determination was augmented by using a formula for the degradation of paint as suggested by Steve Wilcox of NREL. An extensive set of calibration notes is available upon request. The data in the UO SRML database subtracts the nighttime values from the daytime readings. This accounts for roughly half of the IR radiative losses experienced by the Eppley PSP

pyranometers. The calibration values for the Eppley PSP were determined using this method to obtain the daytime values. This makes the calibration and method of data collection more consistent.

#### Site: Hermiston

Data type	Instrument	Data interval	Period of record
<b>Solar radiation data:</b>			
Global	Eppley PSP	hourly	1979-1994
		5 min.	1994-present
	Ascension Technology RSP	5 min.	1995-present
Direct normal	Eppley NIP	hourly	1979-1994
		5 min.	1994-present
	Ascension Technology RSP	5 min.	1995-present
Diffuse	[Calculated]	hourly	1979-1994
		5 min.	1994-present
	Ascension Technology RSP	5 min.	1995-present
<b>Meteorological data</b>			
Temperature		hourly	1980-1994
		5 min.	1994-present
Auxiliary station Hermiston – AgriMet			
Data type	Instrument	Data interval	Period of record
<b>Solar radiation data</b>			
Global	LI-COR pyranometer	15 min.	1994-present
Diffuse	LI-COR pyranometer with shadow band	15 min.	1995-present
<b>Meteorological data:</b>			
Temperature		15 min.	1994-present
Rainfall		15 min.	1994-present
Wind speed		15 min.	1994-present
Wind direction		15 min.	1994-present
Relative humidity		15 min.	1994-present

The uncertainty in the data from the digitized charts is around 5% with a  $\pm 10$  to  $20 \text{ W/m}^2$  uncertainty in the offset. The absolute uncertainty of the instrument calibrations is about  $\pm 2-3\%$ . The accuracy of the Campbell data logger is on the order of 0.1% and accuracy of the UO data logger is on the order of 0.1% [1, 2]. In 1979 and 1980, the UO data logger was undergoing tests and improvements and that data would have a higher uncertainty.

The monthly average values were processed in monthly hourly blocks. First the hourly values were determined and then all identical hours were averaged for the month. If hours were marked bad or missing, they were not used in the averaging. The monthly average hourly values were then summed and divided by 24 to produce the monthly average irradiance. The total number of hours used in the month is given in the database. No nighttime hours were listed missing subtracting out the nighttime average enabled setting all the nighttime values to zero.

#### References for A2.2.6

Brooks, B., D. Fong, D. Hermeyer, L. Laitinen, C. Sstrom, F. Vignola, and D. K. McDaniels  
 “Automatic Data Recording of Direct and Global Insolation in Oregon,” Proceedings of the SOLWEST Solar Energy Conference, University of British Columbia, August 6-10, 1980, p. 332.

Vignola, F. and D. K. McDaniels, Pacific Northwest Solar Radiation Data, published by the UO Solar Monitoring Laboratory, 1980-1998.

<http://solardata.uoregon.edu/PacNWSolarRadiationDataBook.html>

**Site: Burns**

Data type	Instrument	Data interval	Period of record
<b>Solar radiation data:</b>			
Global	Eppley PSP	hourly	1979-1994
		5 min.	1994- present
Direct normal	Eppley NIP	hourly	1979-1994
		5 min.	1994-present
Diffuse	[Calculated]	hourly	1979-1994
		5 min.	1994-present
<b>Meteorological data:</b>			
Temperature		hourly	1980-1994
		5 min.	1994-present

### A.3.1.2: CERES Scanner Surface Data; CERES-SRBAVG-GEO

David Doelling

**Dataset Description:**

The CERES-SRBAVG-GEO surface fluxes are derived using the CERES simple (parameterized) Surface Only Flux Algorithms (SOFA) as described in Kratz et al. 2010 and the CERES SOFA Data Quality Summary. The SOFA algorithm uses the NASA/GEWEX-SRB-QC algorithm, but uses different input sources. There are no surface fluxes derived from the CERES-SRBAVG-nonGEO or CERES only product, since there is not sufficient diurnal sampling with the sun-synchronous Terra orbit.

CERES also computes surface fluxes using the Surface and Atmosphere Radiation Budget (SARB) algorithm, which is based on Fu-Liou radiative transfer models. This data is available in the CERES CRS, SYN, or AVG products. (See the CERES CRS and SYN/AVG/ZAVG Data Quality Summaries listed in the references.) Surface fluxes, both tuned to the CERES TOA flux observations and untuned, are computed under clear-sky, pristine (clear-sky no aerosol), all-sky, and all-sky-no-aerosol conditions. CERES data can be accessed here <http://ceres.larc.nasa.gov> under order data

**Input data sets and monthly regional temporal interpolation:**

The gridded surface fluxes are calculated for each hourly time step. These hourly increments are then averaged into daily and monthly means. The surface fluxes do not need to be temporally interpolated, since all the input variables have been temporally interpolated into hourly increments, after which the fluxes are derived.

The TOA fluxes are from the CERES-SRBAVG-GEO dataset described in this document under *section A.1.4*. The TOA fluxes are from the Terra (10:30 AM local equator crossing time) CERES TOA observed fluxes within a 70° view zenith angle swath along the groundtrack.

Three-hourly geostationary (GEO) derived broadband fluxes, which have been carefully normalized to the CERES observations to remove the Terra sampling bias, are used to compute the daily mean. GEO data is only used between  $\pm 60^\circ$  in latitude. The Terra sun-synchronous orbit crosses the pole  $\sim 14$  times per day, allowing for sufficient diurnal sampling poleward of  $\pm 60^\circ$ . The GEO/CERES coincident flux normalization method preserves the CERES instrument calibration. The CERES and GEO instantaneous fluxes are first gridded into  $1^\circ$  latitude by  $1^\circ$  longitude regions that are increasingly nested poleward. CERES daily and monthly gridded fluxes are averaged from hourly flux increments. The CERES and GEO flux observations are first placed in these hourly increments. The CERES flux has precedence over the GEO. TOA observed SW fluxes are then temporally interpolated to fill in the missing hourly increments using CERES-TRMM directional models (SZA vs albedo) based on the angular directional model data set used to convert CERES radiances into fluxes (Loeb et al 2005). The LW TOA fluxes are linearly interpolated in time.

The cloud properties are from a combination of Terra MODIS (multi-channel) and 3-hourly geostationary (2-channel similar to ISCCP) retrievals. Neither geostationary or MODIS cloud properties are from the official products but retrieved based on Minnis et al. 2003. The instantaneous retrievals are then stratified into four layers bounded by TOA, 300mb, 500mb, 700mb, and surface pressure levels. Gridded cloud properties are temporally interpolated to hourly increments over the month for each layer. Coincident MODIS cloud properties take precedent over GEO clouds. Optical depth is temporally interpolated in terms of logarithm. All other cloud properties are linearly interpolated in time. No cloud overlap is assumed.

The atmosphere is from GEOS-4 from Goddard Earth Observing System Data Assimilation System (Bloom et al. 2005). 6-hourly atmospheric profiles are temporally interpolated to hourly increments linearly. 3-hourly skin temperatures are also interpolated to hourly increments. Ozone is from SMOBA (Stratospheric Monitoring-group Ozone Blended Analysis) from NOAA/CPC. The aerosol inputs are identical to the GEWEX-SRB-QC datasets. All GEOS-4 properties are interpolated linearly in time into hourly increments

### **Regional temporal gap filling within the month:**

For periods with extensive satellite data drop out, for example during a two week period in June 2001 for CERES and MODIS, only days with observations are used to derive the monthly mean. For the SW TOA, the daily albedos are averaged to compute the monthly mean albedo and multiplied by the monthly mean solar incoming flux.

### **Regional/zonal/global averaging technique and spatial gap filling:**

There are two cases where the monthly regional surface flux is missing. The first case is for clear-sky SW and LW surface fluxes over very cloudy regions. CERES defines clear-sky if the CERES footprint (20km nominal) is greater than 99% clear, or if most of the MODIS pixels inside the footprint have been identified as clear. This is different than the definition used by modelers, where clear-sky fluxes are computed with no cloud input, although the atmosphere can be from completely overcast conditions. The 20-km cloud free definition, determines that only clear-sky profiles are used to compute surface fluxes. Given this restriction, there are clear-sky cases near clouds, which are not observed by CERES. This could bias certain nearly overcast regions to observe fluxes from less humid clear-sky conditions. A monthly regional clear-sky flux is available as long as there is at least one CERES footprint over the month. If there are no clear-sky footprints identified during the month, the monthly clear-sky fluxes are set to default.

It is extremely rare that all-sky monthly mean surface fluxes are missing, except near terminator regions. All-sky SW and net TOA and therefore surface fluxes are not parameterized for regions with solar zenith angles greater than  $85^\circ$  near the polar terminator. In this case there are usually four  $1^\circ$  zones that are missing. No attempt is made to fill in missing regional surface fluxes. Regional surface fluxes inside a  $1^\circ$  zone are averaged. Missing zonal monthly means are linearly interpolated from valid zones in the LW. In the SW the zonal albedo is interpolated linearly from valid zonal albedoes. All 180 zonal surface fluxes are averaged to derive the global monthly mean fluxes. A bug in the zonal averaging technique was discovered after the GEWEX Flux Assessment time period and affects surface shortwave products used in the Assessment and found in the Flux Assessment archive.

### **Input Data Sets:**

Every effort was made to have consistent input versions for the 5-years during March 2000 TO October 2005 to derive the CERES-SRABVG-GEO surface fluxes. All input parameters are resolved at a spatial nested  $1^\circ$  by  $1^\circ$  lat/lon grid and temporally at hourly increments to calculate the surface fluxes. Radiative transfer modeled (computed) surface fluxes are only as good as the input parameters. The CERES-SRBAVG-GEO surface fluxes are parameterized and may not resolve the extreme events as well as the computed fluxes.

### **Atmospheric Profile:**

- Pressure/Temperature/humidity: GEOS-4 (Goddard Earth Observing System Data Assimilation System) GFDL (MOA product) (Bloom et al. 2005) 6-hourly profiles at 15 pressure levels.
- Ozone: SMOBA (Stratospheric Monitoring-group Ozone Blended Analysis) from NOAA/CPC.

### **Skin Temperature:**

- GEOS-4 (Goddard Earth Observing System Data Assimilation System) (Bloom et al. 2005) 3-hourly skin temperatures.

### **Surface Albedo:**

- 5-year climatology derived from clear-sky CERES broadband TOA fluxes.

### **Clouds:**

- MODIS multi-channel 2-km CERES algorithm cloud retrievals at Terra overpass times (10:30AM local equator crossing time). MODIS clouds are priority over geostationary. Not the official GSFC-MODIS cloud product.
- 5-satellite 3-hourly geostationary 2-channel (VIS and IR) 4-km CERES algorithm cloud retrievals encompassing  $60^\circ\text{N}$  and  $60^\circ\text{S}$ . Not the official GISS ISCCP product.

### **TOA fluxes:**

- $1365 \text{ Wm}^{-2}$  solar constant.
- CERES observed TOA 20km footprint fluxes at CERES Terra overpass times (10:30AM local equator crossing time).
- 5-satellite 3-hourly geostationary narrowband to broadband derived radiances converted to fluxes using the CERES angular directional models based on scene type. The

geostationary broadband fluxes are then carefully normalized to the CERES calibration to preserve the CERES calibration.

- SW TOA fluxes are temporally interpolated using CERES (TRMM based) directional models based on scene type to define albedo as a function of solar zenith angle.
- Described in section A.1.4.

**Aerosols:**

- MATCH based 3-year climatology optical depth and specie concentrations.
- OPAC based asymmetry factor and single scattering albedo as a function of specie.

**Snow/Ice:**

- NESDIC NSICD (National Snow and Ice Data Center) daily snow maps.

**Error analysis against ground site surface monthly mean fluxes**

Ground site radiometers provide the only independent broadband fluxes to compare the accuracy of computed surface fluxes. 23 global surface sites were selected to provide seasonal monthly error analysis during the CERES observation time period between April 2000 and ending with October 2005. These sites had the greatest data availability, radiometric accuracy and greatest proximity from other nearby sites. These sites are mostly over land and do not represent the majority of the earth's ocean. *Table 3.1.2.1* shows the results for the GEWEX-SRB-QC (parameterized using ISCCP clouds), CERES-SRBAVG-GEO (parameterized using MODIS/GEO clouds, this study) and CERES-AVG (radiative transfer, same input as CERES-SRBAVG-GEO) based on the Terra derived CERES products. The CERES untuned radiative fluxes are computed with the Fu-Liou radiative transfer and is more robust than the SRBAVG-GEO parameterized surface fluxes. The CERES tuned radiative transfer fluxes provide consistent TOA fluxes, cloud properties and atmosphere. The clouds and atmosphere properties are minimally adjusted to best match the CERES TOA fluxes but are not forced to match them.

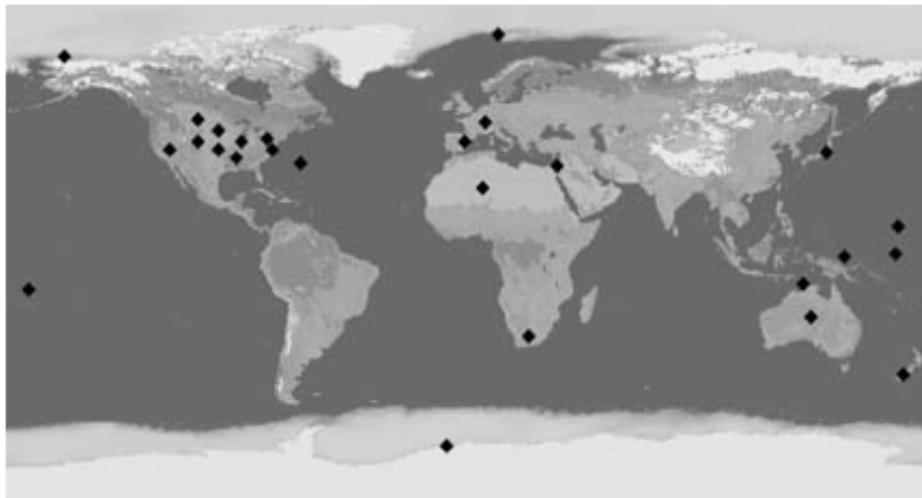


**Figure 3.1.2.1:** Location of the 23 sites used in the error analysis in Table 1.

The surface LW fluxes are generally consistent between products and are most dependent to the near surface lapse rate, PW, cloud base height, and skin temperature and independent from the TOA flux. All products rely on the same GEOS-4 atmosphere. Cloud base is different for SRB-QC than the other products, but since it is difficult parameter to retrieve cloud base source did not have much of an impact.

**Table 3.1.2.1:** Comparison of the GEWEX-SRB-QC, CERES-SRBAVG-GEO and CERES-AVG based on the Terra products for the seasonal monthly surface fluxes during April 2000 to October 2005 against 23 ground site surface fluxes. See above text for more information

Parameter Surface Mean ( $Wm^{-2}$ )	SWdown 188		SWup 42		LWdown 344		LWup 380	
	Bias	Sigma	Bias	Sigma	Bias	Sigma	Bias	Sigma
SRB-QC	-2.9	22.4	-18.4	29.9	-0.9	11.2	-2.7	13.9
SRBAVG-GEO	0.5	24.0	-15.7	32.4	-0.5	10.3	-7.6	15.4
AVG-untuned	4.4	12.3	-13.1	21.8	-5.2	10.4	-5.6	16.
AVG-tuned	4.6	12.4	-13.1	21.6	-5.2	10.3	-5.0	15.9

The surface SW fluxes are similar for the SRB-QC and SRBAVG-GEO products and use the same surface parameterizations. For SW surface fluxes the TOA SW flux, cloud amount and optical depth are important. The real improvement is shown using radiative transfer to derive surface fluxes, using the same inputs. Also the minimal adjustment of clouds and atmosphere during tuning did not impact the surface fluxes. Further information on other comparisons and error analysis performed on CERES derived surface fluxes can be obtained in the CERES SYN/AVG/ZAVG Data Quality Summary listed in the references.

#### Uncertainty estimate

- 23 BSRN/ARM/SURFRAD globally distributed sites were used to validate the CERES-SRBAVG-GEO product. These stations had continuous coverage during the 5-year product time frame and all sites followed the BSRN guidelines for climate quality surface fluxes

- Comparisons using surface sites reveal that during April 2000 and October 2005 the SRBAVG-GEO monthly averaged surface fluxes are as good as the SRB-QC or NASA/GEWEX-SRB fluxes. However if using the same input dataset with computed radiative transfer (AVG-untuned) the results show significant improvement in the SWdown compared to the SRBAVG-GEO product surface fluxes.

#### References:

Bloom, S. J., A. da Silva, D. Dee, M. Bosilovich, J-D. Chern, S. Pawson, S. Schubert, M. Sienkiewicz, I. Stajner, M-L. Wu, 2005: Documentation and Validation of the Goddard Earth Observing System (GEOS) Data Assimilation System–Version 4. NASA/TM–2005-104606, Vol. 26.

CERES SYN/AVG/ZAVG Data Quality Summary [http://eosweb.larc.nasa.gov/PRODOCS/ceres/SYN-AVG-ZAVG/Quality\\_Summaries/CER\\_SYN-AVG-ZAVG\\_Edition2.html](http://eosweb.larc.nasa.gov/PRODOCS/ceres/SYN-AVG-ZAVG/Quality_Summaries/CER_SYN-AVG-ZAVG_Edition2.html)

CERES CRS Data Quality Summary

[http://eosweb.larc.nasa.gov/PRODOCS/ceres/CRS/Quality\\_Summaries/CER\\_CRS\\_Terra\\_Edition2G.html](http://eosweb.larc.nasa.gov/PRODOCS/ceres/CRS/Quality_Summaries/CER_CRS_Terra_Edition2G.html)

CERES SOFA Data Quality Summary

[http://eosweb.larc.nasa.gov/PRODOCS/ceres/SSF/Quality\\_Summaries/ssf\\_surface\\_flux\\_terra\\_ed2B.html](http://eosweb.larc.nasa.gov/PRODOCS/ceres/SSF/Quality_Summaries/ssf_surface_flux_terra_ed2B.html)

Kratz, D. P.; Stackhouse, P. W.; Wilber, A. C.; Zhang, T.; and Sothcott, V. , 2010, Validation of CERES Edition 2B Surface-Only Flux Algorithms, Journal of Applied Meteorological Climatology, Volume 49, Issue 1 (January 2010) pp. 164-180

Loeb, N.G., S. Kato, K. Loukachine, and N.M. Smith, 2005: Angular distribution models for top-of-atmosphere radiative flux estimation from the Clouds and the Earth's Radiant Energy System instrument on the Terra Satellite. Part I: Methodology, *J. Atmos. Ocean. Tech.*, **22**,

338-351

Minnis, P., D. F. Young, S. Sun-Mack, P. W. Heck, D. R. Doelling, and Q. Trepte, 2003: "CERES Cloud Property Retrievals from Imagers on *TRMM*, *Terra*, and *Aqua*" Proc. SPIE 10th International Symposium on Remote Sensing: Conference on Remote Sensing of Clouds and the Atmosphere VII, Barcelona, Spain, September 8-12, 37-48.

### **A.3.1.3: NASA/GEWEX Surface Radiation Budget (SRB) Algorithm**

P. W. Stackhouse

See section A.1.6

### **A.3.1.4 ISCCP-FD SRF Data Set**

Y. – C. Zhang and W. B. Rossow

See section A.1.7 above

### **A.3.1.6 University of Maryland Shortwave Radiation Budget**

Rachel Pinker

See section A.1.9 above.

### **A.3.1.8: ERA-40 Reanalysis Data Set**

Jean-Jacques Morcrette, ECMWF

See section A.1.10 above.

### **A.3.1.9: NCEP/-DOE AMIP-II Reanalysis (R-2)**

Shi-Keng Yang, Climate Prediction Center/NCEP

See section A.1.11 above.

### **A.3.1.10: AR4 GCM Data**

S. Kinne

See section A.1.12 above.

### A.3.1.5 FORTH

Ilias Vardavas, Nikos Hatzianastassiou, and Christos Matsoukas

The FORTH surface and top-of-atmosphere (TOA) shortwave (SW) and longwave (LW) radiative fluxes were generated with the FORTH (Foundation for Research and Technology-Hellas) broadband radiative transfer model using ISCCP-D2 and NCEP-NCAR Reanalysis data. An analytical description of the model and radiative fluxes is given in the book by Vardavas and Taylor (2007). The fluxes are available on a planetary basis and cover the 21-yr period from January 1984 to December 2004. The spatial resolution is at  $2.5^\circ \times 2.5^\circ$  in latitude and longitude and they are given on a monthly basis for each year. Apart from pixel (geographical cell)-level fluxes, they are also available as averages for  $10^\circ$ -zones and as hemispheric and global averages. Their quality is ensured by comparisons against measurements, at both surface and TOA, from reference databases such as ERBE (Earth Radiation Budget Experiment), BSRN (Baseline Surface Radiation Network) and GEBA (Global Energy Balance Archive). The model has been also successfully tested with respect to the Intercomparison of Radiation Codes in Climate Models (ICRCCM). The FORTH climatological radiative fluxes have been used in applications extending from local/regional to meso- and global scales (e.g. Pavlakis et al., 2008).

#### Model Description

##### *Model for shortwave radiation*

The SW RTM divides the SW radiation into two spectral bands, one for the ultraviolet-visible (UV-vis) wavelengths ( $\lambda < 0.85 \mu\text{m}$ ), accounting for about 60% of the total solar radiation, and a second band for the near infrared (near-IR) wavelengths ( $0.85 \mu\text{m} \leq \lambda \leq 5 \mu\text{m}$ ), accounting for about 40% of total solar radiation. The model achieves a compromise between accuracy of spectral model computations and speed of computation of parameterization schemes. The UV-vis and near-IR components are treated separately in terms of their radiation transfer, and the model accounts for absorption and multiple scattering. Ozone ( $\text{O}_3$ ), carbon dioxide ( $\text{CO}_2$ ), water vapour ( $\text{H}_2\text{O}$ ) and Rayleigh scattering layers are considered together with cloud and aerosol layers in the atmosphere, all above an isotropically reflecting Earth's surface (cf. Vardavas and Koutoulaki, 1995). The sky is divided into clear and cloudy fractions. The cloudy part is subdivided into components covered by low, mid-, and high-level clouds. The model also accounts for the direct effect of aerosols on SW radiation (Hatzianastassiou et al., 2004d). The monthly mean incoming total solar flux at TOA for each  $2.5^\circ \times 2.5^\circ$  latitude-longitude grid cell, is computed theoretically as explained in detail by Hatzianastassiou et al., 2004a) using a solar constant  $S_0 = 1367 \text{ W m}^{-2}$ , and has been compared successfully against satellite data from ERBE (Hatzianastassiou et al., 2004b). The net incoming solar radiation at TOA (planetary absorption),  $F_{net,top}^\downarrow$ , the outgoing SW radiation (ASWUP) at TOA,  $F_{top}^\uparrow$ , and the planetary albedo  $R_p$  and planetary absorptivity  $\alpha_p$ , are computed as in Vardavas and Koutoulaki (1995). The reflectivity, transmissivity, and absorptivity of each of the various atmospheric layers ( $\text{O}_3$ ,  $\text{CO}_2$ ,  $\text{H}_2\text{O}$ , and Rayleigh) are computed using simple expressions derived from laboratory measurements, whereas for each cloud or the aerosol layer, computations are performed using two-stream approximation for purely scattering clouds in the UV-vis and a modified two-stream approximation allowing for cloud absorption in the near-IR (Vardavas and Koutoulaki, 1995) and aerosol particle scattering

and absorption in the UV-vis and near-IR. The atmosphere is divided vertically (from the surface up to 50hPa) in layers of about 5hPa each, and surface topography is considered (cf. Hatzianastassiou et al., 2005). The surface reflectance is computed for every pixel by considering four general types of surface: land, ocean, snow, and ice. Given that land shows a strong spatial variability in terms of its type and associated reflectance values, the data used were derived from ERBE data for clear-sky while overcast albedoes were obtained modifying the corresponding clear-sky values for diffuse radiation conditions. Information for fractional coverage for each surface-type is obtained from ISCCP-D2 data, whereas suitable values of reflectivity for each surface-type are assigned based on recent literature, allowing for its spectral dependence in UV-vis and near-IR, which is shown to be very important, but also for different values for the direct and diffuse solar radiation. A correction was applied to land-surface albedo for high-altitude mountainous areas such as Tibet, the Rocky Mountains, or the Antarctic plateau, consisting in a reduction of the albedo, in order to take into account the decrease of surface reflectivity over mountainous non-forested areas, especially during winter, due to the sub-grid orography. Furthermore, we include the condition that if the Fresnel reflectivity is greater than the ice or snow reflectivity, which occurs at low solar elevations, then the reflectivities of both snow and ice are set equal to the Fresnel reflectivity. Finally, the SW fluxes (upward and downward) are computed at TOA, at the Earth's surface, and within the atmosphere.

#### *Model for longwave radiation*

The LW radiative fluxes at TOA, within the atmosphere, and at the surface are computed using the code described in Hatzianastassiou et al. (2001a) but modified to derive fluxes on a  $2.5^\circ \times 2.5^\circ$  grid (Pavlakakis et al., 2004). The model uses separate radiative transfer schemes for clear and cloudy sky, which is divided into three non-overlapping layers of low, mid, and high-level clouds. However, this fact, which is a known limitation of the ISCCP-D2 dataset, leads to an underestimation of low-level cloud amount, which is associated with an underestimation in the global average downward LW radiation at the surface of  $1.2\text{-}3.2 \text{ Wm}^{-2}$  (Pavlakakis et al., 2004). Simple expressions (Hatzianastassiou et al., 1999a) are used for the total absorption of infrared radiation by the active gases of methane ( $\text{CH}_4$ ),  $\text{H}_2\text{O}$ ,  $\text{CO}_2$ ,  $\text{O}_3$ , and nitrous oxide ( $\text{N}_2\text{O}$ ), using simple transmission coefficients that depend on the amount of the absorbing gases in each layer. Aerosols are currently included in the longwave model. The atmosphere is divided vertically in layers of about 5 hPa each to ensure that they are optically thin with respect to the Planck mean longwave opacity. The low and middle-level clouds are considered black bodies, while the emissivity of high clouds is lower than unity and is determined from the infrared cloud optical depth. Apart from the thermal emission of each atmospheric layer, the surface emissivity is also computed in a corresponding way to that of the surface reflectivity, by considering the same four surface type and using recent estimates of the emissivity values.

#### **Model Input Data**

Most of the climatological data used, especially those for cloud properties, were taken from the ISCCP-D2 data set, which is the latest released and improved ISCCP series of mean monthly cloud climatologies, for the time period 1984-1993. We also used long-term data from the NCEP/NCAR Reanalysis Project, and from other sources, such as the Global Aerosol Data Set (GADS) and from the TIROS Operational Vertical Sounder (TOVS).

The data taken from ISCCP-D2 were cloud amount  $A_c$ , cloud scattering optical depth  $\tau_c^s$ , cloud-top pressure and temperature, and surface temperature. The ISCCP data for cloud parameters were taken separately for 15 different cloud types, allowing for 3 cloud types in each of three (low, mid-, or high-level) cloud layers and for liquid water or ice phase clouds for the low and mid-level cloud types. The values for the 15 independent cloud types were then appropriately averaged to yield data for low, mid-, and high-level clouds used in our model. Also, data for the surface-type characterization (land/ocean, snow/ice) were obtained from ISCCP-D2. ISCCP provides  $\tau_c^s$  only for the visible wavelength of  $\lambda=0.6 \mu\text{m}$ , which is essentially scattering only, or for the infrared wavelength of  $11 \mu\text{m}$  (cf. Rossow et al., 1996). Since the model also requires cloud absorption optical depth  $\tau_c^a$ , which is relevant to the near-IR solar radiation, values of  $\tau_c^a$  were estimated from  $\tau_c^s$  based on ratios of  $\tau_c^a/\tau_c^s$  resulting from Mie computations (Hatzianastassiou and Vardavas, 1999b) using the ISCCP-D2 liquid water droplet spectrum or from existing parameterizations for the ISCCP-D2 ice crystals spectrum for ice clouds. The cloud-base temperature (or height), which is particularly relevant to LW radiative fluxes at the Earth's surface and is not provided by ISCCP, is estimated as in Hatzianastassiou et al. (1999) from the ISCCP-D2 cloud-top pressure and the cloud physical thickness values given by Peng et al. (1982). This approximate treatment of the cloud-base temperature is shown (cf. Pavlakis et al., 2004) to be sufficient if the required accuracy for the LW radiation at the surface is of the order of  $1\text{-}2 \text{ Wm}^{-2}$ .

Atmospheric profiles of humidity and temperature were derived from NCEP/NCAR Global Reanalysis Project data, given at 17 pressure levels in the atmosphere. Specific humidity and atmospheric temperature data were used to compute the total water vapour content ( $W_{\text{H}_2\text{O}}$ ). The surface pressure, related to topography, is taken from the TOVS-derived ISCCP-D2 data gridded on  $2.5^\circ \times 2.5^\circ$  pixels. Consideration of topography is used to correct for the NCEP/NCAR data, which are given globally at the standard pressure level of 1000 hPa (as surface conditions). The gridded mean monthly data of ozone-column abundance were taken from ISCCP-D2 data, which were derived from TOVS for the 10-year period. A fixed  $\text{CO}_2$  total column atmospheric amount was taken, equal to  $0.54 \text{ gcm}^{-2}$ , corresponding to 345 parts per million by volume (ppmv). Similarly, we set the amounts for  $\text{CH}_4$ , and  $\text{N}_2\text{O}$  equal to 9 and  $4.5 \cdot 10^{-4} \text{ gcm}^{-2}$ , corresponding to 1.7 and 0.3 ppmv, respectively, as in the work by Hatzianastassiou and Vardavas (2001b). A mean visible Rayleigh scattering optical depth of 0.187 was used, which was derived from the full spectral variation of the optical depth (Vardavas and Carver, 1984) weighted by the solar spectrum, and corrected for the actual extent of the Rayleigh scattering layer based on surface topography. A detailed treatment of cloud microphysics in terms of the cloud asymmetry parameter ( $g_c$ ) was adopted, allowing for the spectral dependence of  $g_c$  as well as dependence on liquid water or ice phase in clouds. Thus, we set  $g_c$  equal to 0.85 and 0.78 for liquid and ice clouds, respectively, in the UV-vis range of wavelengths, while the corresponding values used for the near-IR were 0.82 and 0.8. These values were derived from detailed spectral computations using the ISCCP liquid droplet and ice crystal spectra, and also the parameterizations of Slingo (1989) for liquid clouds and Ebert and Curry (1992) for ice clouds. Data for aerosol optical depth, single scattering albedo, and asymmetry parameter were taken from GADS (Koepke et al., 1997), which is a completely revised version of the aerosol climatology by d'Almeida et al. (1991) consisting of aerosol optical properties averaged over space and time. The GADS data were originally gridded on a  $5^\circ$  resolution then downscaled to  $2.5^\circ$  resolution. The original GADS aerosol properties are re-computed based on the prevailing relative humidity in each geographical cell, which enables them to vary by year and month. Comparisons of GADS aerosol properties

with corresponding MODIS data beyond 2000 show that their uncertainty is of the order of  $\pm 10\%$ . A series of sensitivity tests were performed to investigate how much uncertainty is introduced to the model all-sky surface downwelling SW and LW fluxes (ASWDN and ALWDN, respectively) by uncertainties in the input parameters. Each test calculation covers the entire globe for one month. The results are summarised in the following two tables

### Uncertainty Analysis and Sensitivity of Model Fluxes

*Table 3.1.5.1: Sensitivity results for surface downwelling shortwave fluxes.*

Changed Parameter	DSR difference( $\text{Wm}^{-2}$ )
Low- $A_c +10\%$	+0.1/-22.0
Middle- $A_c +10\%$	+0.4/-17.5
High- $A_c +10\%$	+0.8/-15.3
Low- $\tau_{\nu}^S +10\%$	0/-5.9
Middle- $\tau_{\nu}^S +10\%$	0/-5.2
High- $\tau_{\nu}^S +10\%$	0/-5.8
Low- $\tau_{\nu}^a +10\%$	0/-1.6
Middle- $\tau_{\nu}^a +10\%$	0/-1.5
High- $\tau_{\nu}^a +10\%$	0/-1.4
$g_c +5\%$	0/20.6
$W_{\text{H}_2\text{O}} +10\%$	+0.02/-6.6
$W_{\text{O}_3} +10\%$	+0.01/-3.4
$W_{\text{CO}_2} +10\%$	+0.01/-0.5
$R_e +10\%$	0.02/13.4
ISR +1%	0/4.6
AOT +10%	+0.01/-2.6
$\omega_{\text{aer}} +10\%$	0/11.8
$g_{\text{aer}} +10\%$	+4.8/-0.02

*Table 3.1.5.2: Sensitivity results for surface downwelling longwave fluxes.*

Changed Parameter	DLR difference( $\text{Wm}^{-2}$ )
Precipitable water $\pm 25\%$	+6.2/-8.3
Air temperature $\pm 2$ K	+9.0/-8.9
Surface temperature $\pm 2$ K	$\pm 2.0$
Total cloud cover $\pm 30\%$	+9.8/-11.0
Low cloud cover $\pm 30\%$	+5.9/-6.0
Middle cloud cover $\pm 30\%$	+4.1/-4.2
High cloud cover $\pm 30\%$	+0.8/-0.8
Cloud physical thickness $\pm 20\%$	+1.8/-1.7
Random cloud overlap scheme (Compared to no cloud overlap scheme)	+1.2
Maximum cloud overlap scheme (Compared to no cloud overlap scheme)	+3.2

## Validation of Model Fluxes

The model all-sky downwelling shortwave (ASWDN) and longwave (ALWDN) fluxes at the surface have been validated through comparison with extensive measurements from stations. Such high-quality surface-based data were taken from two sources, namely the Baseline Surface Radiation Network (BSRN, Ohmura et al., 1998) and the Global Energy Balance Archive (GEBA). The comparison of observed versus calculated monthly mean DSR fluxes within the  $2.5^\circ \times 2.5^\circ$  cell containing the BSRN station for 22 stations is shown in the scatterplot of *Figure 3.1.5.1*. The scatterplot shows a bias of  $-14 \text{ Wm}^{-2}$  and a relatively small scatter (RMS equal to  $30.6 \text{ Wm}^{-2}$ ). The biases do not exceed  $10 \text{ Wm}^{-2}$  in tropical and mid-latitude areas of both hemispheres, while the corresponding RMS values remain smaller than about  $20 \text{ Wm}^{-2}$ . There is some underestimation of ASWDN fluxes with respect to BSRN in stations situated in southern polar areas ( $67^\circ$ - $90^\circ$ S). This is also found in similar comparisons of model ASWDN with GEBA data (Hatzianastassiou et al., 2005). The largest biases, RMS, and least square line slope values are found along Antarctica's coast, while the situation is improved at the South Pole. The model underestimation of ASWDN in the Antarctic might be due to errors in model input data, like clouds, but could also arise from problems with the site measurements. Examination of the seasonal behaviour of our model performance against BSRN data shows that generally, zero bias is within the error bars, except for the polar regions during summer, and most of the year in the southern mid-latitude areas.

The model ALWDN values were also compared against BSRN fluxes. Data from 8 BSRN stations were used for this purpose. In the following figure, we show the corresponding scatter plot comparing model fluxes against station measurements. There is a  $7.9 \text{ Wm}^{-2}$  negative bias of the model fluxes when compared against BSRN fluxes. It must be emphasized here that although the number of BSRN stations used for the comparison is small, the geographical distribution of these stations represents a wide variety of climates. The slope of the line best fitted to the data is larger than 1, indicating that low fluxes are underestimated and high fluxes are somewhat overestimated. This underestimation of ALWDN in cold and dry climates seems to be caused by a clear-sky bias of our simple radiation scheme, found also with other simple radiation codes used in GCMs and reanalyses as reported in Wild et al. (2001).

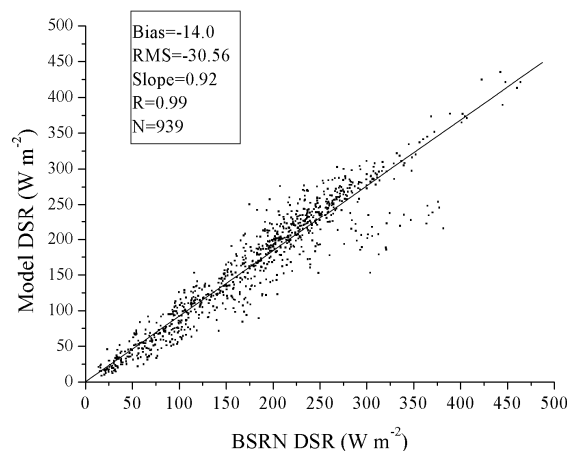


**Figure 3.1.5.1:** Scatter plot comparison between model-computed and BSRN pixel data of monthly average DSR, over the time period 1992-2000. *R* and *N* are the correlation coefficient and number of matched data pairs, respectively.

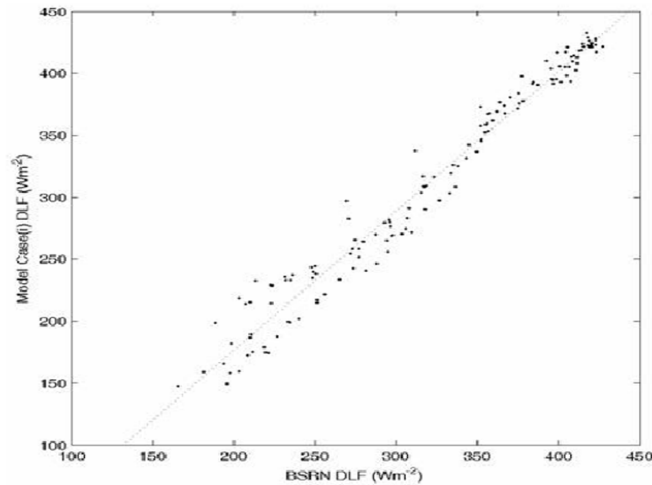


**Figure 3.1.5.2:** Scatter plot comparison between model-computed pixel data and BSRN measurements of monthly average ALWDN over the time period 1992-2000.

The scatter around the best-fit line is  $22.6 \text{ Wm}^{-2}$ . It must be noted that the model fluxes have been slightly adjusted, prior to the comparison against station fluxes, to account for any elevation difference between the station site and the much larger  $2.5^\circ \times 2.5^\circ$  grid box. We adopted a height gradient of  $2.8 \text{ Wm}^{-2}$  per 100 m (Wild et al., 1995) to allow for this effect. The mismatch between model and BSRN fluxes was related in most cases to low cloud cover and less frequently to temperature and specific humidity differences. Although the ISCCP low-level cloud amounts generally agree with the ones observed at the BSRN locations, sometimes they are substantially lower, particularly at mid and high latitudes in winter, i.e. at the low end of the DLR scatter plot. There is a clear correlation between the model underestimation of the ALWDN and the underestimation of low-level cloud cover by ISCCP-D2.

## References:

- Ebert, E. E. and Curry, J. A.: A parameterization of ice cloud optical properties for climate models, *J. Geophys. Res.*, 97, 3831-3836, 1992.
- Fotiadi, A., N. Hatzianastassiou, P. W. Stackhouse Jr., C. Matsoukas, E. Drakakis, K.G. Pavlakis, D. Hatzidimitriou, and I. Vardavas: Spatial and temporal distribution of long-term solar surface radiation budget over Greece, *Quart. J. R. Meteorol. Soc.*, 132, No 621, 2693-2718, 2006.
- Hatzianastassiou, N., Croke, B., Kortsalioudakis, N., Vardavas, I., and Koutoulaki, K.: A model for the longwave radiation budget of the NH: Comparison with Earth Radiation Budget Experiment data, *J. Geophys. Res.*, 104, 9489–9500, 1999a.
- Hatzianastassiou, N. and Vardavas, I.: Shortwave radiation budget of the Northern Hemisphere using International Satellite Cloud Climatology Project and NCEP/NCAR climatological data, *J. Geophys. Res.*, 104, 24 401-24 421, 1999b.
- Hatzianastassiou, N. and Vardavas, I.: Longwave radiation budget of the Southern Hemisphere using ISCCP C2 climatological data, *J. Geophys. Res.*, 106, 17 785–17 798, 2001a.
- Hatzianastassiou, N. and I. Vardavas: Shortwave radiation budget of the Southern Hemisphere using ISCCP C2 and NCEP/NCAR climatological data, *J. Climate*, 14, 4319-4329, 2001b.

- Hatzianastassiou, N., Fotiadi, A., Matsoukas, C., Drakakis, E., Pavlakis, K. G., Hatzidimitriou and Vardavas, I.: Long-term global distribution of Earth's shortwave radiation budget at the top of atmosphere, *Atmos. Chem. Phys.*, 4, 1217-1235, 2004b.
- Hatzianastassiou, N., B. Katsoulis, and I. Vardavas: Global distributions of aerosol direct radiative forcings in the ultraviolet and visible arising under clear skies. Model, input Data and model results, *Tellus*, 56B, 51-71, 2004d.
- Hatzidimitriou, D., I. Vardavas, K.G. Pavlakis, N. Hatzianastassiou, C. Matsoukas, and E. Drakakis: On the decadal increase in the tropical mean outgoing longwave radiation for the period 1984-2000, *Atmos. Chem. Phys.*, 4, 1419-1425, 2004.
- Koepke, P., Hess, M., Schult, I. and Shettle, E. P.: Global aerosol data set. Rep. No 243, Max-Planck Institut für Meteorologie, 44 pp., Hamburg, Germany, 1997..
- Matsoukas, C., N. Hatzianastassiou, A. Fotiadi, K.G. Pavlakis, and I. Vardavas: The effect of Arctic sea-ice extent on the absorbed (net) solar flux at the surface, based on ISCCP-D2 cloud data for 1983-2007, *Atmos. Chem. Phys.*, 10, 777-787, 2010
- Ohmura, A., Gilgen, H., Hegner, H., Muller, G., Wild, M., Dutton, E. G., Forgan, B., Fröhlich, C., Philipona, R., Heimo, A., König-Langlo, G., McArthur, B., Pinker, R., Whitlock, C. H., and Dehne, K.: Baseline Surface Radiation Network (BSRN/WCRP), a new precision radiometry for climate research, *Bull. Am. Meteorol. Soc.*, 79, 2115–2136, 1998.
- Pavlakis, K.G., Hatzidimitriou, D., Matsoukas, C., Drakakis, E., Hatzianastassiou, N., and Vardavas, I.: Ten-year global distribution of downwelling longwave radiation, *Atmos. Chem. Phys.*, 4, 127–142, 2004.
- Pavlakis, K.G., D. Hatzidimitriou, E. Drakakis, C. Matsoukas, A. Fotiadi, N. Hatzianastassiou, I. M. Vardavas: ENSO surface longwave radiation forcing over the tropical Pacific, *Atmos. Chem. Phys.*, 7, 2013-2026, 2007.
- Pavlakis, K.G., N. Hatzianastassiou, C. Matsoukas, A. Fotiadi, and I. Vardavas: ENSO surface shortwave radiation forcing over the tropical Pacific, *Atmos. Chem. Phys.*, 8, 5565-5577, 2008.
- Peng, L., Chou, M.-D., and Arking, A.: Climate studies with a multi-layer energy balance model, part I, Model description and sensitivity to the solar constant, *J. Atmos. Sci.*, 39, 2639–2656, 1982.
- Slingo, A.: A GCM parameterization for the shortwave radiative properties of water clouds, *J. Atmos. Sci.*, 46, 1419-1427, 1989.
- Vardavas, I. and Carver, J. H.: Solar and terrestrial parameterizations for radiative convective models, *Planet. Space Sci.*, 32, 1307–1325, 1984.
- Vardavas, I. M., and Koutoulaki, K.: A model for the solar radiation budget of the Northern Hemisphere: Comparison with Earth Radiation Budget Experiment data, *J. Geophys. Res.*, 100, 7303-7314, 1995.
- Vardavas, I. and Taylor, F. W. (2007), *Radiation and Climate*, International Series of Monographs on Physics, No. 138, pp512, Oxford Science Publications, Oxford
- Wild, M., Ohmura, A., Gilgen, H., and Roeckner, E.: Validation of general circulation model radiative fluxes using surface observations, *J. Climate*, 8, 1309–1324, 1995.

### A.3.1.7 DLR-ISIS Surface Irradiance Data Set

Luca Bugliaro, Sina Lohmann, Bernhard Mayer

#### Description of the DLR-ISIS surface irradiance data set

The ISIS dataset (Irradiance at the Surface derived from ISCCP cloud data) consists of three-hourly values of direct normal and global irradiances at the surface for a time period of 21 years (1984-2004) that have been derived by means of one dimensional radiative transfer computations based on satellite observations of clouds, aerosol, and trace gases. The necessary input parameters have been obtained from various sources. Most parameters were adopted from the FD (flux D series) input dataset of the International Satellite Cloud Climatology Project (ISCCP), composed of 6596 equal area grid boxes with a surface of 280 x 280 km<sup>2</sup> (Zhang et al 2004), in particular, all cloud parameters, the mean topographic altitude, as well as the average solar zenith angle for every three hourly interval have been extracted for every grid box. For that reason, the derived global irradiance (GHI) should be close to the global irradiance in the FD data set and the strength of ISIS is that it additionally provides direct normal irradiance (DNI), as required e.g. for the operation and planning of concentrating solar power plants.

All cloud parameters (cloud top pressure, cloud optical thickness, cloud top temperature, cloud type, cloud amount) stem from the ISCCP FD data set, which in turn represent the ISCCP D1 cloud data set (Rossow and Schiffer 1999). Cloud top height has been derived from cloud top pressure, while cloud geometrical thickness was always set to 1000m. For water clouds the transformation of liquid water content and effective droplet radius to optical properties is done with the parameterisation of Hu and Stamnes (1993) with an effective droplet radius of 10 µm. For ice clouds the parameterisation of Yang and Key (Yang et al., 2000; Key et al., 2002) is used with an effective particle radius of 30 µm. This is consistent with the cloud optical properties retrieved in ISCCP (Rossow et al., 1996). The mean topographic altitude, based on the U.S. Navy dataset of the National Center for Atmospheric Research NCAR, is also extracted directly from ISCCP FD. The average solar zenith angle, according to the Astronomic Almanac of 1950-2050, is taken from ISCCP FD as well. Total ozone and water vapour vertical columns have been adopted in the ISCCP project (and used for ISIS) from various datasets. The ozone columns stem from data of the Total Ozone Mapping Spectrometer (TOMS, Version 7, Mc-Peters et al. 1996). In case these were not available, data of the Television Infrared Observation Satellite (TIROS) Operational Vertical Sounder (TOVS) has been used. Water vapour profiles have been produced using the TOVS instrument (Kidwell 1995). Gaps have been filled by a combination of the 5 year means of the Stratospheric Aerosol and Gas Experiment SAGE II for the upper troposphere and stratosphere with  $p \leq 200$  mbar (Rind and Liao 1997, Liao and Rind 1997) with a 10 year pressure climatology ( $p \geq 300$  mbar, Oort 1983). Surface albedo values for the solar spectral range are contained in the ISCCP FD input dataset and have been adopted for ISIS also. Atmospheric profiles of trace gases are taken from five US standard atmospheres according to (Anderson et al. 1986): a winter and a summer atmosphere for mid and high latitudes as well as a tropical atmosphere. They comprise vertical profiles of pressure, temperature and particle density for air, ozone, oxygen, water vapour and carbon dioxide up to 50 km altitude.

The assignment of the correct atmospheric profile occurs under consideration of the mean geographical latitude of every ISCCP box. The tropical atmosphere is selected up to 23° North and South of the Equator, the mid latitude atmosphere between  $\pm 23^\circ$  and  $\pm 67^\circ$ , and the high latitude atmosphere further North of 67°N or South of 67°S. In the Northern hemisphere the summer profiles are used between April and September and the winter profiles during the

remaining months. In the Southern hemisphere summer and winter are interchanged. Values of water vapour and ozone columns have been scaled to the corresponding ISCCP values. Special attention is given to aerosols that are not treated as in ISCCP FD. For the distribution of aerosols in the atmosphere a vertical profile of (Shettle 1989) has been assumed. The optical thickness of the tropospheric aerosols has been extracted from the NASA Goddard Institute for Space Studies (GISS) dataset that contains climatological means of the most important aerosol types with a spatial resolution of  $4^\circ \times 5^\circ$  (Tegen et al., 1997). In addition, the index by (Sato et al. 1993 + updates) has been used that consists of monthly averages of the optical thickness of the stratospheric aerosols at 550 nm in  $7.5^\circ$  latitude steps.

To derive direct (and global) irradiance at the surface from this input data sets the two-stream solver of Kylling et al. (1995) is used, which is part of the library for radiative transfer (libRadtran, Mayer and Kylling, 2005). The two-stream method solves the linear transport equation applicable to radiative transfer in a vertically inhomogeneous layered media. A 32-band correlated-k parameterisation after Kato et al. (1999) is used for the calculation of spectrally integrated values over the solar spectral range (200-4300 nm). Radiative transfer calculations are carried out separately for clear sky and for each of the 15 ISCCP cloud types assuming homogeneous cloud layers. The results are summed, weighted with the cloud amount of each cloud type and the proportion of clear sky respectively to get 3-hourly irradiance values.

Two versions of the ISIS dataset exist: one includes the impact of stratospheric aerosols while the other one does not.

## Uncertainty Parameters

### Clouds:

- ISCCP overestimates cloud optical thickness and/or cloud cover due to misinterpretation of stratospheric aerosol as clouds (Rossow 2006).
- ISCCP tends to overestimate cloud cover, especially in regions observed under a large satellite zenith angle (Rossow and Schiffer 1999; Wielicki and Parker 2002).
- ISCCP tends to underestimate cloud coverage for regions with high surface albedo.

### Aerosols:

- The aerosol climatology used well reproduces the mean actual optical thickness of the single boxes, and the impact of aerosols is small with respect to cloud effects. However, aerosols can be responsible for high undetected variability.
- Since global long-term data are not available for tropospheric aerosol properties, a climatological annual cycle is included that does not vary from year to year. Thus, the true variability of the irradiance might actually be stronger than calculated in DLR-ISIS.
- Comparisons of calculations with and without volcanic aerosol reveal a decrease of up to 16% in annual averages of the direct normal irradiance due to volcanic eruptions. Changes in GHI are much smaller: Volcano eruptions reduce annual averages of GHI by less than 2.2%

### Grid box size:

- The spatial averaging of the ISCCP cloud data causes a smoothing of extreme values that are encountered in single satellite pixels, and minimum and maximum values of cloud coverage are less pronounced.
- The real variability of clouds, aerosols and topography can lead to discrepancies between ISIS and surface instruments located at selected sites.

## Uncertainty Estimate

- Comparison of the results with GHI provided by the ISCCP FD srf data set shows very good agreement of the temporal characteristics. For two regions ISCCP FD srf underestimates GHI by 1%. The Near East region reveals an average deviation of 4.4% between the two curves. Data refer to a spatial average of nine ISCCP boxes, therefore the effect is not spatially confined. Monthly means of DLR-ISIS are validated against surface measurements from
  - a) the Baseline Surface Radiation Network (BSRN, Ohmura et al. 1998): 6 stations with GHI and 31 with GHI and DNI
  - b) the Solar Radiation Monitoring Laboratory of the University of Oregon in Eugene: 18 stations
  - c) 12 stations in Saudi Arabia in the framework of the NASA Remote Sensing Validation Data
  - d) the Ben-Gurion National Solar Energy Center in Sede Boqer (Israel): 8 stations (Faiman et al. 2004)
  - e) single stations: data from the Fraunhofer-Institut für Solare Energiesysteme (ISE) in Freiburg, from the Global Atmosphere Watch (GAW) project, from the Kramer Junction Power Plant in California, from the SKAL-ET (HochSKALierung der EuroTrough Technologie) and SWERA (Solar and Wind Energy Resource Assessment) projects, and from the German Weather Service (Deutscher Wetterdienst, DWD).
  - f) In total, time series from 89 stations with different length and temporal resolution could be compared to ISIS results. All surface measurements are quality controlled and have a mean error estimated by the data providers between 1% and 5%.

	# sites	n	MB		RMSD		r	r <sub>A</sub>
			[W/m <sup>2</sup> ]	[%]	[W/m <sup>2</sup> ]	[%]		
GHI	89	6458	+3.0	+2.6	15.1	11.7	0.96	0.64
DNI	78	5433	-22.2	-2.9	49.6	35.1	0.83	0.63

n = number of months investigated, RMSD = root mean square deviation, MB = mean bias, r = correlation coefficient, r<sub>A</sub> = annual cycle adjusted correlation coefficient.

- Comparison of DLR-ISIS monthly values for 10 ISCCP boxes during 1999-2000 against Meteosat-derived surface irradiance (Meyer et al. 2004; Schillings et al. 2004) that was averaged temporally and spatially to match the ISCCP resolution:

ISCCP box no.	rMB (%)	Correlation coefficient r	RMSD (W/m <sup>2</sup> )	RMSD (%)
1759	3.2	0.98	10.5	9.5
4563	-10.4	0.96	32.0	11.3
4578	-3.1	0.76	31.1	13.3
4834	-2.0	0.94	18.6	7.6
4959	-7.3	0.97	24.7	9.8
4960	-2.4	0.94	24.9	10.1
5417	-1.5	0.99	14.5	6.4
5528	5.0	0.98	13.8	7.7
5632	-1.0	0.98	10.4	10.3
5829	0.5	0.99	18.7	18.7
<b>All boxes</b>	<b>-1.7</b>	<b>0.95</b>	<b>19.3</b>	<b>10.5</b>

rMB = relative mean bias, RMSD = root mean square deviation, r = correlation coefficient.

- Variability of DNI and GHI inside one ISCCP box has been quantified exemplarily by considering 8 measurement stations in Israel (1989-1999) and 3 in Oregon, USA (1984-2004):

For Israel systematic deviations of single sites to the stations mean is between -13.5% and +8.6%. Deviations between surface measurements and DLR-ISIS for the corresponding box lie in the same range: between -20 % and +4 %. For Oregon, the bias between measurements and satellite-derived DNI amounts to  $34 \text{ W/m}^2$  (16%) while root mean square deviation amounts to  $36 \text{ W/m}^2$  (17%). The correlation coefficient of annual anomalies is 0.75.

## References

- Anderson, G.P., S. Clough, F. Kneizys, J. Chetwynd und E. Shettle (1986). AFGL Atmospheric Constituent Profiles (0-120 km). AFGL-TR-86-0110, AFGL(OPI), Hanscom AFB, MA 01736.
- Faiman, D., D. Feuermann, P. Ibbetson, B. Medwed, A. Zemel, A. Ianetz, V. Liubansky, I. Setter and S. Suraqui (2004). The Negev radiation survey. Transactions of the ASME, 126: 906-914.
- Hu, Y.X. and K. Stamnes (1993). An accurate parameterization of the radiative properties of water clouds suitable for use in climate models. *J. Climate* 6: 728-742.
- Kato, S., T.P. Ackerman, J.H. Mather and E.E. Clothiaux (1999). The k-distribution method and correlated-k approximation for a shortwave radiative transfer model. *J. Quant. Spectrosc. Radiat. Transfer* 62: 109-121.
- Key, J., P. Yang, B. Baum, and S. Nasiri (2002). Parameterization of shortwave ice cloud optical properties for various particle habits. *J. Geophys. Res.*, 107 (D3). doi:10.1029/2001JD000742.
- Kidwell, K. (1995). NOAA Polar Orbiter Data Products Users Guide. Natl. Environ. Satell., Data and Inf. Serv., Silver Spring, Md, USA.
- Kylling, A., K. Stamnes and S.-C. Tsay (1995). A reliable and efficient two-stream algorithm for spherical radiative transfer: documentation of accuracy in realistic layered media. *J. Atmos. Chem.* 21: 115-150.
- Liao, X. and D. Rind (1997). Local upper tropospheric/lower stratospheric clear-sky watervapor and tropospheric deep convection. *J. Geophys. Res.*, 102: 19543–19557.
- Mayer, B. and A. Kylling (2005). Technical note: The libRadtran software package for radiative transfer calculations - description and examples of use. *Atmos. Chem. Phys.*, 5, doi:10.5194/acp-5-1855-2005.
- Lohmann, S., C. Schillings, B. Mayer and R. Meyer (2006). Long-term variability of solar direct and global irradiance derived from ISCCP data and comparison with re-analysis data. *Solar Energy*, 80, doi:10.1016/j.solener.2006.03.004.
- Lohmann, S., L. Riihimaki, F. Vignola, and R. Meyer (2007). Trends in direct normal irradiance in Oregon: Comparison of surface measurements and ISCCP-derived irradiance. *Geophys. Res. Lett.*, 34, L02705, doi:10.1029/2006GL027322.
- Lohmann, S. (2006) (in german). Langzeitvariabilität der globalen und direkten Solarstrahlung für Solarenergieanwendungen. DLR-Forschungsbericht Nr. 2006-13.
- McPeters, R.D., P. Bhartia, A. Krueger and J. Herman (1996). Nimbus-7 Total Ozone Mapping Spectrometer (TOMS) data products user's guide. NASA Ref. Publ., 1384.
- Oort, A.H. (1983). Global Atmospheric Circulation Statistics, 1958-1973. NOAA Prof. Pap. 14. 180 pp. + 47 microfiches, U.S. Govt. Print. Off., Washington, D.C.

- Meyer, R., S. Lohmann, C. Schillings and C. Hoyer (2004). Climate statistics for planning and siting of solar energy systems: Long-term variability of solar radiation derived from satellite data. Workshop Solar Resource from the Local Level to Global Scale in Support of the Resource Management of Renewable Electricity Generation, 6-7 December 2004 EC Joint Research Centre, Ispra (Varese), Italy.
- Ohmura, A., H. Gilgen, H. Hegner, G. Müller and M. Wild (1998). Baseline Surface Radiation Network (BSRN/WCRP): New precision radiometry for climate research. *Bull. Am. Met. Soc.*, 79: 2115-2136.
- Rind, D. and X. Liao (1997). Stratospheric Aerosol and Gas Experiment II CD-ROM atlas of global mean monthly mean aerosols, ozone, NO<sub>2</sub>, water vapor, and relative humidity (1985-1993). *Earth Interact.*, 1: doi:10.1175/1087-3562(1997)001.
- Rossow, W.B., A.W. Walker, D. Beuschel and M. Roiter, (1996). International Satellite Cloud Climatology Project (ISCCP) description of new cloud datasets. WMO/TD 737, World Climate Research Programme (ICSU and WMO), 115 pp.
- Rossow, W.B. and R. Schiffer (1999). Advances in understanding clouds from ISCCP. *Bull. Am. Met. Soc.*, 80: 2261-2287.
- Sato, M., J. Hansen, M. McCormick and J. Pollack (1993). Stratospheric aerosol optical depths, 1850-1990. *J. Geophys. Res.*, 98(D12): 22987-22994.
- Schillings, C., H. Mannstein and R. Meyer (2004). Operational method for deriving high resolution direct normal irradiance from satellite data. *Sol. Energy*, 76: 475-484.
- Shettle, E.P. (1989). Models of aerosols, clouds and precipitation for atmospheric propagation studies. AGARD Conference Proceedings No. 454.
- Tegen, I., P. Hollrig, M. Chin, I. Fung, D. Jacob, and J. Penner (1997). Contribution of different aerosol species to the global aerosol extinction optical thickness: Estimates from model results. *J. Geophys. Res.* 102 (D20): 23895-23915.
- Wielicki, B.A. and L. Parker (1992). On the determination of cloud cover from satellite sensors: The effect of sensor spatial resolution. *J. Geophys. Res.*, 97: 12799-12823.
- Yang, P., B.-C. Gao, B.A. Baum, X.H. Yong, W.J. Wiscombe, S.-C. Tsay, D.M. Winker, D.M. and S.L. Nasiri (2000). Parameterization of the scattering and absorption properties of individual ice crystals. *J. Geophys. Res.*, 105 (D4): 4699-4718.
- Zhang, Y.-C., W. Rossow, A. Lacis, V. Oinas and M. Mishchenko (2004). Calculation of radiative fluxes from the surface to top of atmosphere based on ISCCP and other global data sets: Refinements of the radiative transfer model and the input data. *J. Geophys. Res.*, 109: doi:10.1029/2003JD004457.

## Appendix B:

### B1: Radiative Model Comparisons

Seiji Kato

**Abstract:**

*This appendix discusses the error in the modeled broadband irradiance due to treatments of gaseous absorption, two-stream approximations, and the independent column approximation (ICA). These techniques and approximations are widely used in computing vertical profiles of irradiances. These techniques can be applied to both shortwave and longwave, but the focus of this appendix is on shortwave, especially for sections discussing the error caused by two-stream approximations and ICA.*

*The following sections are not intended to review earlier studies on these subjects but simply to provide a range of errors caused by the approximations. Currently, comparisons of radiative transfer models are conducted by Oreopoulos et al. (2012). Such modeling comparisons might provide further insights of modeling errors caused by specific approximations.*

#### B.1.1. Gaseous absorption

The  $k$ -distribution method and correlated- $k$  approximation are widely used to treat gaseous absorption in the shortwave and longwave. Descriptions of the  $k$ -distribution and correlated- $k$  approximation can be found in, for example, Arking and Grossman (1972), Ackerman (1983), Goody et al. (1989), West et al. (1990), Holloweg (1993), Lacis and Oinas (1996), Fu and Liou (1992), Chou (1992), Chou et al. (1995), Kratz (1995), Chou and Lee (1996), Mlawer et al. (1997), Kato et al. (1999), and Yang et al. (2000). Descriptions of a slightly different approach called the exponential sum fitting, which leads to an identical form, can be found in, Ackerman et al. (1976) Wiscombe and Evans (1977) and Asano and Uchiyama (1987), among others.

The error due to the correlated- $k$  assumption in computing direct shortwave irradiance at the surface for the mid-latitude summer standard atmosphere is 0.2% or  $2.1 \text{ Wm}^{-2}$  (Kato et al. 1999) compared with MODTRAN3 (Kneizys et al. 1988). According to a model comparison by Barker et al. (2003), the clear-sky broadband top-of-atmosphere (TOA) albedo computed with four Monte Carlo models agrees to within 1%, and the atmospheric shortwave absorption agrees to within 2% compared with a line-by-line code (CHARTS). The TOA albedo computed with Monte Carlo models agrees to within 3% and the atmospheric absorption agrees to within 7% under cloudy conditions (Barker et al. 2003). The relative difference of modeled and measured surface shortwave direct irradiance reported by Michalsky et al. (2006) is less than 1% and the relative difference of the diffuse irradiance is less than 1.9%. The difference in the modeled and measured irradiance is predominately caused by the uncertainty in model inputs such as the column water vapor amount, ozone amount, and aerosol optical properties rather than the assumptions in the model such as the correlated- $k$  and two-stream approximations (Kato et al. 1997).

### B.1.2. Comparison of two-stream and n-stream models

The error due to a two-stream approximation depends on the type of approximation (Meador and Weaver 1980). The two-stream error derived by comparisons with results of models with a larger number of streams is given by King and Harshvardhan (1986), Liou et al. (1988), and Toon et al (1989). In general, two- or four- stream approximations are sufficient for computing clear-sky irradiances. For cloudy atmospheres, the two-stream error decreases with increasing optical thickness of clouds, because the diffuse field is more uniform within optically thick clouds and the two-stream approximation is based on diffusion theory (Bohren and Clothiaux 2006). In addition to this optical thickness dependence, the error also depends on single scattering albedo, asymmetry parameter, and solar zenith angle. King and Harshvardhan (1986) investigated the error on various two-stream approximations including asymptotic theory, delta-Eddington, Meador-Weaver, and Coakley-Chylek for  $\omega = 1.0$  and  $0.9$ . Liou et al. (1988) investigated the error by the quadrature two- and four-stream approximations for  $\omega = 1.0, 0.8, 0.5,$  and  $0.3$ . For conservative clouds, the relative two-stream error in the albedo caused by the delta-Eddington and quadrature two-stream approximations is less than 5% when the cloud optical thickness is greater than 10. For the transmittance of conservative clouds, the relative two-stream error is less than 5% for optical thickness from 0.1 to 100 when the solar zenith angle is less than about  $60^\circ$ . The relative error is larger for absorbing clouds because the albedo and transmittance are small. When the optical thickness is less than 1 and  $\omega = 0.9$  or  $0.8$ , the relative two-stream error in the transmittance and reflectance is less than 10% when the solar zenith angle is less than about  $60^\circ$ .

The relative error in the transmittance caused by the four-stream model given by Liou et al. (1988) is less than 2% when the optical thickness is greater than 1 and  $\omega = 1.0$  for all solar zenith angles. The relative four-stream error in the transmittance is less than 2% for optical thickness between 0.1 and 50 when  $\omega = 1.0$  and the solar zenith angle is less than  $80^\circ$  (Liou et al. 1988). When  $\omega = 0.8$ , the relative four-stream error is less than 5% the optical thickness between 0.1 and 50 when solar zenith angle is less than  $80^\circ$ .

These values provide a range of errors in two-stream and four-stream approximations at a monochromatic wavelength. To obtain the exact error estimate by a particular two-stream approximation, however, researchers need to check the error in the two-stream approximation against a better model such as DISORT (Stamnes et al. 1988) or a Monte Carlo model.

We compute the broadband shortwave two-stream error with the Eddington approximation compared with DISORT in Figure A1. A water cloud layer is placed between 1 and 2 km in the midlatitude summer standard atmosphere for the plot. The size of cloud droplets is  $10\mu\text{m}$  and the asymmetry parameter is give by Mie theory.

### B.1.3. Flux at large solar zenith angles

A plane parallel approximation that neglects the spherical geometry of the Earth introduces a larger error when the solar zenith angle is greater than  $85^\circ$  (Kato and Loeb 2005, Li and Shibata 2006). Using the airmass factor from a spherical Earth for a path through the atmosphere and the insolation as the solar constant multiplied by the cosine of the solar zenith angle, significantly reduces the plane parallel error for solar zenith angle greater than  $85^\circ$ . When the solar zenith angle is greater than  $90^\circ$ , the TOA reflected irradiance is not negligible in some

applications. The annual and global mean reflected shortwave irradiance from the night hemisphere of the Earth is approximately  $0.2 \text{ Wm}^{-2}$  (Kato and Loeb 2003).

#### B.1.4. Vertical inhomogeneity

The vertical inhomogeneity of clouds can be treated by increasing the number of computational layers representing the atmosphere. The vertical resolution to compute the shortwave irradiance needs to be sufficient to capture the vertical change of the molecular scattering coefficient, water and ozone vertical profiles, and the variation of cloud properties. Error in the longwave irradiance computation is also caused by a coarse vertical resolution because longwave radiative transfer models usually assume that the Planck function changes linearly with optical thickness within the computational layer (Toon et al. 1989). Wiscombe (1976) investigated the error due to this approximation and showed that it is a function of the temperature of the layer, temperature gradient within the layer, and of the wavelength.

#### B.1.5. Error by the independent column approximation (ICA)

When clouds are horizontally inhomogeneous, clouds in the domain can be further divided into subgrid-scale clouds. The irradiance vertical profile is computed for each subgrid-scale cloud by a plane parallel radiative transfer model. Those subgrid-scale irradiance profiles  $F_i$  are averaged over the domain to get the mean irradiance profile  $F_{ICA}$ ,

$$F_{ICA} = \frac{1}{N} \sum_{i=1}^N F_i \quad (\text{C1})$$

where  $N$  is the number of subgrid-scale columns in the domain. The ICA, therefore, neglects horizontal photon transport.

Marshak et al. (1999) and Marshak and Davis (2005) investigated albedo, transmittance, and absorptance errors at the pixel scale caused by neglecting horizontal transport. The domain averaged irradiance error by ICA compared with the irradiance computed from the 3D radiation field has also been studied. Qualitatively, the reflected shortwave irradiance from ICA is larger than the irradiance from a 3D calculation when the solar zenith angle is small and vice versa when the solar zenith angle is large (Barker et al. 2003). The exact value of relative albedo and transmittance errors depends on the 3D cloud fields. As the cloud fraction over the domain decreases, the underestimation of the TOA albedo by ICA for a large solar zenith angle increases because the projected area of clouds in the direction of the direct solar radiation is constant with solar zenith angle in the ICA framework but increases in 3D.

Horizontal inhomogeneity of clouds causes error in longwave irradiance computations if it is neglected. Studies on this topic can be found in, for example, Fu et al. (2000) and Ellingson and Takara (2005).

#### B.1.6. Gamma-weighted two-stream and effective thickness approximations

If the distribution of cloud optical thickness is approximated by a gamma distribution, an analytical solution of two-stream reflectance and transmittance functions integrated over the

optical thickness distribution is available (Barker et al. 1996; Kato et al. 2005). The gamma-weighted two-stream approximation is a specific form of the independent column approximation. When the gamma-weighted two-stream approximation is made, the subgrid-scale irradiance profile does not have to be computed for all subgrid-scale clouds. Only one computation is necessary for the domain averaged irradiance profile.

The irradiance by the gamma-weighted two-stream approximation is a function of mean optical thickness and the shape parameter of a gamma distribution of cloud optical thicknesses.

The mean optical thickness is given by the linear mean of optical thicknesses in the domain. In principle, the shape parameter is given by the square of the mean over the standard deviation. When the sampling is not sufficient to determine the standard deviation, the shape parameter needs to be estimated from the difference between the linear and logarithmic means of the optical thicknesses (Wilks 1995). Because of this, the shape parameter  $\nu$  of a gamma distribution is related to the scaling factor  $\chi$  of the effective thickness approximation (Barker 1996, Kato et al. 2005) given by

$$\chi = \exp(\overline{\ln \tau} - \ln \bar{\tau}). \quad (\text{C2})$$

The approximate relation between  $\nu$  and  $\chi$  is given by Rossow et al. (2002).

General circulation model applications of the gamma-weighted two-stream model are given by Oreopoulos et al. (2004). The application of the computing irradiances from distributions of imager-derived cloud optical thickness is discussed in Kato et al. (2005).

Treating horizontal inhomogeneity by a scaling factor in computing irradiance from satellite derived cloud properties is given by Rossow et al. (2002). Barker and Wielicki (1997) and Li and Barker (2002) applied the gamma-weighted two-stream approximation to longwave. The error caused by the gamma-weighted two-stream and effective thickness approximation is given by Barker and Davis (2005).

In addition to the error by ICA, the gamma-weighted two-stream approximation introduces error when the cloud optical distribution significantly deviates from a gamma distribution. In addition, when the optical thickness is vertically correlated and computational layers divide the cloud layer into multiple layers, the reflected irradiance computed with the gamma-weighted two-stream approximation is larger than the actual value (Oreopoulos and Barker 1999). This is because the gamma-weighted two-stream approximation neglects the correlation of optical thicknesses across the computational layers.

### B.1.7 Assumption of cloud microphysics

When a two-stream assumption is made in a radiative transfer model, the asymmetry parameter, average cosine of the scattering angle, is the parameter that determine the direction of scattering in the model. The asymmetry parameter of liquid water cloud particles can be computed by Mie theory with a spherical particle assumption. The asymmetry parameter of liquid water particles for a given wavelength is then a function of their size. The asymmetry parameter of ice particles depends on their habits and surface roughness in addition to their size (e.g. Fu 1996; Fu et al. 1998; Yang et al. 2001; McFarquhar et al. 2002, Yang et al. 2008). As a result, the asymmetry parameter of ice particles in visible wavelengths can vary from 0.73 to 0.85 (Fu 2007).

### **B.1.8 Input to radiative transfer models**

In addition to assumptions made in radiative transfer modes described above, the error in the inputs to the radiative transfer model affect computations. Inputs are including, temperature and humidity profiles, cloud properties (cloud fraction, optical thickness, droplet size, top and base heights, phase), aerosol properties (optical thickness, single scattering albedo, size distribution), and surface properties (albedo, emissivity, elevation). These inputs variable uncertainties case a larger uncertainty in computing irradiance. For example, Zhang et al. (2006) using passive sensor derived clouds and Kato et al. (2011) using active and passive sensor derived clouds show that the uncertainty in near surface temperature and precipitable water cause the largest uncertainty in the global annual mean surface downward longwave irradiance among input uncertainties. Irradiance uncertainties are estimated through sensitivity studies in which input variables are perturbed by the amount of their uncertainties. When the difference between modeled and observed irradiances falls within the uncertainty, it increases the confidence of modeled irradiances and the estimate of uncertainty bounds. Note that CERES takes into account for the irradiance reference level (Loeb et al. 2002) in deriving TOA irradiances so that modeled irradiance can be compared directly. The spatial sampling noise dominates in the comparison of modeled surface irradiance with observations. Quantifying sampling noise, and understanding how well surface sites represent a grid where sites locate are necessary to relate surface irradiance comparison with uncertainties in modeled irradiance.

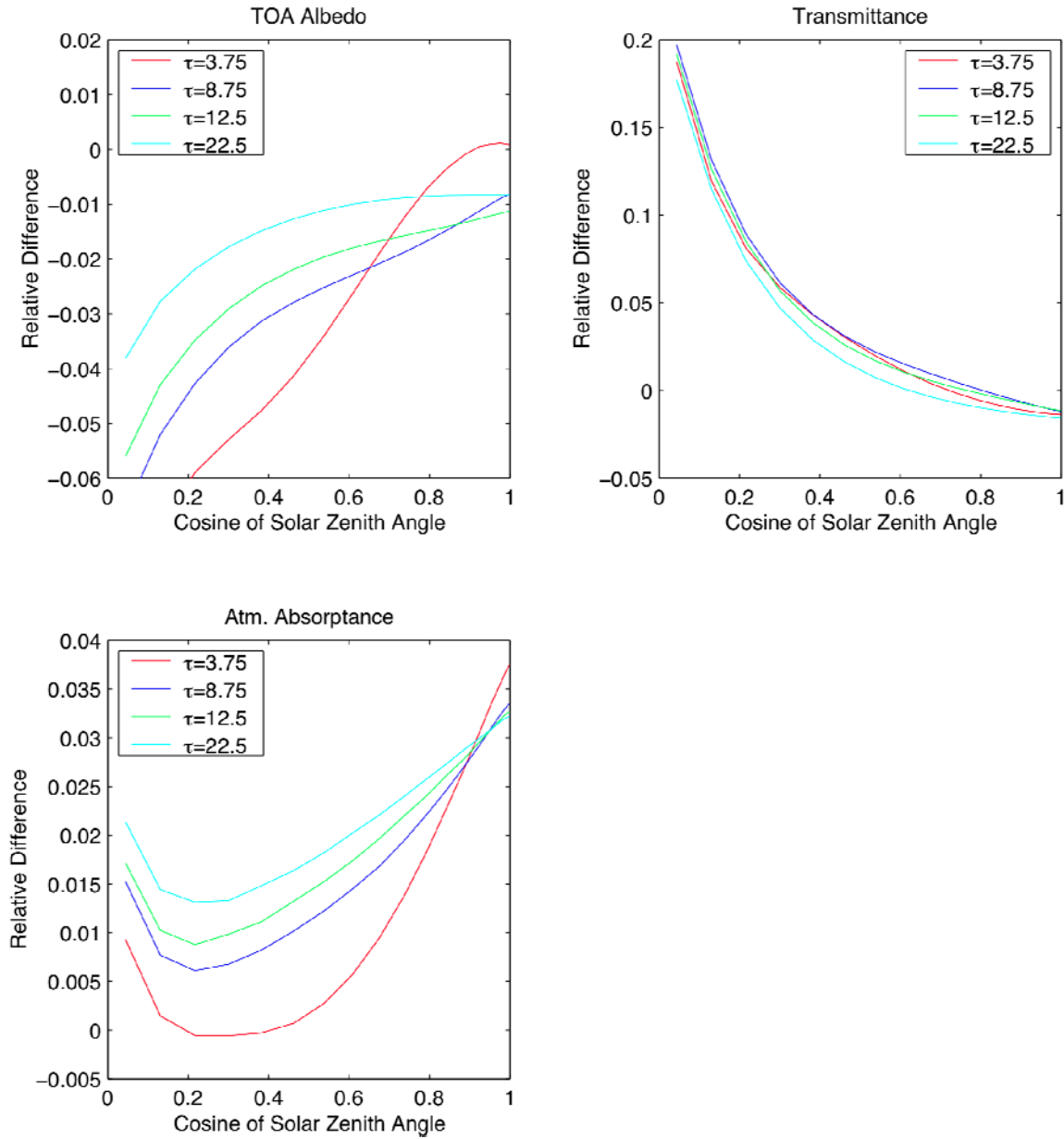


**Figure B1:** The relative error by the Eddington two-stream approximation in computing broadband shortwave TOA albedo, transmittance, atmospheric absorption. A water cloud layer is placed between 2 to 1 km in the standard midlatitude summer profile. The surface albedo is 0.05. The relative difference is defined as  $(2\text{-stream} - 12\text{-stream}) / 12\text{-stream}$ .

## References:

Ackerman, T. P., 1983: Equivalent absorption coefficients generated from frequency probability distributions, *Fifth Conference on Atmospheric Radiation*, Oct. 31-Nov. 4, Baltimore, MD.

- Asano, S., A. Uchiyama, 1987: Application of an extended ESFT method to calculation of solar heating rates by water vapor absorption, *J. Quant. Spectrosc. Radiat. Transfer*, 38, 147-158.
- Barker, H. W. and A. B. Davis, 2005: Approximation method in atmospheric 3D radiative transfer part2: Unresolved variability and climate applications, in *3D radiative transfer in cloudy atmosphere*, Marshak and Davis ed. Springer.
- Barker, H. W. and co-authors, 2003: Assessing 1D atmospheric solar radiative transfer models: Intercomparison and handling unresolved clouds, *J. Climate*, 16, 2676-2699.
- Barker, H. W. and B. A. Wielicki, 1997: Parameterizing grid-averaged longwave fluxes for inhomogeneous marine boundary layer clouds, *J. Atmos. Sci.*, 54, 2785-2798.
- Barker, H. W., 1996: A parameterization for computing grid-averaged solar fluxes for inhomogeneous marine boundary layer clouds Part I: methodology and homogeneous biases, *J. Atmos. Sci.*, 53, 2289-2303.
- Bohren, C. F. and E. E. Clothiaux, 2006: *Fundamentals of atmospheric radiation*, Wiley-VCH, pp297-300.
- Chou, M.-D., W. Ridgway, and M. M.-H. Yan 1995: Parameterizations for water vapor IR radiative transfer in both middle and lower atmosphere, *J. Atmos. Sci.*, 52, 1159-1167.
- Chou, M.-D., and K.-T. Lee 1996: Parameterizations for the absorption of solar radiation by water vapor and ozone, *J. Atmos. Sci.*, 53, 1203-1208.
- Chou, M.-D., 1992: A solar radiation model for use in climate studies, *J. Atmos. Sci.*, 49, 762-772.
- Ellingson, R. G., , E. E. Takara, 2005: Longwave radiative transfer in inhomogeneous cloud layers, in *3D radiative transfer in cloudy atmosphere*, Marshak and Davis ed. Springer.
- Fu, Q., 2007: A new parameterization of an asymmetry factor of cirrus clouds for climate models, *J. Atmos. Sci.*, 64, 4140-4150.
- Fu, Q., B. Carlin, and G. Mace, 2000: Cirrus horizontal inhomogeneity and OLR bias, *Geophys. Res. Lett.*, 27, 3341-3344.
- Fu, Qiang, Ping Yang, W. B. Sun, 1998: An Accurate Parameterization of the Infrared Radiative Properties of Cirrus Clouds for Climate Models. *J. Climate*, 11, 2223–2237.
- Fu, Q., 1996: An accurate parameterization of the solar radiative properties of cirrus clouds. *J. Climate*, 9.
- Fu, Q. and K.-N. Liou, 1992: On the correlated k-distribution method for radiative transfer in nonhomogeneous atmosphere, *J. Atmos. Sci.*, 15, 2139-2156.
- Goody, R., R. West, L. Chen, and D. Crisp, 1989: The correlated-k method for radiation calculations in nonhomogeneous atmosphere, *J. Quant. Spectrosc. Radiat. Transfer*, 42, 539-550.
- Hollweg, H.-D., 1993: A k distribution method considering centres and wings of atmospheric absorption lines, *J. Geophys. Res.*, 98, 2747-2756.
- Kato, S., F. G. Rose, S. Sun-Mack, W. F. Miller, Y. Chen, D. A. Rutan, G. L. Stephens, N. G. Loeb, P. Minnis, B. A. Wielicki, D. M. Winker, T. P. Charlock, P. W. Stackhouse, K.-M. Xu, and W. Collins, 2011, Computation of top-of-atmosphere and surface irradiances with CALIPSO, CloudSat, and MODIS derived cloud and aerosol properties, *J. Geophys. Res.*, VOL 116, D19209, doi:10.1029/s011JD16050.
- Kato, S., and N. G. Loeb, 2005: Top-of-atmosphere shortwave broadband observed radiance and estimated irradiance over polar regions from Clouds and the Earth's Radiant Energy System (CERES) instruments on Terra, *J. Geophys. Res.*, 110, D7, D07202 10.1029/2004JD005308.

- Kato, S., F. G. Rose, and T. P. Charlock, 2005: Computation of Domain-averaged Irradiance Using Satellite-derived Cloud Properties, *J. Atmos. Oceanic Technol.*, 22, 146-164.
- Kato, S., T. P. Ackerman, J. H. Mather, and E. E. Clothiaux, 1999: The k-distribution method and correlated-k approximation for a shortwave transfer model, *J. Quant. Spectrosc. Radiat. Transfer*, 62, 109-121.
- Kato, S., T. P. Ackerman, E. E. Clothiaux, J. H. Mather, G. G. Mace, M. L. Wesely, F. Murcray, and J. Michalsky, 1997: Uncertainties in modeled and measured clear-sky surface irradiances, *J. Geophys. Res.*, 102, 25881-25898.
- King, M. D., and Harshvardhan, 1986: Comparative accuracy of selected multiple scattering approximations, *J. Atmos. Sci.*, 43, 784-801.
- Kratz, D. P., 1995: The correlated-k distribution technique as applied to the AVHRR channels, *J. Quant. Spectrosc. Radiat. Transfer*, 53, 501-517.
- Lacis, A. A., and V. Oinas, 1991: A description of the correlated k distribution method for modeling nongray absorption, thermal emission, and multiple scattering in vertically inhomogeneous atmosphere, *J. Geophys. Res.*, 96, 9027-9063.
- Li, J. and K. Shibata, 2006: On the effective solar pathlength, *J. Atmos. Sci.*, 63, 1365-1373.
- Li, J. and H. W. Barker, 2002: Accounting for unresolved clouds in a 1D infrared radiative transfer model, part II: Horizontal variability of cloud water path, *J. Atmos. Sci.*, 59, 3302-3320.
- Liou, K.-N., Q. Fu, and T. P. Ackerman, 1988: A simple formulation of the delta-four-stream approximation for radiative transfer parameterizations, *J. Atmos. Sci.*, 45, 1940-1947.
- Loeb, N. G. S. Kato, B. A. Wielicki, 2002: Defining top-of-atmosphere flux reference level for earth radiation budget studies, *J. Climate*, 15, 3301-3309.
- McFarquhar, Greg M., Ping Yang, Andreas Macke, Anthony J. Baran, 2002: A New Parameterization of Single Scattering Solar Radiative Properties for Tropical Anvils Using Observed Ice Crystal Size and Shape Distributions. *J. Atmos. Sci.*, 59, 2458-2478.
- Meador, W. E. and W. R. Weaver, 1980: Two-stream approximation to radiative transfer in planetary atmospheres: A united description of existing methods and a new improvement, *J. Atmos. Sci.*, 37, 630-643.
- Marshak, A., A. B. Davis, 2005: Horizontal fluxes and radiative smoothing, in *3D radiative transfer in cloudy atmosphere*, Marshak and Davis ed. Springer.
- Marshak A., L. Oreopoulos, A. B. Davis, W. J. Wiscombe, and R. F. Cahalan, 1999: Horizontal radiative fluxes in clouds and accuracy of the independent pixel approximation at absorbing wavelengths, *Geophys. Res. Lett.*, 11, 1585-1588}.
- Michalsky, J. J. G. P. Anderson, J. Barnard, J. Delamere, C. Gueymard, S. Kato, P. Kiedron, A. McComiskey, and P. Ricchiazzi, 2006: Shortwave radiative closure studies for clear skies during the Atmospheric Radiation Measurement 2003 aerosol intensive observation period, *J. Geophys. Res.*, 111, D14S90 doi:10.1029/2005JD006341.
- Mlawer, E. J., S. J. Taubman, P. D. Brown, M. J. Iacono, and S. A. Clough, 1997: Radiative transfer for inhomogeneous atmosphere: RRTM, a validated correlated-k model for the longwave, *J. Geophys. Res.*, 102, 16663-16682.
- Oreopoulos, L., E. Mlawer, J. Delamere, T. Shippert, J. Cole, B. Fomin, M. Iacono, Z. Jin, J. Manners, P. Räisänen, F. Rose, Y. Zhang, M. J. Wilson, W. Rossow, 2012: The Continual Intercomparison of Radiation Codes: Results from Phase I, *J. Geophys. Res.*, 117, DOI: 10.1029/2011JD016821.
- Oreopoulos, L., M.-D. Chou, M. Khairoutdinov, H. W. Barker, R. F. Cahalan, 2004: Performance of Goddard earth observing system GCM column radiative models under heterogeneous cloud conditions, *Atmos. Res.*, 72, 365-382.

- Oreopoulos, L. and H. W. Barker, 1999: Accounting for subgrid-scale cloud variability in a multi-layer 1D solar radiative transfer algorithm, *Q. J. R. Meteorol. Soc.*, 125, 301-330.
- Rossow, W. B., C. Delo, and B. Cairns, 2002: Implications of the observed mesoscale variations of clouds for the earth's radiation budget, *J. Climate*, 15, 557-585.
- Stamnes, K., S-C. Tsay, W. Wiscombe, and K. Jayaweera, 1988: Numerically stable algorithm for discrete-ordinate-method radiative transfer in multiple scattering and emitting layered media, *Appl. Opt.*, 27, 2502-2509.
- Toon, O. B., C. P. McKay, T. P. Ackerman, and K. Santhanam, 1989: Rapid calculation of radiative heating rates and photodissociation rates in inhomogeneous multiple scattering atmosphere, *J. Geophys. Res.*, 102, 16287-16301.
- West, R., D. Crisp, and L. Chen, 1990: Mapping transformations for broadband atmospheric radiation calculations, *J. Quant. Spectrosc. Radiat. Transfer*, 43, 191-199.
- Wilks, D. S., 1995: *Statistical methods in the atmospheric sciences*, Academic Press.
- Wiscombe, W. J., 1976: Extension of the doubling method to inhomogeneous sources, *J. Quant. Spectrosc. Radiat. Transfer*, 16, 477-489.
- Wiscombe, W. J. and J. W. Evans, 1976: Exponential-sum fitting of radiative transmission functions, *J. Comp. Phys*, 24, 416-444.
- Yang, P., Kattawar, G. W., G. Hong, P. Minnis, Y. X. Hu, 2008: Uncertainties associated with the surface texture of ice particles in satellite-based retrieval of cirrus clouds-part I: single-scattering properties of ice crystals with surface roughness, *IEEE trans. Geoscience and remote sensing* 46, 1940-1947.
- Yang, P., B.-C. Gao, B. A. Baum, Y. X. Hu, W. J. Wiscombe, S. C. Tsay, D. M. Winker, S. H. Nasiri, Radiative properties of cirrus clouds in the infrared (8 – 13  $\mu\text{m}$ ) spectral region, *JQSRT*, 70, 473-504.
- Yang, S., P. Ricchiazzi, and C. Gautier, 2000: Modified correlated k-distribution methods for remote sensing applications, *J. Quant. Spectrosc. Radiat. Transfer*, 64, 585-608.
- Zhang, Y.-C., W. B. Rossow, and P. W. Stackhouse Jr., 2006: Comparison of different global information sources used in surface radiative flux calculation: Radiative properties of the surface, *J. Geophys. Res.*, 112, D01102, doi:10.1029/2005JD007008.

## B2: The Climate Model of the GFDL

S.M. Freidenreich, M.D. Schwarzkopf, and V. Ramaswamy

### B2.1: Introduction

The shortwave and longwave flux values that have been submitted to the GEWEX-RFA archive are derived from a new coupled climate general circulation model that has been developed at the Geophysical Fluid Dynamics Laboratory (GFDL). This model has been used to run a number of climate change experiments, part of which were submitted to the 2007 IPCC Assessment Report 4 (AR4). The model consists of four separate components: atmosphere, land, sea ice, and ocean, which interact through a flux coupler module. The most recent version of the model (called CM2.1) is used here. A notable improvement compared to an earlier version (CM2.0) is a substantial reduction of an overall cold bias at the surface. This is achieved partly through the use of finite volume dynamical core numerics (Lin, 2004) in the atmospheric model, and partly by tuning parameters that reduce cloudiness and increase net surface shortwave radiation. The salient features that pertain to the determination of the shortwave and longwave fluxes at the surface are summarized here. Further details with respect to the atmospheric and land components are described in a paper by the GFDL Global Atmospheric Model Development Team (2004), while details pertaining to the ocean and sea-ice components and their coupling to the atmospheric/land component are described in Delworth et al. (2006).

### B2.2: Model Description

The model's horizontal resolution is  $2.5^\circ$  longitude by  $2^\circ$  latitude. There are twenty-four vertical levels, of which five are in the stratosphere, with the top level at about 3 mb. A three-hour time step for atmospheric radiation and a half-hour time step for other atmospheric physics are assumed. A diurnal cycle of insolation is also assumed.

Both the shortwave and longwave parameterizations are developed from and tested with benchmark computations based on the HITRAN 2000 line catalogue (Rothman et al. 2003). The shortwave radiation algorithm follows Freidenreich and Ramaswamy (1999) with updates discussed in Freidenreich and Ramaswamy (2005). The number of spectral bands is eighteen, while the total number of pseudo-monochromatic column calculations required per grid-box is thirty-eight. Included are absorption by  $\text{H}_2\text{O}$ ,  $\text{CO}_2$ ,  $\text{O}_3$ ,  $\text{O}_2$ , molecular scattering, and absorption and scattering by aerosols and clouds. Clouds are assumed to be horizontally homogeneous and to randomly overlap. For water clouds, the optical properties are based on Slingo (1989); for ice clouds, they are based on Fu and Liou (1993). For aerosols, the optical properties follow Haywood et al. (1999) and Haywood (personal communication). The band averaging of the single-scattering parameters is performed using the thick-averaging technique (Edwards and Slingo 1996). The delta-Eddington technique is employed to compute the layer reflection and transmission based on the single scattering properties of that layer, while the total shortwave fluxes and heating rates are computed using an adding scheme (Ramaswamy and Bowen 1994). The diffuse incident beam is assumed to be isotropic and its reflection and transmission are computed using an effective angle of  $53^\circ$ . Compared with line-by-line calculations, the maximum error in the clear-sky heating rate is less than 10%. The maximum error in the overcast sky heating rate for the water cloud model considered (Slingo 1989) is about 15%; for ice clouds, the errors could reach 25%.

The longwave radiation algorithm follows the modified form of the Simplified Exchange Approximation (Schwarzkopf and Ramaswamy 1999). It accounts for the absorption and emission by H<sub>2</sub>O, CO<sub>2</sub>, O<sub>3</sub>, N<sub>2</sub>O, CH<sub>4</sub>, and the halocarbons CFC-11, CFC-12, CFC-113 and HCFC-22. The water vapor continuum is parameterized according to the CKD 2.1 formulation of Clough et al. (1992). Aerosols and clouds are treated as absorbers, with non-grey absorption coefficients specified in eight spectral bands, following the methodology adopted in Ramachandran et al. (2000). For water clouds, the absorption coefficients follow those employed in Held et al. (1993); for ice clouds, the Fu and Liou (1993) prescription is used. Compared with line-by-line calculations, the maximum error in the clear-sky heating rate is generally < 10%.

Large-scale clouds are parameterized with separate prognostic variables for specific humidity of cloud liquid and ice. Cloud microphysics are parameterized according to Rotstaysn (1997) with an updated treatment of mixed phase clouds (Rotstaysn et al. 2000). The particle size of liquid clouds needed for radiation calculations is diagnosed from the prognosed liquid water content and an assumed cloud droplet number concentration which is specified to be 300 cm<sup>-3</sup> over land and 100 cm<sup>-3</sup> over ocean. For ice clouds, the particle size is specified as a function of temperature based upon an analysis of aircraft observations (Donner et al. 1997). Cloud fraction is also treated as a prognostic variable of the model mostly following the parameterization of Tiedtke (1993). The model's radiation budget is tuned so that the long-term global and annual mean outgoing longwave and absorbed solar radiation are close to observed and that the net radiative balance is between 0 and 1 W m<sup>-2</sup>.

The anthropogenic aerosols include black carbon, organic carbon, and sulfate, while natural aerosols include sea salt and dust. Volcanic aerosols are also included. The distributions of monthly mean sulfate and carbonaceous aerosols are based on output from the MOZART chemical transport model (Horowitz et al., 2003), which uses input emissions from Olivier et al. (1996) and Cooke et al. (1999). Dust concentrations are from multi-year simulations driven by the NCEP reanalysis. The dust-size distribution is discretized into 8 bins ranging in size from 0.1 to 10 microns. For sea-salt, a constant concentration is assigned throughout the well-mixed marine boundary layer (up to 850 mb), and a zero concentration is prescribed above 850 mb and over land (Haywood et al., 1999). Aerosols do not directly interact with the cloud scheme (indirect effects omitted).

Further specifications are applied for well-mixed greenhouse gases, tropospheric and stratospheric ozone, solar irradiance, and the distribution of land-cover types. Tropospheric ozone is based on output from the MOZART chemical transport model. Stratospheric ozone distributions are prescribed based on Randel and Wu (1999). The derivation of the solar irradiance data is described in Fröhlich and Lean (2004) and have been provided by Lean (personal communication). The land model is based on the Land Dynamics model described in Milly and Shmakin (2002). Parameters affecting surface albedo were tuned on the basis of a comparison of model output with NASA Langley Surface Radiation Budget data analyses (Darnell et al. 1988, Gupta et al. 1992). Further steps to improve albedo fields are described in the paper by the GFDL Global Atmospheric Model Development Team (2004). The ocean surface is assumed to be Lambertian, with the albedo a function of the solar zenith angle following the formulation of Taylor et al. (1996).

### **B2.3: Application of Model Results**

The dataset submitted to the GEWEX-RFA archive is based on an ensemble of five experiments run with the aforementioned time-dependent specifications, for the period 1860 to 2003. Each is initialized with a different year of integration from a control experiment that uses

aerosol and trace gas concentrations, insolation, and distribution of land-cover types representative of 1860 conditions. A binomial interpolation in latitude is applied to the ensemble flux data in order to be compatible with the 2.5° resolution adopted for the GEWEX-RFA archive. The submitted data covers the time period from July 1983 (to correspond with the ISCCP-FD and SRB observational datasets) through 2003. It consists of the downward, upward, and net (downward minus upward) fluxes for clear-sky and all-sky atmospheres; also included are the total (shortwave+longwave) fluxes and the shortwave albedo. Both a global distribution of values, and averaged values for various regional and zonal sectors (outlined in the assessment document), are included.

## References:

- Clough, S. A., M. J. Iacono and J-L. Moncet, 1992: Line-by-line calculations of atmospheric fluxes and cooling rates: Application to water vapor. *J. Geophys. Res.*, **97**, 15761-15785
- Cooke, W.F., C. Liousse, H. Cashier, and J. Feichter, 1999: Construction of a 1° X 1° fossil fuel emission dataset for carbonaceous aerosol and implementation and radiative impact in the ECHAM-4 model. *J. Geophys. Res.*, **104**, 22137-22162.
- Darnell, W. L., W. F. Staylor, S. K. Gupta, and F. M. Denn, 1988: Estimation of surface insolation using sun-synchronous satellite data. *J. Clim.*, **1**, 820-836.
- Delworth, T.L., and Coauthors, 2006: GFDL's CM2 global coupled climate models. Part I: Formulation and simulation characteristics, *J. Climate*, **19**, 643-674.
- Donner, L. J., C. J. Seman, B. J. Soden, R. S. Hemler, J. C. Warren, J. Strom, and K.-N. Liou, 1997: Large-scale ice clouds in the GFDL SKYHI general circulation model. *J. Geophys. Res.*, **102**, 21745-21768.
- Edwards, J. M. and A. Slingo, 1996: Studies with a flexible new radiation code. I: Choosing a configuration for a large-scale model. *Quart. J. Roy. Meteor. Soc.*, **122**, 689-719.
- Freidenreich, S.M., and V. Ramaswamy, 2005: Refinement of the Geophysical Fluid Dynamics Laboratory solar benchmark computations and an improved parameterization for climate models, *J. Geophys. Res.*, **110**, D17105, doi:10.1029/2004JD005471.
- Freidenreich, S.M., and V. Ramaswamy, 1999: A new multiple-band solar radiative parameterization for general circulation models, *J. Geophys. Res.*, **104**, 31,389-31,409.
- Fröhlich, C. and J. Lean, 2004: Solar radiative output and its variability: evidence and mechanisms, *The Astronomy and Astrophysics Rev*, doi:10.1007/s00159-004-0024-1.
- Fu, Q. and K.N. Liou, 1993: Parameterization of the radiative properties of cirrus clouds. *J. Atmos. Sci.*, **50**, 2008-2025.
- GFDL Global Atmospheric Model Development Team, 2004: The new GFDL global atmosphere and land model AM2/LM2: Evaluation with prescribed SST simulations. *J. Climate*, **17**, 4641-4673.
- Gupta, S. K., W. L. Darnell, and A. C. Wilber, 1992: A parameterization for longwave surface radiation from satellite data: Recent improvements. *J Appl. Met.*, **31**, 1361-1367.
- Haywood, J. M., V. Ramaswamy, and B. J. Soden, 1999: Tropospheric aerosol climate forcing in clear-sky satellite observations over the oceans. *Science*, **283**, 1299-1303.
- Held, I., R. S. Hemler and V. Ramaswamy, 1993: Radiative-convective equilibrium with explicit two-dimensional moist convection. *J. Atmos. Sci.*, **50**, 3909-3927.
- Horowitz, L. W., S. Walters, D. L. Mauzerall, L. K. Emmons, P. J. Rasch, C. Granier, X. X. Tie, J.-F. Lamarque, M. G. Schultz, G. S. Tyndall, J. J. Orlando, and G. P. Brasseur, 2003: A global simulation of tropospheric ozone and related tracers: Description and evaluation of MOZART, version 2. *J. Geophys. Res.*, **108**, 4784, doi:10.1029/2002JD002853.

- Lin, S.-J., 2004: A “vertically Lagrangian” finite-volume dynamical core for global models. *Mon. Weather Rev.*, **132**, 2293-2307.
- Milly, P. C. D., and A. B. Shmakin, 2002: Global modeling of land water and energy balances. Part I: The land dynamics (LaD) model. *J. Hydrometeor.*, **3**, 283-299.
- Olivier, J.G.J., A.F. Bouwman, C.W.M. Van der Maas, J.J.M. Berdowski, C. Veldt, J.P.J. Bloos, A.J.H. Visschedijk, P.Y.J. Zandveld, and J.L. Haverlag, Description of EDGAR Version 2.0: A set of global emission inventories of greenhouse gases and ozone depleting substances for all anthropogenic and most natural sources on a per country basis and on 1°x1° grid, National Institute of Public Health and the Environment (RIVM) report no. 771060 002 / TNO-MEP report no. R96/119, 1996
- Ramachandran, S., V. Ramaswamy, G. L. Stenchikov, and A. Robock, 2000: Radiative impact of the Mount Pinatubo volcanic eruption: Lower stratospheric response. *J. Geophys. Res.*, **105**, 24409-24429.
- Ramaswamy, V., and M. M. Bowen, 1994: Effect of changes in radiatively active species upon the lower stratospheric temperatures. *J. Geophys. Res.*, **99**, 18909-18921.
- Randel, W.J., and F. Wu, 1999: A stratospheric ozone trends data set for global modeling studies, *Geophys. Res. Lett.*, **26**, 3089-3092.
- Rothman, L.S. and 30 co-authors, 2003: The HITRAN molecular spectroscopic database: edition of 2000 including updates through 2001. *J. Quant. Spectr. Rad. Transfer*, **82**, 5-44.
- Rotstayn, L. D., 1997: A physically based scheme for the treatment of stratiform clouds and precipitation in large-scale models. I: Description and evaluation of microphysical processes. *Quart. J. Roy. Meteor. Soc.*, **123**, 1227-1282.
- Rotstayn, L. D., B. F. Ryan, and J. Katzfey, 2000: A scheme for calculation of the liquid fraction in mixed-phase clouds in large-scale models. *Mon. Wea. Rev.*, **128**, 1070-1088.
- Schwarzkopf, M. D. and V. Ramaswamy, 1999: Radiative effects of CH<sub>4</sub>, N<sub>2</sub>O, halocarbons and the foreign-broadened H<sub>2</sub>O continuum: A GCM experiment. *J. Geophys. Res.*, **104**, 9467-9488.
- Slingo, A., 1989: A GCM parameterization for the shortwave radiative properties of water clouds. *J. Atmos. Sci.*, **46**, 1419-1427.
- Taylor, J. P., J. M. Edwards, M. D. Glew, P. Hignett, and A. Slingo, 1996: Studies with a flexible new radiation code. Part II: Comparisons with aircraft short-wave observations. *Quart. J. Roy. Meteor. Soc.*, **122**, 839-861.
- Tiedtke, M., 1993: Representation of clouds in large-scale models. *Mon. Wea. Rev.*, **121**, 3040-3061.

## Appendix C3.3 for Chapter 3.3:

# Comparisons of TOA Earth Radiation Budget Datasets

T. Wong

*This appendix contains additional tables and figures for Chapter 3.3. Table C3.3.1-4 list the actual climatological mean values for each of the TOA variables and datasets for both the ERBE and CERES period. Figure C3.3.1-24 show the corresponding regional and regional difference map.*

**Table C3.3.1:** Global average climatology (February 1985 to January 1989) from each of the seven datasets

	LW	SW	Net	SWdn	CLW	CSW	Cnet
ERBE Scanners	235.2	101.2	4.9	341.3	264.9	53.6	22.8
GEWEX SRB	240.0	102.4	-0.6	341.8	268.4	55.4	18.1
ISCCP FD	233.3	105.9	2.6	341.8	259.5	55.5	26.8
UMD SW & HIRS OLR	237.7	99.5	2.6	339.9	---	---	---

**Table C3.3.2:** Same as Table 1; but for tropical mean (20°N to 20°S) climatology.

	LW	SW	Net	SWdn	CLW	CSW	Cnet
ERBE Scanners	252.8	96.7	59.9	409.4	288.3	50.5	70.6
GEWEX SRB	258.9	100.8	50.2	410.0	290.6	55.3	64.1
ISCCP FD	250.1	102.8	57.1	410.0	281.7	49.8	78.5
UMD SW & HIRS OLR	255.8	95.7	56.1	407.6	---	---	---

**Table C3.3.3:** Global average climatology (March 2000 to February 2004) from each of the six datasets

	LW	SW	Net	SWdn	CLW	CSW	Cnet
CERES-EBAF	239.7	99.5	0.8	340.0	269.5	52.4	18.1
CERES SRBAVG-GEO	237.1	97.7	6.5	341.3	264.0	51.1	26.2
CERES SRBAVG-NonGEO	237.7	96.6	7.0	341.3	266.3	51.2	23.3
CERES ERBE-like	238.9	98.3	4.1	341.3	266.8	49.2	25.3
GEWEX SRB	240.5	101.8	-0.4	341.8	268.0	53.7	20.1
ISCCP FD	235.6	105.2	1.0	341.8	262.0	54.5	25.3

**Table C3.3.4:** Same as Table 2; but for tropical mean (20°N to 20°S) climatology.

	LW	SW	Net	SWdn	CLW	CSW	Cnet
CERES EBAF	256.6	94.5	56.9	408.1	290.6	48.0	69.4
CERES SRBAVG-GEO	254.0	92.8	62.6	409.4	286.3	45.7	77.2
CERES SRBAVG-NonGEO	255.0	91.0	63.4	409.4	288.5	45.7	74.3
CERES ERBE-like	256.2	91.1	62.1	409.4	288.5	46.3	74.7
GEWEX SRB	259.3	98.0	52.7	410.0	288.8	52.8	68.4
ISCCP FD	253.3	101.1	55.6	410.0	284.8	48.3	76.8

**All-sky Longwave Climatology, February 1985 to January 1989**

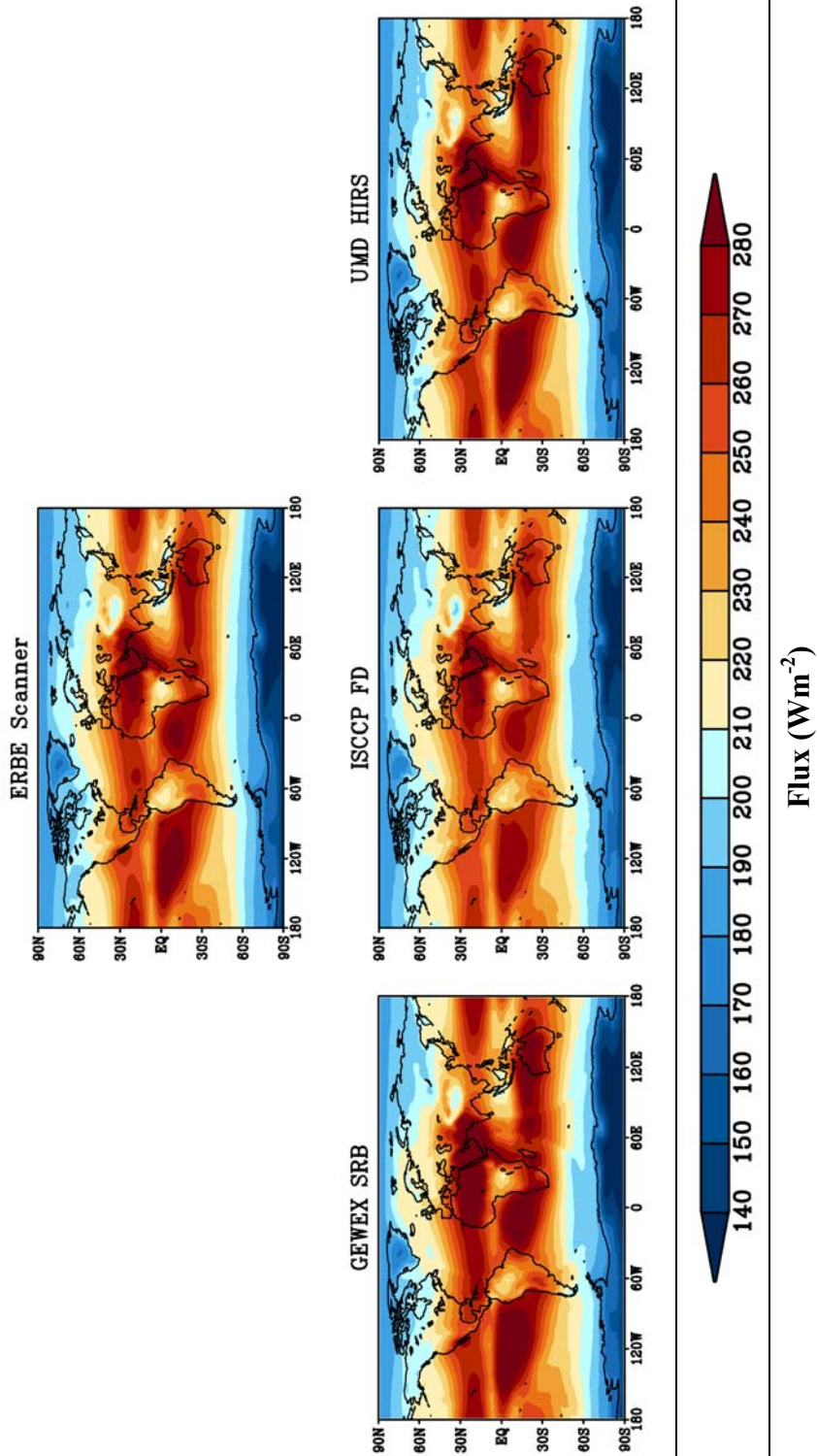


**Figure C3.3.1:** All-sky regional map of longwave flux for ERBE Scanner, GEWEX SRB, ISCCP FD, and UMD HIRS.

**All-sky Shortwave Climatology, February 1985 to January 1989**

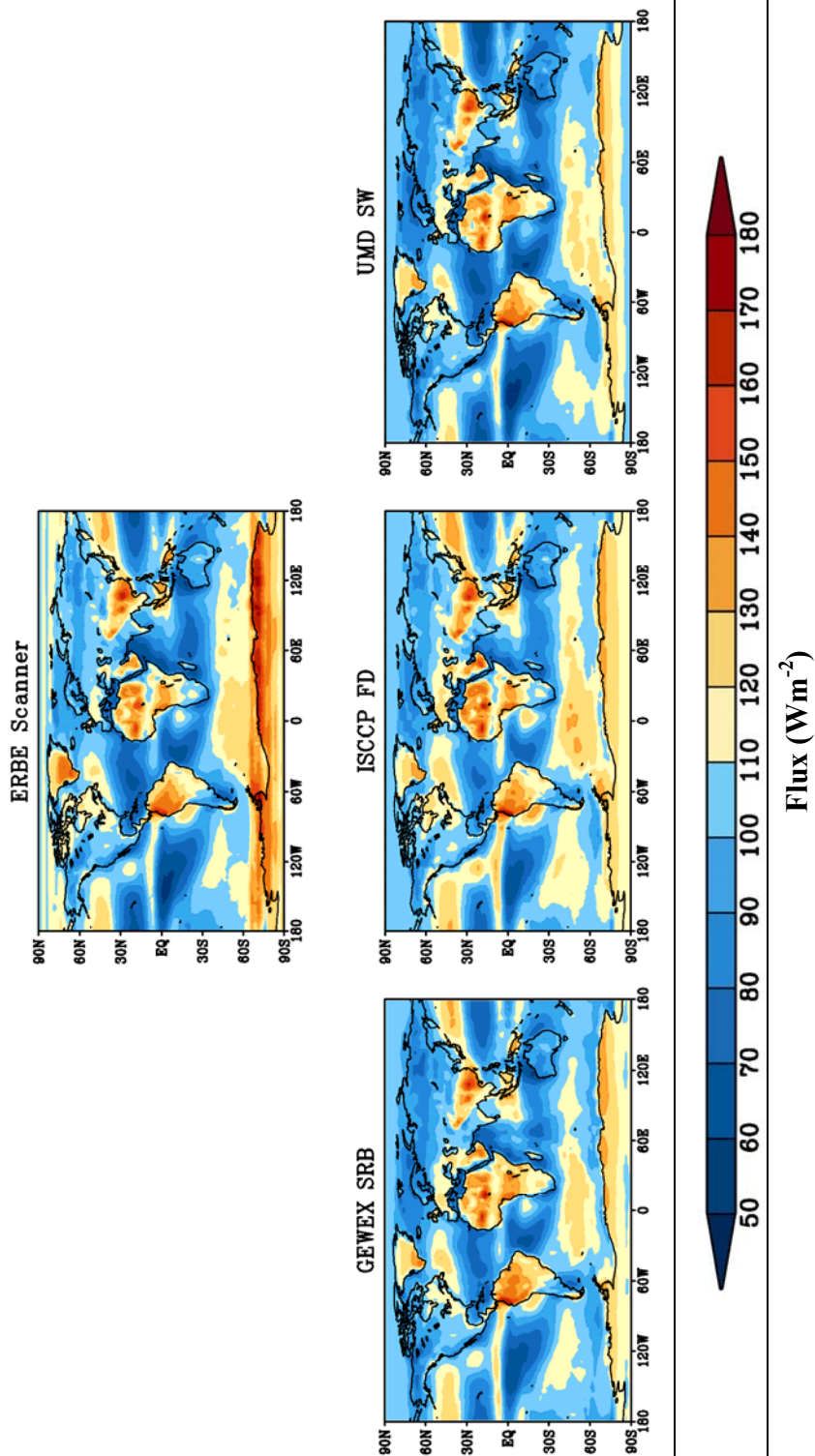


*Figure C3.3.2: All-sky regional map of shortwave flux for ERBE Scanner, GEWEX SRB, ISCCP FD, and UMD HIRS.*

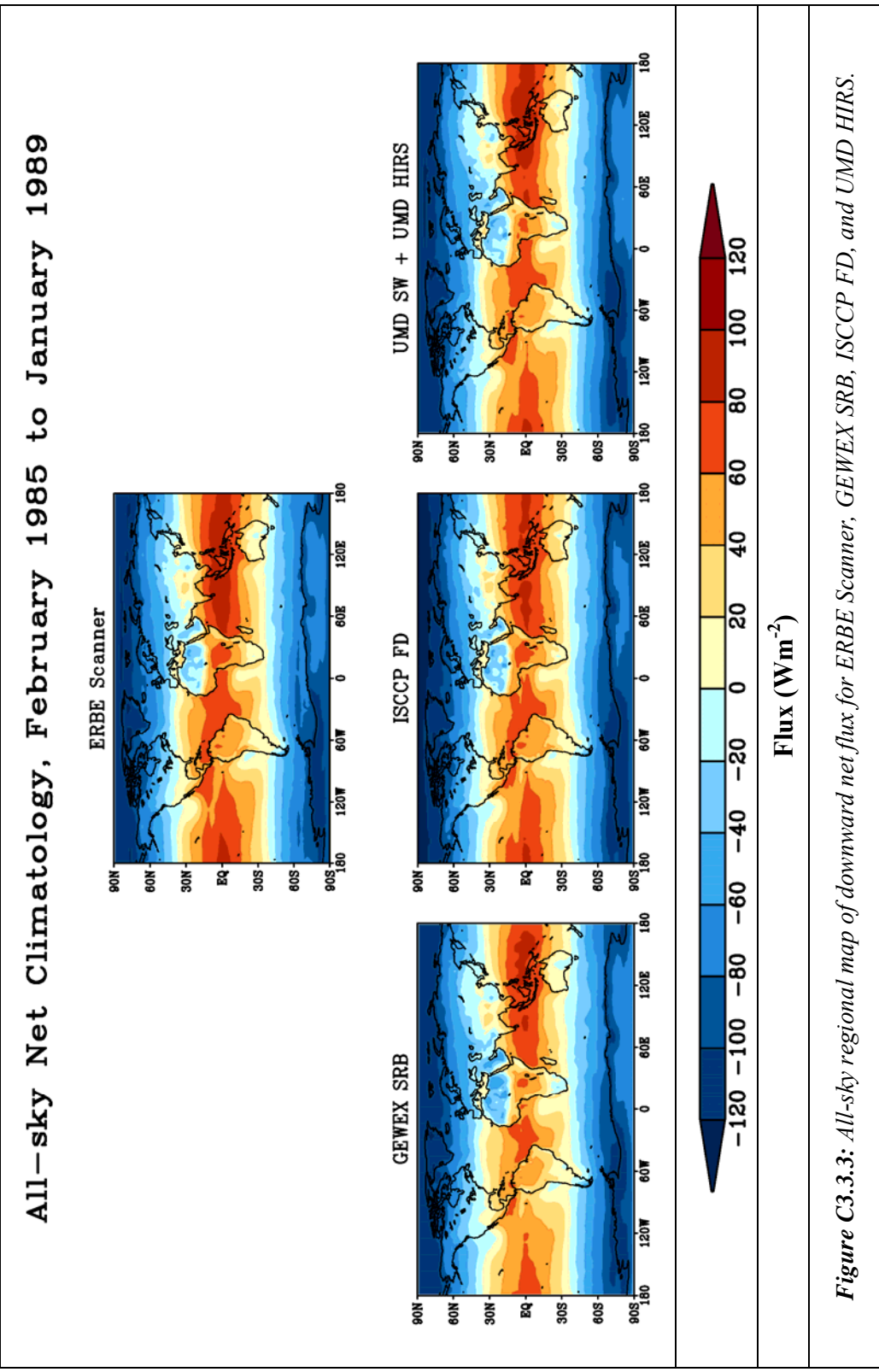


*Figure C3.3.3: All-sky regional map of downward net flux for ERBE Scanner, GEWEX SRB, ISCCP FD, and UMD HIRS.*

Clear-sky Longwave Climatology, February 1985 to January 1989

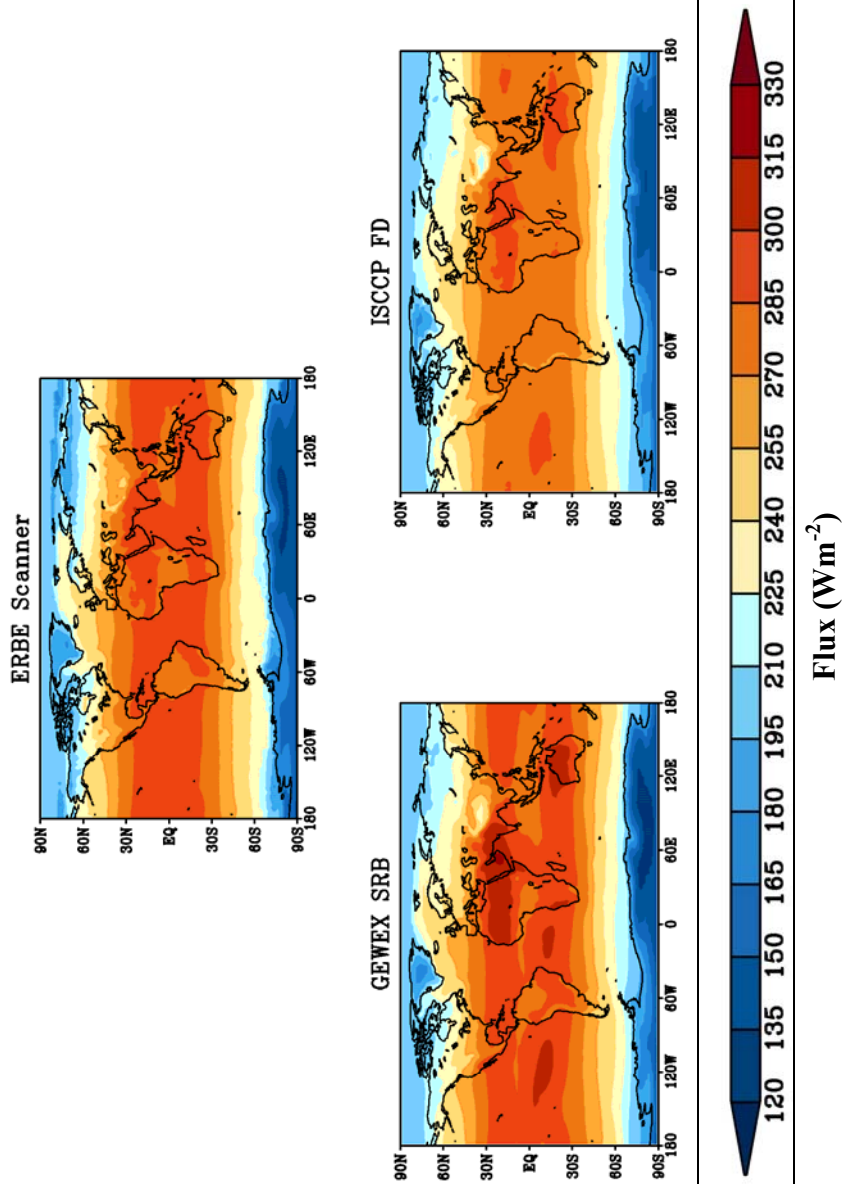


Figure C3.3.4: Clear-sky regional map of longwave flux for ERBE Scanner, GEWEX SRB, ISCCP FD, and UMD HIRS.

Clear-sky Shortwave Climatology, February 1985 to January 1989

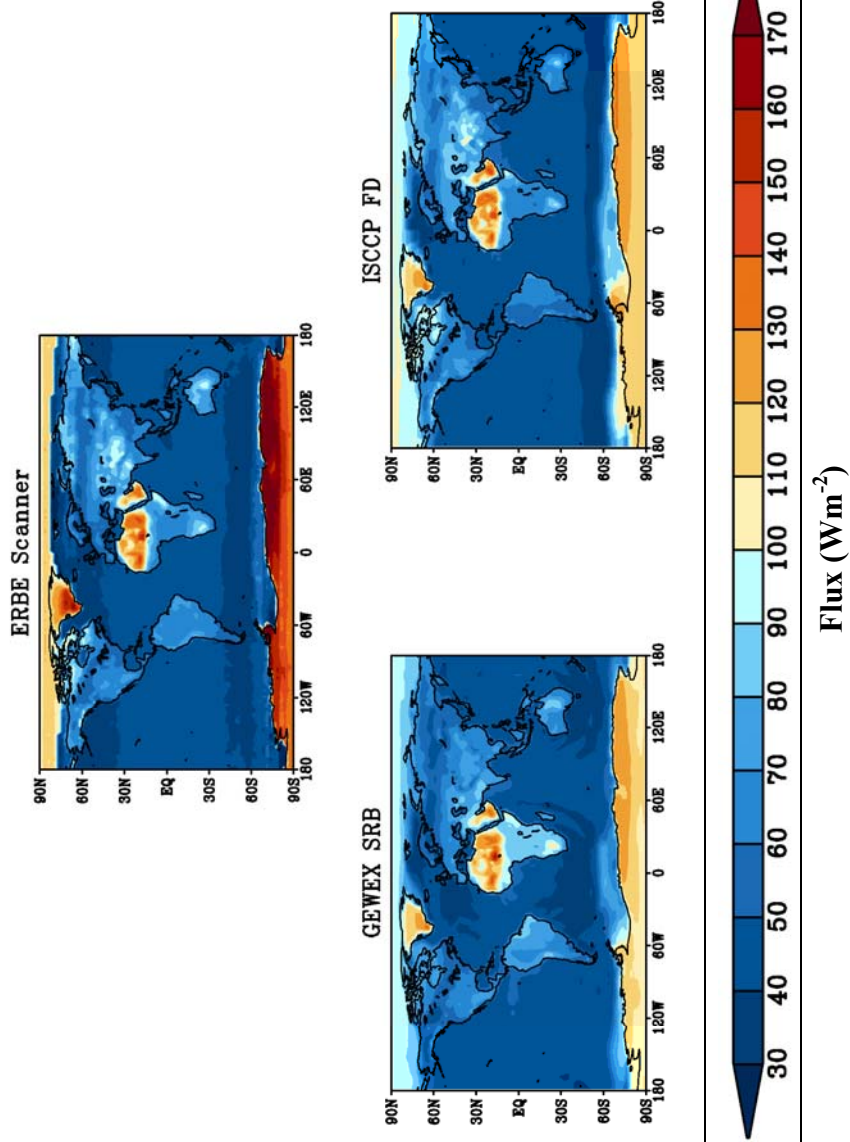
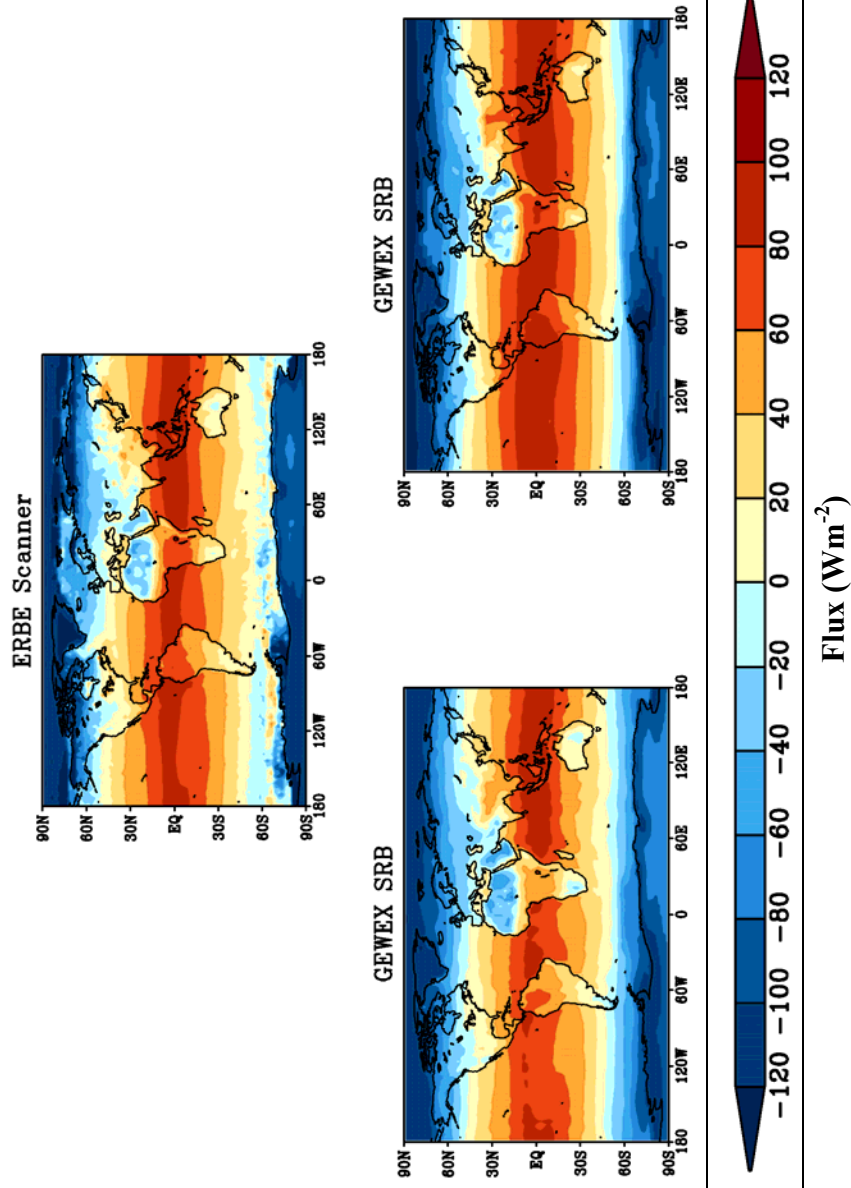
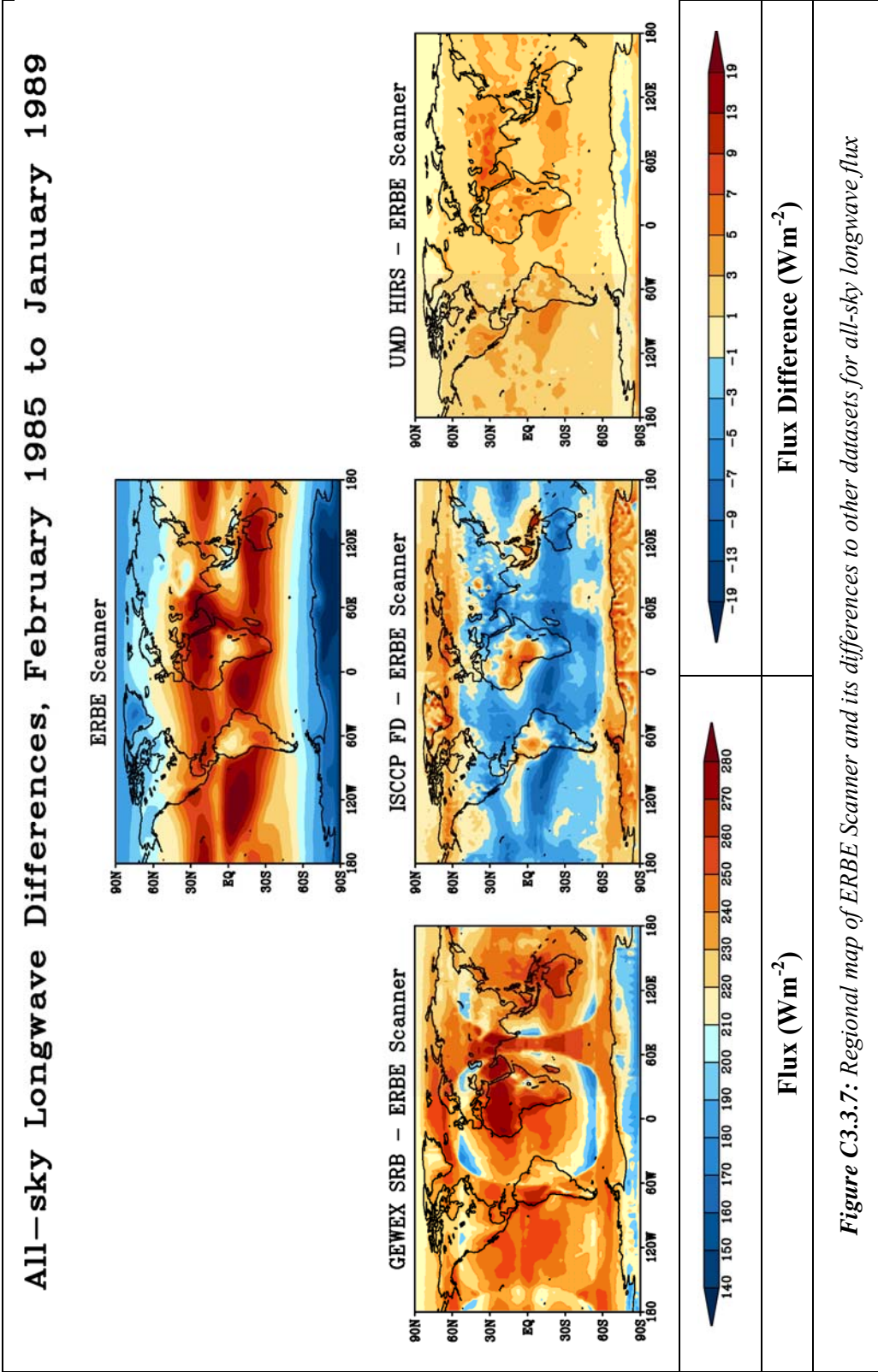


Figure C3.3.5: Clear-sky regional map of shortwave flux for ERBE Scanner, GEWEX SRB, ISCCP FD, and UMD HIRS.

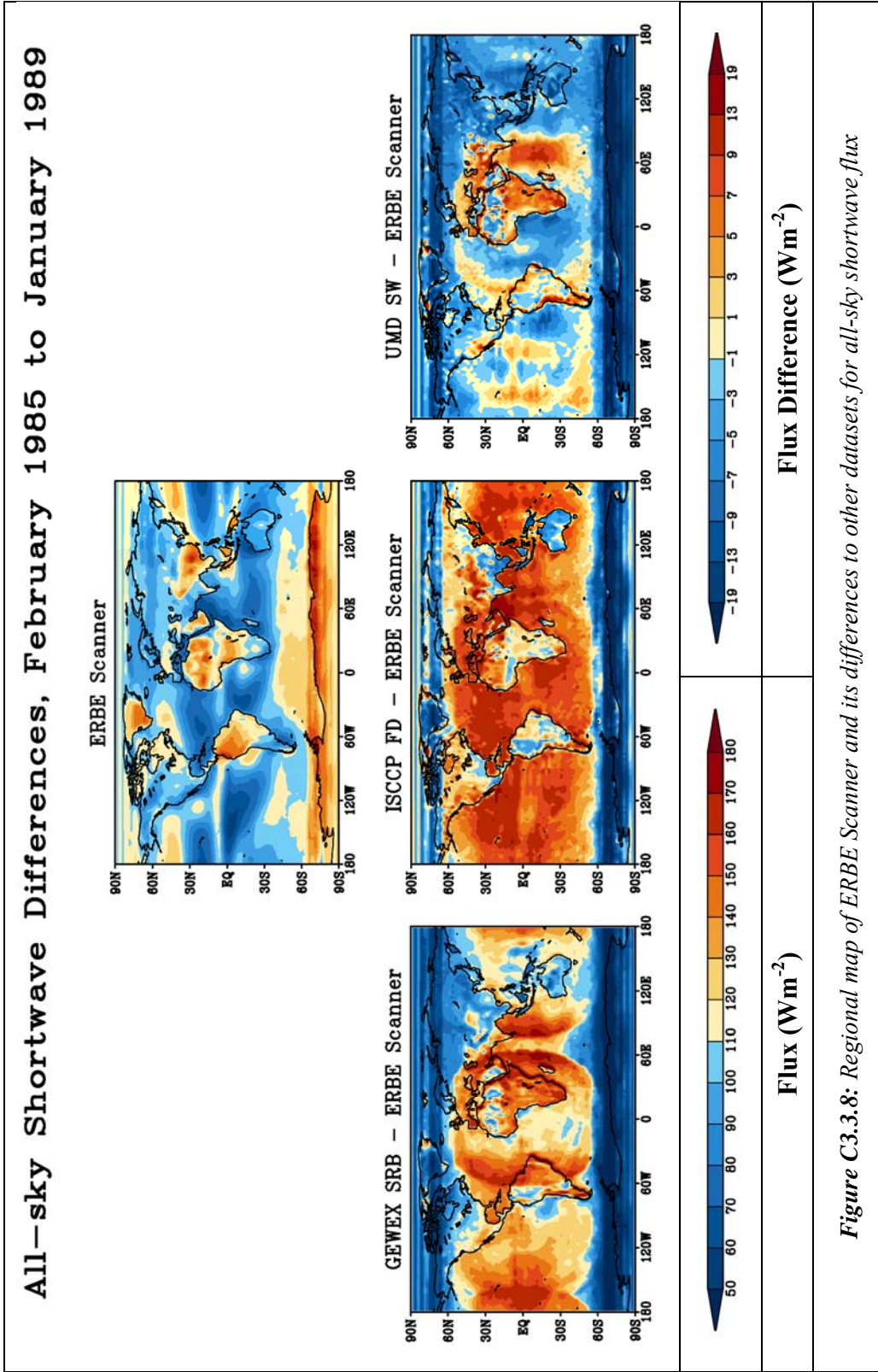
Clear-sky Net Climatology, February 1985 to January 1989



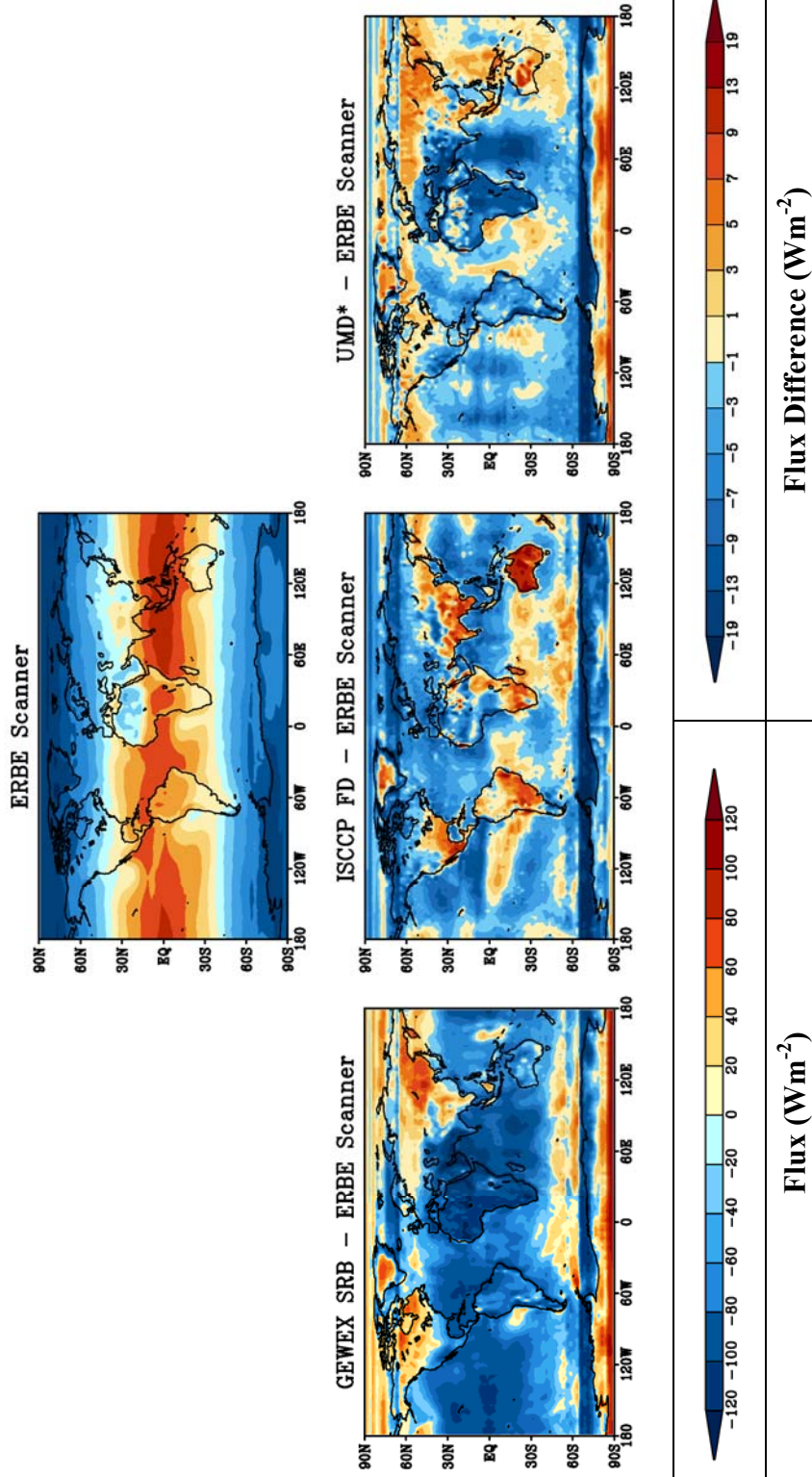
**Figure C3.3.6:** All-sky regional map of net downward flux for CERES EBAF, CERES ERBE-like, CERES SRBAVG-GEO, CERES SRBAVG-NonGEO, GEWEX SRB-LaRC, and ISCCP-FD.



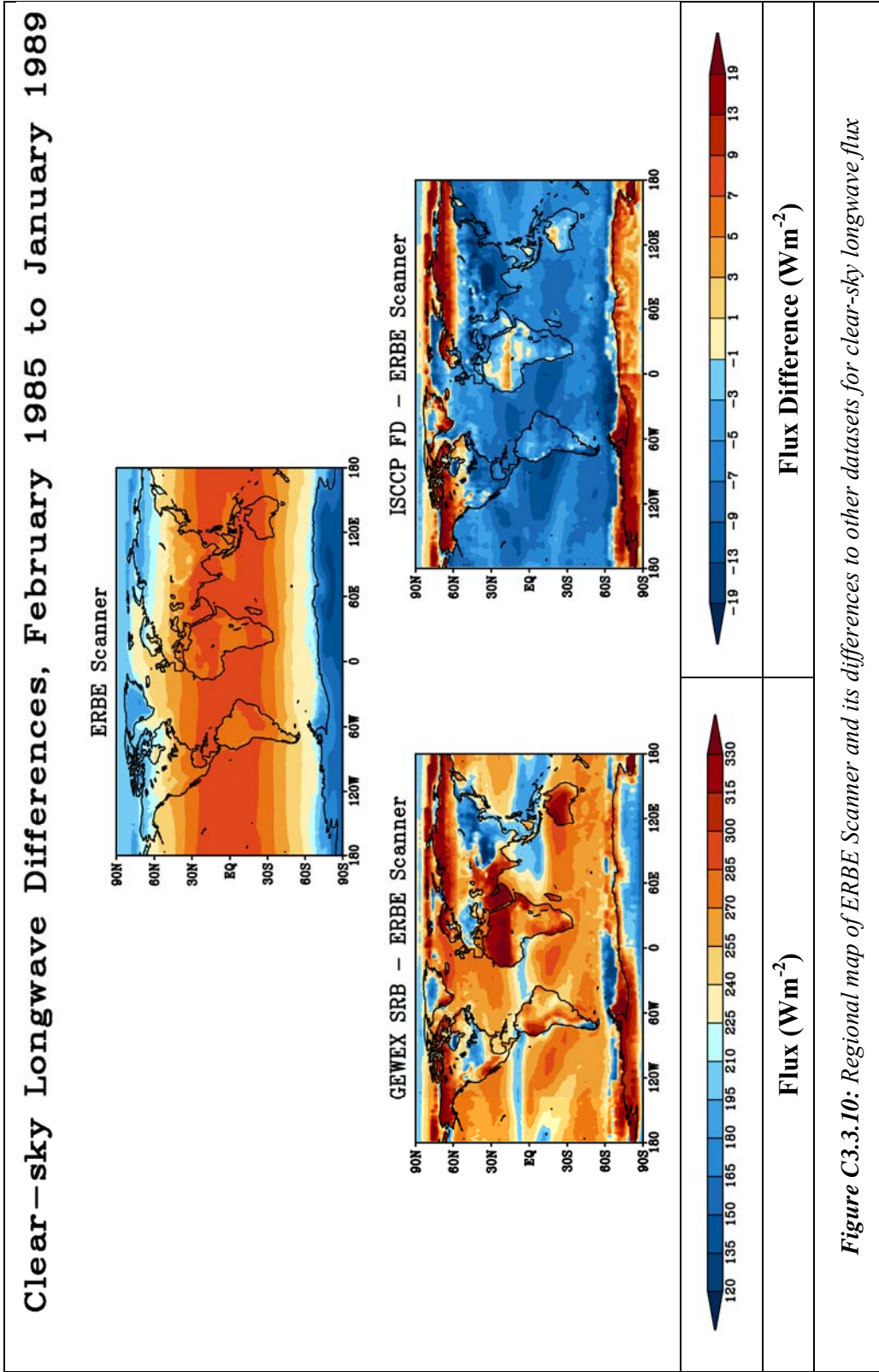
*Figure C3.3.7: Regional map of ERBE Scanner and its differences to other datasets for all-sky longwave flux*

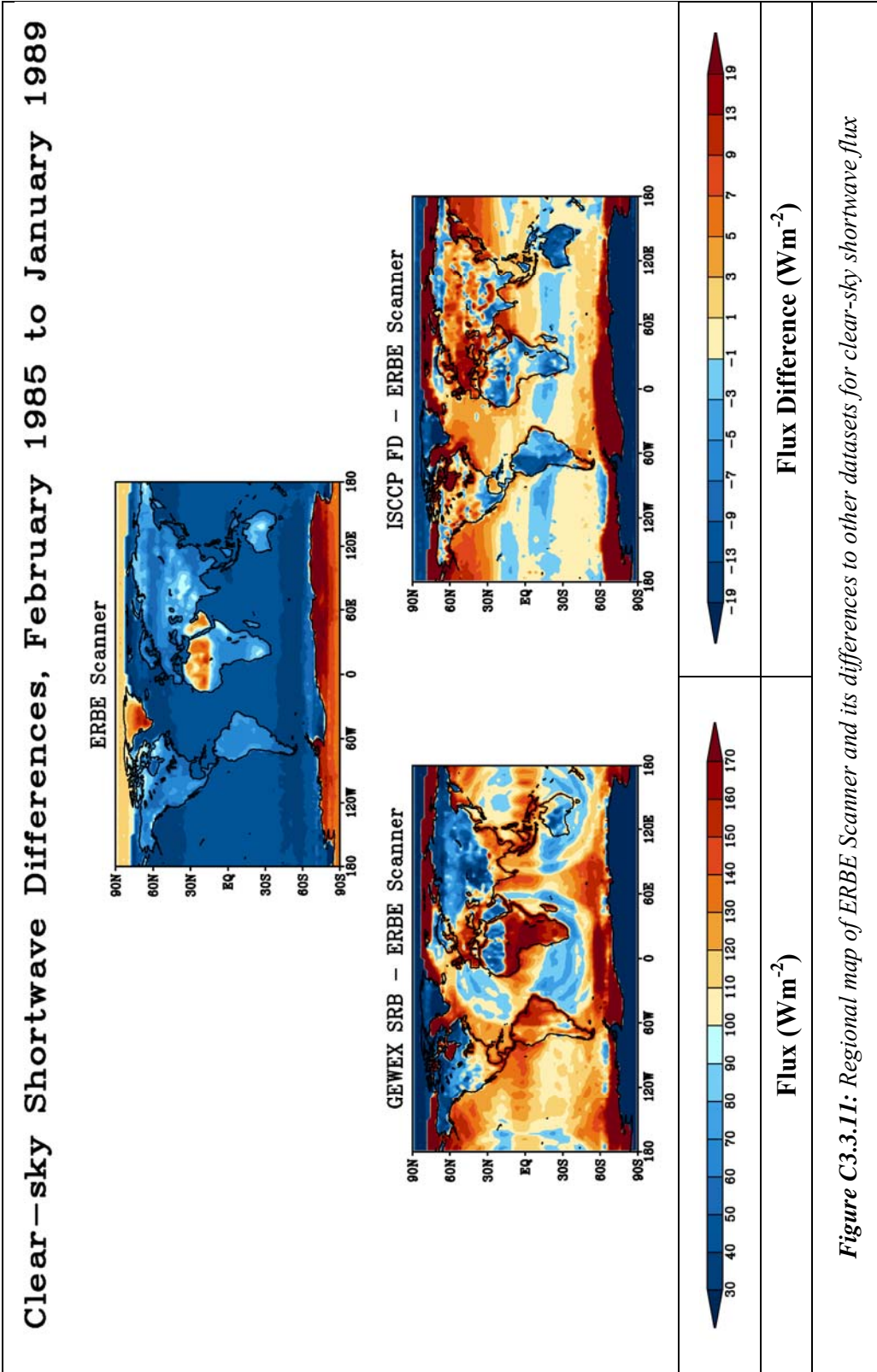


**All-sky Net Differences, February 1985 to January 1989**



*Figure C3.3.9: Regional map of ERBE Scanner and its differences to other datasets for all-sky net downward flux*





Clear-sky Net Differences, February 1985 to January 1989

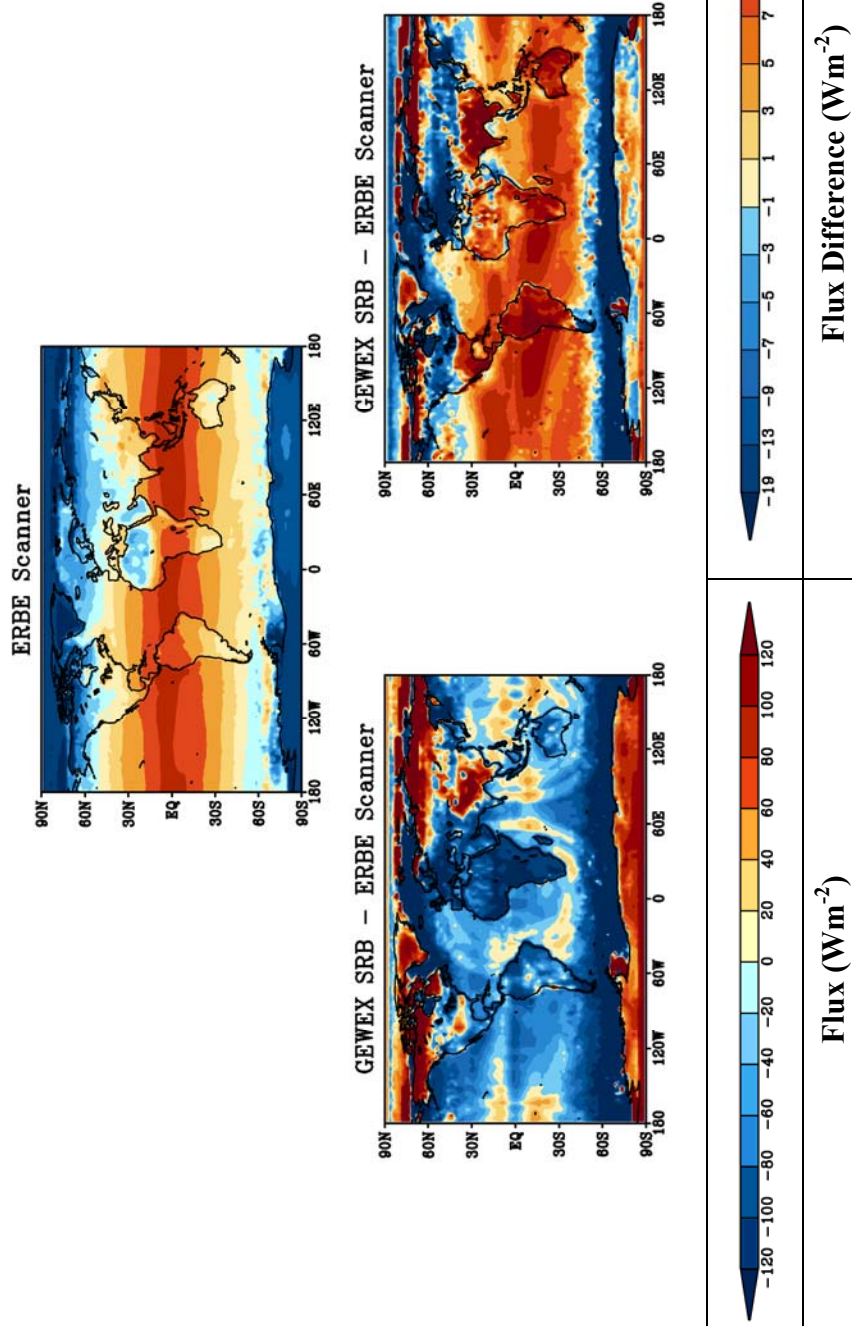
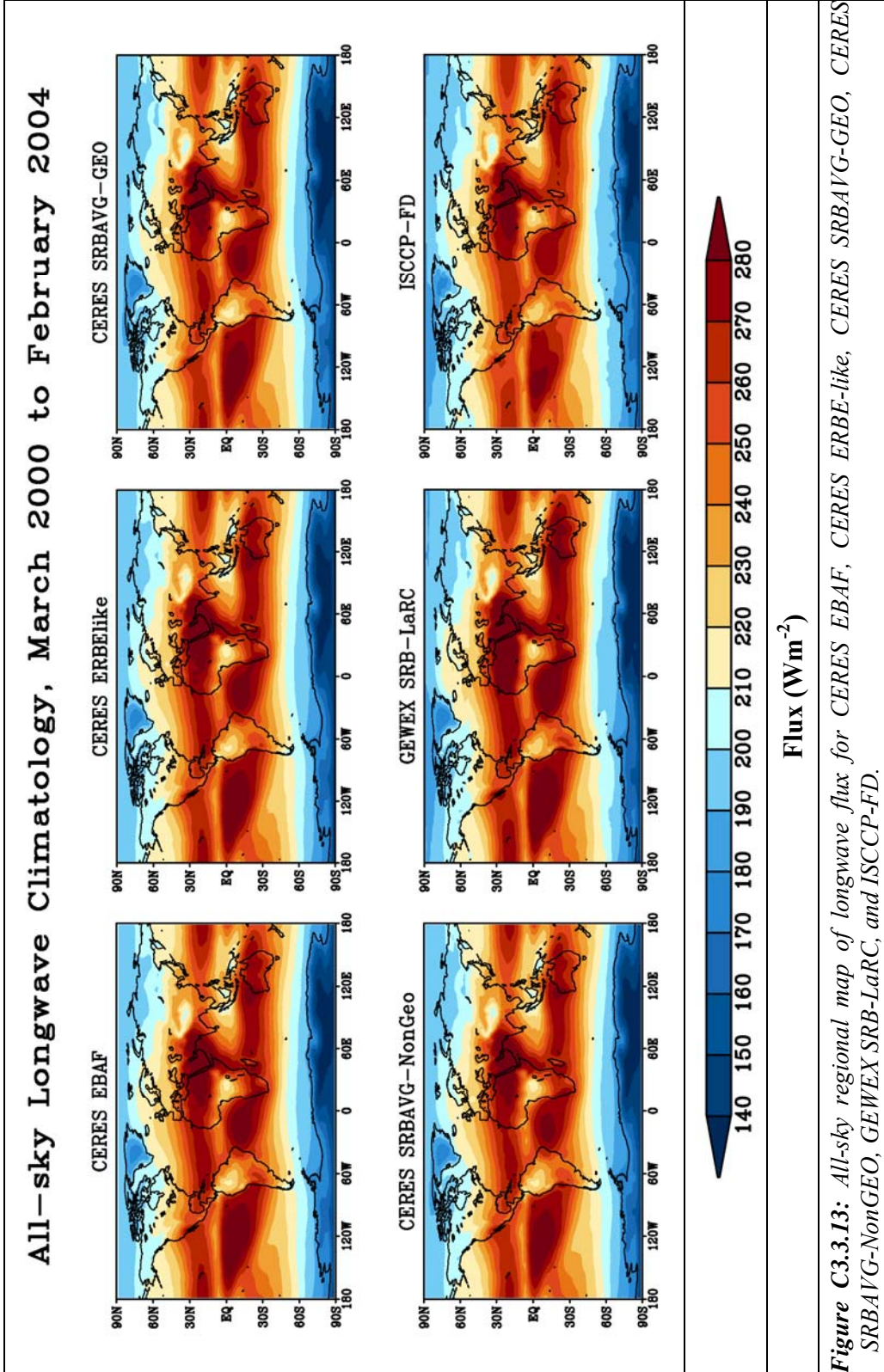
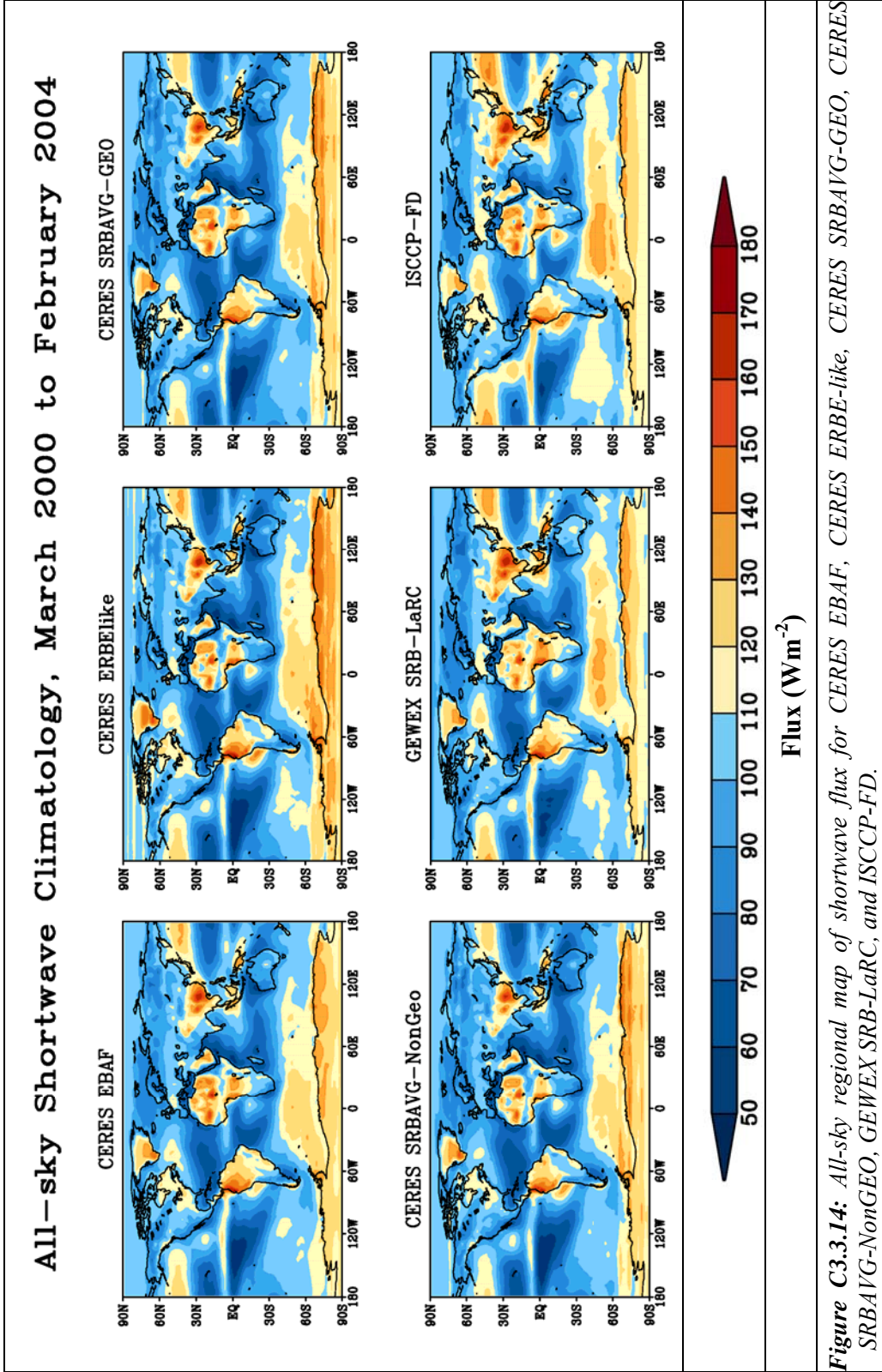


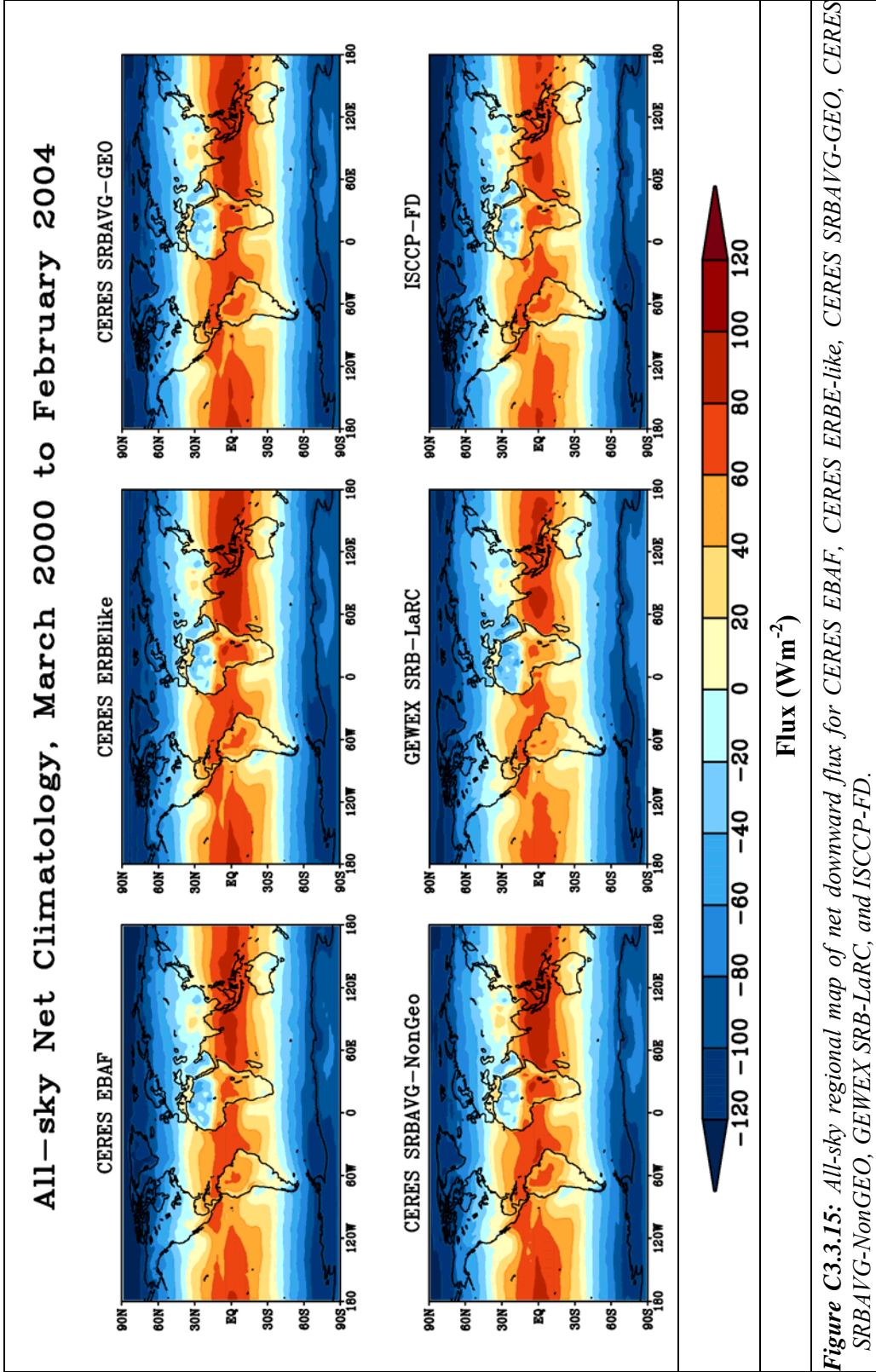
Figure C3.3.12: Regional map of ERBE Scanner and its differences to other datasets for clear-sky net downward flux



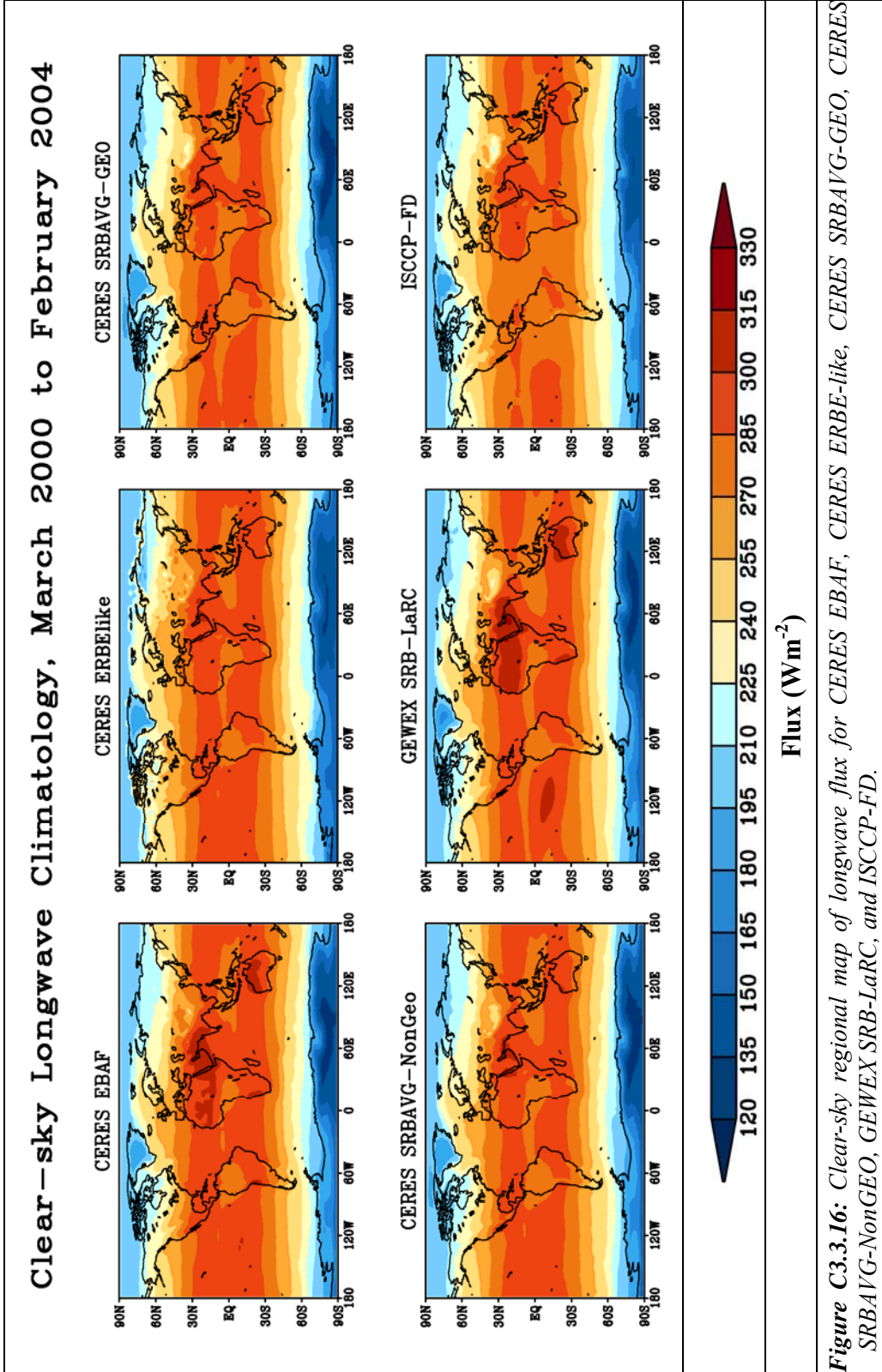
**Figure C3.3.13:** All-sky regional map of longwave flux for CERES EBAF, CERES SRBAVG-NonGeo, CERES ERBE-like, CERES SRBAVG-GEO, CERES SRBAVG-NonGeo, GEWEX SRB-LaRC, and ISCCP-FD.



**Figure C3.3.14:** All-sky regional map of shortwave flux for CERES EBAF, CERES ERBE-like, CERES SRBAVG-GEO, CERES SRBAVG-NonGeo, GEWEX SRB-LaRC, and ISCCP-FD.

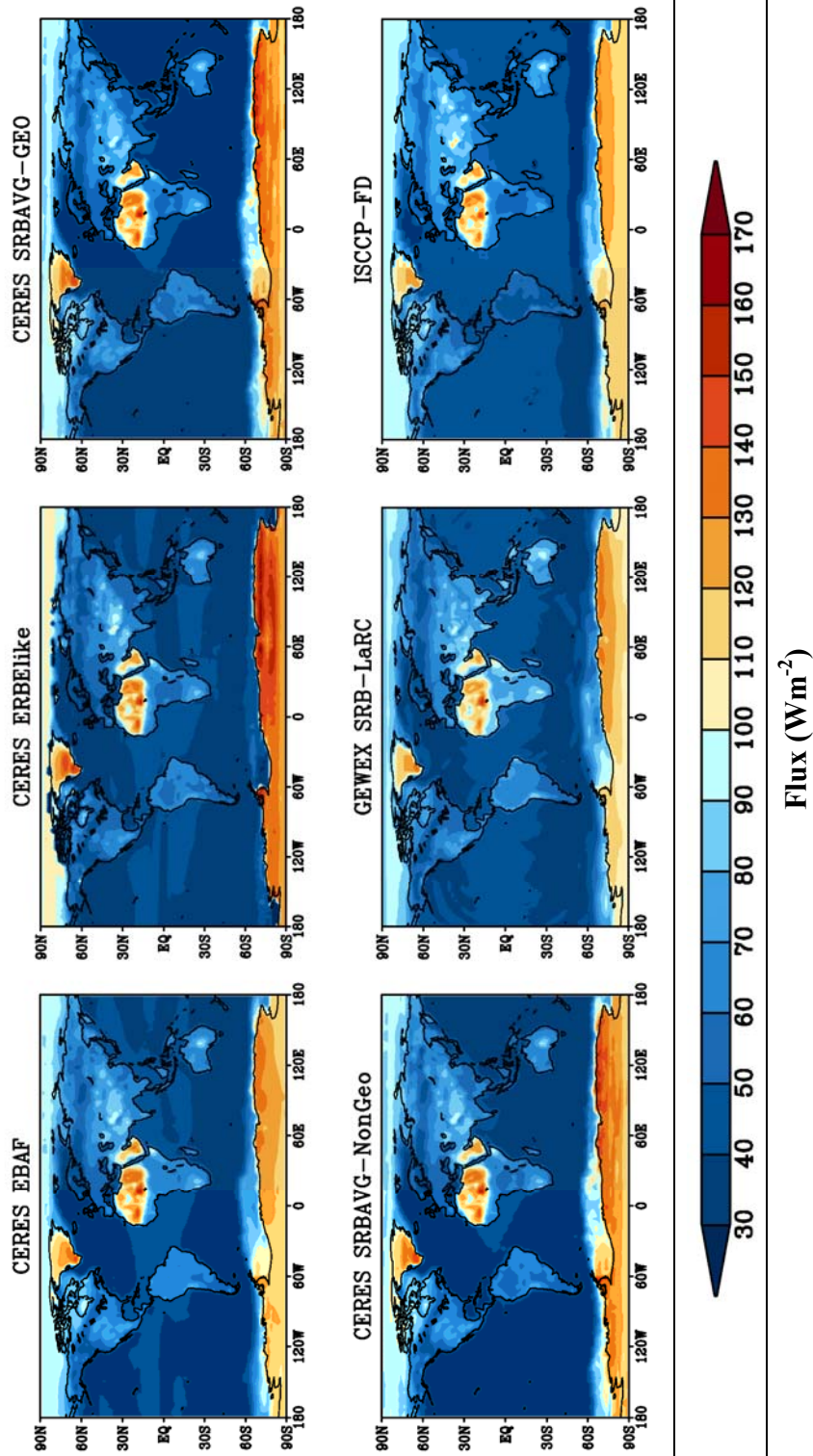


**Figure C3.3.15:** All-sky regional map of net downward flux for CERES EBAF, CERES ERBE-like, CERES SRBAVG-GEO, CERES SRBAVG-NonGeo, GEWEX SRB-LaRC, and ISCCP-FD.

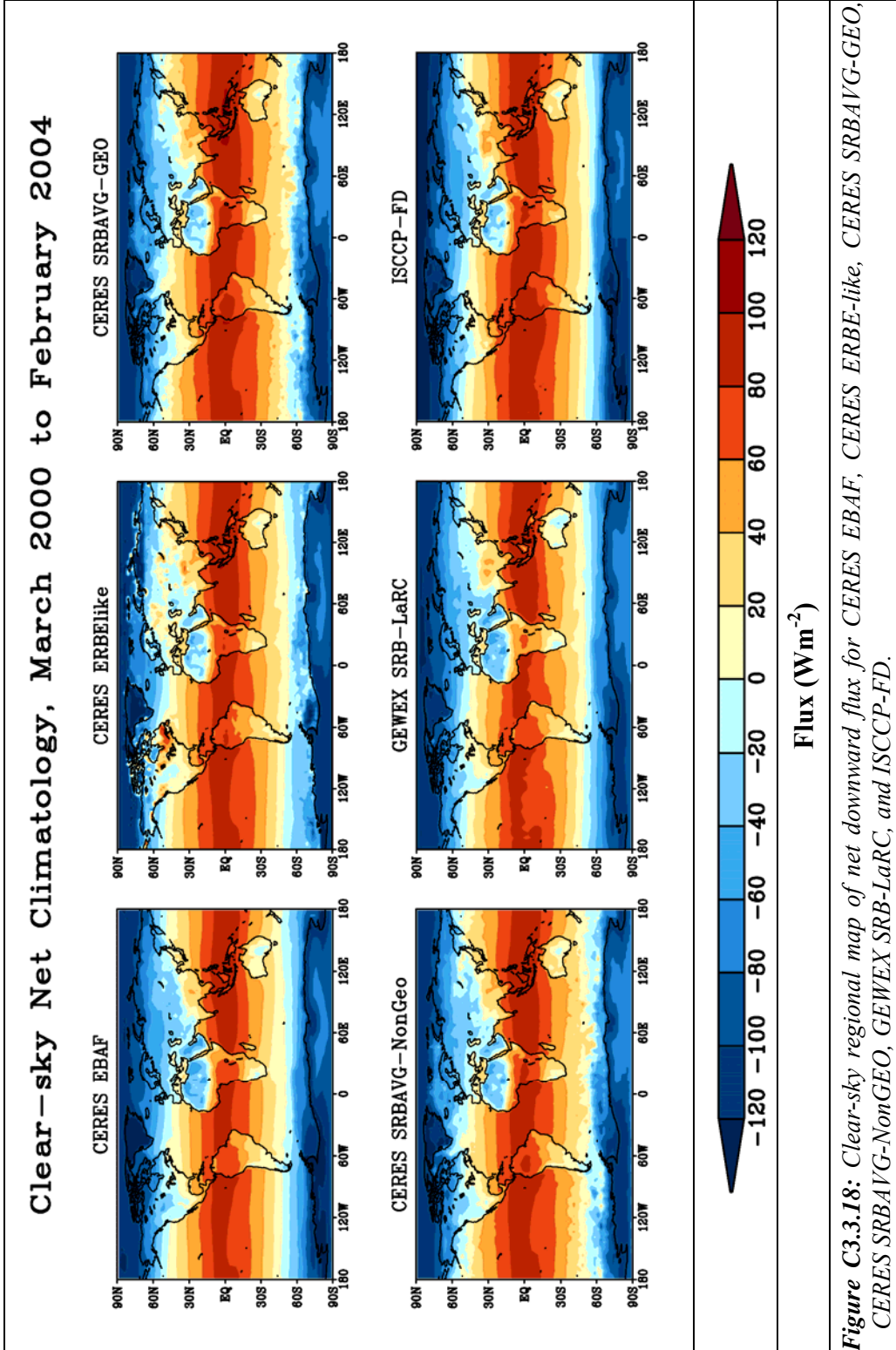


**Figure C3.3.16:** Clear-sky regional map of longwave flux for CERES EBAF, CERES ERBE-like, CERES SRBAVG-GEO, CERES SRBAVG-NonGeo, GEWEX SRB-LaRC, and ISCCP-FD.

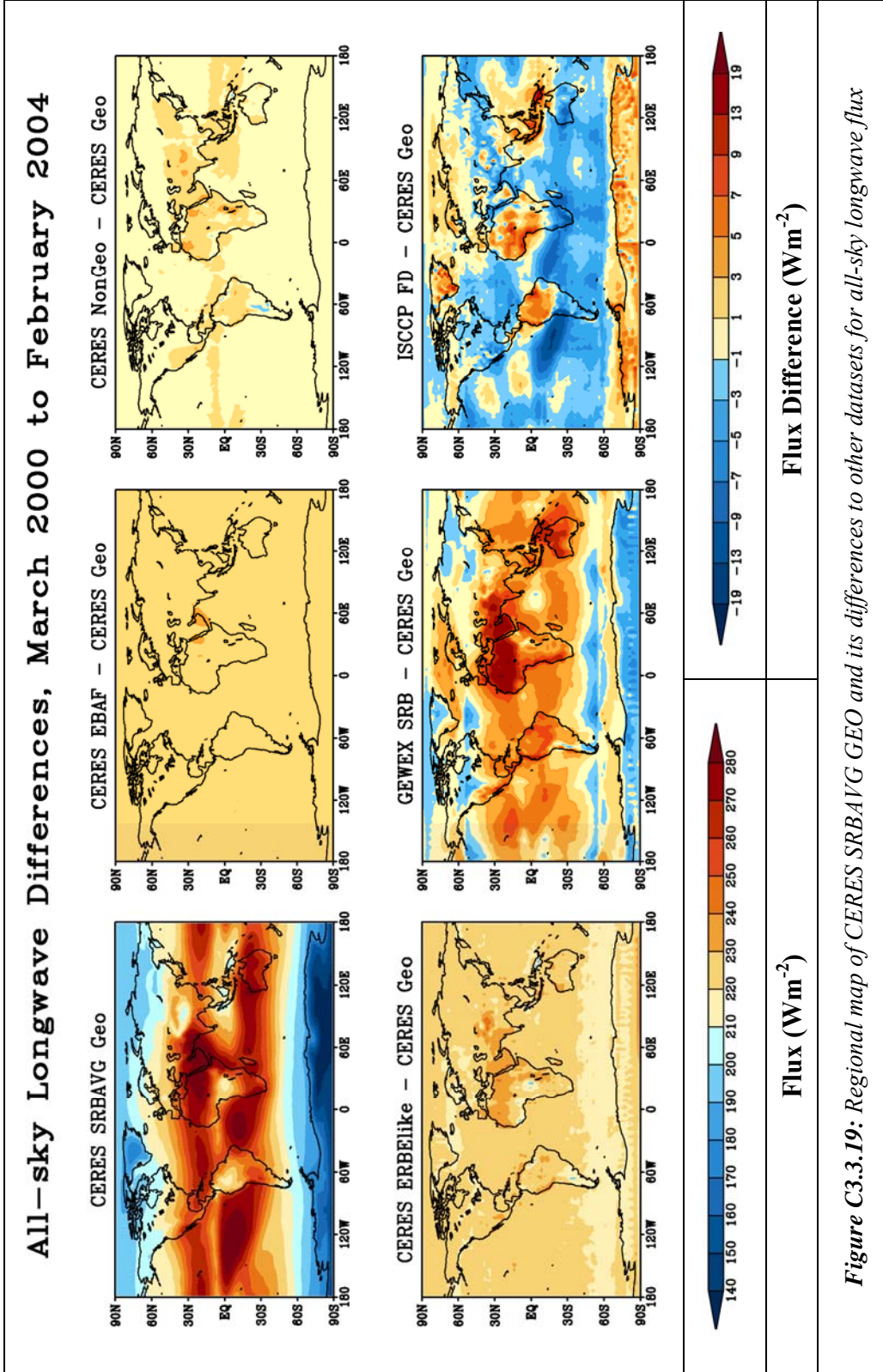
## Clear-sky Shortwave Climatology, March 2000 to February 2004

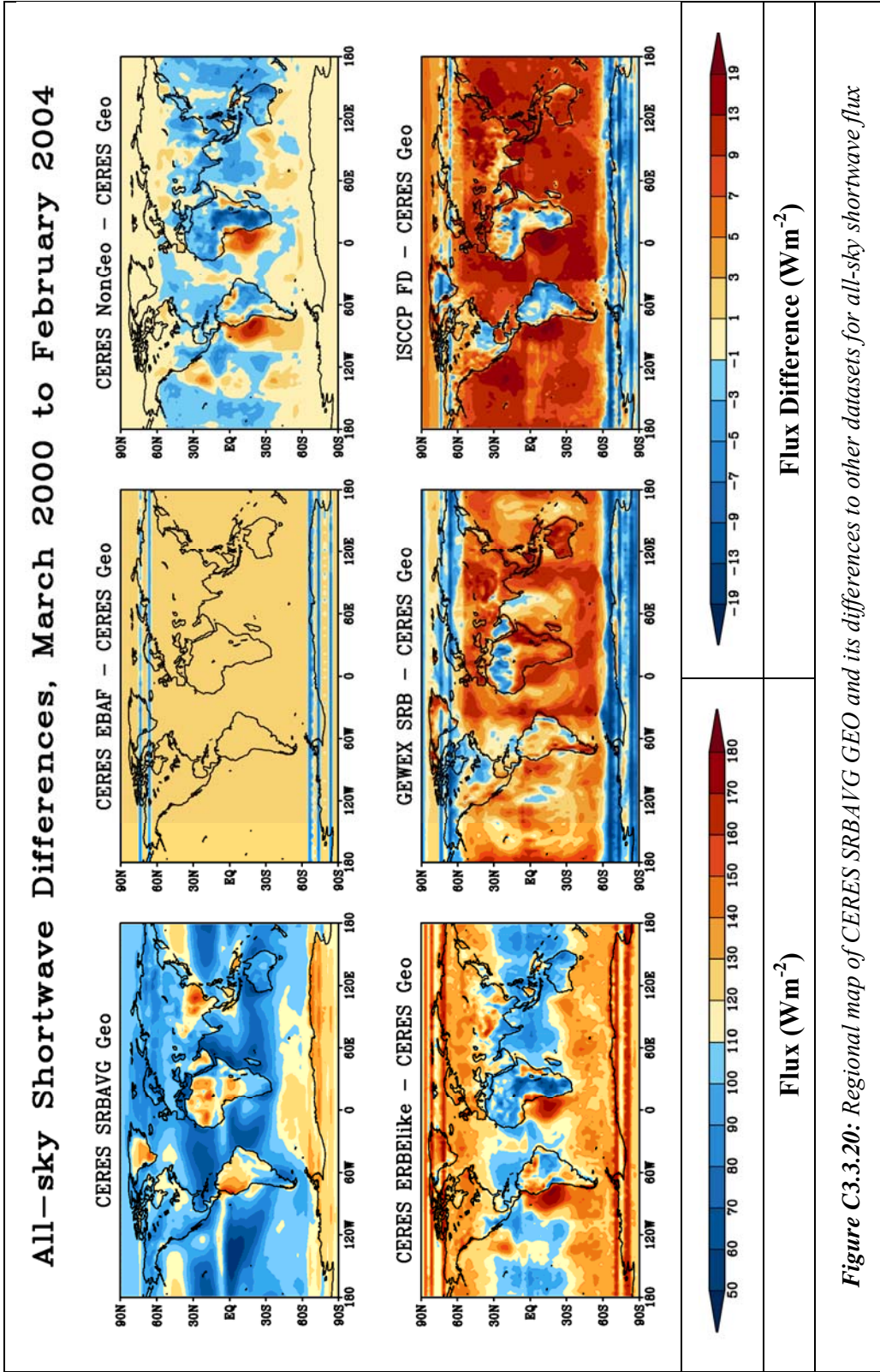


**Figure C3.3.17:** Clear-sky regional map of shortwave flux for CERES EBAF, CERES ERBE-like, CERES SRBAVG-GEO, CERES SRBAVG-NonGeo, GEWEX SRB-LaRC, and ISCCP-FD.

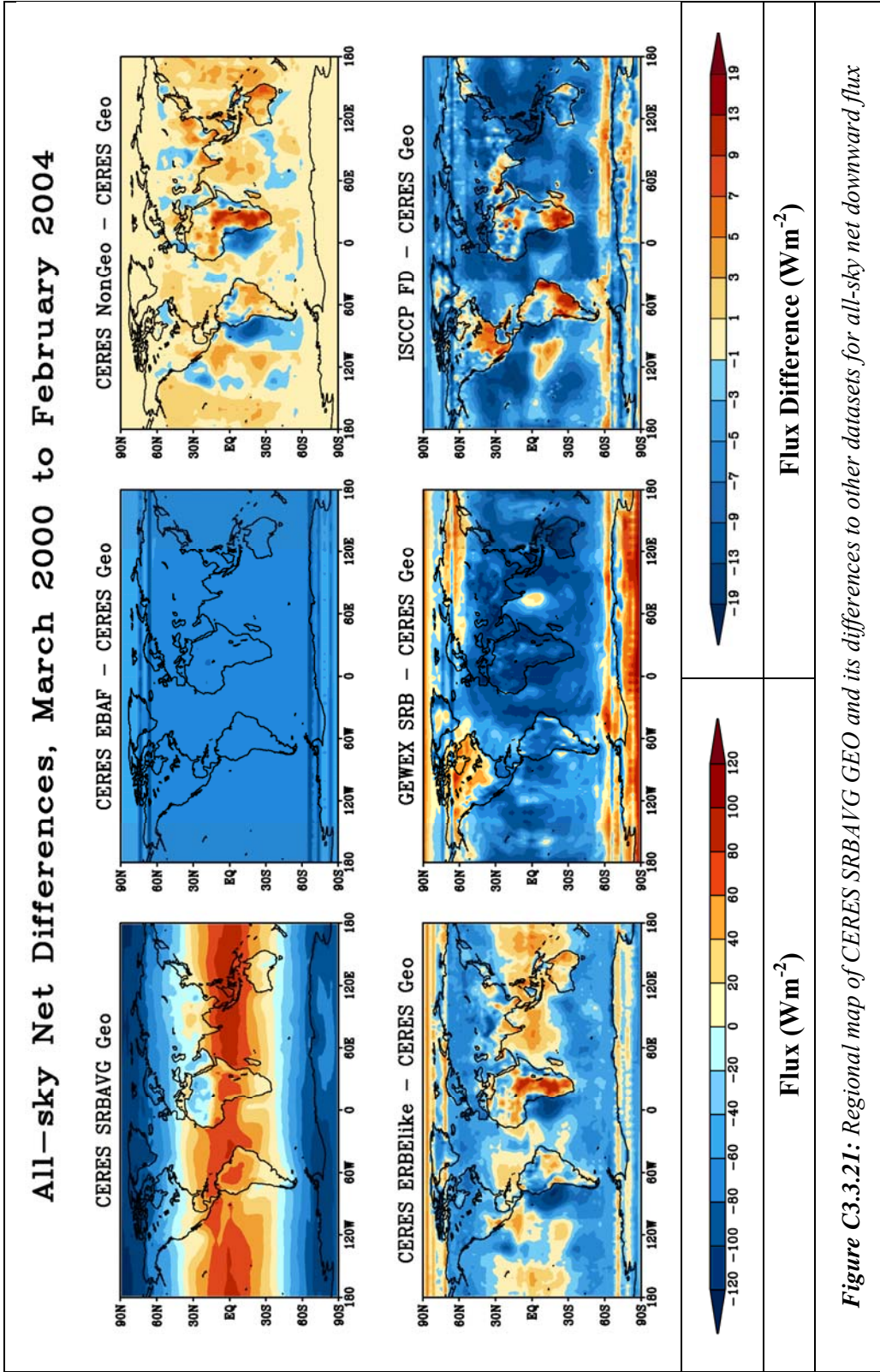


**Figure C3.3.18:** Clear-sky regional map of net downward flux for CERES EBAF, CERES ERBE-like, CERES SRBAVG-GEO, CERES SRBAVG-NonGeo, GEWEX SRB-LaRC, and ISCCP-FD.

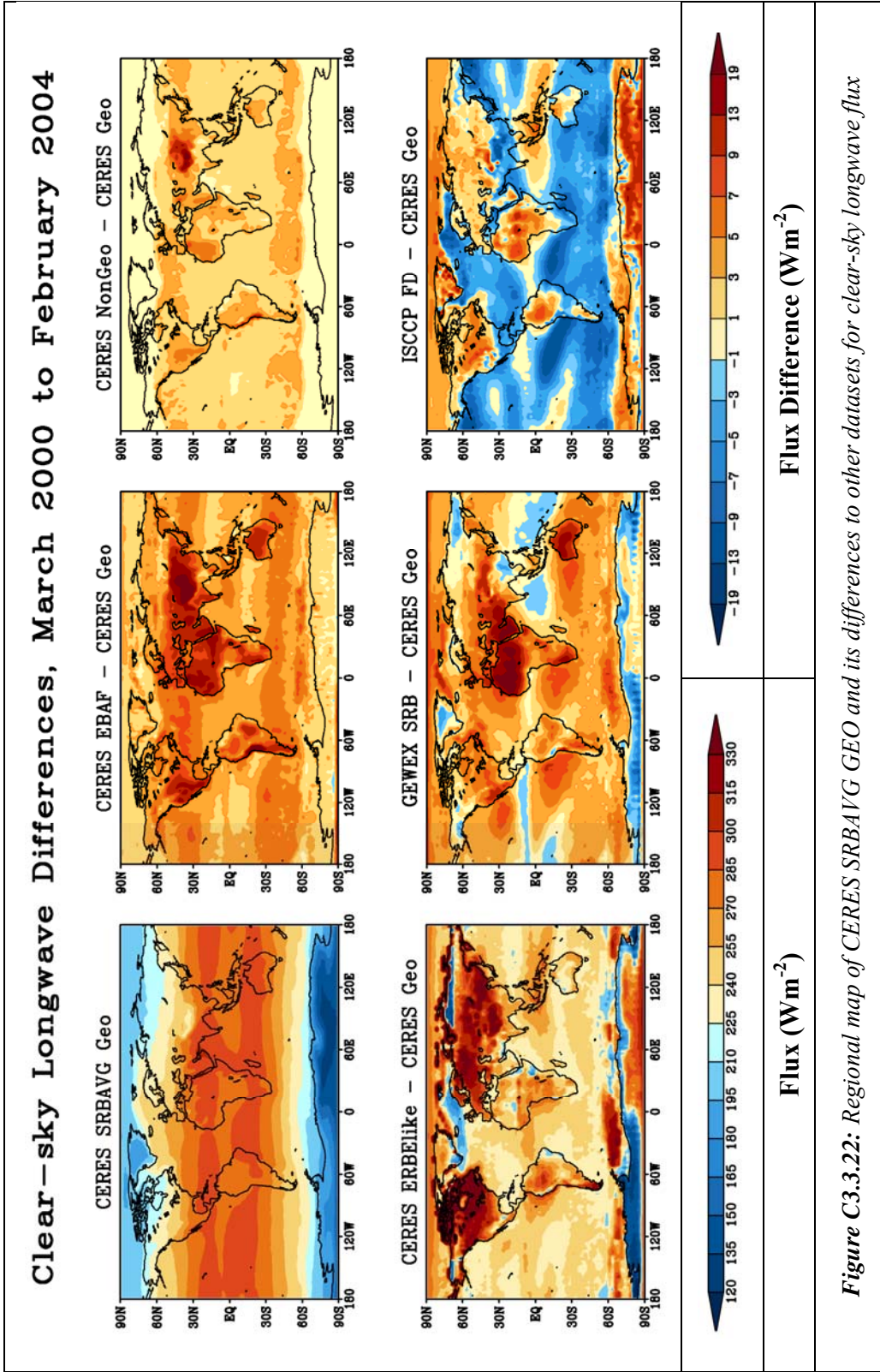




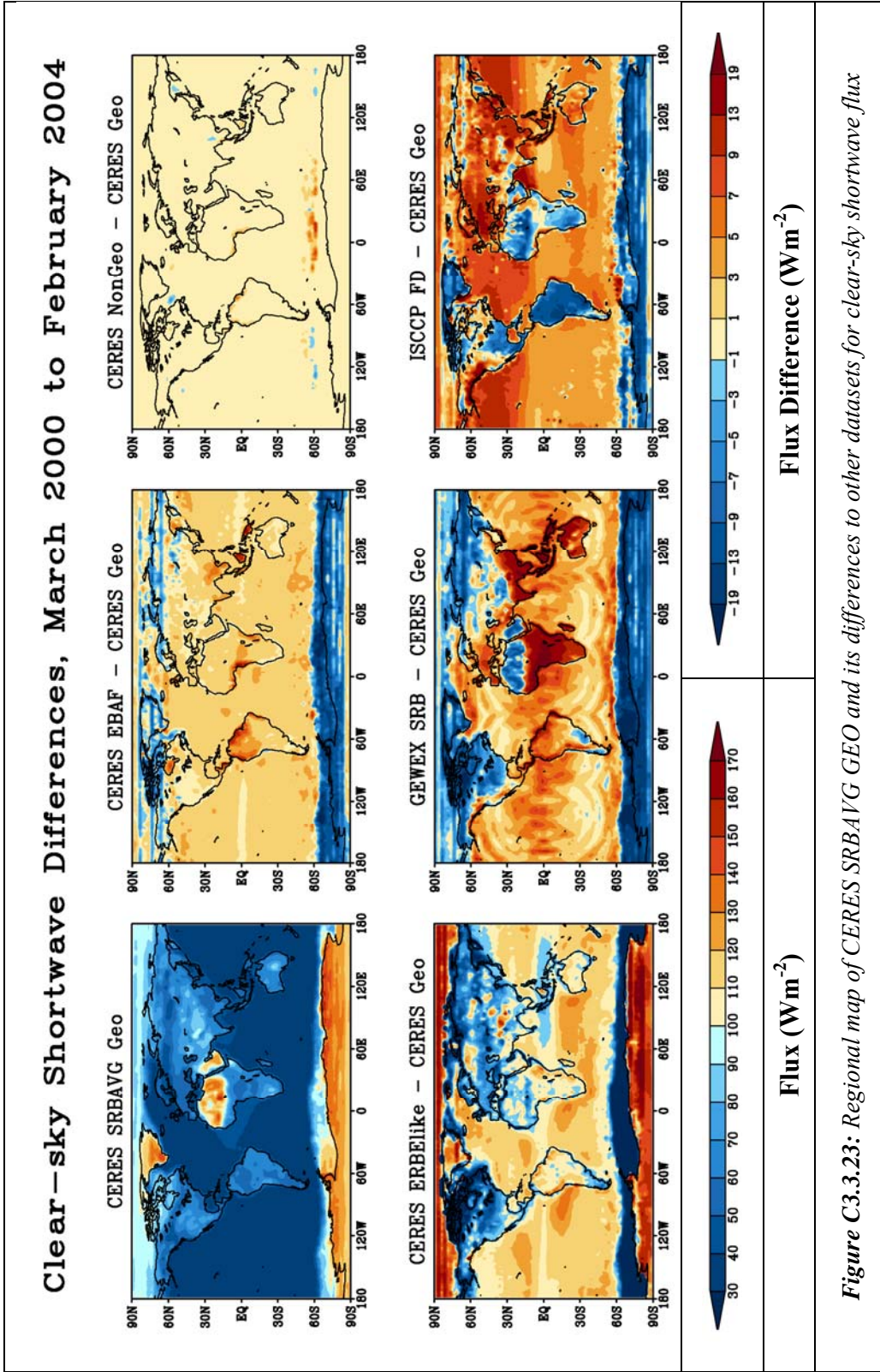
*Figure C3.3.20: Regional map of CERES SRBAVG GEO and its differences to other datasets for all-sky shortwave flux*



**Figure C3.3.21:** Regional map of CERES SRBAVG GEO and its differences to other datasets for all-sky net downward flux



*Figure C3.3.22: Regional map of CERES SRBAVG GEO and its differences to other datasets for clear-sky longwave flux*



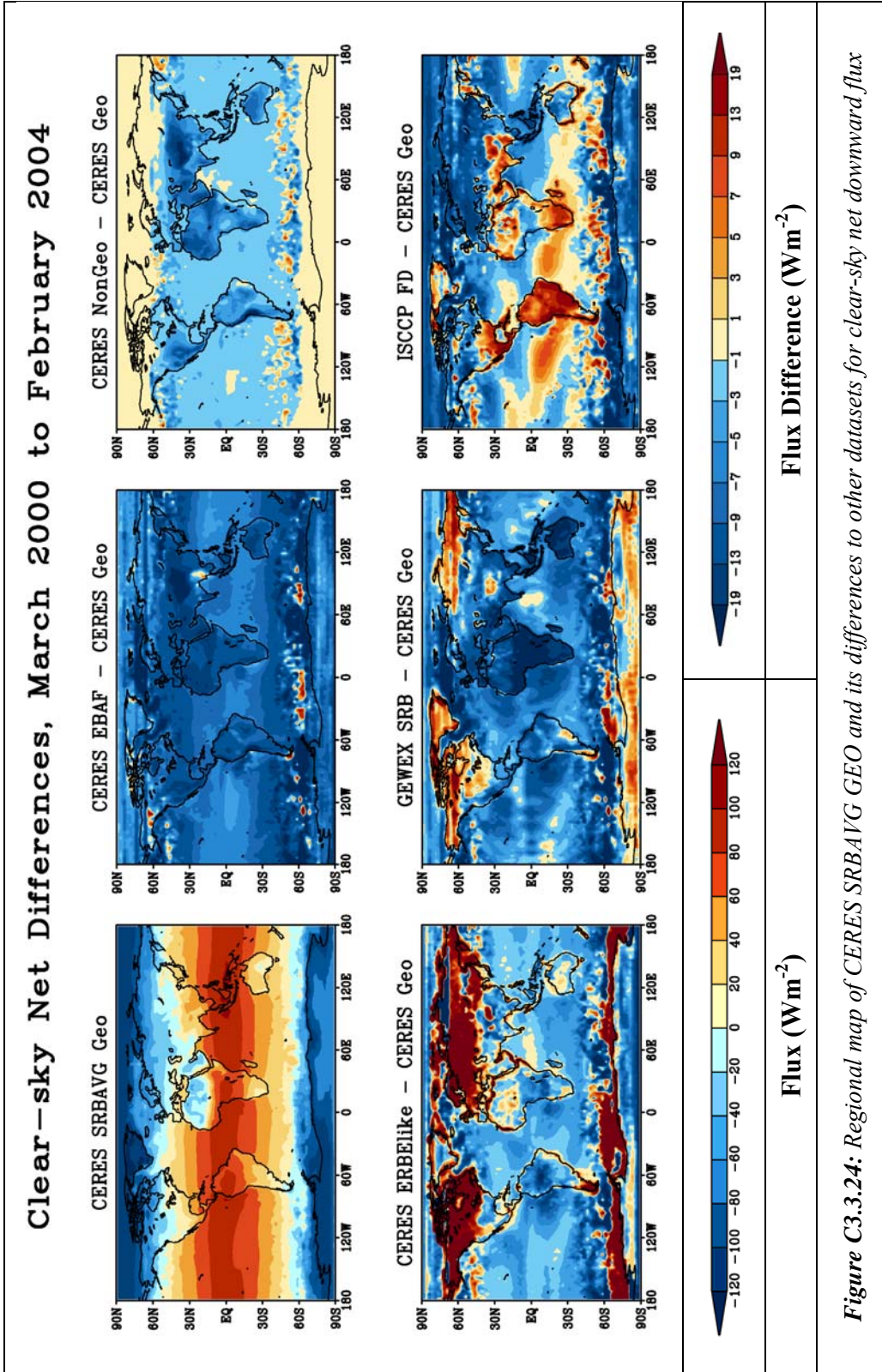


*Figure C3.3.24: Regional map of CERES SRBAVG GEO and its differences to other datasets for clear-sky net downward flux*

## Appendix C3.4 for Chapter 3.4

### Annual Cycle Variability of top-of-atmosphere (TOA) Radiative Fluxes Laura Hinkelman

This appendix contains complete sets of tables and figures from Chapter 3.4 on annual cycle variability of top-of-atmosphere radiative fluxes. The quantitative results for variability among the annual cycles from different satellite surface products are summarized in *Table C3.4.1 to C3.4.20*. The qualitative results of these comparisons are given in *Figure C3.4.1 to C3.4.8*.

**Table C3.4.1:** Global mean annual cycle data for ASWDN over all data sets, ERBE and CERES time periods. All values are for monthly mean anomalies from the overall annual average except for the overall monthly means listed in the first column. Relative standard deviations are computed with respect to the corresponding monthly mean. Annual means: ERBE period =  $341.2 \text{ Wm}^{-2}$ , CERES period =  $341.2 \text{ Wm}^{-2}$ .

Month	ERBE period						CERES period					
	Mean	Anom	St Dev	Rel StD	Range	N	Mean	Anom	St Dev	Rel StD	Range	N
1	352.5	11.2	0.0	0.0%	11.1, 11.2	5	352.4	11.2	0.1	0.0%	11.1, 11.4	8
2	349.7	8.4	0.1	0.0%	8.3, 8.5	5	349.6	8.4	0.1	0.0%	8.3, 8.6	8
3	344.8	3.4	0.1	0.0%	3.3, 3.6	5	344.6	3.4	0.1	0.0%	3.3, 3.6	8
4	338.9	-2.4	0.1	0.0%	-2.5, -2.3	5	338.7	-2.4	0.1	0.0%	-2.5, -2.3	8
5	333.9	-7.5	0.1	0.0%	-7.6, -7.4	5	333.6	-7.5	0.1	0.0%	-7.7, -7.4	8
6	330.8	-10.5	0.1	0.0%	-10.6, -10.4	5	330.6	-10.6	0.2	0.1%	-10.8, -10.4	8
7	330.4	-10.9	0.1	0.0%	-11.0, -10.8	5	330.2	-10.9	0.1	0.0%	-11.1, -10.8	8
8	332.9	-8.4	0.1	0.0%	-8.5, -8.3	5	332.7	-8.4	0.1	0.0%	-8.6, -8.3	8
9	337.6	-3.7	0.1	0.0%	-3.9, -3.6	5	337.4	-3.7	0.1	0.0%	-3.8, -3.6	8
10	343.4	2.1	0.1	0.0%	1.9, 2.2	5	343.3	2.1	0.1	0.0%	2.0, 2.2	8
11	348.8	7.5	0.1	0.0%	7.4, 7.6	5	348.7	7.5	0.1	0.0%	7.4, 7.7	8
12	352.1	10.8	0.1	0.0%	10.6, 10.9	5	352.1	10.9	0.2	0.1%	10.6, 11.1	8

**Table C3.4.2:** Global mean annual cycle data for ASWUP over all data sets, ERBE and CERES time periods. All values are for monthly mean anomalies from the overall annual average except for the overall monthly means listed in the first column. Relative standard deviations are computed with respect to the corresponding monthly mean. Annual means: ERBE period =  $102.3 \text{ Wm}^{-2}$ , CERES period =  $99.6 \text{ Wm}^{-2}$ .

Month	ERBE period						CERES period					
	Mean	Anom	St Dev	Rel StD	Range	N	Mean	Anom	St Dev	Rel StD	Range	N
1	108.9	6.6	0.6	0.5%	6.2, 7.4	4	106.4	6.8	0.7	0.7%	5.7, 7.7	7
2	104.7	2.4	0.3	0.3%	2.0, 2.6	4	102.1	2.5	0.3	0.3%	2.2, 3.1	7
3	101.8	-0.4	0.2	0.2%	-0.8, -0.3	4	98.1	-1.5	0.6	0.7%	-2.4, -0.8	7
4	100.1	-2.1	0.6	0.6%	-2.8, -1.4	4	97.3	-2.3	0.5	0.5%	-3.0, -1.7	7
5	100.5	-1.8	0.5	0.5%	-2.4, -1.3	4	97.1	-2.5	0.4	0.5%	-3.2, -1.9	7
6	99.3	-3.0	0.4	0.4%	-3.4, -2.4	4	96.4	-3.2	0.2	0.3%	-3.4, -2.8	7
7	96.6	-5.7	0.7	0.7%	-6.5, -5.0	4	93.7	-5.9	0.3	0.3%	-6.4, -5.4	7
8	96.5	-5.8	0.4	0.4%	-6.1, -5.2	4	92.8	-6.8	0.3	0.4%	-7.2, -6.4	7
9	97.4	-4.8	0.2	0.2%	-5.1, -4.6	4	94.7	-4.9	0.2	0.2%	-5.0, -4.6	7
10	102.3	0.0	0.5	0.4%	-0.3, 0.7	4	100.4	0.8	0.4	0.4%	0.3, 1.3	7
11	108.7	6.4	0.3	0.3%	6.1, 6.8	4	106.8	7.2	0.8	0.8%	6.2, 8.3	7
12	110.5	8.2	0.6	0.5%	7.6, 9.0	4	109.1	9.6	1.1	1.0%	8.5, 11.1	7

**Table C3.4.3:** Global mean annual cycle data for ASWNET over all data sets, ERBE and CERES time periods. All values are for monthly mean anomalies from the overall annual average except for the overall monthly means listed in the first column. Relative standard deviations are computed with respect to the corresponding monthly mean. Annual means: ERBE period =  $238.9 \text{ Wm}^{-2}$ , CERES period =  $241.5 \text{ Wm}^{-2}$ .

Month	ERBE period						CERES period					
	Mean	Anom	St Dev	Rel StD	Range	N	Mean	Anom	St Dev	Rel StD	Range	N
1	243.5	4.6	0.6	0.2%	3.8, 5.0	4	246.0	4.5	0.7	0.3%	3.4, 5.5	7
2	244.9	6.0	0.3	0.1%	5.7, 6.4	4	247.4	5.9	0.3	0.1%	5.5, 6.2	7
3	242.8	3.9	0.3	0.1%	3.6, 4.2	4	246.4	4.9	0.6	0.3%	4.3, 5.8	7
4	238.6	-0.3	0.6	0.3%	-1.2, 0.3	4	241.3	-0.2	0.5	0.2%	-0.8, 0.5	7
5	233.2	-5.7	0.5	0.2%	-6.2, -5.1	4	236.4	-5.0	0.5	0.2%	-5.6, -4.3	7
6	231.4	-7.5	0.5	0.2%	-8.2, -7.1	4	234.1	-7.4	0.3	0.1%	-7.7, -7.0	7
7	233.8	-5.2	0.7	0.3%	-6.0, -4.3	4	236.4	-5.1	0.4	0.2%	-5.5, -4.5	7
8	236.3	-2.6	0.4	0.2%	-3.2, -2.3	4	239.8	-1.7	0.4	0.2%	-2.2, -1.2	7
9	240.1	1.1	0.2	0.1%	0.9, 1.5	4	242.6	1.1	0.2	0.1%	0.8, 1.3	7
10	241.0	2.1	0.5	0.2%	1.4, 2.4	4	242.8	1.3	0.5	0.2%	0.7, 1.9	7
11	240.0	1.1	0.3	0.1%	0.7, 1.5	4	241.8	0.4	0.9	0.4%	-0.9, 1.5	7
12	241.6	2.6	0.6	0.2%	1.9, 3.2	4	242.9	1.4	1.1	0.5%	-0.3, 2.4	7

**Table C3.4.4:** Global mean annual cycle data for ALWUP over all data sets, ERBE and CERES time periods. All values are for monthly mean anomalies from the overall annual average except for the overall monthly means listed in the first column. Relative standard deviations are computed with respect to the corresponding monthly mean. Annual means: ERBE period =  $237.0 \text{ Wm}^{-2}$ , CERES period =  $238.8 \text{ Wm}^{-2}$ .

Month	ERBE period						CERES period					
	Mean	Anom	St Dev	Rel StD	Range	N	Mean	Anom	St Dev	Rel StD	Range	N
1	234.3	-2.7	0.6	0.2%	-3.5, -2.0	5	235.5	-3.2	0.5	0.2%	-4.1, -2.3	8
2	234.0	-3.0	0.5	0.2%	-3.5, -2.2	5	236.0	-2.8	0.5	0.2%	-3.7, -2.1	8
3	234.3	-2.7	0.5	0.2%	-3.1, -2.0	5	236.8	-2.0	0.2	0.1%	-2.4, -1.7	8
4	235.6	-1.4	0.3	0.1%	-1.8, -1.0	5	237.6	-1.2	0.2	0.1%	-1.4, -1.0	8
5	237.2	0.2	0.6	0.3%	-0.4, 0.9	5	240.0	1.3	0.2	0.1%	0.8, 1.5	8
6	240.2	3.2	0.5	0.2%	2.5, 3.6	5	241.9	3.2	0.4	0.2%	2.4, 3.7	8
7	241.2	4.2	0.9	0.4%	2.8, 5.0	5	243.1	4.3	0.5	0.2%	3.2, 4.8	8
8	241.3	4.3	0.6	0.3%	3.2, 4.7	5	243.0	4.2	0.5	0.2%	3.4, 5.1	8
9	239.9	2.9	0.2	0.1%	2.8, 3.3	5	241.3	2.5	0.3	0.1%	2.1, 3.1	8
10	237.0	0.0	0.3	0.1%	-0.5, 0.3	5	238.4	-0.4	0.2	0.1%	-0.6, 0.0	8
11	234.7	-2.3	0.4	0.2%	-2.8, -1.7	5	236.1	-2.6	0.2	0.1%	-2.9, -2.2	8
12	234.1	-2.9	0.7	0.3%	-3.4, -1.7	5	235.5	-3.3	0.7	0.3%	-4.0, -1.8	8

**Table C3.4.5:** Global mean annual cycle data for ATOTNET over all data sets, ERBE and CERES time periods. All values are for monthly mean anomalies from the overall annual average except for the overall monthly means listed in the first column. Relative standard deviations are computed with respect to the corresponding monthly mean. Annual means: ERBE period =  $2.3 \text{ Wm}^{-2}$ , CERES period =  $3.1 \text{ Wm}^{-2}$ .

Month	ERBE period						CERES period					
	Mean	Anom	St Dev	Rel StD	Range	N	Mean	Anom	St Dev	Rel StD	Range	N
1	9.6	7.3	0.3	3.2%	6.9, 7.5	3	10.8	7.6	0.8	7.8%	6.1, 8.6	6
2	11.2	8.9	0.9	8.4%	7.9, 9.7	3	11.5	8.4	0.5	4.7%	7.7, 9.2	6
3	8.7	6.4	0.9	9.8%	5.5, 7.2	3	9.8	6.6	0.7	7.3%	6.0, 8.0	6
4	3.0	0.7	0.5	16.6%	0.2, 1.2	3	4.1	0.9	0.5	11.6%	0.4, 1.8	6
5	-3.6	-5.9	0.4	-9.9%	-6.3, -5.7	3	-3.1	-6.3	0.4	-12.5%	-6.9, -5.8	6
6	-8.4	-10.7	1.0	-12.3%	-11.8, -9.8	3	-7.2	-10.4	0.6	-8.4%	-11.3, -9.6	6
7	-7.0	-9.3	1.6	-22.4%	-10.4, -7.5	3	-6.1	-9.2	0.8	-12.6%	-9.8, -7.7	6
8	-4.5	-6.8	1.0	-22.3%	-7.8, -5.8	3	-2.6	-5.8	0.6	-23.4%	-6.2, -4.5	6
9	0.6	-1.7	0.3	41.7%	-1.9, -1.4	3	1.8	-1.3	0.3	17.7%	-1.7, -0.8	6
10	4.6	2.2	0.3	6.1%	2.0, 2.5	3	4.7	1.6	0.5	9.9%	1.1, 2.2	6
11	5.7	3.4	0.7	12.0%	2.8, 4.1	3	6.2	3.1	0.8	12.1%	2.1, 3.9	6
12	7.8	5.4	0.7	9.0%	4.6, 5.9	3	7.8	4.7	1.2	15.1%	2.8, 5.7	6

**Table C3.4.6:** Global mean annual cycle data for CSWDN over all data sets, ERBE and CERES time periods. All values are for monthly mean anomalies from the overall annual average except for the overall monthly means listed in the first column. Relative standard deviations are computed with respect to the corresponding monthly mean. Annual means: ERBE period =  $341.7 \text{ Wm}^{-2}$ , CERES period =  $341.3 \text{ Wm}^{-2}$ .

Month	ERBE period						CERES period					
	Mean	Anom	St Dev	Rel StD	Range	N	Mean	Anom	St Dev	Rel StD	Range	N
1	352.8	11.2	0.0	0.0%	11.2, 11.2	3	352.5	11.3	0.1	0.0%	11.2, 11.4	6
2	350.1	8.4	0.1	0.0%	8.3, 8.5	3	349.7	8.4	0.1	0.0%	8.3, 8.6	6
3	345.1	3.4	0.1	0.0%	3.3, 3.6	3	344.7	3.4	0.1	0.0%	3.3, 3.5	6
4	339.2	-2.4	0.1	0.0%	-2.5, -2.3	3	338.8	-2.5	0.0	0.0%	-2.5, -2.4	6
5	334.2	-7.5	0.1	0.0%	-7.6, -7.4	3	333.7	-7.6	0.1	0.0%	-7.7, -7.4	6
6	331.1	-10.5	0.0	0.0%	-10.6, -10.5	3	330.7	-10.6	0.2	0.1%	-10.8, -10.4	6
7	330.8	-10.9	0.0	0.0%	-10.9, -10.9	3	330.3	-10.9	0.2	0.0%	-11.1, -10.8	6
8	333.2	-8.4	0.1	0.0%	-8.5, -8.3	3	332.8	-8.5	0.1	0.0%	-8.6, -8.3	6
9	337.9	-3.7	0.1	0.0%	-3.9, -3.6	3	337.5	-3.7	0.1	0.0%	-3.8, -3.6	6
10	343.7	2.1	0.1	0.0%	1.9, 2.2	3	343.4	2.1	0.1	0.0%	2.0, 2.2	6
11	349.1	7.5	0.1	0.0%	7.4, 7.6	3	348.9	7.6	0.1	0.0%	7.5, 7.7	6
12	352.5	10.9	0.1	0.0%	10.8, 10.9	3	352.3	11.0	0.1	0.0%	10.9, 11.1	6

**Table C3.4.7:** Global mean annual cycle data for CSWUP over all data sets, ERBE and CERES time periods. All values are for monthly mean anomalies from the overall annual average except for the overall monthly means listed in the first column. Relative standard deviations are computed with respect to the corresponding monthly mean. Annual means: ERBE period =  $54.8 \text{ Wm}^{-2}$ , CERES period =  $52.0 \text{ Wm}^{-2}$ .

Month	ERBE period						CERES period					
	Mean	Anom	St Dev	Rel StD	Range	N	Mean	Anom	St Dev	Rel StD	Range	N
1	57.1	2.2	1.1	1.9%	1.0, 2.8	3	54.0	2.0	0.4	0.8%	1.6, 2.7	6
2	55.1	0.3	1.2	2.2%	-0.8, 1.6	3	52.6	0.6	0.4	0.8%	0.1, 1.2	6
3	54.8	-0.1	1.3	2.4%	-1.6, 1.0	3	52.4	0.4	0.9	1.8%	-1.1, 1.4	6
4	55.9	1.1	1.0	1.8%	0.1, 2.1	3	53.2	1.2	0.8	1.5%	0.0, 1.9	6
5	57.1	2.3	0.6	1.0%	1.9, 3.0	3	53.5	1.4	0.9	1.6%	-0.2, 2.3	6
6	54.8	0.0	1.5	2.7%	-1.6, 1.3	3	51.3	-0.8	0.7	1.3%	-1.5, 0.3	6
7	52.0	-2.8	1.1	2.0%	-3.5, -1.6	3	48.7	-3.3	0.9	1.8%	-4.2, -2.1	6
8	50.6	-4.2	0.7	1.5%	-4.8, -3.4	3	47.7	-4.4	0.8	1.7%	-5.1, -3.2	6
9	51.3	-3.5	0.8	1.6%	-4.0, -2.6	3	48.8	-3.2	0.8	1.7%	-3.7, -1.6	6
10	53.3	-1.6	0.9	1.6%	-2.5, -0.9	3	51.5	-0.5	0.5	1.0%	-1.4, 0.1	6
11	57.5	2.7	0.3	0.5%	2.4, 2.9	3	54.9	2.9	0.5	0.9%	2.0, 3.2	6
12	58.4	3.6	1.1	1.9%	2.8, 4.8	3	55.6	3.6	0.6	1.0%	2.8, 4.5	6

**Table C3.4.8:** Global mean annual cycle data for CSWNET over all data sets, ERBE and CERES time periods. All values are for monthly mean anomalies from the overall annual average except for the overall monthly means listed in the first column. Relative standard deviations are computed with respect to the corresponding monthly mean. Annual means: ERBE period =  $286.8 \text{ Wm}^{-2}$ , CERES period =  $289.3 \text{ Wm}^{-2}$ .

Month	ERBE period						CERES period					
	Mean	Anom	St Dev	Rel StD	Range	N	Mean	Anom	St Dev	Rel StD	Range	N
1	295.8	9.0	1.0	0.4%	8.3, 10.2	3	298.5	9.3	0.4	0.1%	8.5, 9.6	6
2	294.9	8.1	1.1	0.4%	6.9, 9.2	3	297.1	7.8	0.4	0.1%	7.2, 8.3	6
3	290.3	3.5	1.3	0.4%	2.6, 5.0	3	292.3	3.0	0.9	0.3%	2.2, 4.6	6
4	283.3	-3.5	1.1	0.4%	-4.7, -2.6	3	285.6	-3.7	0.9	0.3%	-4.5, -2.4	6
5	277.1	-9.8	0.7	0.2%	-10.5, -9.3	3	280.3	-9.0	0.9	0.3%	-9.9, -7.3	6
6	276.3	-10.5	1.5	0.5%	-11.9, -8.9	3	279.4	-9.9	0.6	0.2%	-10.8, -9.3	6
7	278.8	-8.0	1.1	0.4%	-9.3, -7.4	3	281.6	-7.6	0.8	0.3%	-8.7, -7.0	6
8	282.6	-4.2	0.8	0.3%	-5.0, -3.5	3	285.2	-4.1	0.8	0.3%	-5.2, -3.5	6
9	286.6	-0.2	0.9	0.3%	-1.3, 0.3	3	288.8	-0.5	0.8	0.3%	-2.1, -0.0	6
10	290.5	3.7	0.9	0.3%	3.1, 4.7	3	291.9	2.6	0.5	0.2%	2.1, 3.5	6
11	291.6	4.8	0.2	0.1%	4.7, 5.0	3	293.9	4.7	0.4	0.1%	4.4, 5.5	6
12	294.1	7.3	1.1	0.4%	6.1, 8.1	3	296.7	7.4	0.6	0.2%	6.4, 8.1	6

**Table C3.4.9:** Global mean annual cycle data for CLWUP over all data sets, ERBE and CERES time periods. All values are for monthly mean anomalies from the overall annual average except for the overall monthly means listed in the first column. Relative standard deviations are computed with respect to the corresponding monthly mean. Annual means: ERBE period =  $264.3 \text{ Wm}^{-2}$ , CERES period =  $266.0 \text{ Wm}^{-2}$ .

Month	ERBE period						CERES period					
	Mean	Anom	St Dev	Rel StD	Range	N	Mean	Anom	St Dev	Rel StD	Range	N
1	261.3	-3.0	0.7	0.3%	-3.4, -2.2	3	262.8	-3.3	0.6	0.2%	-3.6, -2.0	6
2	261.1	-3.2	1.0	0.4%	-4.0, -2.1	3	263.1	-3.0	0.6	0.2%	-3.4, -1.8	6
3	262.6	-1.7	0.7	0.3%	-2.5, -1.3	3	263.9	-2.1	0.6	0.2%	-2.5, -1.2	6
4	264.3	0.0	0.5	0.2%	-0.4, 0.5	3	265.4	-0.6	0.3	0.1%	-0.9, -0.1	6
5	265.6	1.3	0.4	0.2%	1.0, 1.8	3	268.1	2.0	0.3	0.1%	1.4, 2.3	6
6	267.3	3.0	0.7	0.3%	2.6, 3.9	3	269.7	3.7	0.7	0.3%	2.6, 4.3	6
7	267.5	3.2	1.2	0.4%	2.3, 4.5	3	269.8	3.8	1.2	0.4%	2.1, 4.8	6
8	267.6	3.3	0.9	0.3%	2.3, 3.9	3	269.3	3.2	0.8	0.3%	2.2, 3.8	6
9	266.0	1.7	0.3	0.1%	1.4, 2.1	3	267.7	1.6	0.5	0.2%	0.8, 2.2	6
10	264.1	-0.2	0.6	0.2%	-0.7, 0.5	3	265.8	-0.3	0.4	0.2%	-0.6, 0.4	6
11	262.4	-1.9	0.7	0.3%	-2.7, -1.3	3	264.0	-2.1	0.8	0.3%	-2.6, -0.6	6
12	261.6	-2.7	0.9	0.3%	-3.3, -1.7	3	263.0	-3.1	0.8	0.3%	-3.6, -1.6	6

**Table C3.4.10:** Global mean annual cycle data for CTOTNET over all data sets, ERBE and CERES time periods. All values are for monthly mean anomalies from the overall annual average except for the overall monthly means listed in the first column. Relative standard deviations are computed with respect to the corresponding monthly mean. Annual means: ERBE period =  $22.6 \text{ Wm}^{-2}$ , CERES period =  $23.1 \text{ Wm}^{-2}$ .

Month	ERBE period						CERES period					
	Mean	Anom	St Dev	Rel StD	Range	N	Mean	Anom	St Dev	Rel StD	Range	N
1	34.5	12.0	0.4	1.1%	11.8, 12.4	3	35.6	12.5	0.6	1.8%	11.6, 13.1	6
2	33.9	11.3	1.2	3.7%	10.3, 12.7	3	33.9	10.7	0.6	1.8%	9.9, 11.7	6
3	27.7	5.2	2.0	7.3%	3.9, 7.5	3	28.2	5.1	0.9	3.3%	4.4, 7.0	6
4	19.1	-3.5	1.2	6.3%	-4.6, -2.2	3	20.1	-3.0	0.8	4.0%	-4.0, -1.7	6
5	11.5	-11.1	0.6	5.3%	-11.6, -10.4	3	12.2	-10.9	0.9	7.4%	-11.7, -9.2	6
6	9.0	-13.6	2.1	23.9%	-15.8, -11.5	3	9.7	-13.5	0.7	7.2%	-14.7, -12.6	6
7	11.3	-11.3	2.2	19.3%	-13.8, -9.8	3	11.8	-11.3	1.1	9.7%	-12.8, -9.3	6
8	15.1	-7.5	1.6	10.5%	-8.9, -5.8	3	15.9	-7.3	0.9	5.9%	-8.7, -5.8	6
9	20.6	-2.0	0.7	3.4%	-2.7, -1.4	3	20.9	-2.2	0.5	2.6%	-3.0, -1.3	6
10	26.4	3.8	1.2	4.4%	2.7, 5.0	3	25.9	2.8	0.5	1.9%	2.3, 3.6	6
11	29.2	6.7	0.6	2.2%	6.2, 7.4	3	29.8	6.6	0.4	1.3%	6.1, 6.9	6
12	32.5	10.0	1.0	3.0%	9.4, 11.1	3	33.6	10.4	0.8	2.3%	9.1, 11.1	6

**Table C3.4.11:** Tropical (20°S-20°N) mean annual cycle data for ASWDN over all data sets, ERBE and CERES time periods. All values are for monthly mean anomalies from the overall annual average except for the overall monthly means listed in the first column. Relative standard deviations are computed with respect to the corresponding monthly mean. Annual means: ERBE period = 409.5 Wm<sup>-2</sup>, CERES period = 409.3 Wm<sup>-2</sup>.

Month	ERBE period						CERES period					
	Mean	Anom	St Dev	Rel StD	Range	N	Mean	Anom	St Dev	Rel StD	Range	N
1	412.4	3.0	0.2	0.1%	2.7, 3.2	6	412.5	3.2	0.1	0.0%	2.9, 3.3	8
2	425.7	16.2	0.3	0.1%	15.9, 16.7	6	425.7	16.4	0.2	0.0%	16.2, 16.8	8
3	429.5	20.0	0.2	0.1%	19.8, 20.4	6	429.3	20.0	0.2	0.1%	19.8, 20.5	8
4	416.7	7.2	0.3	0.1%	6.9, 7.6	6	416.3	7.0	0.2	0.0%	6.8, 7.4	8
5	395.1	-14.3	0.4	0.1%	-14.7, -13.9	6	394.7	-14.6	0.1	0.0%	-14.7, -14.5	8
6	381.3	-28.2	0.2	0.1%	-28.5, -28.0	6	381.0	-28.3	0.2	0.0%	-28.6, -28.1	8
7	385.6	-23.8	0.3	0.1%	-24.2, -23.5	6	385.6	-23.7	0.3	0.1%	-24.1, -23.4	8
8	403.8	-5.7	0.3	0.1%	-6.1, -5.4	6	403.8	-5.5	0.2	0.1%	-5.9, -5.3	8
9	420.2	10.8	0.2	0.1%	10.5, 11.1	6	420.1	10.8	0.1	0.0%	10.7, 11.0	8
10	423.3	13.8	0.2	0.0%	13.6, 14.2	6	423.0	13.7	0.2	0.0%	13.5, 14.1	8
11	413.9	4.4	0.2	0.0%	4.3, 4.6	6	413.6	4.3	0.2	0.1%	4.2, 4.7	8
12	406.1	-3.4	0.3	0.1%	-3.9, -3.3	6	406.0	-3.3	0.3	0.1%	-3.9, -3.0	8

**Table C3.4.12:** Tropical (20°S-20°N) mean annual cycle data for ASWUP over all data sets, ERBE and CERES time periods. All values are for monthly mean anomalies from the overall annual average except for the overall monthly means listed in the first column. Relative standard deviations are computed with respect to the corresponding monthly mean. Annual means: ERBE period = 98.7 Wm<sup>-2</sup>, CERES period = 94.8 Wm<sup>-2</sup>.

Month	ERBE period						CERES period					
	Mean	Anom	St Dev	Rel StD	Range	N	Mean	Anom	St Dev	Rel StD	Range	N
1	102.3	3.6	0.5	0.5%	3.1, 4.4	6	97.2	2.5	0.9	1.0%	1.2, 3.7	8
2	99.5	0.8	0.5	0.5%	0.3, 1.6	6	96.7	1.9	0.6	0.6%	0.8, 2.5	8
3	98.2	-0.5	0.7	0.7%	-1.3, 0.4	6	93.1	-1.7	0.7	0.8%	-2.8, -1.0	8
4	94.7	-4.0	0.6	0.6%	-4.9, -3.4	6	90.7	-4.1	0.5	0.5%	-5.1, -3.6	8
5	93.0	-5.7	0.6	0.7%	-6.5, -4.7	6	88.6	-6.1	0.9	1.1%	-7.3, -4.6	8
6	94.2	-4.5	0.4	0.4%	-5.0, -4.1	6	90.6	-4.2	0.8	0.9%	-4.9, -2.2	8
7	96.0	-2.7	0.8	0.8%	-3.5, -1.7	6	92.3	-2.4	0.8	0.9%	-3.4, -0.7	8
8	100.4	1.7	0.6	0.6%	0.9, 2.6	6	96.3	1.5	0.5	0.5%	1.0, 2.5	8
9	101.6	2.9	0.7	0.7%	2.2, 3.8	6	96.7	2.0	0.5	0.5%	1.2, 2.7	8
10	101.3	2.6	0.4	0.4%	2.0, 3.0	6	98.0	3.2	0.5	0.5%	2.5, 3.9	8
11	102.0	3.3	0.4	0.4%	2.9, 3.9	6	98.8	4.0	0.7	0.7%	3.0, 4.8	8
12	101.2	2.5	0.7	0.7%	1.8, 3.6	6	98.2	3.4	0.9	0.9%	2.6, 4.6	8

**Table C3.4.13:** Tropical (20°S-20°N) mean annual cycle data for ASWNET over all data sets, ERBE and CERES time periods. All values are for monthly mean anomalies from the overall annual average except for the overall monthly means listed in the first column. Relative standard deviations are computed with respect to the corresponding monthly mean. Annual means: ERBE period = 310.8 Wm<sup>-2</sup>, CERES period = 314.5 Wm<sup>-2</sup>.

Month	ERBE period						CERES period					
	Mean	Anom	St Dev	Rel StD	Range	N	Mean	Anom	St Dev	Rel StD	Range	N
1	310.1	-0.7	0.6	0.2%	-1.6, -0.0	6	315.2	0.7	1.0	0.3%	-0.7, 2.0	8
2	326.1	15.4	0.6	0.2%	14.6, 16.5	6	329.0	14.5	0.6	0.2%	13.7, 15.6	8
3	331.3	20.5	0.9	0.3%	19.5, 21.8	6	336.2	21.7	0.9	0.3%	21.0, 23.3	8
4	322.0	11.2	0.6	0.2%	10.8, 12.3	6	325.6	11.1	0.6	0.2%	10.6, 12.4	8
5	302.1	-8.7	0.3	0.1%	-9.2, -8.2	6	306.1	-8.4	0.9	0.3%	-10.0, -7.5	8
6	287.1	-23.7	0.4	0.1%	-24.1, -23.3	6	290.4	-24.1	0.8	0.3%	-26.0, -23.3	8
7	289.7	-21.1	1.0	0.3%	-22.4, -20.1	6	293.2	-21.3	0.9	0.3%	-22.9, -20.1	8
8	303.4	-7.3	0.5	0.1%	-8.2, -6.9	6	307.5	-7.1	0.6	0.2%	-7.8, -6.3	8
9	318.6	7.9	0.6	0.2%	7.0, 8.7	6	323.4	8.9	0.5	0.2%	8.2, 9.6	8
10	322.0	11.3	0.5	0.2%	10.7, 11.8	6	325.1	10.5	0.5	0.2%	9.6, 11.3	8
11	311.9	1.1	0.4	0.1%	0.4, 1.6	6	314.9	0.3	0.8	0.3%	-0.5, 1.4	8
12	304.9	-5.9	0.9	0.3%	-7.5, -5.1	6	307.8	-6.8	1.1	0.4%	-8.3, -5.6	8

**Table C3.4.14:** Tropical (20°S-20°N) mean annual cycle data for ALWUP over all data sets, ERBE and CERES time periods. All values are for monthly mean anomalies from the overall annual average except for the overall monthly means listed in the first column. Relative standard deviations are computed with respect to the corresponding monthly mean. Annual means: ERBE period = 254.7 Wm<sup>-2</sup>, CERES period = 256.4 Wm<sup>-2</sup>.

Month	ERBE period						CERES period					
	Mean	Anom	St Dev	Rel StD	Range	N	Mean	Anom	St Dev	Rel StD	Range	N
1	253.2	-1.5	0.5	0.2%	-2.5, -1.1	6	254.9	-1.6	0.4	0.1%	-2.1, -1.0	8
2	254.1	-0.6	0.3	0.1%	-0.9, -0.3	6	255.4	-1.0	0.3	0.1%	-1.6, -0.6	8
3	254.2	-0.5	0.4	0.2%	-1.1, -0.1	6	256.0	-0.4	0.3	0.1%	-0.8, -0.1	8
4	254.6	-0.1	0.4	0.2%	-0.9, 0.2	6	256.1	-0.3	0.5	0.2%	-1.1, 0.6	8
5	255.5	0.8	0.5	0.2%	0.2, 1.4	6	258.2	1.8	0.2	0.1%	1.5, 2.0	8
6	256.4	1.7	0.5	0.2%	1.1, 2.4	6	257.6	1.2	0.2	0.1%	0.7, 1.5	8
7	255.5	0.8	0.5	0.2%	-0.1, 1.5	6	257.8	1.4	0.5	0.2%	0.5, 2.1	8
8	255.7	0.9	0.4	0.2%	0.2, 1.4	6	257.6	1.2	0.5	0.2%	0.1, 1.8	8
9	255.8	1.1	0.3	0.1%	0.7, 1.5	6	257.3	0.9	0.4	0.1%	0.5, 1.5	8
10	255.1	0.4	0.4	0.2%	-0.0, 1.0	6	256.4	0.0	0.4	0.1%	-0.5, 0.7	8
11	253.5	-1.2	0.3	0.1%	-1.6, -0.8	6	255.0	-1.4	0.2	0.1%	-1.7, -1.1	8
12	253.0	-1.7	0.6	0.2%	-2.2, -0.7	6	254.7	-1.7	0.7	0.3%	-2.5, -0.1	8

**Table C3.4.15:** Tropical (20°S-20°N) mean annual cycle data for ATOTNET over all data sets, ERBE and CERES time periods. All values are for monthly mean anomalies from the overall annual average except for the overall monthly means listed in the first column. Relative standard deviations are computed with respect to the corresponding monthly mean. Annual means: ERBE period = 186.1 Wm<sup>-2</sup>, CERES period = 186.6 Wm<sup>-2</sup>.

Month	ERBE period						CERES period					
	Mean	Anom	St Dev	Rel StD	Range	N	Mean	Anom	St Dev	Rel StD	Range	N
1	56.9	0.8	0.6	1.0%	-0.0, 1.5	5	60.4	2.3	1.1	1.9%	0.5, 3.6	7
2	72.1	16.1	0.8	1.1%	15.3, 17.2	5	73.5	15.4	0.9	1.2%	14.4, 16.6	7
3	77.2	21.2	0.8	1.0%	20.3, 22.3	5	80.2	22.1	0.9	1.1%	21.2, 23.3	7
4	67.2	11.1	0.6	0.9%	10.6, 12.2	5	69.4	11.3	0.4	0.5%	10.8, 11.8	7
5	46.6	-9.5	0.4	0.8%	-10.1, -9.1	5	47.8	-10.3	1.0	2.1%	-12.0, -9.0	7
6	30.8	-25.3	0.3	0.9%	-25.6, -24.9	5	32.9	-25.2	0.9	2.8%	-27.2, -24.5	7
7	34.1	-22.0	1.1	3.2%	-23.1, -20.5	5	35.5	-22.6	1.0	2.8%	-24.4, -21.3	7
8	47.8	-8.2	0.7	1.5%	-9.3, -7.5	5	49.9	-8.2	0.8	1.7%	-9.0, -6.5	7
9	62.9	6.9	0.5	0.8%	6.3, 7.4	5	66.2	8.1	0.7	1.0%	7.4, 9.2	7
10	66.9	10.9	0.5	0.7%	10.3, 11.5	5	68.5	10.4	0.5	0.7%	9.7, 11.1	7
11	58.3	2.2	0.5	0.9%	1.6, 2.8	5	59.8	1.7	0.8	1.3%	0.5, 2.4	7
12	51.8	-4.2	1.2	2.2%	-5.6, -3.1	5	53.0	-5.1	1.4	2.6%	-7.8, -4.0	7

**Table C3.4.16:** Tropical (20°S-20°N) mean annual cycle data for CSWDN over all data sets, ERBE and CERES time periods. All values are for monthly mean anomalies from the overall annual average except for the overall monthly means listed in the first column. Relative standard deviations are computed with respect to the corresponding monthly mean. Annual means: ERBE period = 409.7 Wm<sup>-2</sup>, CERES period = 409.4 Wm<sup>-2</sup>.

Month	ERBE period						CERES period					
	Mean	Anom	St Dev	Rel StD	Range	N	Mean	Anom	St Dev	Rel StD	Range	N
1	412.7	2.9	0.2	0.1%	2.7, 3.2	4	412.6	3.2	0.1	0.0%	3.2, 3.3	6
2	425.8	16.1	0.2	0.0%	15.9, 16.3	4	425.7	16.3	0.1	0.0%	16.2, 16.4	6
3	429.7	19.9	0.1	0.0%	19.8, 20.0	4	429.3	19.9	0.1	0.0%	19.8, 20.0	6
4	417.0	7.3	0.4	0.1%	6.9, 7.6	4	416.3	7.0	0.1	0.0%	6.8, 7.0	6
5	395.5	-14.2	0.4	0.1%	-14.6, -13.9	4	394.8	-14.6	0.0	0.0%	-14.7, -14.5	6
6	381.6	-28.1	0.1	0.0%	-28.3, -28.0	4	381.1	-28.3	0.1	0.0%	-28.5, -28.1	6
7	385.9	-23.8	0.2	0.1%	-24.0, -23.6	4	385.7	-23.7	0.3	0.1%	-24.0, -23.4	6
8	404.0	-5.7	0.4	0.1%	-6.1, -5.4	4	403.9	-5.5	0.3	0.1%	-5.9, -5.3	6
9	420.4	10.7	0.2	0.1%	10.5, 11.0	4	420.2	10.8	0.1	0.0%	10.7, 11.0	6
10	423.5	13.8	0.1	0.0%	13.7, 13.8	4	423.1	13.7	0.2	0.0%	13.5, 13.9	6
11	414.2	4.5	0.2	0.0%	4.3, 4.6	4	413.8	4.4	0.3	0.1%	4.2, 4.7	6
12	406.4	-3.3	0.0	0.0%	-3.3, -3.3	4	406.2	-3.2	0.2	0.0%	-3.3, -3.0	6

**Table C3.4.17:** Tropical (20°S-20°N) mean annual cycle data for CSWUP over all data sets, ERBE and CERES time periods. All values are for monthly mean anomalies from the overall annual average except for the overall monthly means listed in the first column. Relative standard deviations are computed with respect to the corresponding monthly mean. Annual means: ERBE period = 51.5 Wm<sup>-2</sup>, CERES period = 47.8 Wm<sup>-2</sup>.

Month	ERBE period						CERES period					
	Mean	Anom	St Dev	Rel StD	Range	N	Mean	Anom	St Dev	Rel StD	Range	N
1	52.7	1.2	0.4	0.7%	0.7, 1.5	4	48.4	0.6	0.3	0.6%	0.2, 0.9	6
2	52.8	1.3	0.6	1.0%	0.6, 2.0	4	49.5	1.7	0.2	0.4%	1.4, 2.0	6
3	52.5	1.0	0.4	0.7%	0.5, 1.5	4	49.2	1.4	0.4	0.8%	0.8, 1.8	6
4	51.6	0.2	0.1	0.1%	0.1, 0.2	4	48.0	0.1	0.3	0.6%	-0.2, 0.6	6
5	50.2	-1.3	0.2	0.4%	-1.4, -1.0	4	46.4	-1.4	0.4	0.8%	-2.0, -1.0	6
6	50.0	-1.5	0.5	1.1%	-2.1, -0.9	4	46.0	-1.8	0.5	1.1%	-2.4, -1.1	6
7	49.9	-1.6	0.3	0.6%	-1.9, -1.2	4	46.2	-1.6	0.4	0.9%	-2.0, -0.9	6
8	51.1	-0.4	0.2	0.4%	-0.6, -0.2	4	47.4	-0.4	0.4	0.8%	-0.7, 0.2	6
9	51.9	0.4	0.2	0.5%	0.2, 0.7	4	48.5	0.6	0.4	0.9%	0.2, 1.4	6
10	51.7	0.3	0.7	1.3%	-0.4, 1.0	4	48.4	0.6	0.6	1.2%	-0.4, 1.2	6
11	51.6	0.2	0.2	0.4%	-0.1, 0.4	4	48.0	0.1	0.2	0.5%	-0.2, 0.4	6
12	51.7	0.2	0.1	0.3%	0.1, 0.4	4	47.8	0.0	0.3	0.6%	-0.3, 0.4	6

**Table C3.4.18:** Tropical (20°S-20°N) mean annual cycle data for CSWNET over all data sets, ERBE and CERES time periods. All values are for monthly mean anomalies from the overall annual average except for the overall monthly means listed in the first column. Relative standard deviations are computed with respect to the corresponding monthly mean. Annual means: ERBE period = 358.2 Wm<sup>-2</sup>, CERES period = 361.6 Wm<sup>-2</sup>.

Month	ERBE period						CERES period					
	Mean	Anom	St Dev	Rel StD	Range	N	Mean	Anom	St Dev	Rel StD	Range	N
1	360.0	1.8	0.5	0.1%	1.3, 2.5	4	364.2	2.7	0.3	0.1%	2.4, 3.1	6
2	373.0	14.8	0.6	0.2%	14.2, 15.6	4	376.2	14.7	0.2	0.1%	14.4, 14.9	6
3	377.1	18.9	0.4	0.1%	18.3, 19.4	4	380.1	18.5	0.3	0.1%	18.2, 19.1	6
4	365.3	7.1	0.4	0.1%	6.7, 7.5	4	368.4	6.8	0.2	0.1%	6.5, 7.0	6
5	345.3	-12.9	0.6	0.2%	-13.5, -12.4	4	348.4	-13.2	0.3	0.1%	-13.5, -12.6	6
6	331.6	-26.6	0.7	0.2%	-27.4, -25.9	4	335.1	-26.4	0.5	0.1%	-27.2, -26.0	6
7	336.0	-22.2	0.1	0.0%	-22.4, -22.1	4	339.5	-22.1	0.3	0.1%	-22.7, -21.8	6
8	352.8	-5.4	0.3	0.1%	-5.7, -5.1	4	356.4	-5.2	0.3	0.1%	-5.6, -4.7	6
9	368.5	10.2	0.4	0.1%	9.9, 10.8	4	371.7	10.1	0.5	0.1%	9.4, 10.6	6
10	371.8	13.6	0.7	0.2%	12.9, 14.2	4	374.7	13.1	0.6	0.2%	12.7, 14.2	6
11	362.5	4.3	0.2	0.0%	4.2, 4.5	4	365.8	4.2	0.2	0.1%	3.9, 4.6	6
12	354.7	-3.5	0.1	0.0%	-3.7, -3.4	4	358.3	-3.2	0.4	0.1%	-3.8, -2.8	6

**Table C3.4.19:** Tropical (20°S-20°N) mean annual cycle data for CLWUP over all data sets, ERBE and CERES time periods. All values are for monthly mean anomalies from the overall annual average except for the overall monthly means listed in the first column. Relative standard deviations are computed with respect to the corresponding monthly mean. Annual means: ERBE period = 286.9  $Wm^{-2}$ , CERES period = 287.8  $Wm^{-2}$ .

Month	ERBE period						CERES period					
	Mean	Anom	St Dev	Rel StD	Range	N	Mean	Anom	St Dev	Rel StD	Range	N
1	286.4	-0.5	0.6	0.2%	-0.9, 0.2	3	287.7	-0.1	0.3	0.1%	-0.6, 0.2	6
2	286.5	-0.3	0.4	0.1%	-0.7, 0.1	3	288.3	0.5	0.4	0.1%	-0.1, 0.8	6
3	287.6	0.7	0.7	0.2%	0.1, 1.5	3	288.0	0.2	0.3	0.1%	-0.2, 0.7	6
4	287.7	0.9	0.6	0.2%	0.5, 1.5	3	288.2	0.4	0.4	0.1%	0.1, 1.1	6
5	287.7	0.9	0.6	0.2%	0.4, 1.5	3	289.2	1.4	0.4	0.1%	0.7, 1.7	6
6	287.1	0.3	0.6	0.2%	-0.3, 1.0	3	288.1	0.3	0.3	0.1%	-0.1, 0.6	6
7	285.9	-1.0	0.8	0.3%	-1.8, -0.1	3	287.1	-0.7	0.7	0.2%	-2.1, -0.2	6
8	286.2	-0.7	0.8	0.3%	-1.6, -0.3	3	287.0	-0.9	0.7	0.2%	-2.0, 0.1	6
9	286.8	-0.1	0.0	0.0%	-0.1, -0.1	3	287.1	-0.7	0.4	0.2%	-1.1, -0.1	6
10	287.1	0.3	0.3	0.1%	0.0, 0.6	3	287.8	-0.1	0.4	0.2%	-0.7, 0.4	6
11	286.7	-0.1	0.6	0.2%	-0.8, 0.4	3	287.8	0.0	0.3	0.1%	-0.5, 0.3	6
12	286.6	-0.3	0.7	0.2%	-1.1, 0.3	3	287.7	-0.2	0.7	0.2%	-1.0, 1.1	6

**Table C3.4.20:** Tropical (20°S-20°N) mean annual cycle data for CTOTNET over all data sets, ERBE and CERES time periods. All values are for monthly mean anomalies from the overall annual average except for the overall monthly means listed in the first column. Relative standard deviations are computed with respect to the corresponding monthly mean. Annual means: ERBE period = 71.1  $Wm^{-2}$ , CERES period = 73.6  $Wm^{-2}$ .

Month	ERBE period						CERES period					
	Mean	Anom	St Dev	Rel StD	Range	N	Mean	Anom	St Dev	Rel StD	Range	N
1	73.5	2.4	1.0	1.4%	1.4, 3.4	3	76.3	2.7	0.1	0.2%	2.5, 2.9	6
2	86.2	15.1	1.0	1.2%	14.0, 16.0	3	87.7	14.2	0.3	0.4%	13.8, 14.6	6
3	89.2	18.2	1.2	1.4%	16.8, 19.2	3	91.9	18.4	0.3	0.4%	17.9, 18.9	6
4	77.2	6.2	0.9	1.2%	5.2, 7.0	3	80.1	6.5	0.3	0.4%	5.9, 6.8	6
5	57.1	-14.0	1.1	2.0%	-15.0, -12.8	3	59.1	-14.5	0.5	0.8%	-15.2, -14.0	6
6	44.0	-27.1	1.2	2.8%	-28.3, -25.9	3	46.9	-26.6	0.3	0.7%	-27.1, -26.2	6
7	49.9	-21.2	0.7	1.5%	-22.1, -20.6	3	52.3	-21.3	0.4	0.7%	-21.6, -20.6	6
8	66.5	-4.6	0.9	1.4%	-5.2, -3.6	3	69.3	-4.3	0.8	1.2%	-5.7, -3.3	6
9	81.5	10.4	0.4	0.5%	10.1, 10.9	3	84.4	10.9	0.8	0.9%	9.5, 11.7	6
10	84.5	13.4	1.0	1.2%	12.3, 14.2	3	86.7	13.1	0.5	0.6%	12.6, 13.8	6
11	75.6	4.5	0.5	0.6%	4.0, 5.0	3	77.7	4.2	0.4	0.5%	3.7, 4.7	6
12	67.8	-3.2	0.6	0.9%	-3.6, -2.5	3	70.3	-3.2	0.8	1.1%	-4.5, -2.1	6

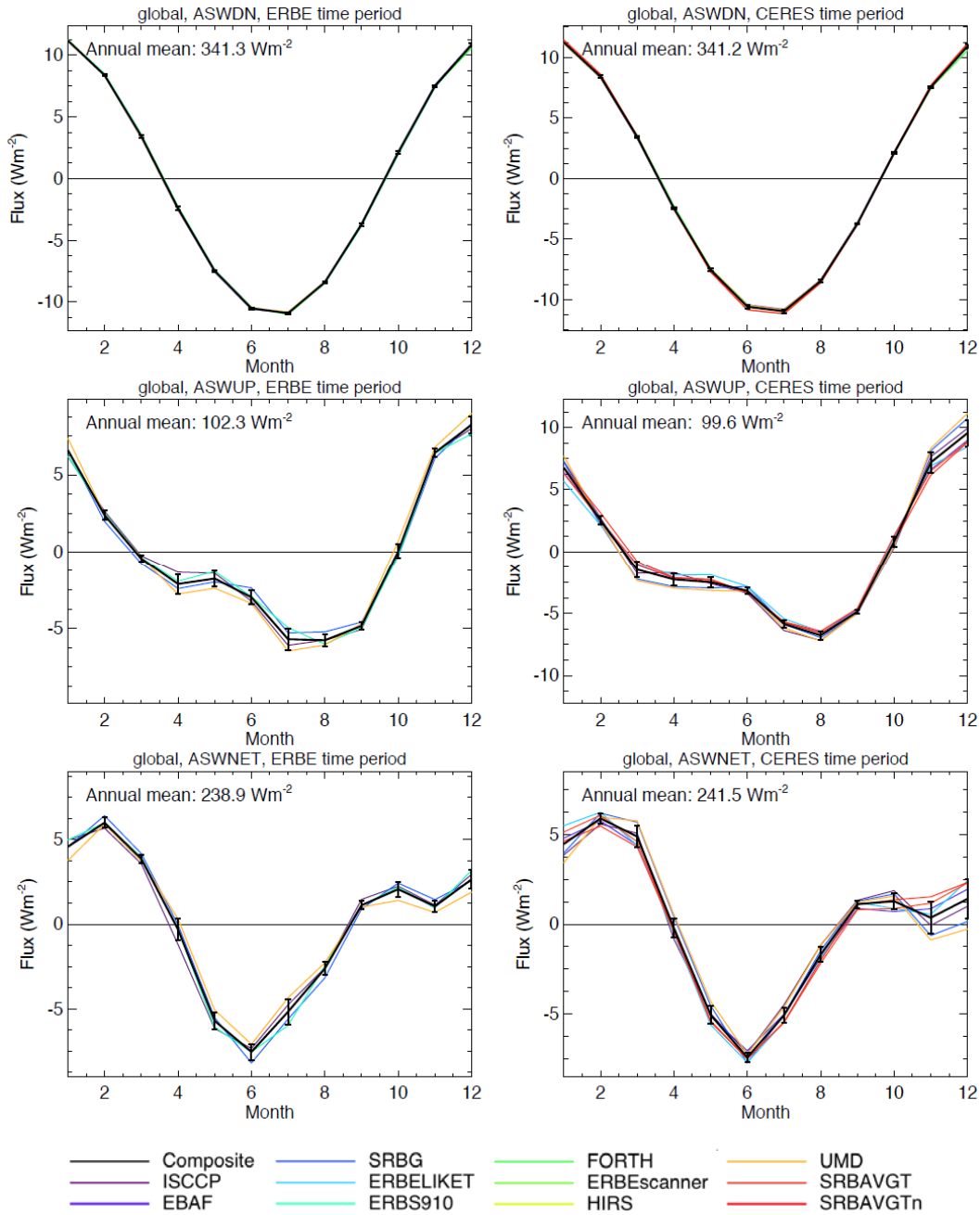


**Figure C3.4.1.** Global mean annual cycles for all-sky shortwave parameters over the ERBE and CERES time periods shown as deviations from the corresponding annual means. Error bars indicate  $\pm$  one standard deviation.

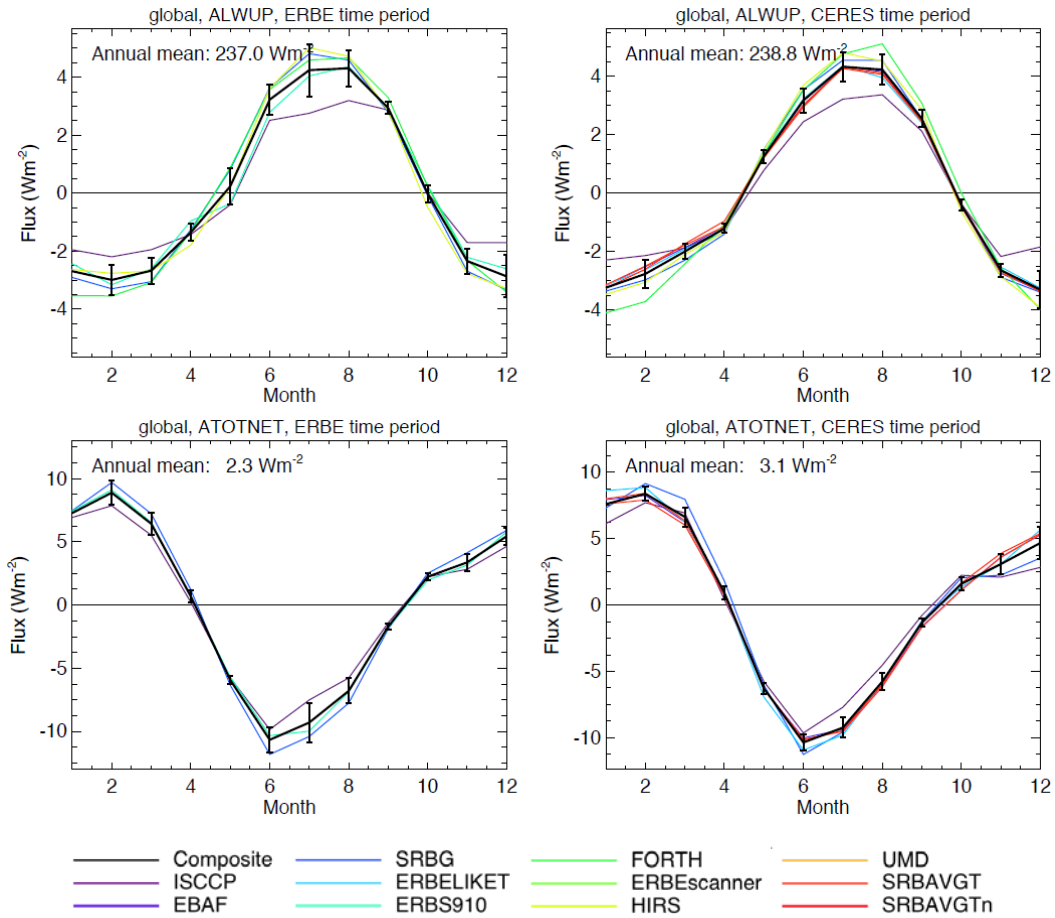


**Figure C3.4.2.** Global mean annual cycles for all-sky outgoing longwave and total net fluxes over the ERBE and CERES time periods shown as deviations from the corresponding annual means. Error bars indicate  $\pm$  one standard deviation.

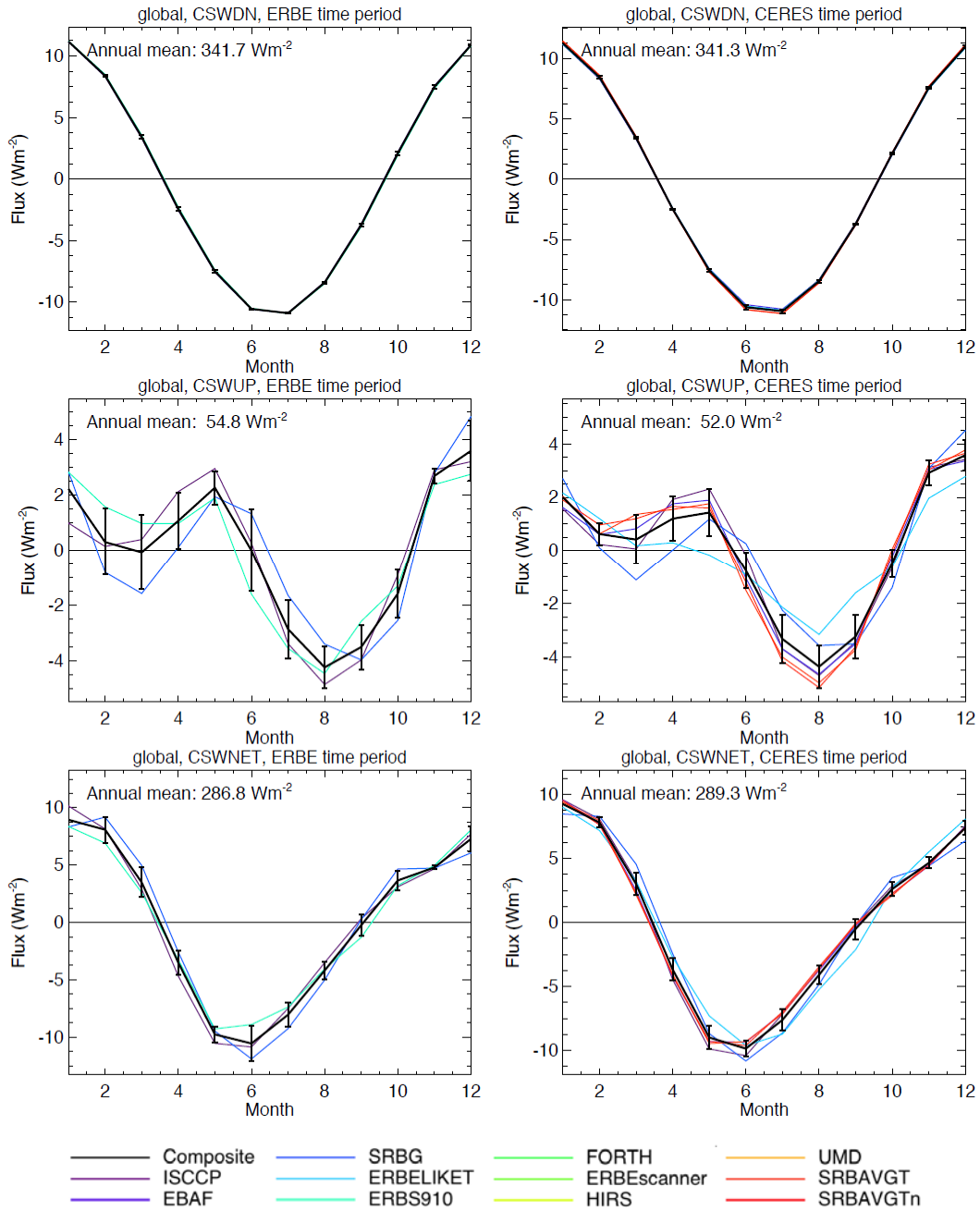


**Figure C3.4.3.** Global mean annual cycles for clear-sky shortwave parameters over the ERBE and CERES time periods shown as deviations from the corresponding annual means. Error bars indicate +/- one standard deviation.

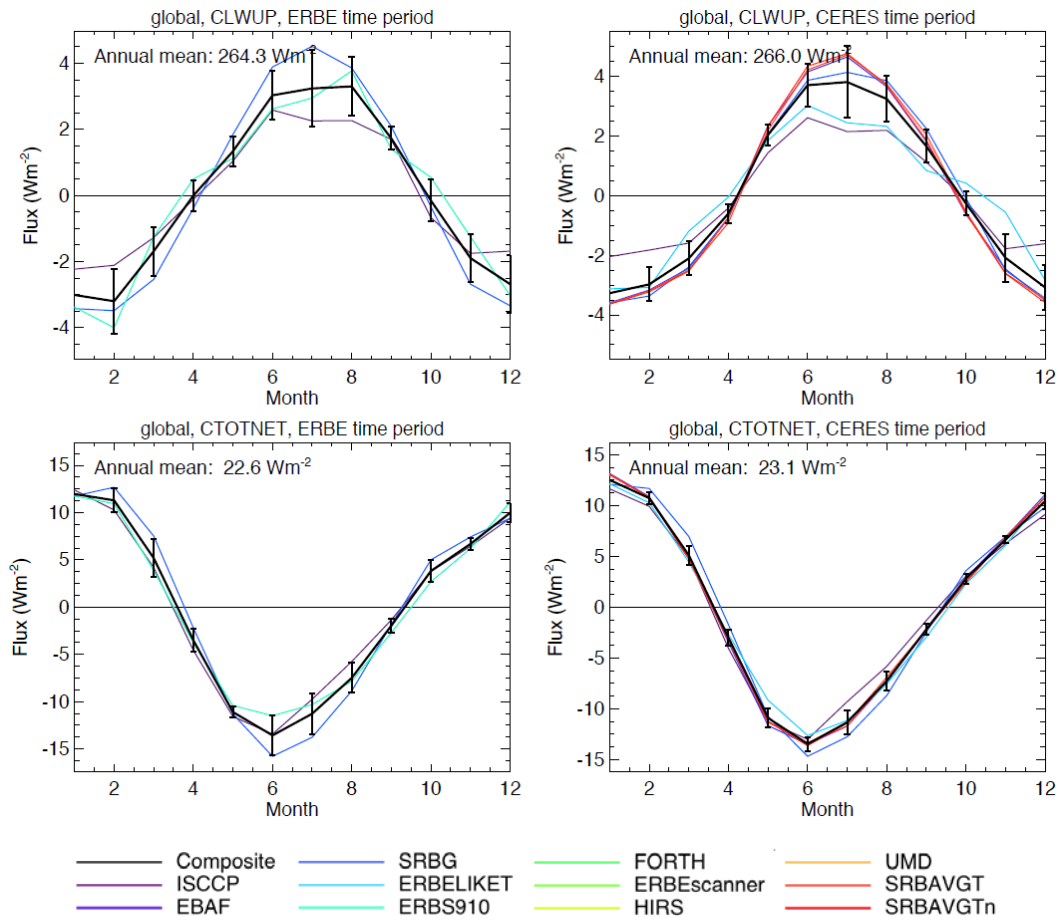


**Figure C3.4.4.** Global mean annual cycles for clear-sky outgoing longwave and total net fluxes over the ERBE and CERES time periods shown as deviations from the corresponding annual means. Error bars indicate  $\pm$  one standard deviation.

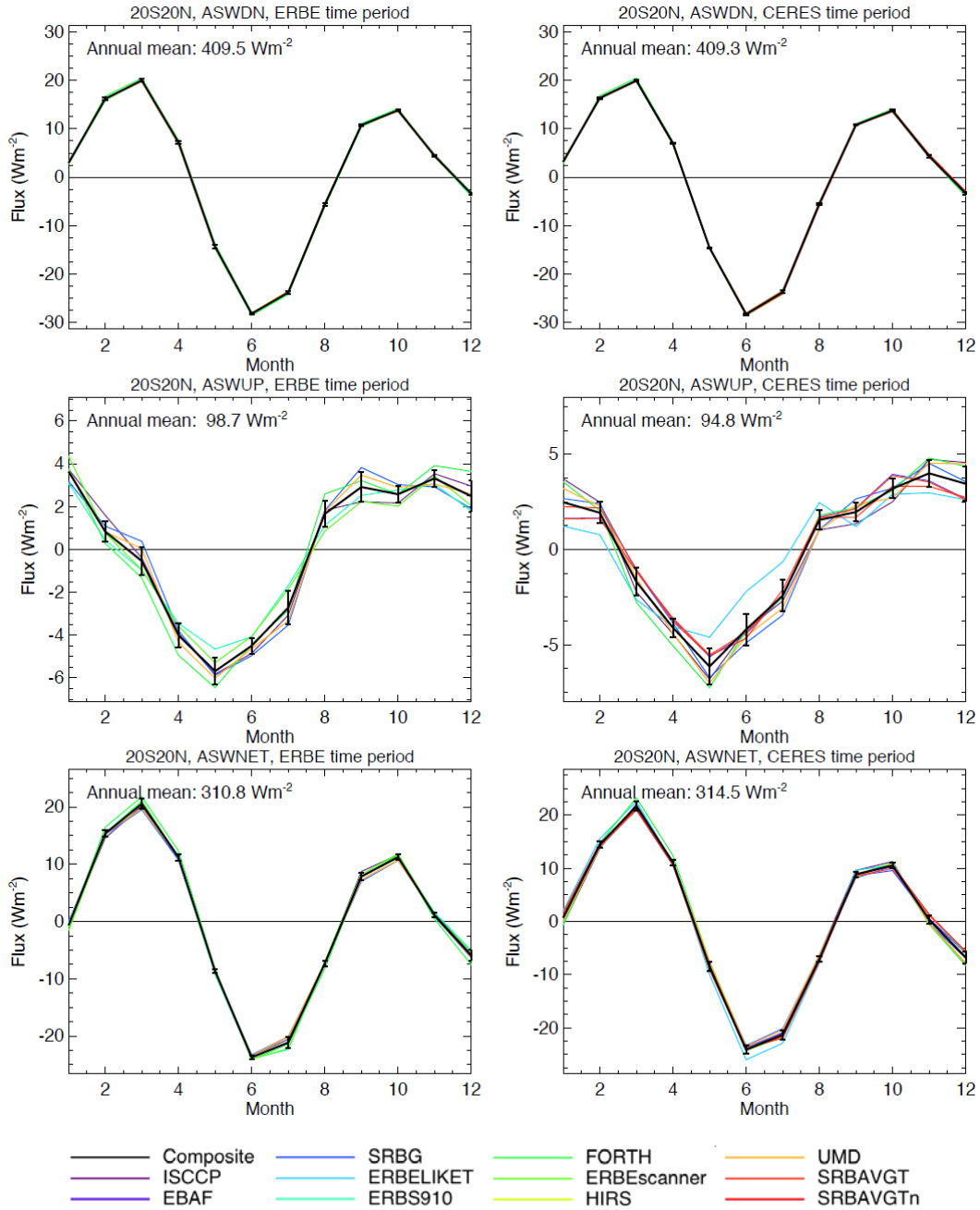


**Figure C3.4.5.** Tropical (20°S-20°N) mean annual cycles for all-sky shortwave parameters over the ERBE and CERES time periods shown as deviations from the corresponding annual means. Error bars indicate  $\pm$  one standard deviation.

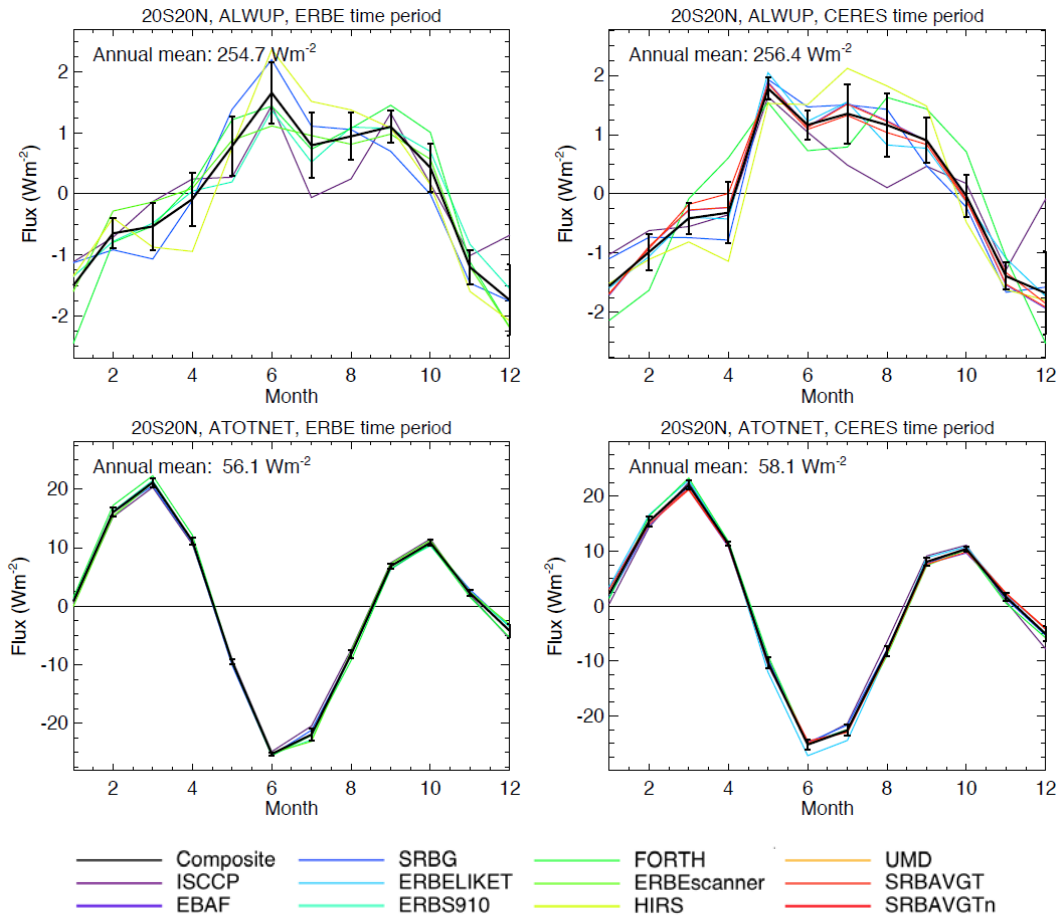


**Figure C3.4.6.** Tropical (20°S-20°N) mean annual cycles for all-sky outgoing longwave and total net fluxes over the ERBE and CERES time periods shown as deviations from the corresponding annual means. Error bars indicate  $\pm$  one standard deviation.

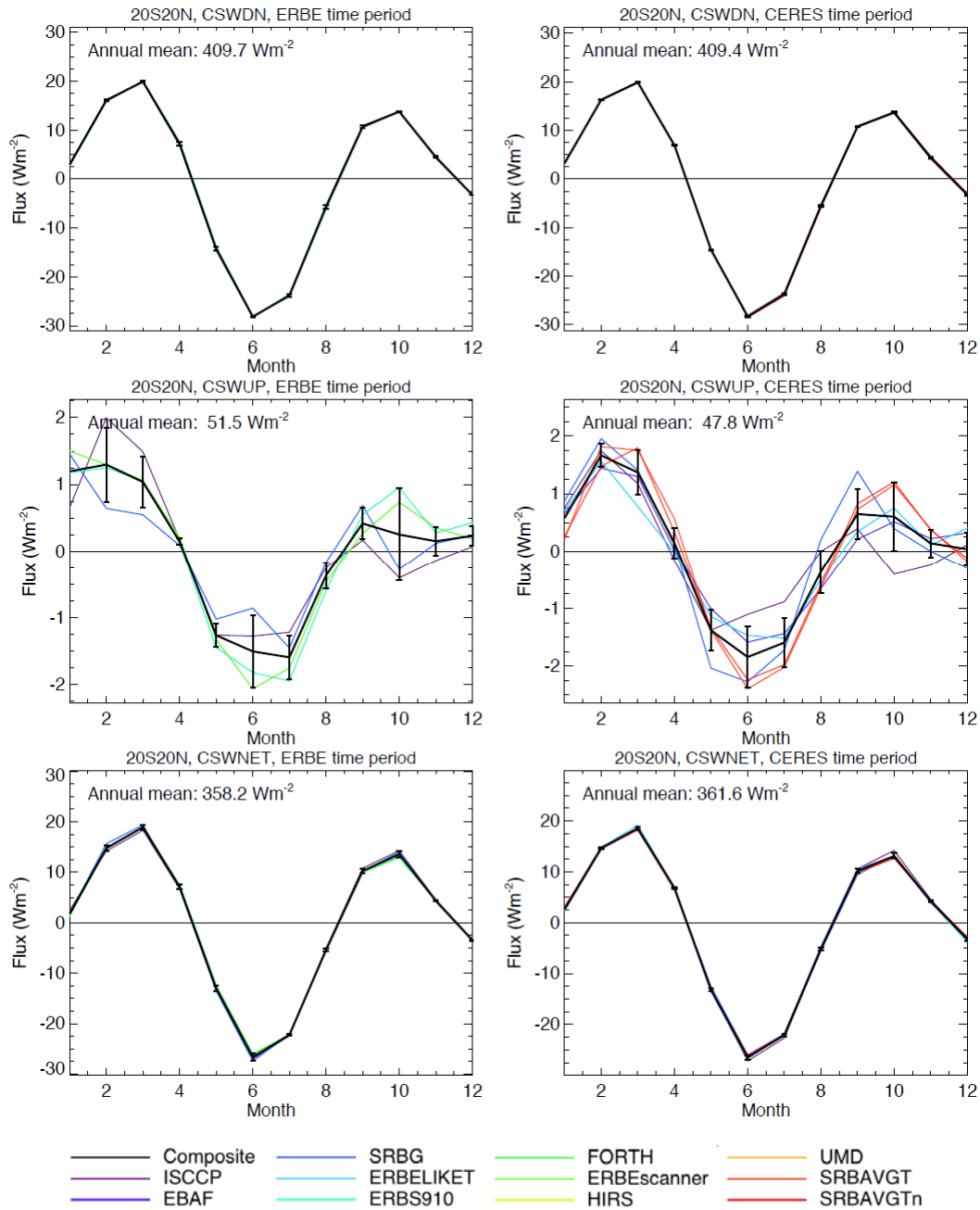


**Figure C3.4.7.** Tropical (20°S-20°N) mean annual cycles for clear-sky shortwave parameters over the ERBE and CERES time periods shown as deviations from the corresponding annual means. Error bars indicate +/- one standard deviation.

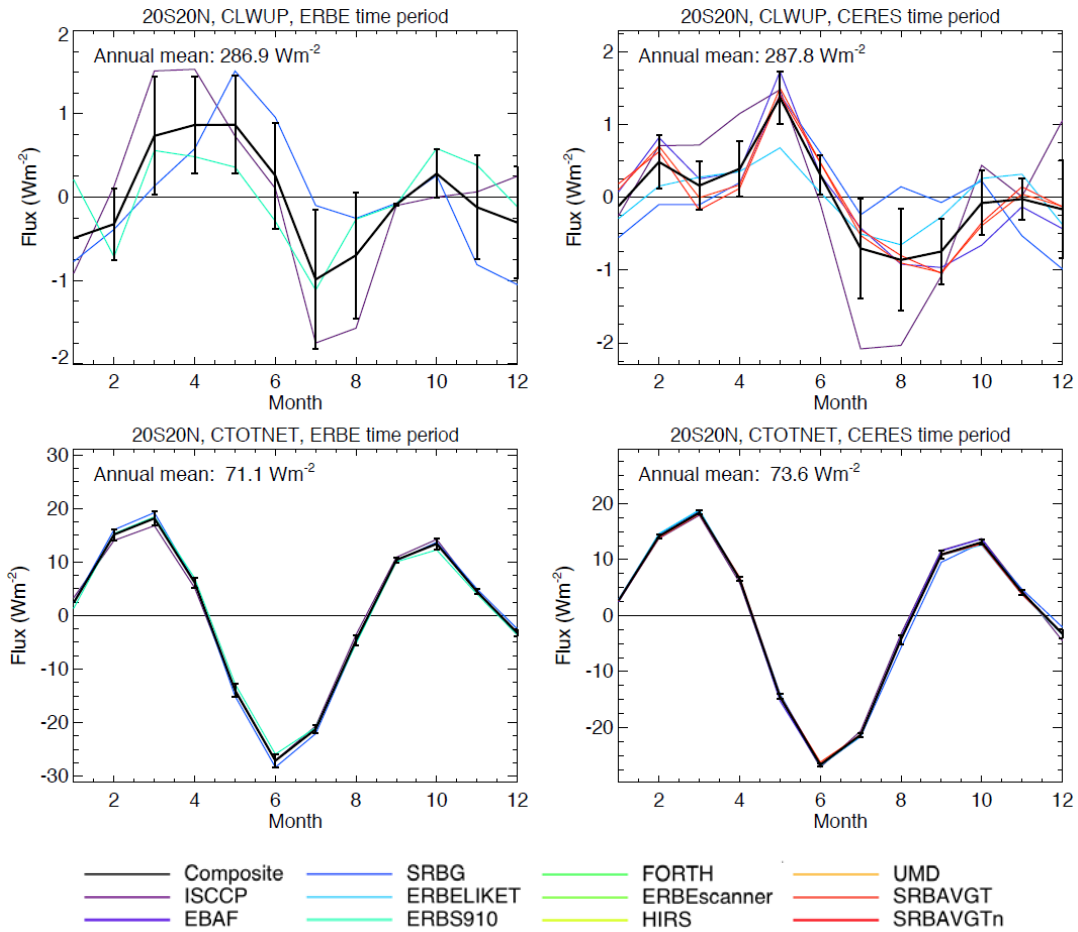


**Figure C3.4.8.** Tropical (20°S-20°N) mean annual cycles for clear-sky outgoing longwave and total net fluxes over the ERBE and CERES time periods shown as deviations from the corresponding annual means. Error bars indicate  $\pm$  one standard deviation.

## Appendix C3.5 for Chapter 3.5:

### Supplementary Results to Chapter 3.5

E. Raschke, S.Kinne

Here are summarized figures with additional information on the subjects presented in *Chapter 3.5*.

#### C3.5.1. Zonal anomalies of clear-sky planetary albedo and outgoing longwave radiation

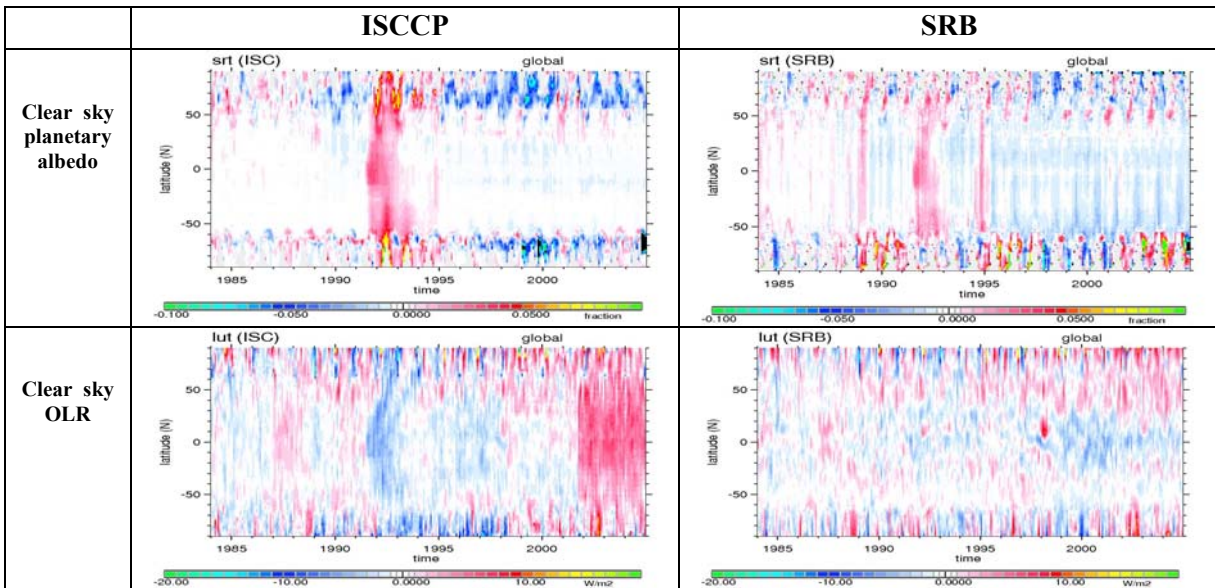


*Figure C.3.5.1: Monthly deseasonalised zonal anomalies of the planetary albedo at TOA (top) and of the upward terrestrial radiation (OLR: bottom) at TOA for clear skies, during the period January 1984 to December 2004 for ISCCP and SRB. The reference period for ISCCP and SRB covers 4 years: January 1985 to December 1988. Changes of satellites occurred in 1985, 1989, 1994-95, 1998 and 2001, which affect the pattern in the diagrams for ISCCP and SRB above.*

## C3.5.2: Interannual variability

### C3.5.2.1: Planetary albedo and outgoing longwave radiation for clear sky at TOA

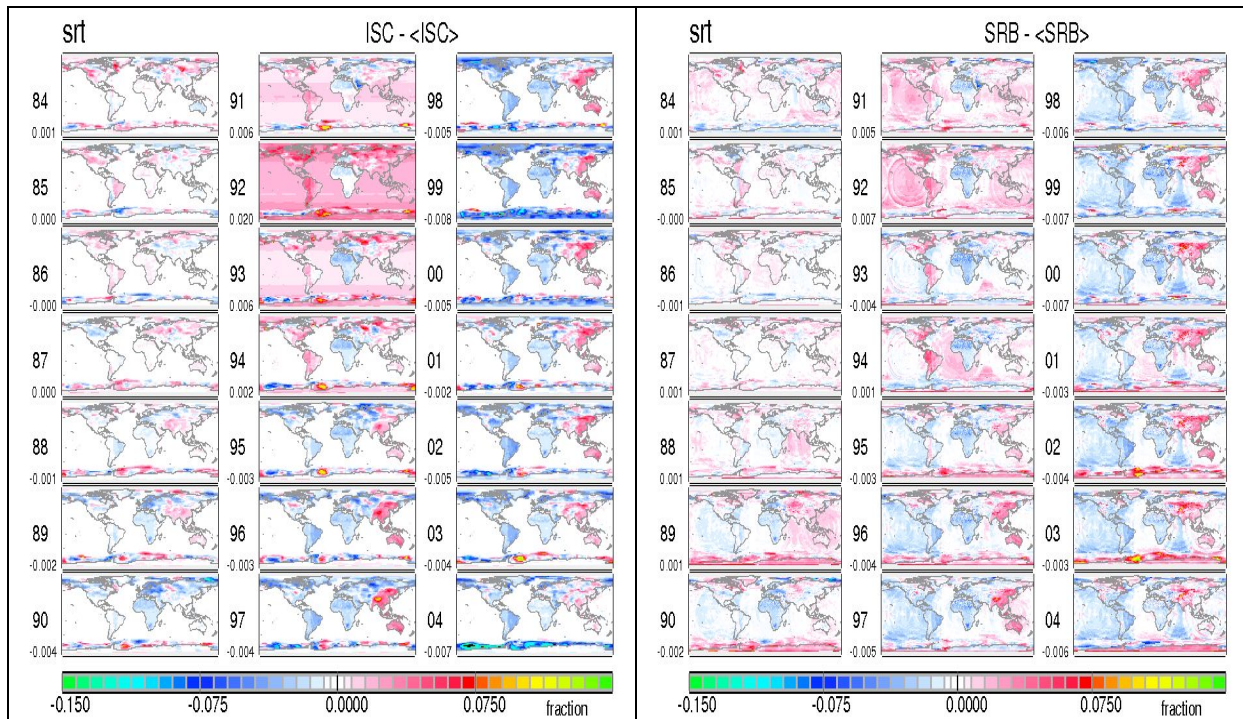


Figure C3.5.2: Anomalies of annual averages of the clear-sky planetary albedo (%).

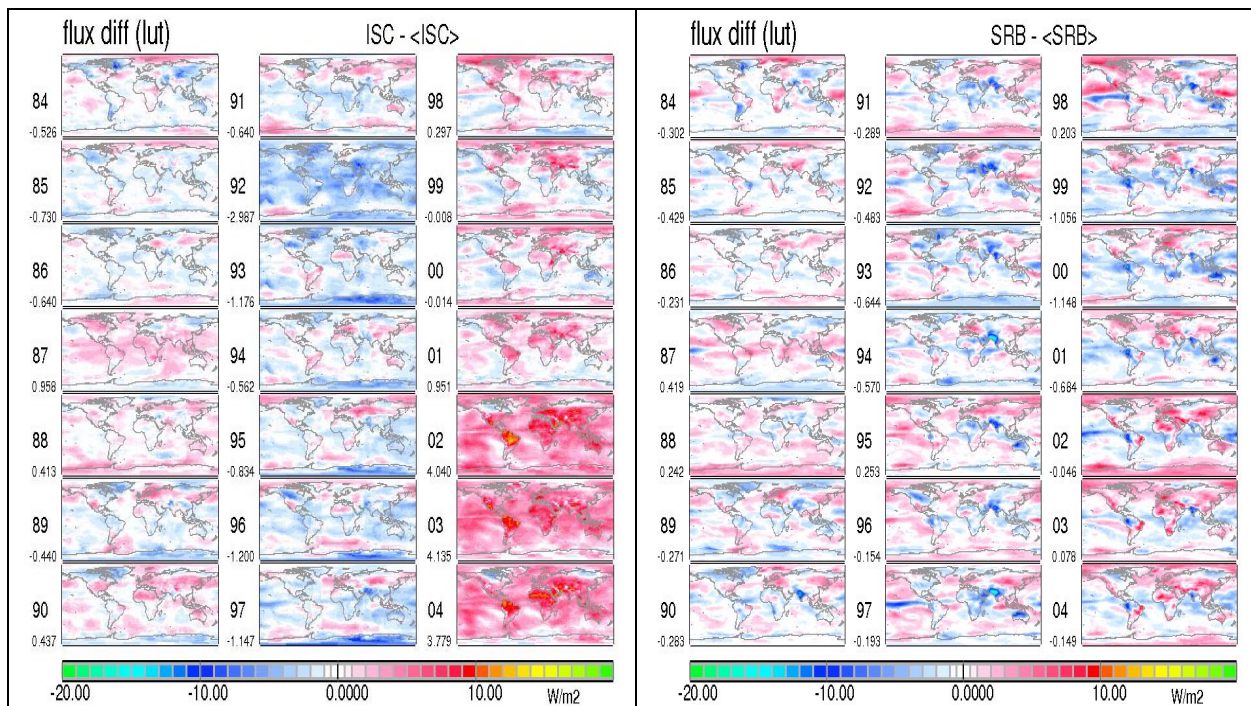
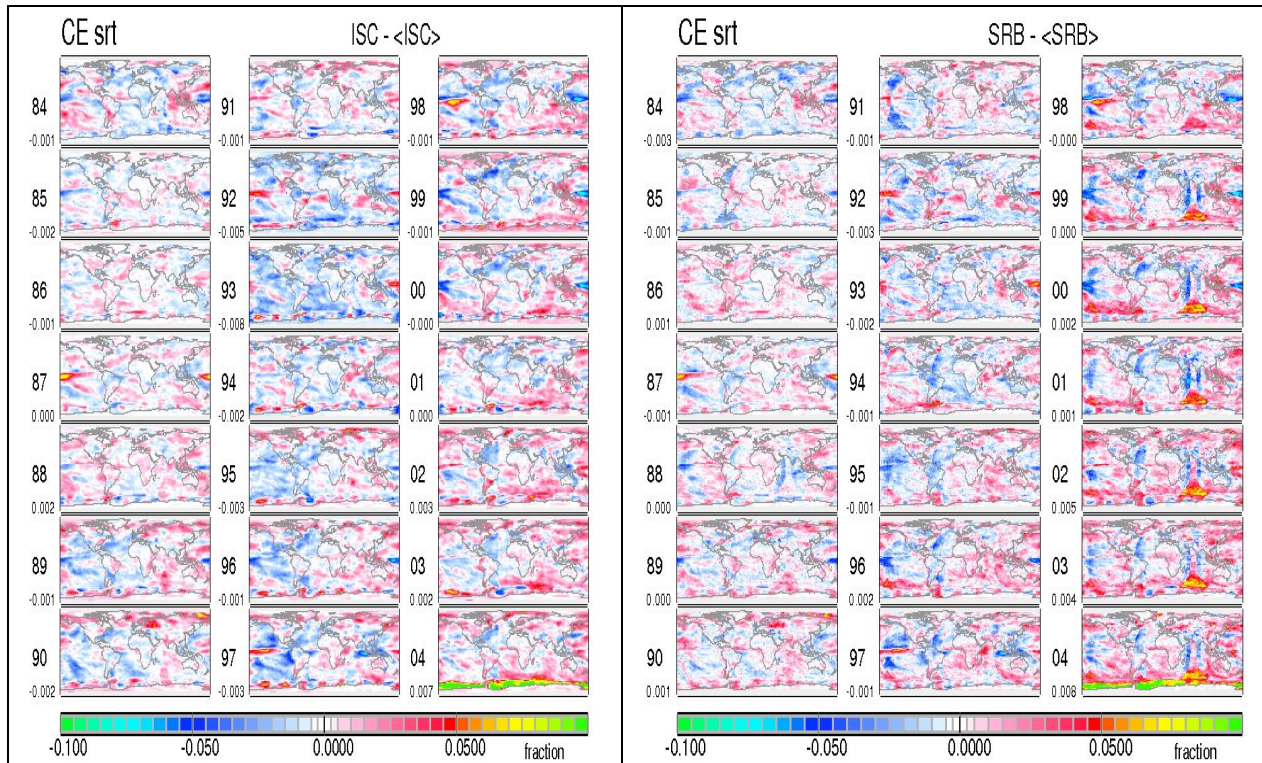
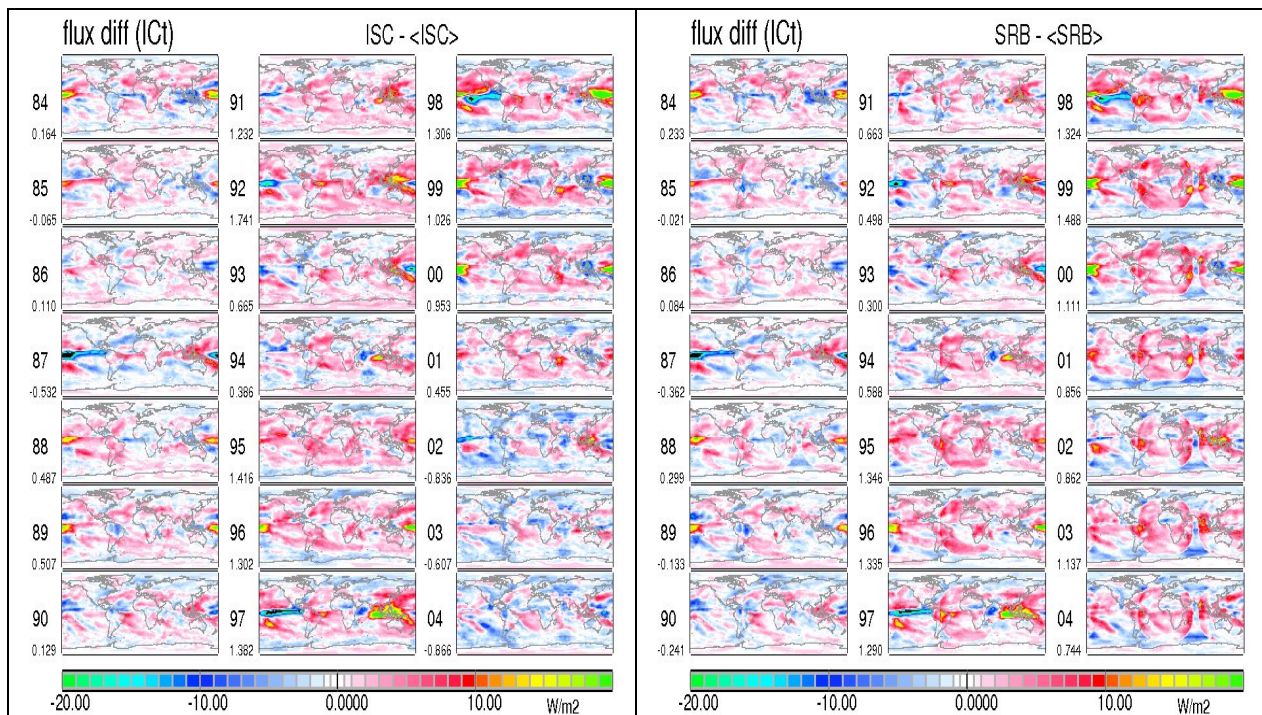


Figure C3.5.3: Clear-sky outgoing longwave radiation at TOA.

### C3.5.2.2 Cloud Radiative Effects on the planetary albedo and OLR at TOA



**Figure C.3.5.4:** Anomalies of annual averages of the cloud radiative effect on the planetary albedo (%) at TOA. Note, the pattern in results of both projects is quite similar, since both use the same cloud information. Both show a tendency of increasing CRE after the year 1994; both however show also artifacts due to geostationary satellites.



**Figure C.3.5.5:** Cloud radiative effect on outgoing longwave radiation at TOA.

### C3.5.2.3 All-sky total net radiation at TOA

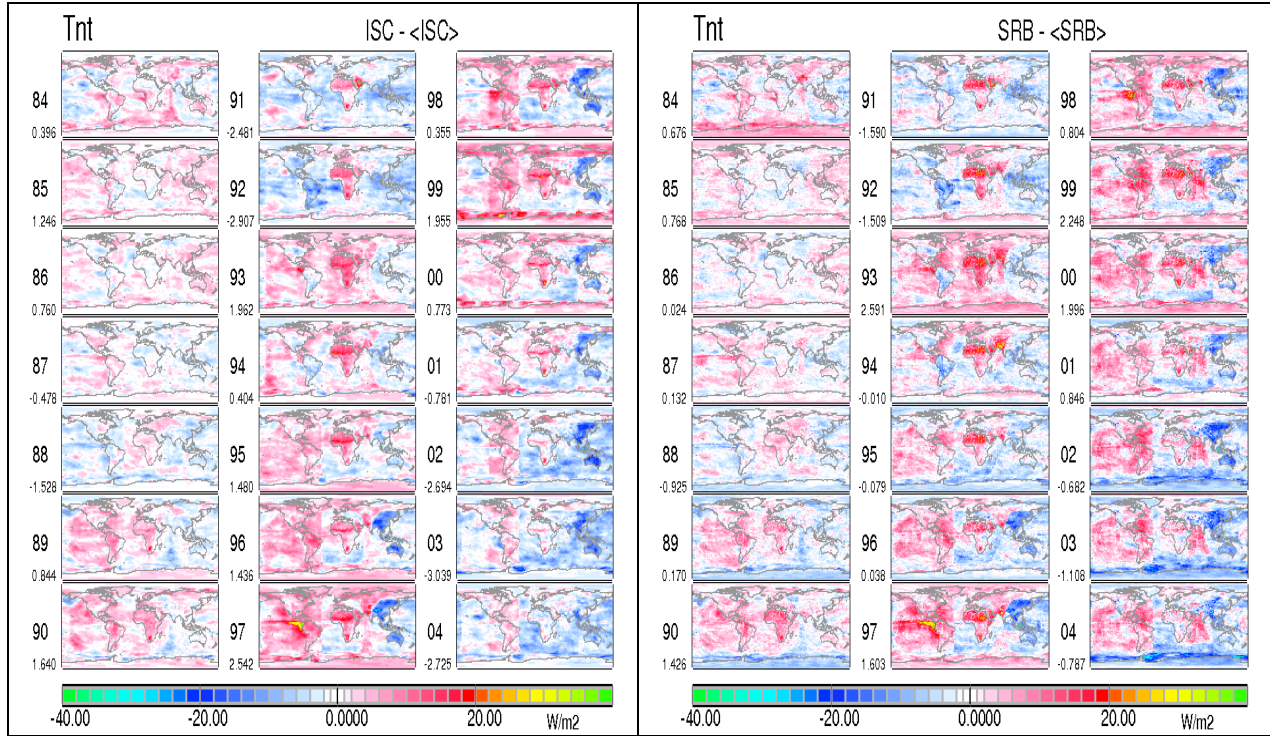


Figure C.3.5.6: All-sky total net radiation at TOA.

### C3.5.3: Comparison of seasonal maps of ISCCP & SRB with CERES (March 2000 to February 2004)

#### C3.5.3.1: Clear-sky planetary albedo at TOA

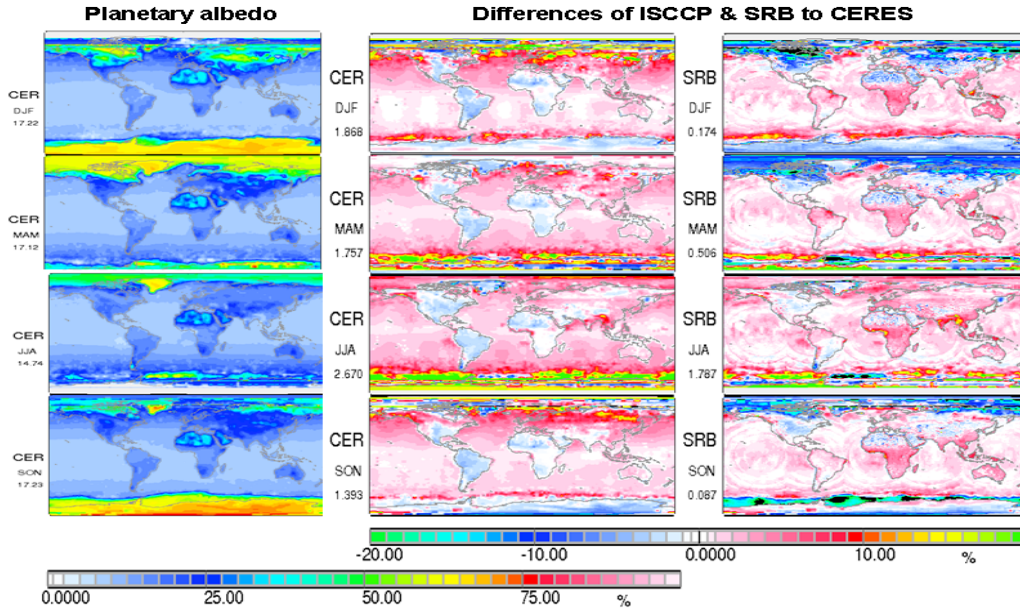


Figure C.3.5.7: Seasonal anomalies of the clear sky albedo at TOA (left and lower scale) and differences of ISCCP & SRB data to CERES.

#### C3.5.3.2 Clear-sky outgoing longwave radiation at TOA

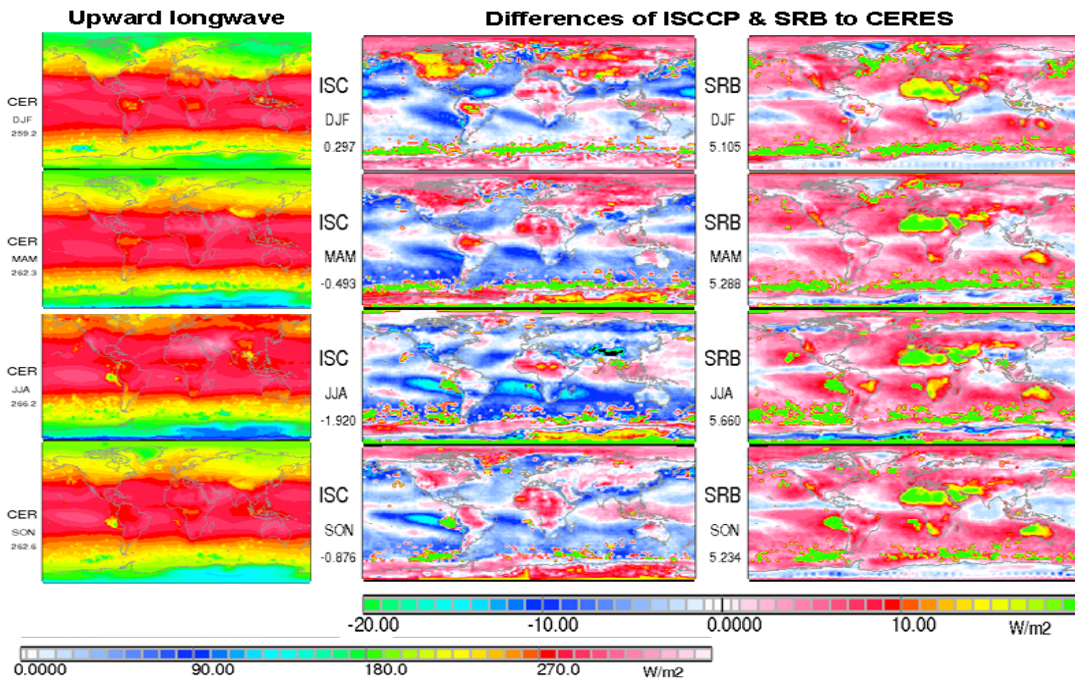
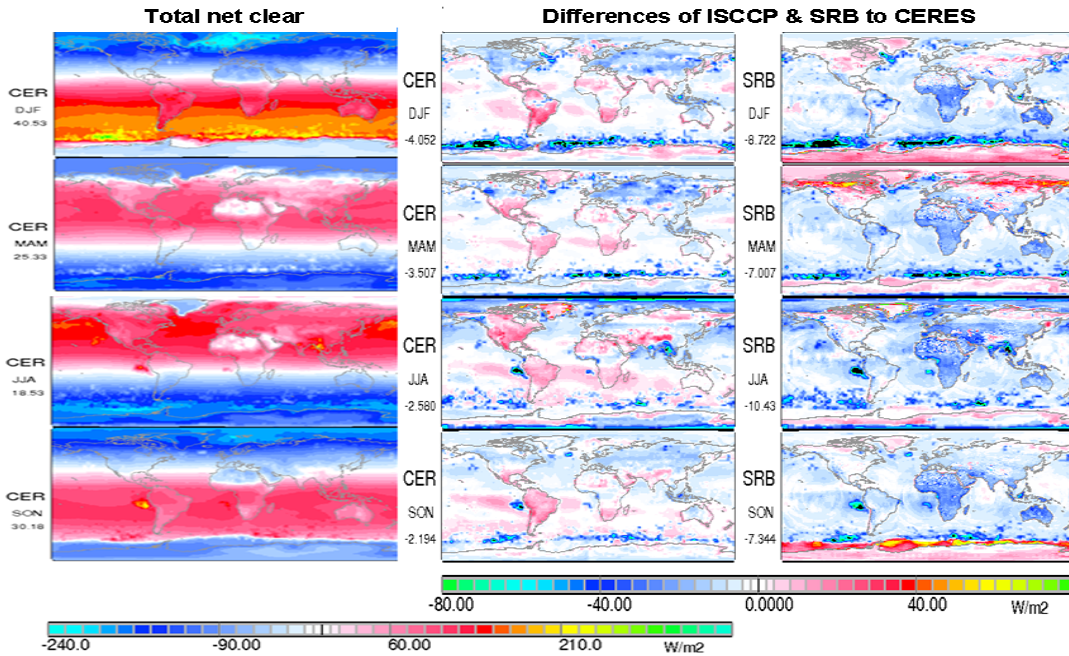
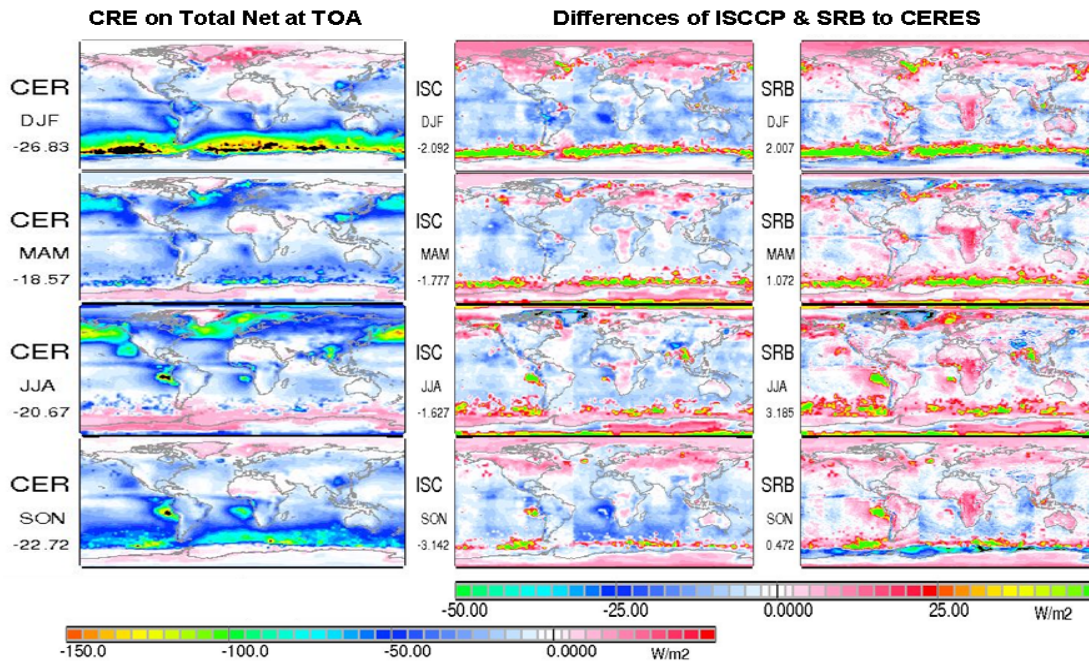


Figure C.3.5.8: Seasonal averages of the clear-sky emission of the earth at TOA (left and lower scale). ISCCP values are mostly smaller of less than 15 W/m<sup>2</sup> over low level cloud decks over the oceans, while the emission of SRB results can be up to 20 W/m<sup>2</sup> higher, in particular over subtropical continental surfaces.

### C3.5.3.3 Clear-sky total net radiation at TOA



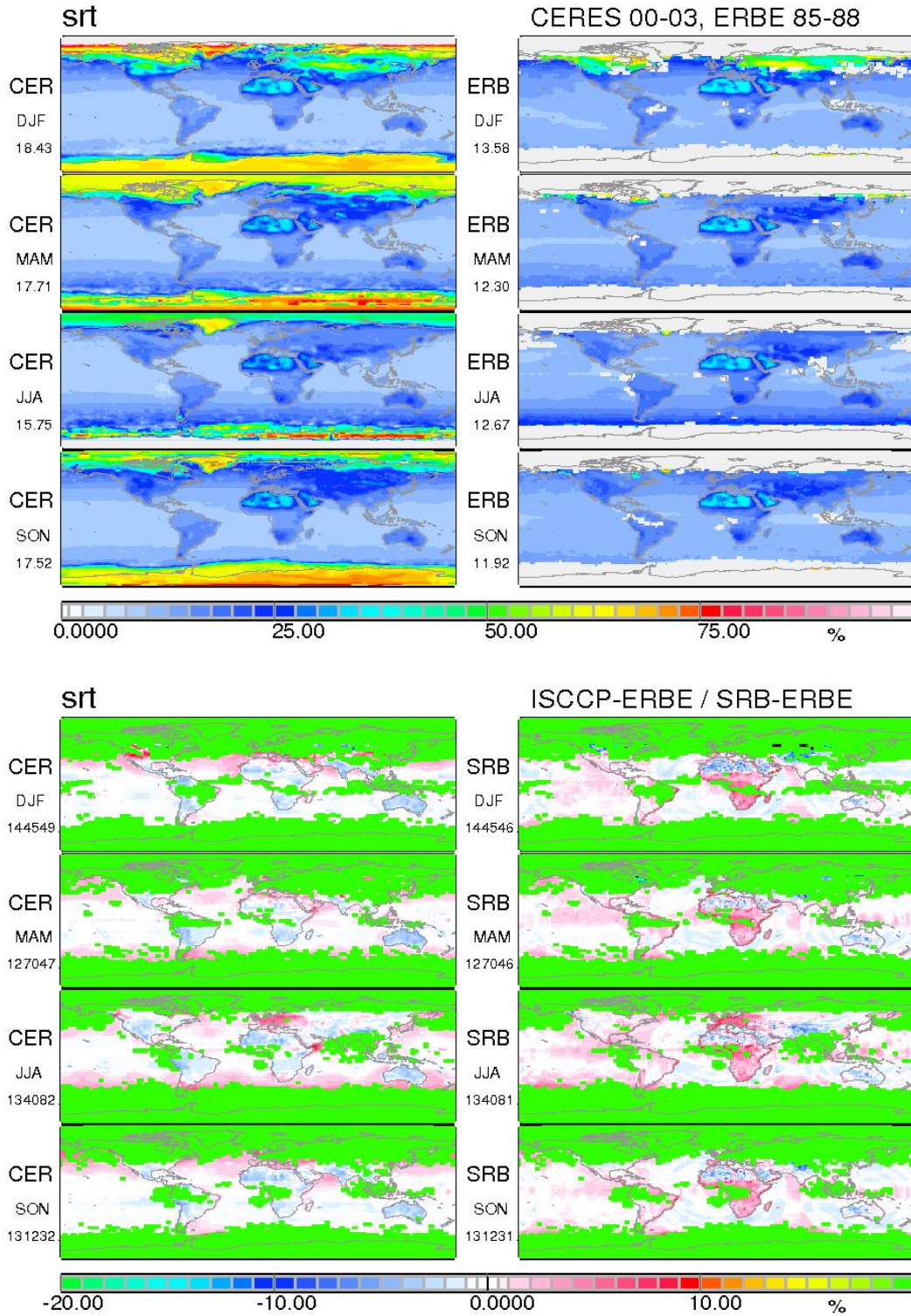
**Figure C.3.5.9:** Seasonal averages of the clear-sky emission of the earth at TOA (left and lower scale). Global averages range between 16 (JJA) and 40 (NDJ)  $Wm^{-2}$ . Over the oceans the ISCCP/SRB results are smaller than CERES by about 20 to 30  $Wm^{-2}$ ; over the continents we find both positive and negative differences of the same order of magnitude.



**Figure C.3.5.10:** Seasonal values of the cloud radiative effects on the total net radiation at TOA (left and lower scale) in CERES data and differences of ISCCP & SRB to values of the ISCCP (right). These are averages over the period of 4 years from March 2000 to February 2004. Note the CERES-CRE is based on statistically selected cloud-free areas.

**C3.5.4: Comparison of ISCCP & SRB with ERBE (January 1985 to December 1988)**

**C3.5.4.1: Clear-sky planetary albedo at TOA**



*Figures C.3.5.11: Clear sky planetary albedo of CERES (March 2000 to February 2004) and ERBE (top) (January 1985 to December 2008) and differences of ISCCP & SRB to ERBE (bottom) (January 1985 to December 2008).*

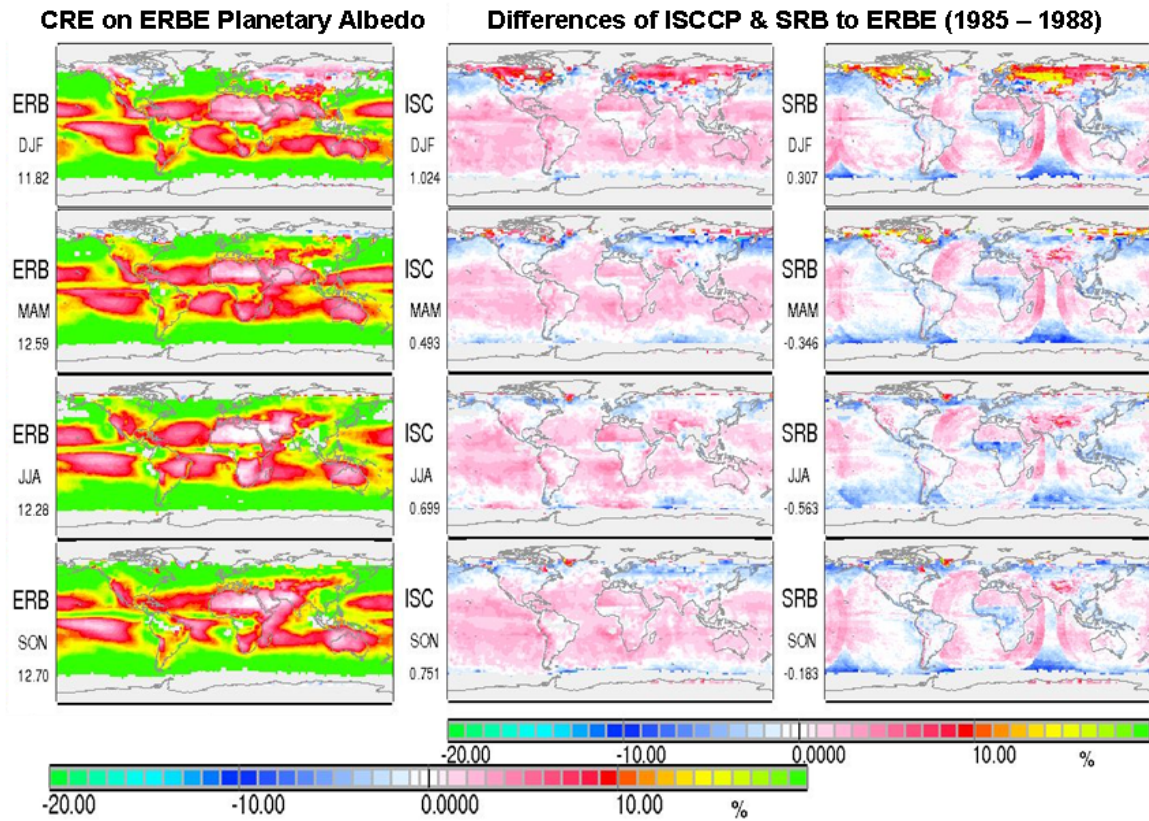
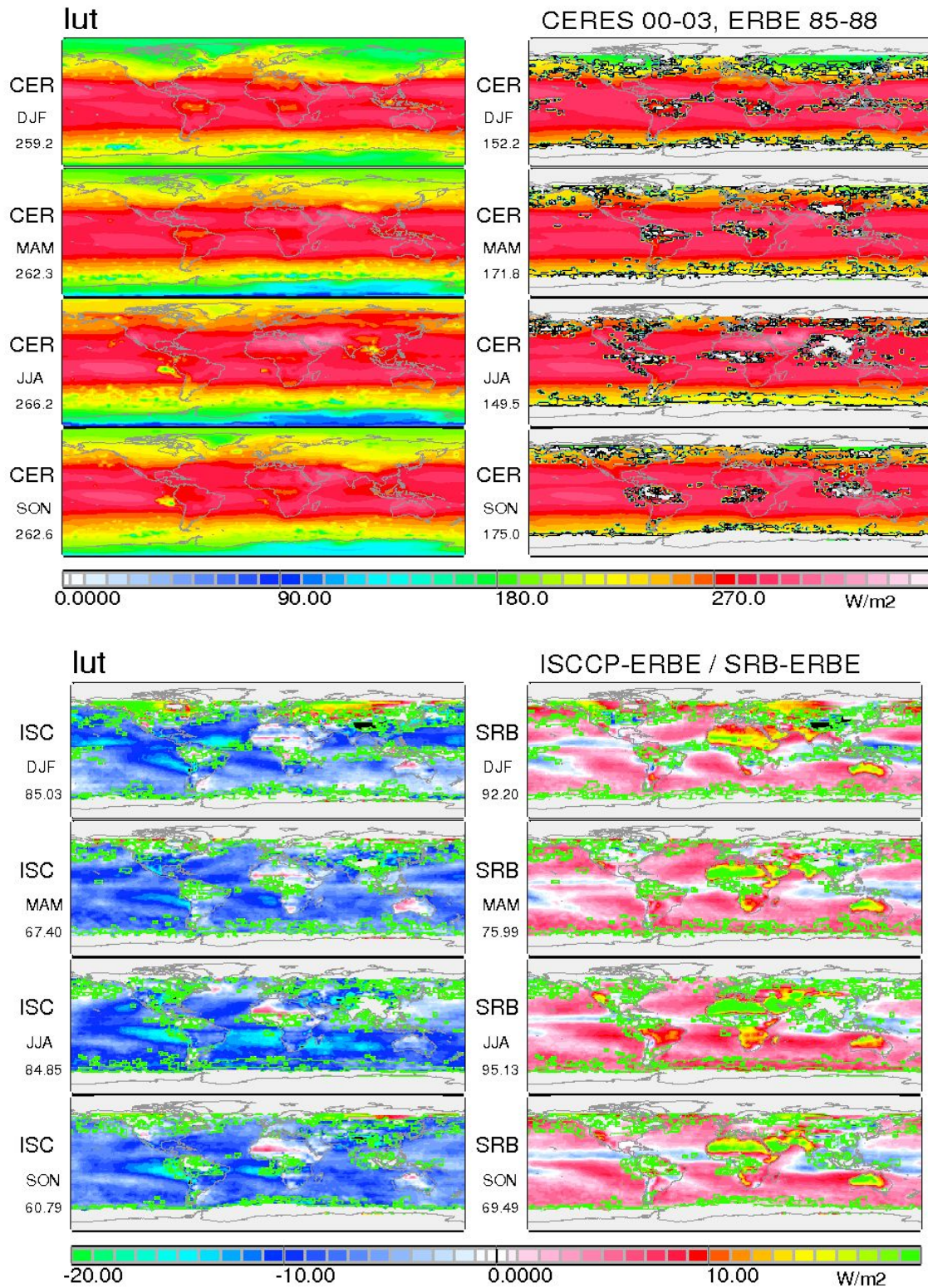


*Figure C.3.5.12: Seasonal averages of the CRE on the planetary albedo (left and lower scale), averaged over 4 seasons of the period January 1985 to December 1988, as derived from measurements of the ERBE project, and their differences to ISCCP and SRB values. Note: ERBE data do not cover both Polar Regions.*

### C3.5.4.2: Clear sky emission of longwave radiation to space



Figures C.3.5.13: Clear sky emission of longwave radiation to space of CERES (March 2000 to February 2004) and ERBE (top) (January 1985 to December 2008) and differences of ISCCP & SRB to ERBE (bottom) (January 1985 to December 2008).

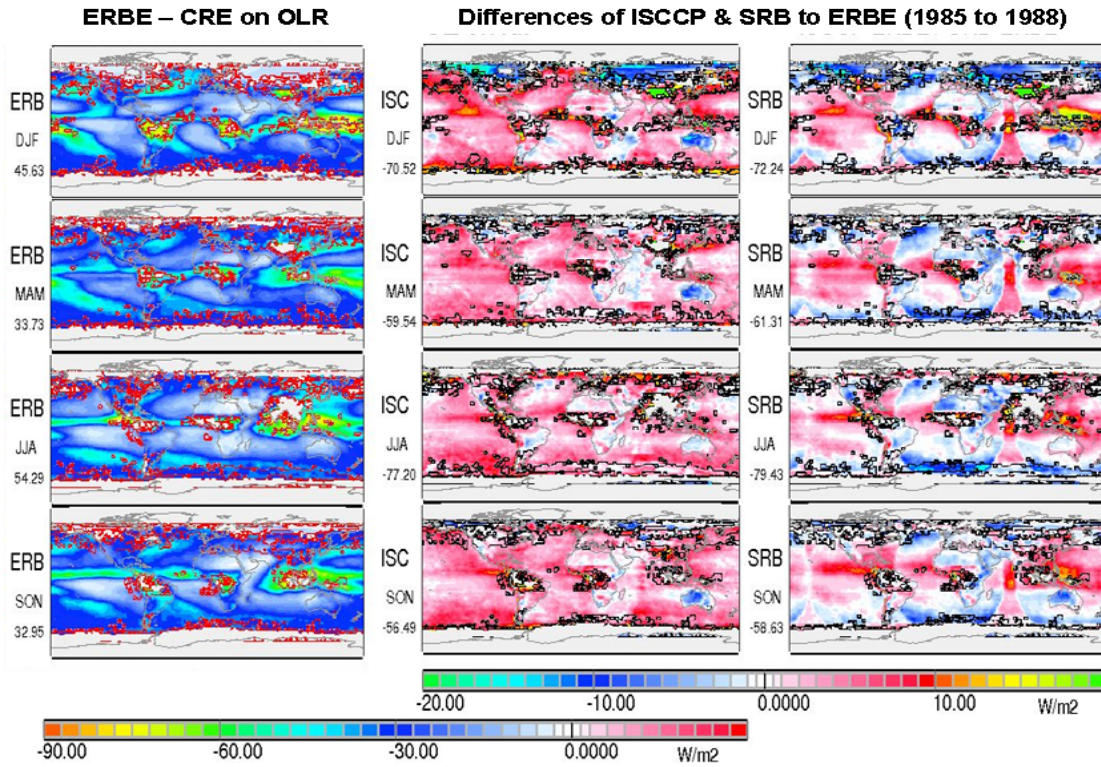
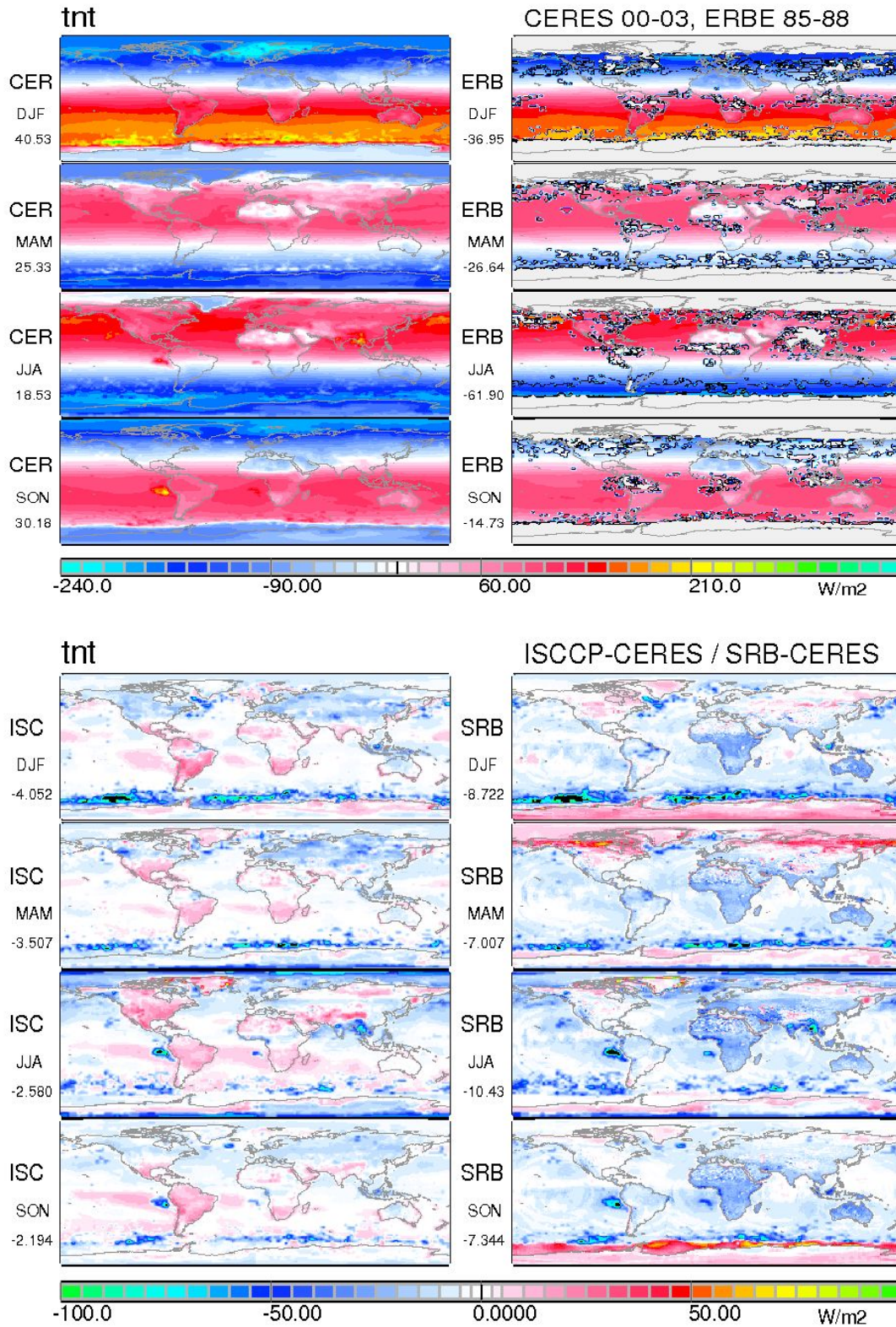


**Figure C.3.5.14:** Seasonal averages of the CRE on the outgoing longwave radiation (left and lower scale), averaged over 4 seasons of the period January 1985 to December 1988, as derived from measurements of the ERBE project, and their differences to ISCCP and SRB values. Note: ERBE data do not cover both polar regions. The colored and black framed spots in the lower diagrams are due to data gaps in cloud-free data fields of the ERBE.

**C3.5.4.3: Total clear sky radiation budget at TOA**



**Figures C.3.5.15: Clear sky total radiation budget at TOA of CERES (March 2000 to February 2004) and ERBE (January 1985 to December 2008) (top) and differences of ISCCP & SRB to ERBE (bottom) (January 1985 to December 2008).**

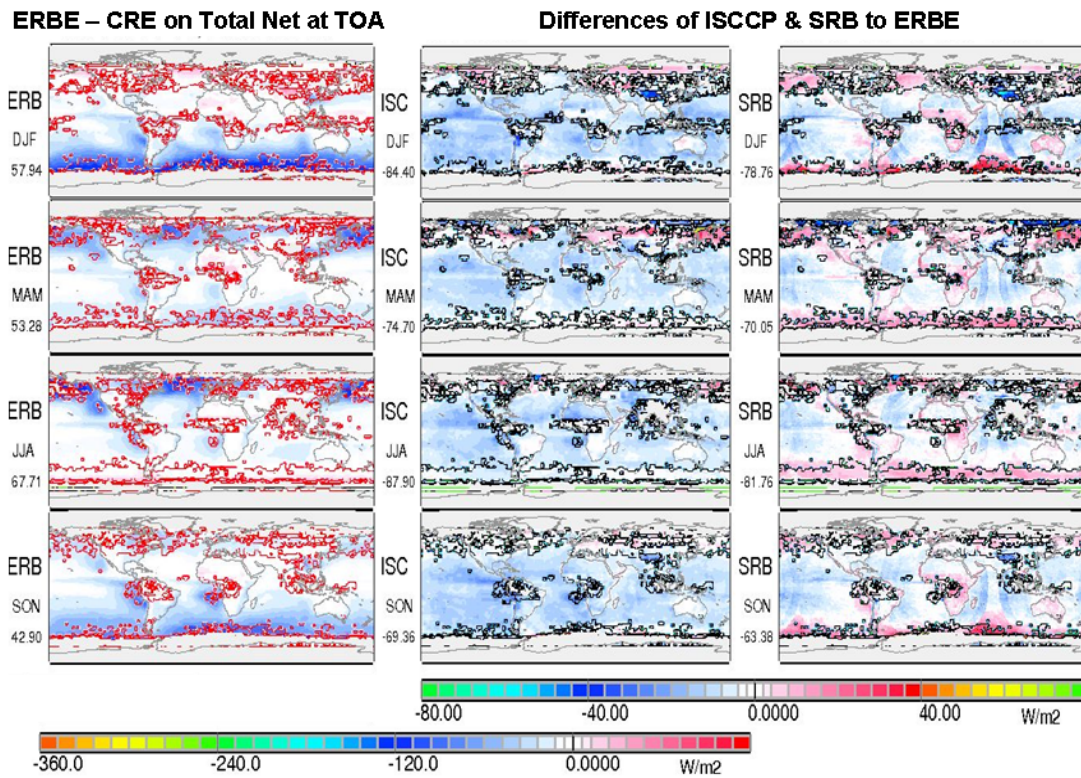


*Figure C.3.5.16: Seasonal averages of the CRE on the total net radiation budget at TOA (left and lower scale), averaged over 4 seasons of the period January 1985 to December 1988, as derived from measurements of the ERBE project, and their differences to ISCCP and SRB values. Note: ERBE data do not cover both Polar regions.*

## Appendix C4.3 for Chapter 4.3:

# Seasonal Cycles

L. Hinkelman

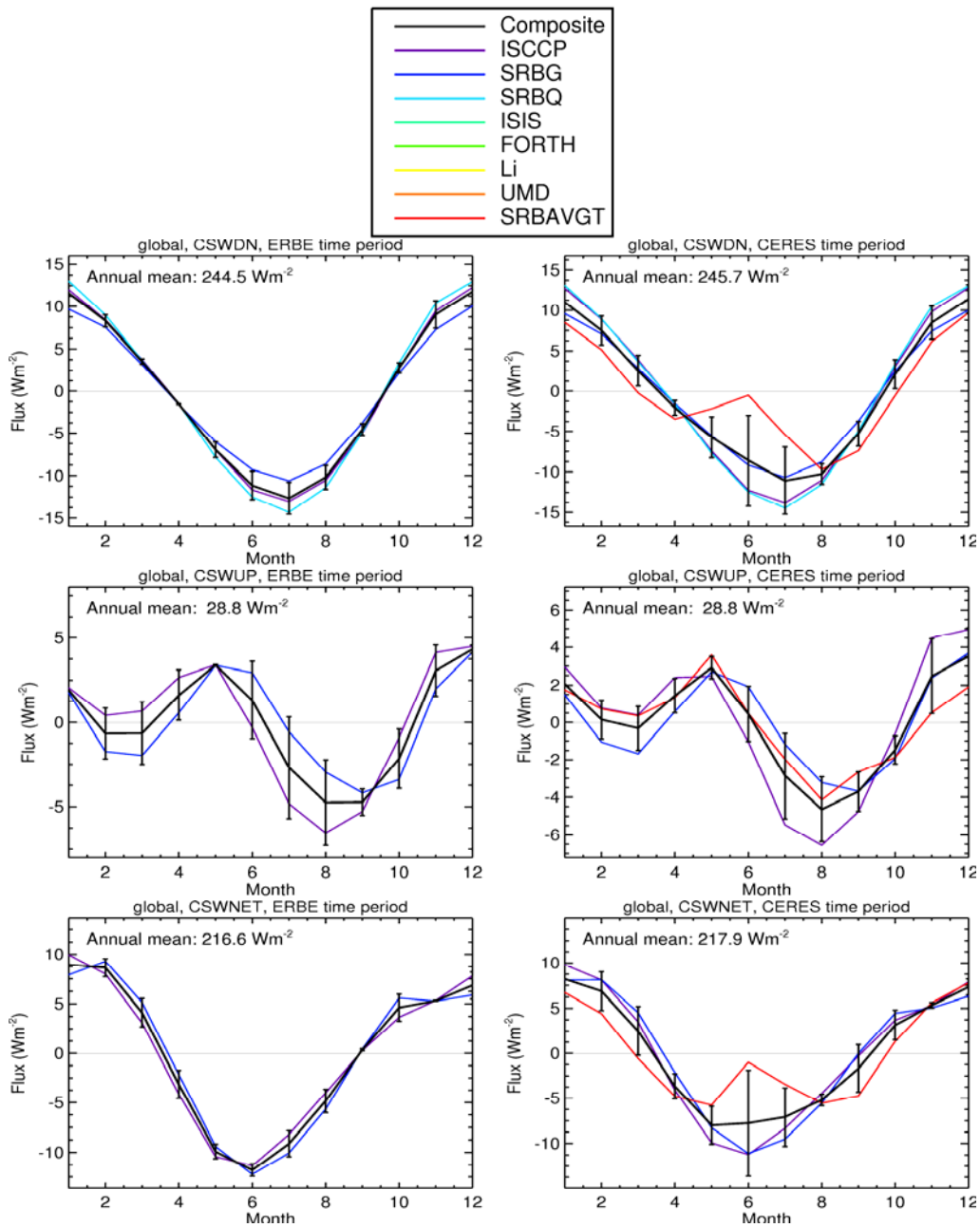


**Figure 4.3.2:** Global mean annual cycles for *clear-sky shortwave parameters* over the ERBE and CERES time periods shown as deviations from the corresponding annual mean. Error bars indicate +/- one standard deviation.

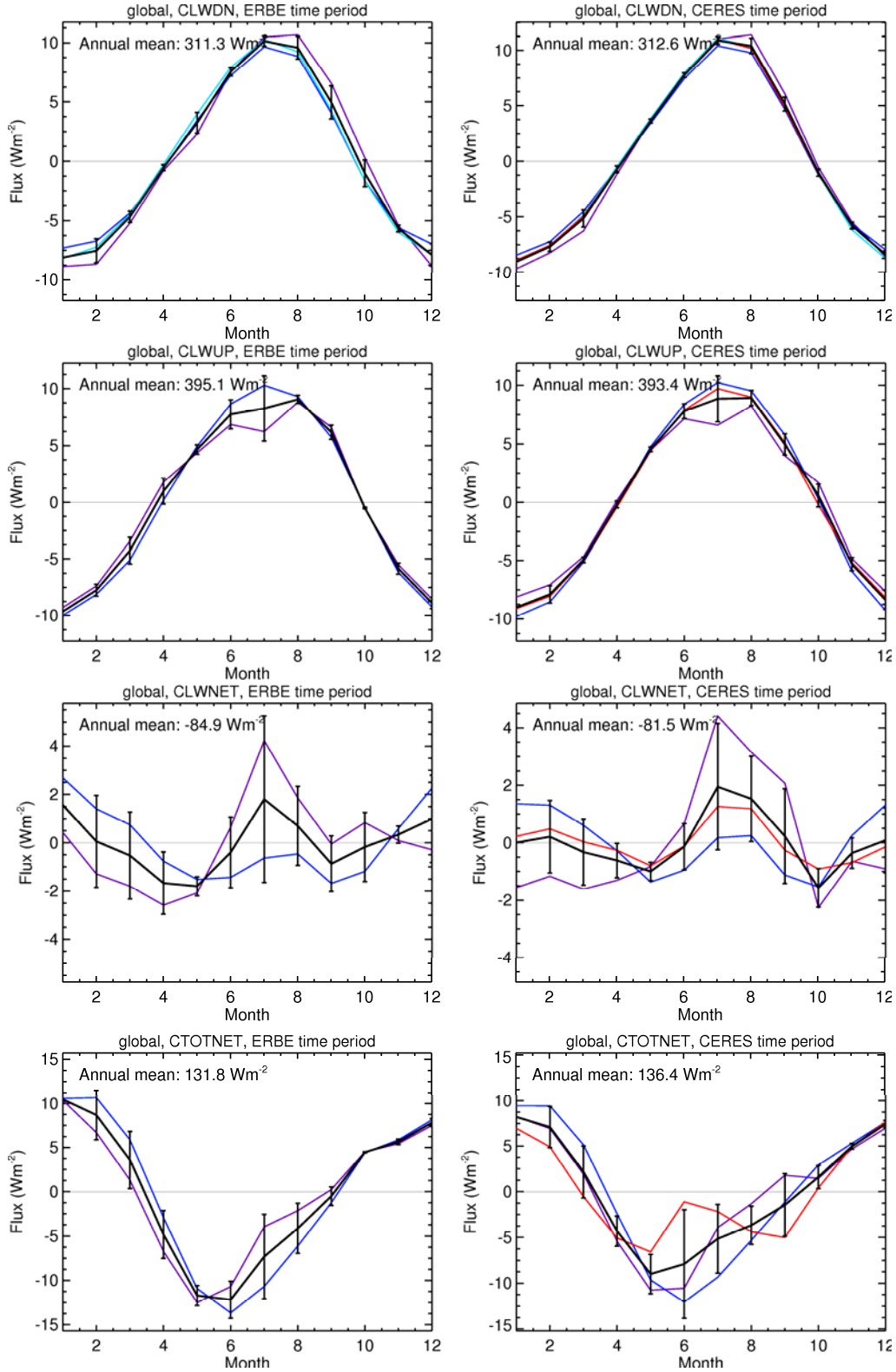


**Figure 4.3.4:** Global mean annual cycles for clear-sky longwave parameters and total net flux over the ERBE and CERES time periods shown as deviations from the corresponding annual mean. Error bars indicate  $\pm$  one standard deviation.

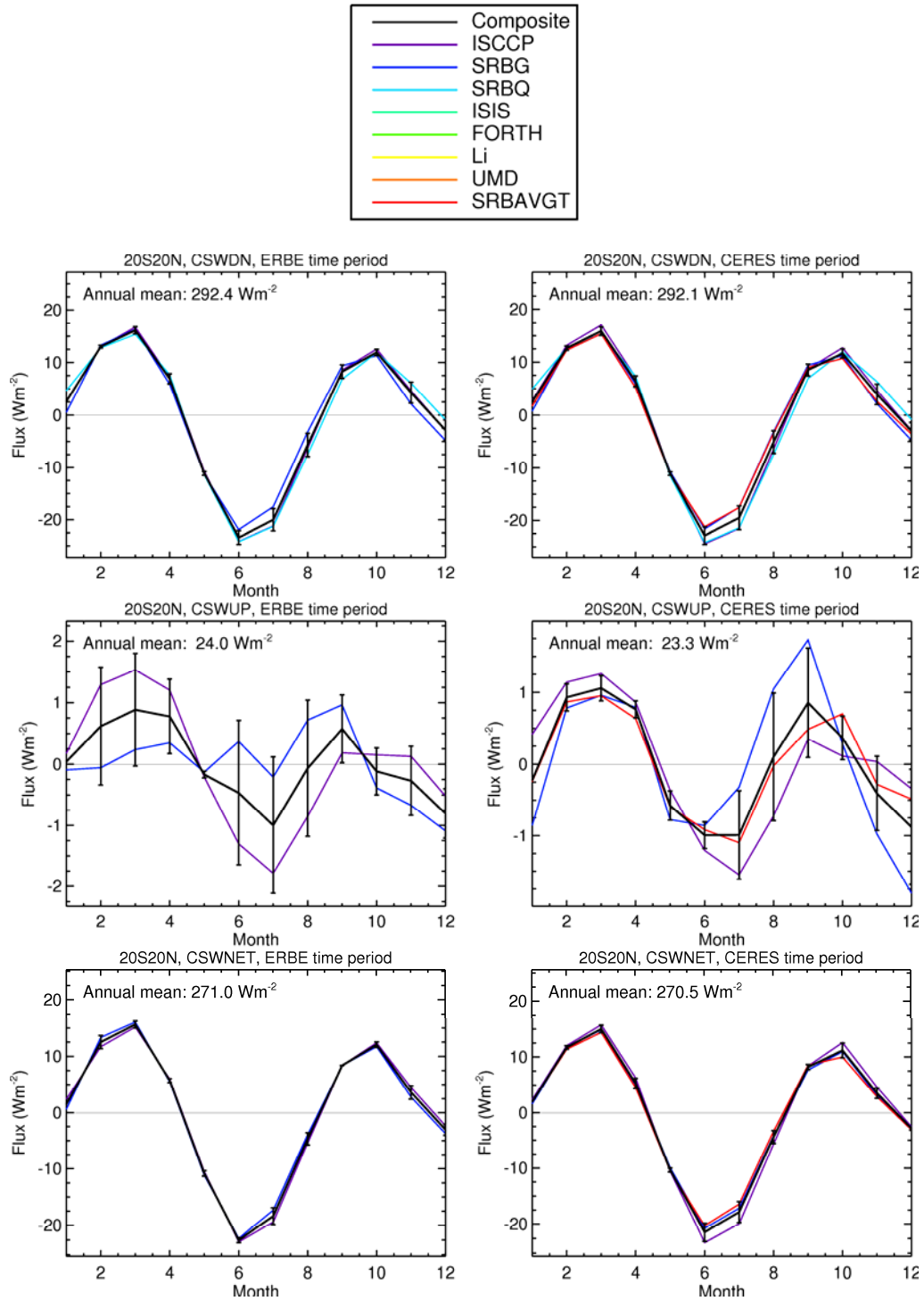


**Figure 4.3.7:** Tropical (20°S-20°N) mean annual cycles for clear-sky shortwave parameters over the ERBE and CERES time periods shown as deviations from the corresponding annual mean. Error bars indicate  $\pm$  one standard deviation.

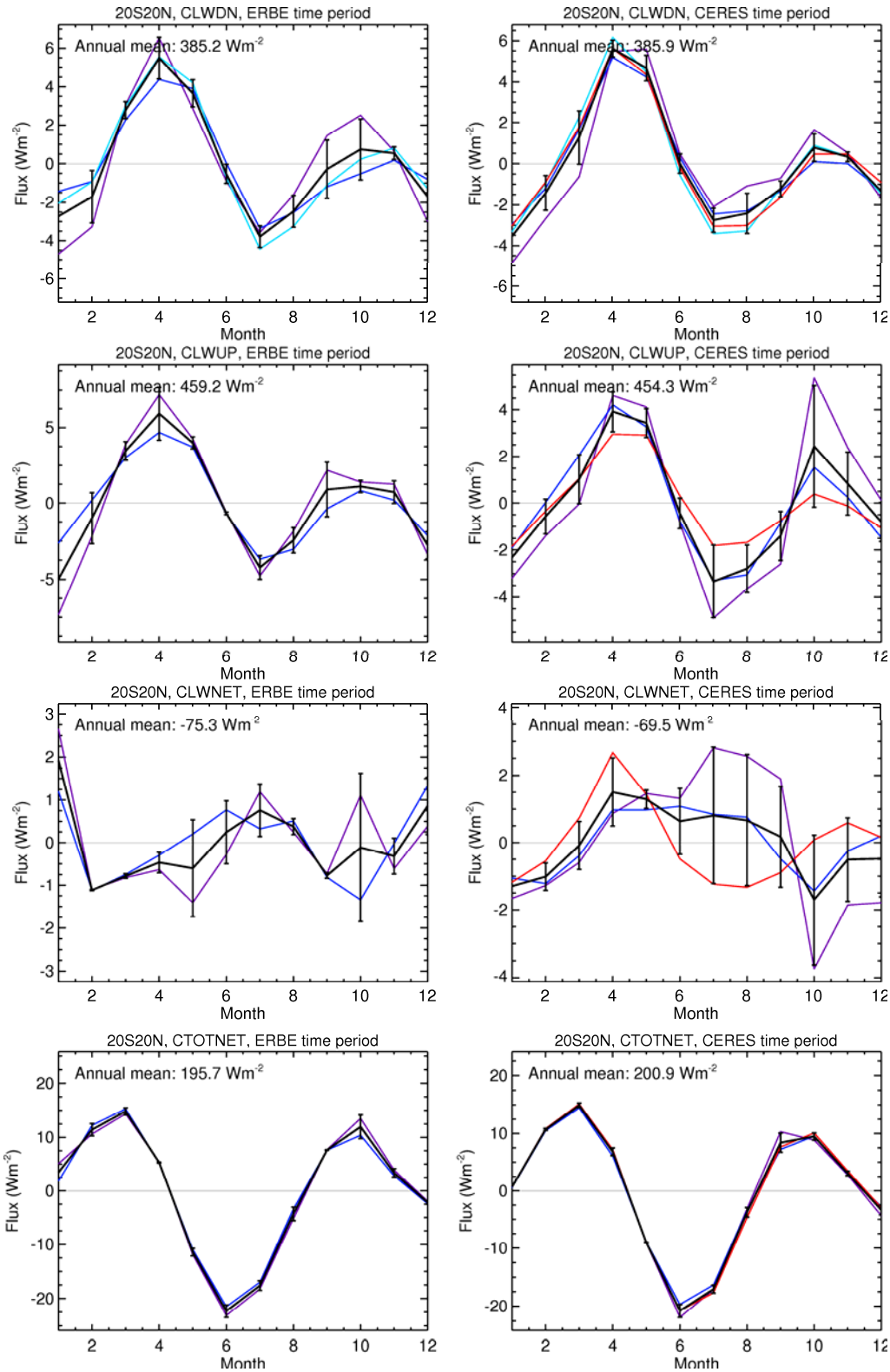


**Figure 4.3.8:** Tropical ( $20^{\circ}\text{S}$ - $20^{\circ}\text{N}$ ) mean annual cycles for clear-sky LW parameters and total net flux over the ERBE and CERES time periods shown as deviations from the corresponding annual mean. Error bars show  $\pm$  one standard deviation.

**Table 4.3.4:** Global mean annual cycle data for ASWUP over all data sets, ERBE and CERES time periods. All values are for monthly mean anomalies from the overall annual average except for the overall monthly means listed in the first column. Relative standard deviations are computed with respect to the corresponding monthly mean. Annual means: ERBE period =  $23.3 \text{ Wm}^{-2}$ , CERES period =  $22.9 \text{ Wm}^{-2}$ .

Month	ERBE period						CERES period					
	Mean	Anom	St Dev	Rel StD	Range	N	Mean	Anom	St Dev	Rel StD	Range	N
1	24.9	1.6	0.2	1.0%	1.4, 1.9	4	24.7	1.8	0.6	2.4%	1.0, 2.6	5
2	23.1	-0.2	0.8	3.5%	-1.1, 0.7	4	23.1	0.2	0.6	2.4%	-0.5, 1.0	5
3	22.7	-0.6	0.9	3.9%	-1.5, 0.5	4	22.6	-0.3	0.8	3.6%	-1.1, 0.7	5
4	24.2	0.9	0.8	3.2%	0.2, 2.0	4	23.7	0.8	0.8	3.5%	-0.3, 1.7	5
5	25.5	2.2	0.4	1.5%	1.7, 2.6	4	24.7	1.9	0.7	3.0%	1.2, 3.1	5
6	24.0	0.7	1.0	4.1%	-0.6, 1.7	4	23.1	0.2	1.0	4.2%	-1.4, 1.0	5
7	21.3	-2.0	1.5	7.2%	-4.2, -0.7	4	20.8	-2.1	1.5	7.3%	-4.7, -1.0	5
8	19.7	-3.6	1.4	6.9%	-5.6, -2.6	4	19.4	-3.5	1.1	5.7%	-5.3, -2.7	5
9	19.9	-3.4	0.5	2.7%	-4.1, -2.9	4	19.8	-3.1	0.6	2.8%	-3.7, -2.4	5
10	22.1	-1.2	0.8	3.6%	-2.3, -0.4	4	21.8	-1.1	0.7	3.0%	-1.9, -0.2	5
11	25.7	2.4	0.8	2.9%	1.7, 3.5	4	24.9	2.1	1.3	5.4%	-0.0, 3.6	5
12	26.6	3.3	0.4	1.5%	3.0, 3.9	4	25.9	3.0	1.1	4.1%	1.3, 4.2	5

**Table 4.3.5:** Global mean annual cycle data for ASWNET over all data sets, ERBE and CERES time periods. All values are for monthly mean anomalies from the overall annual average except for the overall monthly means listed in the first column. Relative standard deviations are computed with respect to the corresponding monthly mean. Annual means: ERBE period =  $163.5 \text{ Wm}^{-2}$ , CERES period =  $167.6 \text{ Wm}^{-2}$ .

Month	ERBE period						CERES period					
	Mean	Anom	St Dev	Rel StD	Range	N	Mean	Anom	St Dev	Rel StD	Range	N
1	167.2	3.7	1.2	0.7%	2.2, 5.4	5	171.0	3.4	1.2	0.7%	2.2, 5.2	5
2	168.9	5.4	0.5	0.3%	4.6, 6.1	5	172.6	5.0	0.9	0.5%	3.6, 5.7	5
3	167.3	3.8	0.6	0.3%	2.9, 4.4	5	172.3	4.7	1.8	1.1%	2.4, 6.3	5
4	164.0	0.5	0.6	0.4%	-0.3, 1.2	5	167.8	0.2	1.0	0.6%	-0.9, 1.4	5
5	158.6	-4.9	0.7	0.5%	-5.8, -3.8	5	163.9	-3.7	1.0	0.6%	-4.8, -2.4	5
6	156.4	-7.1	0.8	0.5%	-8.1, -6.0	5	161.8	-5.8	3.1	1.9%	-7.8, -0.2	5
7	158.3	-5.2	0.9	0.6%	-6.0, -3.7	5	163.3	-4.2	1.6	1.0%	-5.3, -1.4	5
8	161.1	-2.4	0.5	0.3%	-3.1, -1.7	5	166.0	-1.6	0.6	0.4%	-2.4, -0.9	5
9	164.9	1.4	0.5	0.3%	0.7, 2.0	5	168.5	0.9	1.2	0.7%	-1.2, 1.9	5
10	165.7	2.2	0.7	0.4%	1.4, 3.1	5	169.0	1.4	1.3	0.8%	-0.8, 2.5	5
11	164.3	0.8	0.9	0.5%	-0.3, 2.0	5	167.3	-0.3	1.2	0.7%	-1.7, 1.4	5
12	165.2	1.8	0.9	0.6%	0.4, 2.8	5	167.7	0.1	1.5	0.9%	-1.8, 2.1	5

**Table 4.3.6:** Global mean annual cycle data for ALWDN over all data sets, ERBE and CERES time periods. All values are for monthly mean anomalies from the overall annual average except for the overall monthly means listed in the first column. Relative standard deviations are computed with respect to the corresponding monthly mean. Annual means: ERBE period =  $345.5 \text{ Wm}^{-2}$ , CERES period =  $344.9 \text{ Wm}^{-2}$ .

Month	ERBE period						CERES period					
	Mean	Anom	St Dev	Rel StD	Range	N	Mean	Anom	St Dev	Rel StD	Range	N
1	337.6	-7.9	0.6	0.2%	-8.4, -7.2	4	336.9	-8.0	0.6	0.2%	-8.8, -7.2	5
2	338.3	-7.2	0.2	0.1%	-7.4, -6.9	4	337.5	-7.4	0.3	0.1%	-7.8, -7.0	5
3	341.4	-4.0	0.2	0.1%	-4.3, -3.9	4	339.8	-5.1	0.8	0.2%	-6.4, -4.6	5
4	345.2	-0.3	0.9	0.3%	-1.7, 0.4	4	344.1	-0.8	0.7	0.2%	-2.0, -0.1	5
5	348.6	3.1	1.4	0.4%	1.0, 4.0	4	348.3	3.3	0.5	0.1%	2.5, 3.8	5
6	352.7	7.3	0.2	0.1%	7.0, 7.5	4	352.0	7.1	0.2	0.1%	6.8, 7.3	5
7	354.4	8.9	0.5	0.1%	8.5, 9.6	4	354.5	9.6	0.4	0.1%	8.9, 10.0	5
8	354.1	8.6	0.4	0.1%	8.2, 9.1	4	354.1	9.2	0.4	0.1%	8.6, 9.7	5
9	349.9	4.4	0.9	0.3%	3.7, 5.7	4	349.6	4.7	0.5	0.2%	3.9, 5.2	5
10	344.2	-1.3	0.8	0.2%	-1.8, -0.0	4	344.4	-0.6	0.5	0.1%	-1.0, 0.2	5
11	340.6	-4.9	0.6	0.2%	-5.5, -4.1	4	340.1	-4.9	0.7	0.2%	-5.5, -3.8	5
12	338.7	-6.8	0.4	0.1%	-7.1, -6.2	4	337.8	-7.1	0.7	0.2%	-7.9, -6.0	5

**Table 4.3.7:** Global mean annual cycle data for ALWUP over all data sets, ERBE and CERES time periods. All values are for monthly mean anomalies from the overall annual average except for the overall monthly means listed in the first column. Relative standard deviations are computed with respect to the corresponding monthly mean. Annual means: ERBE period =  $395.3 \text{ Wm}^{-2}$ , CERES period =  $394.8 \text{ Wm}^{-2}$ .

Month	ERBE period						CERES period					
	Mean	Anom	St Dev	Rel StD	Range	N	Mean	Anom	St Dev	Rel StD	Range	N
1	386.2	-9.1	0.8	0.2%	-10.0, -8.0	4	385.9	-8.9	0.8	0.2%	-9.8, -8.0	5
2	387.7	-7.5	0.5	0.1%	-8.1, -7.0	4	387.0	-7.8	0.7	0.2%	-8.6, -7.0	5
3	391.0	-4.3	0.7	0.2%	-5.1, -3.4	4	390.0	-4.8	0.3	0.1%	-5.1, -4.3	5
4	395.9	0.6	0.8	0.2%	0.0, 1.8	4	394.6	-0.2	0.2	0.1%	-0.4, 0.1	5
5	399.9	4.6	0.4	0.1%	4.3, 5.0	4	399.2	4.5	0.4	0.1%	3.9, 4.9	5
6	403.0	7.7	0.8	0.2%	6.8, 8.7	4	402.4	7.7	0.6	0.2%	6.9, 8.4	5
7	403.9	8.7	1.8	0.4%	6.1, 10.3	4	403.7	9.0	1.5	0.4%	6.5, 10.2	5
8	403.9	8.6	0.5	0.1%	8.2, 9.3	4	403.6	8.8	0.5	0.1%	8.1, 9.5	5
9	400.6	5.4	1.0	0.3%	4.2, 6.6	4	399.8	5.0	0.7	0.2%	3.9, 5.8	5
10	394.6	-0.7	0.4	0.1%	-1.3, -0.3	4	395.0	0.3	0.9	0.2%	-0.5, 1.7	5
11	389.6	-5.7	0.4	0.1%	-6.2, -5.4	4	389.4	-5.3	0.5	0.1%	-5.9, -4.7	5
12	386.9	-8.3	0.8	0.2%	-9.3, -7.4	4	386.5	-8.3	0.8	0.2%	-9.3, -7.5	5

**Table 4.3.8:** Global mean annual cycle data for ALWNET over all data sets, ERBE and CERES time periods. All values are for monthly mean anomalies from the overall annual average except for the overall monthly means listed in the first column. Relative standard deviations are computed with respect to the corresponding monthly mean. Annual means: ERBE period =  $-26.9 \text{ Wm}^{-2}$ , CERES period =  $-30.8 \text{ Wm}^{-2}$ .

Month	ERBE period						CERES period					
	Mean	Anom	St Dev	Rel StD	Range	N	Mean	Anom	St Dev	Rel StD	Range	N
1	-25.5	1.4	0.9	-3.5%	0.4, 2.3	4	-30.0	0.8	0.9	-3.0%	-0.3, 2.1	5
2	-26.4	0.5	0.6	-2.3%	-0.1, 1.3	4	-30.3	0.5	0.5	-1.8%	-0.0, 1.4	5
3	-26.8	0.2	0.9	-3.5%	-1.0, 1.2	4	-31.0	-0.2	0.9	-3.0%	-1.7, 0.5	5
4	-27.8	-0.9	1.7	-6.1%	-3.4, -0.0	4	-31.3	-0.6	0.9	-2.9%	-2.1, 0.2	5
5	-28.2	-1.3	1.5	-5.3%	-3.3, 0.3	4	-31.7	-0.9	0.9	-2.7%	-1.9, 0.5	5
6	-27.4	-0.5	0.9	-3.3%	-1.7, 0.4	4	-31.4	-0.6	0.5	-1.5%	-1.3, -0.1	5
7	-26.9	0.0	1.7	-6.3%	-1.6, 2.4	4	-30.6	0.2	1.4	-4.5%	-1.1, 2.4	5
8	-27.2	-0.3	0.7	-2.6%	-1.2, 0.4	4	-30.7	0.1	0.9	-2.9%	-1.0, 1.2	5
9	-27.8	-0.9	0.9	-3.2%	-2.0, 0.2	4	-31.0	-0.2	1.2	-3.9%	-1.9, 1.3	5
10	-27.3	-0.4	1.0	-3.6%	-1.2, 0.5	4	-31.5	-0.7	1.1	-3.3%	-2.0, 0.4	5
11	-26.2	0.8	0.7	-2.6%	0.0, 1.4	4	-30.2	0.6	0.5	-1.6%	0.1, 1.2	5
12	-25.5	1.4	1.4	-5.3%	-0.3, 3.0	4	-29.8	1.0	1.1	-3.8%	-0.4, 2.5	5

**Table 4.3.9:** Global mean annual cycle data for ATOTNET over all data sets, ERBE and CERES time periods. All values are for monthly mean anomalies from the overall annual average except for the overall monthly means listed in the first column. Relative standard deviations are computed with respect to the corresponding monthly mean. Annual means: ERBE period =  $-112.5 \text{ Wm}^{-2}$ , CERES period =  $115.8 \text{ Wm}^{-2}$ .

Month	ERBE period						CERES period					
	Mean	Anom	St Dev	Rel StD	Range	N	Mean	Anom	St Dev	Rel StD	Range	N
1	118.6	6.1	0.4	0.3%	5.7, 6.4	3	120.6	4.7	1.3	1.1%	3.3, 6.3	4
2	118.8	6.3	1.0	0.8%	5.4, 7.3	3	121.3	5.4	1.3	1.1%	3.8, 7.1	4
3	116.5	4.1	1.3	1.1%	3.1, 5.6	3	119.8	3.9	1.9	1.6%	2.0, 6.4	4
4	111.5	-1.0	2.4	2.2%	-3.8, 0.7	3	115.1	-0.8	1.4	1.3%	-2.3, 1.1	4
5	105.2	-7.2	1.6	1.5%	-9.1, -6.2	3	110.7	-5.2	1.4	1.3%	-6.6, -3.3	4
6	104.2	-8.3	1.3	1.2%	-9.7, -7.3	3	109.5	-6.4	3.7	3.4%	-8.9, -0.8	4
7	107.1	-5.4	2.4	2.2%	-7.3, -2.7	3	112.2	-3.7	2.1	1.9%	-6.0, -1.2	4
8	109.5	-3.0	1.1	1.0%	-4.3, -2.3	3	114.3	-1.6	0.9	0.8%	-2.3, -0.3	4
9	112.5	0.0	0.7	0.6%	-0.5, 0.8	3	116.2	0.4	1.7	1.4%	-1.1, 2.8	4
10	114.3	1.8	1.4	1.2%	0.4, 3.2	3	116.3	0.4	0.6	0.5%	-0.5, 1.0	4
11	114.9	2.4	0.1	0.1%	2.3, 2.5	3	116.6	0.7	0.8	0.6%	-0.0, 1.7	4
12	116.7	4.2	0.3	0.3%	3.9, 4.6	3	117.8	1.9	1.0	0.9%	1.0, 3.3	4

**Table 4.3.10:** Global mean annual cycle data for CSWDN over all data sets, ERBE and CERES time periods. All values are for monthly mean anomalies from the overall annual average except for the overall monthly means listed in the first column. Relative standard deviations are computed with respect to the corresponding monthly mean. Annual means: ERBE period =  $224.5 \text{ Wm}^{-2}$ , CERES period =  $245.7 \text{ Wm}^{-2}$ .

Month	ERBE period							CERES period						
	Mean	Anom	St Dev	Rel StD	Range	N	Mean	Anom	St Dev	Rel StD	Range	N		
1	256.1	11.6	1.7	0.7%	9.7, 13.1	3	256.6	11.0	2.3	0.9%	8.5, 13.1	4		
2	252.8	8.3	0.7	0.3%	7.5, 9.0	3	253.2	7.5	1.8	0.7%	5.2, 8.9	4		
3	248.0	3.5	0.3	0.1%	3.2, 3.8	3	248.2	2.6	1.9	0.8%	-0.2, 3.9	4		
4	242.9	-1.5	0.1	0.0%	-1.6, -1.5	3	243.6	-2.1	0.9	0.4%	-3.5, -1.5	4		
5	237.5	-7.0	0.9	0.4%	-7.9, -6.0	3	239.9	-5.7	2.6	1.1%	-7.7, -2.2	4		
6	233.3	-11.1	1.7	0.7%	-12.5, -9.3	3	237.1	-8.6	5.6	2.4%	-12.5, -0.5	4		
7	231.8	-12.6	1.9	0.8%	-14.3, -10.6	3	234.6	-11.1	4.1	1.8%	-14.5, -5.4	4		
8	234.3	-10.2	1.4	0.6%	-11.4, -8.6	3	235.4	-10.3	1.2	0.5%	-11.5, -8.8	4		
9	239.9	-4.6	0.7	0.3%	-5.0, -3.8	3	240.4	-5.3	1.5	0.6%	-7.4, -3.7	4		
10	247.3	2.8	0.6	0.2%	2.2, 3.4	3	247.8	2.1	1.8	0.7%	-0.6, 3.4	4		
11	253.5	9.1	1.6	0.6%	7.3, 10.4	3	254.1	8.5	2.0	0.8%	6.2, 10.5	4		
12	256.3	11.8	1.5	0.6%	10.0, 13.0	3	257.1	11.4	1.8	0.7%	9.7, 13.1	4		

**Table 4.3.11:** Global mean annual cycle data for CSWUP over all data sets, ERBE and CERES time periods. All values are for monthly mean anomalies from the overall annual average except for the overall monthly means listed in the first column. Relative standard deviations are computed with respect to the corresponding monthly mean. Annual means: ERBE period =  $28.8 \text{ Wm}^{-2}$ , CERES period =  $28.8 \text{ Wm}^{-2}$ .

Month	ERBE period							CERES period						
	Mean	Anom	St Dev	Rel StD	Range	N	Mean	Anom	St Dev	Rel StD	Range	N		
1	30.7	1.9	0.2	0.7%	1.8, 2.1	2	30.9	2.1	0.8	2.5%	1.5, 3.0	3		
2	28.1	-0.7	1.5	5.4%	-1.7, 0.4	2	29.0	0.1	1.0	3.6%	-1.1, 0.8	3		
3	28.1	-0.6	1.9	6.6%	-2.0, 0.7	2	28.5	-0.3	1.2	4.2%	-1.7, 0.4	3		
4	30.4	1.6	1.5	4.9%	0.6, 2.7	2	30.3	1.4	0.9	3.0%	0.6, 2.4	3		
5	32.2	3.4	0.0	0.1%	3.4, 3.4	2	31.7	2.9	0.6	1.9%	2.5, 3.6	3		
6	30.1	1.3	2.3	7.6%	-0.3, 2.9	2	29.3	0.5	1.5	5.1%	-1.0, 1.9	3		
7	26.1	-2.7	3.0	11.6%	-4.8, -0.6	2	26.0	-2.9	2.3	8.8%	-5.5, -1.2	3		
8	24.0	-4.8	2.5	10.5%	-6.5, -3.0	2	24.2	-4.6	1.7	7.1%	-6.6, -3.2	3		
9	24.0	-4.7	0.8	3.2%	-5.3, -4.2	2	25.1	-3.7	1.0	4.2%	-4.8, -2.7	3		
10	26.6	-2.2	1.8	6.6%	-3.4, -0.9	2	27.3	-1.5	0.8	2.8%	-1.9, -0.6	3		
11	31.8	3.1	1.5	4.7%	2.0, 4.1	2	31.3	2.5	2.0	6.4%	0.5, 4.5	3		
12	33.1	4.3	0.2	0.7%	4.1, 4.5	2	32.3	3.5	1.5	4.7%	1.9, 4.9	3		

**Table 4.3.12:** Global mean annual cycle data for CSWNET over all data sets, ERBE and CERES time periods. All values are for monthly mean anomalies from the overall annual average except for the overall monthly means listed in the first column. Relative standard deviations are computed with respect to the corresponding monthly mean. Annual means: ERBE period =  $216.6 \text{ Wm}^{-2}$ , CERES period =  $217.9 \text{ Wm}^{-2}$ .

Month	ERBE period						CERES period					
	Mean	Anom	St Dev	Rel StD	Range	N	Mean	Anom	St Dev	Rel StD	Range	N
1	225.6	8.9	1.5	0.6%	7.9, 9.9	2	226.1	8.2	1.5	0.7%	6.7, 9.8	3
2	225.3	8.6	0.9	0.4%	8.0, 9.3	2	224.8	6.9	2.1	0.9%	4.4, 8.1	3
3	220.7	4.1	1.4	0.7%	3.1, 5.1	2	220.4	2.5	2.7	1.2%	-0.6, 4.5	3
4	213.5	-3.2	1.4	0.7%	-4.2, -2.2	2	214.2	-3.7	1.4	0.6%	-4.8, -2.1	3
5	206.7	-9.9	0.7	0.4%	-10.4, -9.4	2	209.9	-8.0	2.1	1.0%	-9.9, -5.8	3
6	204.8	-11.8	0.6	0.3%	-12.2, -11.3	2	210.1	-7.8	5.9	2.8%	-11.2, -1.0	3
7	207.5	-9.1	1.3	0.6%	-10.0, -8.2	2	210.8	-7.1	3.2	1.5%	-9.5, -3.4	3
8	211.8	-4.8	1.2	0.6%	-5.7, -4.0	2	212.7	-5.2	0.6	0.3%	-5.6, -4.5	3
9	217.0	0.4	0.1	0.1%	0.3, 0.4	2	216.2	-1.7	2.7	1.2%	-4.7, -0.0	3
10	221.3	4.6	1.4	0.6%	3.7, 5.6	2	221.1	3.2	1.6	0.7%	1.3, 4.5	3
11	221.9	5.3	0.0	0.0%	5.3, 5.3	2	223.2	5.3	0.3	0.1%	5.0, 5.6	3
12	223.5	6.8	1.4	0.6%	5.9, 7.8	2	225.2	7.3	0.9	0.4%	6.3, 7.9	3

**Table 4.3.13:** Global mean annual cycle data for CLWDN over all data sets, ERBE and CERES time periods. All values are for monthly mean anomalies from the overall annual average except for the overall monthly means listed in the first column. Relative standard deviations are computed with respect to the corresponding monthly mean. Annual means: ERBE period =  $311.3 \text{ Wm}^{-2}$ , CERES period =  $312.6 \text{ Wm}^{-2}$ .

Month	ERBE period						CERES period					
	Mean	Anom	St Dev	Rel StD	Range	N	Mean	Anom	St Dev	Rel StD	Range	N
1	303.2	-8.1	0.8	0.3%	-8.9, -7.3	3	303.5	-9.0	0.5	0.2%	-9.7, -8.4	4
2	303.8	-7.5	1.0	0.3%	-8.7, -6.7	3	304.9	-7.7	0.4	0.1%	-8.2, -7.2	4
3	306.6	-4.7	0.5	0.2%	-5.2, -4.4	3	307.4	-5.1	0.8	0.3%	-6.3, -4.5	4
4	310.8	-0.5	0.3	0.1%	-0.8, -0.3	3	311.8	-0.7	0.3	0.1%	-1.2, -0.5	4
5	314.6	3.2	0.9	0.3%	2.3, 4.0	3	316.2	3.6	0.2	0.1%	3.4, 3.8	4
6	318.9	7.5	0.3	0.1%	7.2, 7.9	3	320.3	7.7	0.2	0.1%	7.4, 7.9	4
7	321.5	10.1	0.4	0.1%	9.7, 10.5	3	323.4	10.9	0.3	0.1%	10.4, 11.1	4
8	320.9	9.6	1.0	0.3%	8.8, 10.7	3	323.0	10.4	0.7	0.2%	9.8, 11.4	4
9	316.3	5.0	1.4	0.4%	4.1, 6.6	3	317.7	5.2	0.6	0.2%	4.7, 6.1	4
10	310.3	-1.0	1.1	0.4%	-1.7, 0.3	3	311.5	-1.0	0.3	0.1%	-1.2, -0.6	4
11	305.7	-5.7	0.3	0.1%	-6.0, -5.4	3	306.8	-5.8	0.3	0.1%	-6.2, -5.5	4
12	303.4	-7.9	0.9	0.3%	-8.8, -7.0	3	304.2	-8.4	0.3	0.1%	-8.7, -8.0	4

**Table 4.3.14:** Global mean annual cycle data for CLWUP over all data sets, ERBE and CERES time periods. All values are for monthly mean anomalies from the overall annual average except for the overall monthly means listed in the first column. Relative standard deviations are computed with respect to the corresponding monthly mean. Annual means: ERBE period =  $395.1 \text{ Wm}^{-2}$ , CERES period =  $393.4 \text{ Wm}^{-2}$ .

Month	ERBE period						CERES period					
	Mean	Anom	St Dev	Rel StD	Range	N	Mean	Anom	St Dev	Rel StD	Range	N
1	385.5	-9.6	0.5	0.1%	-10.0, -9.3	2	384.4	-9.0	0.8	0.2%	-9.8, -8.1	3
2	387.3	-7.8	0.5	0.1%	-8.1, -7.4	2	385.5	-7.9	0.8	0.2%	-8.5, -7.1	3
3	390.8	-4.3	1.2	0.3%	-5.1, -3.4	2	388.5	-4.9	0.2	0.1%	-5.1, -4.7	3
4	396.1	1.0	1.1	0.3%	0.2, 1.8	2	393.2	-0.2	0.3	0.1%	-0.4, 0.2	3
5	399.8	4.7	0.4	0.1%	4.4, 4.9	2	397.9	4.5	0.2	0.0%	4.4, 4.8	3
6	402.9	7.8	1.3	0.3%	6.9, 8.7	2	401.2	7.8	0.6	0.2%	7.2, 8.4	3
7	403.4	8.3	2.9	0.7%	6.2, 10.3	2	402.2	8.9	2.0	0.5%	6.6, 10.2	3
8	404.2	9.1	0.4	0.1%	8.8, 9.3	2	402.3	8.9	0.6	0.2%	8.2, 9.5	3
9	401.3	6.2	0.6	0.2%	5.7, 6.6	2	398.4	5.0	0.9	0.2%	4.0, 5.8	3
10	394.6	-0.5	0.1	0.0%	-0.6, -0.5	2	394.0	0.6	1.0	0.3%	-0.2, 1.7	3
11	389.3	-5.8	0.5	0.1%	-6.2, -5.5	2	388.1	-5.3	0.6	0.1%	-5.9, -4.8	3
12	386.2	-8.9	0.5	0.1%	-9.2, -8.5	2	385.0	-8.4	0.8	0.2%	-9.3, -7.7	3

**Table 4.3.15:** Global mean annual cycle data for CLWNET over all data sets, ERBE and CERES time periods. All values are for monthly mean anomalies from the overall annual average except for the overall monthly means listed in the first column. Relative standard deviations are computed with respect to the corresponding monthly mean. Annual means: ERBE period =  $-84.9 \text{ Wm}^{-2}$ , CERES period =  $-81.5 \text{ Wm}^{-2}$ .

Month	ERBE period						CERES period					
	Mean	Anom	St Dev	Rel StD	Range	N	Mean	Anom	St Dev	Rel StD	Range	N
1	-83.3	1.6	1.6	-1.9%	0.4, 2.7	2	-81.5	0.0	1.5	-1.8%	-1.6, 1.4	3
2	-84.8	0.1	1.9	-2.2%	-1.3, 1.4	2	-81.3	0.2	1.3	-1.5%	-1.2, 1.3	3
3	-85.4	-0.5	1.8	-2.1%	-1.8, 0.7	2	-81.8	-0.3	1.2	-1.4%	-1.6, 0.6	3
4	-86.5	-1.7	1.3	-1.5%	-2.6, -0.8	2	-82.1	-0.6	0.6	-0.7%	-1.3, -0.3	3
5	-86.7	-1.8	0.4	-0.5%	-2.1, -1.5	2	-82.5	-1.0	0.3	-0.4%	-1.4, -0.8	3
6	-85.3	-0.4	1.5	-1.7%	-1.4, 0.6	2	-81.7	-0.1	0.8	-1.0%	-1.0, 0.7	3
7	-83.1	1.8	3.4	-4.1%	-0.6, 4.2	2	-79.6	1.9	2.2	-2.8%	0.2, 4.4	3
8	-84.2	0.7	1.6	-2.0%	-0.5, 1.9	2	-80.0	1.5	1.5	-1.9%	0.2, 3.2	3
9	-85.7	-0.9	1.2	-1.3%	-1.7, -0.1	2	-81.3	0.2	1.7	-2.0%	-1.1, 2.1	3
10	-85.0	-0.2	1.4	-1.7%	-1.2, 0.8	2	-83.1	-1.6	0.7	-0.8%	-2.3, -0.9	3
11	-84.5	0.3	0.3	-0.4%	0.1, 0.6	2	-81.9	-0.4	0.5	-0.7%	-0.7, 0.3	3
12	-83.9	1.0	1.8	-2.2%	-0.3, 2.3	2	-81.4	0.1	1.1	-1.4%	-0.9, 1.3	3

**Table 4.3.16:** Global mean annual cycle data for CTOTNET over all data sets, ERBE and CERES time periods. All values are for monthly mean anomalies from the overall annual average except for the overall monthly means listed in the first column. Relative standard deviations are computed with respect to the corresponding monthly mean. Annual means: ERBE period =  $131.8 \text{ Wm}^{-2}$ , CERES period =  $136.4 \text{ Wm}^{-2}$ .

Month	ERBE period						CERES period					
	Mean	Anom	St Dev	Rel StD	Range	N	Mean	Anom	St Dev	Rel StD	Range	N
1	142.3	10.5	0.1	0.1%	10.4, 10.6	2	144.6	8.2	1.2	0.9%	7.0, 9.4	3
2	140.5	8.7	2.8	2.0%	6.7, 10.7	2	143.5	7.1	2.3	1.6%	4.9, 9.4	3
3	135.4	3.6	3.2	2.4%	1.3, 5.9	2	138.5	2.2	2.9	2.1%	-0.5, 5.1	3
4	126.9	-4.8	2.7	2.1%	-6.7, -2.9	2	132.1	-4.3	1.6	1.2%	-5.4, -2.4	3
5	120.1	-11.7	1.1	0.9%	-12.5, -10.9	2	127.4	-9.0	2.2	1.7%	-10.8, -6.6	3
6	119.6	-12.2	2.1	1.7%	-13.7, -10.7	2	128.5	-7.9	5.9	4.6%	-12.0, -1.1	3
7	124.4	-7.3	4.8	3.8%	-10.7, -4.0	2	131.2	-5.1	3.7	2.8%	-9.3, -2.2	3
8	127.6	-4.1	2.8	2.2%	-6.1, -2.1	2	132.7	-3.7	2.1	1.6%	-5.3, -1.3	3
9	131.3	-0.5	1.0	0.8%	-1.2, 0.2	2	134.9	-1.5	3.4	2.5%	-5.0, 1.8	3
10	136.2	4.5	0.1	0.1%	4.4, 4.5	2	138.0	1.6	1.3	0.9%	0.4, 2.9	3
11	137.4	5.6	0.3	0.2%	5.4, 5.9	2	141.3	5.0	0.3	0.2%	4.7, 5.3	3
12	139.6	7.8	0.5	0.3%	7.5, 8.2	2	143.8	7.4	0.4	0.3%	7.0, 7.6	3

**Table 4.3.17:** Tropical ( $20^{\circ}\text{S}$ - $20^{\circ}\text{N}$ ) mean annual cycle data for ASWDN over all data sets, ERBE and CERES time periods. All values are for monthly mean anomalies from the overall annual average except for the overall monthly means listed in the first column. Relative standard deviations are computed with respect to the corresponding monthly mean. Annual means: ERBE period =  $236.0 \text{ Wm}^{-2}$ , CERES period =  $238.6 \text{ Wm}^{-2}$ .

Month	ERBE period						CERES period					
	Mean	Anom	St Dev	Rel StD	Range	N	Mean	Anom	St Dev	Rel StD	Range	N
1	235.4	-0.6	1.6	0.7%	-2.4, 1.9	5	238.9	0.2	1.5	0.6%	-1.9, 2.9	7
2	249.2	13.2	0.9	0.4%	12.0, 14.5	5	250.8	12.2	0.6	0.2%	11.2, 13.1	7
3	253.5	17.5	1.5	0.6%	15.8, 19.2	5	258.2	19.6	2.0	0.8%	17.0, 22.5	7
4	247.5	11.5	1.0	0.4%	10.3, 13.0	5	249.9	11.2	1.5	0.6%	9.1, 13.6	7
5	231.0	-5.1	0.8	0.3%	-5.9, -3.8	5	233.7	-5.0	1.3	0.5%	-6.9, -3.0	7
6	217.3	-18.7	1.3	0.6%	-20.4, -17.5	5	219.2	-19.4	1.2	0.6%	-21.3, -18.0	7
7	218.7	-17.3	1.9	0.9%	-19.6, -15.6	5	220.7	-18.0	1.4	0.7%	-20.1, -16.0	7
8	228.2	-7.8	1.1	0.5%	-9.1, -6.6	5	231.6	-7.1	1.2	0.5%	-8.6, -5.4	7
9	240.8	4.8	0.8	0.3%	3.9, 5.9	5	245.2	6.5	0.7	0.3%	5.5, 7.2	7
10	244.5	8.4	1.0	0.4%	7.4, 9.8	5	246.8	8.2	0.8	0.3%	7.4, 9.6	7
11	236.1	0.1	1.9	0.8%	-2.4, 2.7	5	237.5	-1.1	1.9	0.8%	-3.7, 2.4	7
12	230.1	-5.9	1.9	0.8%	-8.8, -3.4	5	231.4	-7.2	2.0	0.9%	-9.9, -3.7	7

**Table 4.3.18:** Tropical (20°S-20°N) mean annual cycle data for ASWUP over all data sets, ERBE and CERES time periods. All values are for monthly mean anomalies from the overall annual average except for the overall monthly means listed in the first column. Relative standard deviations are computed with respect to the corresponding monthly mean. Annual means: ERBE period = 20.3 Wm<sup>-2</sup>, CERES period = 19.8 Wm<sup>-2</sup>.

Month	ERBE period						CERES period					
	Mean	Anom	St Dev	Rel StD	Range	N	Mean	Anom	St Dev	Rel StD	Range	N
1	20.2	-0.1	0.3	1.3%	-0.5, 0.2	5	19.7	-0.1	0.4	2.2%	-0.7, 0.5	6
2	21.0	0.6	0.4	2.0%	0.1, 1.2	5	20.6	0.8	0.1	0.7%	0.7, 1.0	6
3	21.3	1.0	0.4	1.8%	0.7, 1.6	5	21.0	1.2	0.2	1.0%	0.9, 1.6	6
4	21.3	0.9	0.3	1.4%	0.6, 1.4	5	20.6	0.9	0.3	1.7%	0.2, 1.2	6
5	20.5	0.2	0.2	1.0%	-0.1, 0.4	5	19.7	-0.1	0.2	1.2%	-0.4, 0.3	6
6	19.8	-0.5	0.5	2.6%	-1.2, -0.0	5	18.9	-0.8	0.3	1.4%	-1.2, -0.5	6
7	19.3	-1.0	0.5	2.4%	-1.7, -0.6	5	18.7	-1.1	0.3	1.7%	-1.6, -0.7	6
8	19.8	-0.5	0.3	1.3%	-0.9, -0.2	5	19.3	-0.4	0.3	1.7%	-0.8, 0.1	6
9	20.5	0.2	0.2	1.2%	-0.0, 0.5	5	20.2	0.4	0.4	1.8%	-0.0, 1.1	6
10	20.4	0.1	0.3	1.5%	-0.4, 0.4	5	20.0	0.2	0.2	1.1%	-0.1, 0.5	6
11	20.1	-0.2	0.2	1.1%	-0.5, -0.1	5	19.4	-0.3	0.3	1.4%	-0.7, -0.0	6
12	19.7	-0.7	0.4	2.0%	-1.2, -0.2	5	19.1	-0.7	0.4	2.3%	-1.5, -0.2	6

**Table 4.3.19:** Tropical (20°S-20°N) mean annual cycle data for ASWNET over all data sets, ERBE and CERES time periods. All values are for monthly mean anomalies from the overall annual average except for the overall monthly means listed in the first column. Relative standard deviations are computed with respect to the corresponding monthly mean. Annual means: ERBE period = 214.8 Wm<sup>-2</sup>, CERES period = 219.3 Wm<sup>-2</sup>.

Month	ERBE period						CERES period					
	Mean	Anom	St Dev	Rel StD	Range	N	Mean	Anom	St Dev	Rel StD	Range	N
1	214.1	-0.7	1.4	0.6%	-2.2, 1.8	6	219.7	0.4	1.5	0.7%	-1.6, 2.8	6
2	227.3	12.5	0.8	0.4%	11.2, 13.8	6	230.7	11.3	0.7	0.3%	10.5, 12.4	6
3	231.5	16.7	1.4	0.6%	14.7, 18.4	6	237.5	18.1	2.1	0.9%	15.7, 21.3	6
4	225.2	10.4	1.0	0.4%	9.7, 12.1	6	229.6	10.3	1.5	0.7%	8.2, 12.6	6
5	209.2	-5.5	0.9	0.4%	-6.7, -4.1	6	214.4	-5.0	1.3	0.6%	-6.6, -3.3	6
6	196.5	-18.3	0.8	0.4%	-19.2, -17.5	6	200.9	-18.5	1.1	0.5%	-20.0, -17.3	6
7	198.2	-16.6	1.4	0.7%	-18.0, -15.0	6	202.6	-16.8	1.3	0.6%	-18.5, -15.2	6
8	207.8	-6.9	1.2	0.6%	-8.2, -5.1	6	212.8	-6.6	1.0	0.5%	-8.0, -5.5	6
9	219.9	5.1	1.3	0.6%	3.8, 7.5	6	225.4	6.0	0.6	0.3%	5.4, 6.8	6
10	223.1	8.4	0.6	0.3%	7.7, 9.5	6	227.2	7.8	0.8	0.4%	6.9, 9.3	6
11	214.9	0.1	1.6	0.7%	-2.0, 2.8	6	218.6	-0.8	1.9	0.9%	-3.2, 2.5	6
12	209.5	-5.3	1.7	0.8%	-8.2, -3.0	6	213.0	-6.4	2.1	1.0%	-9.2, -3.3	6

**Table 4.3.20:** Tropical (20°S-20°N) mean annual cycle data for ALWDN over all data sets, ERBE and CERES time periods. All values are for monthly mean anomalies from the overall annual average except for the overall monthly means listed in the first column. Relative standard deviations are computed with respect to the corresponding monthly mean. Annual means: ERBE period = 407.1 Wm<sup>-2</sup>, CERES period = 405.3 Wm<sup>-2</sup>.

Month	ERBE period						CERES period					
	Mean	Anom	St Dev	Rel StD	Range	N	Mean	Anom	St Dev	Rel StD	Range	N
1	404.0	-3.2	0.7	0.2%	-3.8, -2.4	4	402.4	-2.9	0.5	0.1%	-3.7, -2.3	5
2	404.7	-2.5	0.8	0.2%	-3.6, -2.1	4	403.2	-2.1	0.5	0.1%	-2.9, -1.8	5
3	409.2	2.0	0.3	0.1%	1.5, 2.2	4	404.9	-0.4	1.1	0.3%	-2.4, 0.6	5
4	411.1	4.0	0.3	0.1%	3.5, 4.3	4	408.6	3.3	0.5	0.1%	2.6, 4.1	5
5	409.8	2.6	1.2	0.3%	0.9, 3.4	4	408.2	3.0	0.3	0.1%	2.6, 3.5	5
6	407.0	-0.1	0.3	0.1%	-0.5, 0.3	4	405.5	0.2	0.4	0.1%	-0.3, 0.8	5
7	404.5	-2.6	0.6	0.1%	-3.2, -2.0	4	403.4	-1.9	0.4	0.1%	-2.6, -1.6	5
8	406.0	-1.2	0.4	0.1%	-1.7, -0.7	4	404.2	-1.1	0.7	0.2%	-1.9, -0.0	5
9	407.8	0.7	1.0	0.3%	-0.0, 2.2	4	405.1	-0.2	0.3	0.1%	-0.4, 0.3	5
10	407.8	0.7	1.1	0.3%	-0.1, 2.2	4	406.7	1.4	0.3	0.1%	1.0, 1.9	5
11	407.8	0.7	0.5	0.1%	0.1, 1.3	4	406.4	1.1	0.4	0.1%	0.7, 1.6	5
12	406.1	-1.1	0.6	0.2%	-1.6, -0.3	4	404.8	-0.5	0.2	0.0%	-0.8, -0.2	5

**Table 4.3.21:** Tropical (20°S-20°N) mean annual cycle data for ALWUP over all data sets, ERBE and CERES time periods. All values are for monthly mean anomalies from the overall annual average except for the overall monthly means listed in the first column. Relative standard deviations are computed with respect to the corresponding monthly mean. Annual means: ERBE period = 458.1 Wm<sup>-2</sup>, CERES period = 455.6 Wm<sup>-2</sup>.

Month	ERBE period						CERES period					
	Mean	Anom	St Dev	Rel StD	Range	N	Mean	Anom	St Dev	Rel StD	Range	N
1	454.3	-3.7	2.4	0.5%	-7.3, -2.4	4	453.4	-2.2	0.5	0.1%	-3.1, -1.8	5
2	457.5	-0.6	1.1	0.2%	-2.2, 0.2	4	455.1	-0.5	0.6	0.1%	-1.4, 0.0	5
3	461.2	3.1	0.5	0.1%	2.7, 3.9	4	457.0	1.4	0.9	0.2%	-0.1, 2.0	5
4	463.1	5.0	1.4	0.3%	4.2, 7.0	4	459.6	4.0	0.6	0.1%	2.9, 4.5	5
5	461.7	3.7	0.4	0.1%	3.2, 4.2	4	458.9	3.3	0.5	0.1%	2.9, 4.0	5
6	457.6	-0.5	0.5	0.1%	-0.7, 0.2	4	455.3	-0.3	0.6	0.1%	-0.8, 0.5	5
7	454.6	-3.5	1.0	0.2%	-4.7, -2.3	4	452.6	-3.0	1.2	0.3%	-4.9, -1.8	5
8	455.6	-2.4	0.5	0.1%	-3.0, -1.8	4	453.0	-2.6	0.7	0.2%	-3.6, -1.6	5
9	458.3	0.2	1.3	0.3%	-0.8, 2.2	4	454.5	-1.1	0.9	0.2%	-2.5, -0.2	5
10	458.8	0.7	0.7	0.1%	-0.2, 1.4	4	457.3	1.7	2.1	0.5%	0.1, 5.4	5
11	458.3	0.2	0.8	0.2%	-0.5, 1.3	4	456.0	0.4	1.2	0.3%	-0.5, 2.4	5
12	455.7	-2.3	0.7	0.1%	-3.3, -1.8	4	454.4	-1.2	0.8	0.2%	-1.8, 0.2	5

**Table 4.3.22:** Tropical (20°S-20°N) mean annual cycle data for ALWNET over all data sets, ERBE and CERES time periods. All values are for monthly mean anomalies from the overall annual average except for the overall monthly means listed in the first column. Relative standard deviations are computed with respect to the corresponding monthly mean. Annual means: ERBE period =  $-27.8 \text{ Wm}^{-2}$ , CERES period =  $-30.9 \text{ Wm}^{-2}$ .

Month	ERBE period						CERES period					
	Mean	Anom	St Dev	Rel StD	Range	N	Mean	Anom	St Dev	Rel StD	Range	N
1	-26.6	1.2	1.7	-6.5%	-0.3, 3.6	4	-31.5	-0.6	0.5	-1.6%	-1.2, 0.2	5
2	-28.8	-1.0	1.9	-6.7%	-2.4, 1.8	4	-31.9	-1.0	1.4	-4.3%	-2.0, 1.4	5
3	-28.6	-0.8	1.0	-3.6%	-1.7, 0.6	4	-31.9	-1.0	1.7	-5.3%	-2.2, 1.9	5
4	-28.8	-1.0	1.5	-5.2%	-3.0, 0.1	4	-31.1	-0.2	1.2	-3.8%	-1.8, 1.2	5
5	-28.7	-0.9	1.6	-5.6%	-3.3, 0.2	4	-31.0	-0.1	0.5	-1.8%	-0.6, 0.8	5
6	-27.4	0.3	0.3	-1.2%	-0.0, 0.8	4	-30.2	0.7	0.7	-2.3%	-0.1, 1.6	5
7	-27.1	0.7	1.0	-3.6%	-0.2, 1.7	4	-29.9	1.0	1.5	-4.9%	-0.4, 3.3	5
8	-27.1	0.7	1.3	-4.7%	-1.2, 1.8	4	-29.7	1.1	1.7	-5.6%	-1.0, 3.6	5
9	-27.9	-0.1	0.7	-2.5%	-1.2, 0.3	4	-30.3	0.6	1.4	-4.5%	-0.8, 2.9	5
10	-28.0	-0.2	0.7	-2.7%	-0.9, 0.9	4	-31.7	-0.9	1.7	-5.2%	-3.5, 0.8	5
11	-27.7	0.1	0.6	-2.2%	-0.7, 0.8	4	-30.7	0.2	1.1	-3.7%	-1.2, 1.2	5
12	-26.8	1.0	1.1	-4.0%	-0.5, 1.8	4	-30.7	0.2	1.0	-3.3%	-1.2, 1.1	5

**Table 4.3.23:** Tropical (20°S-20°N) mean annual cycle data for ATOTNET over all data sets, ERBE and CERES time periods. All values are for monthly mean anomalies from the overall annual average except for the overall monthly means listed in the first column. Relative standard deviations are computed with respect to the corresponding monthly mean. Annual means: ERBE period =  $186.1 \text{ Wm}^{-2}$ , CERES period =  $186.6 \text{ Wm}^{-2}$ .

Month	ERBE period						CERES period					
	Mean	Anom	St Dev	Rel StD	Range	N	Mean	Anom	St Dev	Rel StD	Range	N
1	186.8	0.8	1.9	1.0%	-0.9, 3.1	4	186.5	-0.1	1.3	0.7%	-1.4, 2.0	5
2	197.5	11.5	2.8	1.4%	9.1, 15.6	4	196.9	10.3	2.0	1.0%	8.8, 13.8	5
3	201.8	15.8	2.2	1.1%	14.1, 19.0	4	203.7	17.1	3.6	1.8%	14.3, 23.3	5
4	195.9	9.8	2.2	1.1%	7.6, 12.2	4	196.7	10.1	2.2	1.1%	8.3, 13.8	5
5	179.9	-6.2	2.0	1.1%	-8.7, -3.9	4	181.4	-5.2	1.6	0.9%	-6.7, -2.6	5
6	168.1	-18.0	1.0	0.6%	-18.8, -16.7	4	168.7	-17.9	1.1	0.6%	-19.3, -16.4	5
7	170.1	-16.0	1.7	1.0%	-18.0, -13.8	4	170.6	-16.0	1.6	0.9%	-17.7, -13.8	5
8	179.2	-6.9	1.7	1.0%	-8.8, -4.6	4	181.0	-5.6	1.9	1.1%	-7.8, -3.7	5
9	190.6	4.6	0.8	0.4%	3.8, 5.6	4	193.3	6.7	1.8	0.9%	5.3, 9.6	5
10	194.4	8.3	1.5	0.8%	6.9, 10.4	4	193.6	7.0	1.1	0.5%	5.9, 8.3	5
11	186.5	0.5	2.5	1.4%	-2.7, 3.6	4	186.2	-0.4	2.9	1.6%	-4.4, 3.7	5
12	181.8	-4.2	3.0	1.7%	-8.6, -1.9	4	180.7	-5.9	3.1	1.7%	-10.4, -2.2	5

**Table 4.3.24:** Tropical (20°S-20°N) mean annual cycle data for CSWDN over all data sets, ERBE and CERES time periods. All values are for monthly mean anomalies from the overall annual average except for the overall monthly means listed in the first column. Relative standard deviations are computed with respect to the corresponding monthly mean. Annual means: ERBE period = 292.4  $Wm^{-2}$ , CERES period = 292.1  $Wm^{-2}$ .

Month	ERBE period						CERES period					
	Mean	Anom	St Dev	Rel StD	Range	N	Mean	Anom	St Dev	Rel StD	Range	N
1	295.0	2.6	2.1	0.7%	0.5, 4.7	3	294.6	2.5	1.8	0.6%	0.7, 4.9	4
2	305.5	13.0	0.2	0.1%	12.8, 13.3	3	304.7	12.7	0.4	0.1%	12.3, 13.2	4
3	308.6	16.1	0.7	0.2%	15.4, 16.7	3	307.9	15.9	0.8	0.3%	15.3, 17.0	4
4	299.4	6.9	0.9	0.3%	5.9, 7.7	3	298.4	6.4	1.0	0.3%	5.2, 7.3	4
5	281.3	-11.1	0.4	0.1%	-11.4, -10.7	3	281.0	-11.1	0.3	0.1%	-11.5, -10.7	4
6	269.0	-23.4	1.3	0.5%	-24.2, -21.9	3	269.2	-22.9	1.7	0.6%	-24.4, -21.2	4
7	272.4	-20.0	2.1	0.8%	-21.3, -17.5	3	272.6	-19.5	2.3	0.8%	-21.5, -17.5	4
8	286.8	-5.7	2.2	0.8%	-7.5, -3.2	3	287.0	-5.1	2.2	0.8%	-7.4, -3.1	4
9	300.7	8.3	1.3	0.4%	6.8, 9.4	3	300.6	8.5	1.1	0.4%	6.9, 9.4	4
10	304.4	11.9	0.6	0.2%	11.3, 12.5	3	303.7	11.6	0.9	0.3%	10.7, 12.7	4
11	296.7	4.3	2.0	0.7%	2.1, 6.1	3	296.0	3.9	1.9	0.7%	2.2, 6.3	4
12	289.6	-2.9	2.0	0.7%	-4.8, -0.9	3	289.0	-3.0	1.6	0.6%	-4.8, -0.8	4

**Table 4.3.25:** Tropical (20°S-20°N) mean annual cycle data for CSWUP over all data sets, ERBE and CERES time periods. All values are for monthly mean anomalies from the overall annual average except for the overall monthly means listed in the first column. Relative standard deviations are computed with respect to the corresponding monthly mean. Annual means: ERBE period = 24.0  $Wm^{-2}$ , CERES period = 23.3  $Wm^{-2}$ .

Month	ERBE period						CERES period					
	Mean	Anom	St Dev	Rel StD	Range	N	Mean	Anom	St Dev	Rel StD	Range	N
1	24.0	0.0	0.2	0.8%	-0.1, 0.2	2	23.1	-0.2	0.6	2.8%	-0.9, 0.4	3
2	24.6	0.6	1.0	3.9%	-0.1, 1.3	2	24.2	0.9	0.2	0.8%	0.8, 1.1	3
3	24.9	0.9	0.9	3.7%	0.2, 1.5	2	24.4	1.1	0.2	0.7%	1.0, 1.3	3
4	24.8	0.8	0.6	2.4%	0.3, 1.2	2	24.1	0.8	0.1	0.5%	0.6, 0.9	3
5	23.8	-0.2	0.1	0.2%	-0.2, -0.1	2	22.7	-0.6	0.2	0.9%	-0.8, -0.4	3
6	23.5	-0.5	1.2	5.0%	-1.3, 0.4	2	22.3	-1.0	0.2	0.8%	-1.2, -0.9	3
7	23.0	-1.0	1.1	4.9%	-1.8, -0.2	2	22.3	-1.0	0.6	2.8%	-1.6, -0.3	3
8	23.9	-0.1	1.1	4.6%	-0.9, 0.7	2	23.4	0.1	0.9	3.8%	-0.7, 1.0	3
9	24.6	0.6	0.6	2.2%	0.2, 1.0	2	24.2	0.9	0.8	3.1%	0.4, 1.7	3
10	23.9	-0.1	0.4	1.6%	-0.4, 0.2	2	23.7	0.4	0.3	1.3%	0.1, 0.7	3
11	23.7	-0.3	0.6	2.4%	-0.7, 0.1	2	22.9	-0.4	0.5	2.3%	-1.0, 0.0	3
12	23.2	-0.8	0.4	1.7%	-1.1, -0.5	2	22.4	-0.9	0.8	3.6%	-1.8, -0.3	3

**Table 4.3.26:** Tropical (20°S-20°N) mean annual cycle data for CSWNET over all data sets, ERBE and CERES time periods. All values are for monthly mean anomalies from the overall annual average except for the overall monthly means listed in the first column. Relative standard deviations are computed with respect to the corresponding monthly mean. Annual means: ERBE period = 271.0 Wm<sup>-2</sup>, CERES period = 270.5 Wm<sup>-2</sup>.

Month	ERBE period						CERES period					
	Mean	Anom	St Dev	Rel StD	Range	N	Mean	Anom	St Dev	Rel StD	Range	N
1	272.5	1.5	1.3	0.5%	0.6, 2.4	2	272.4	2.0	0.4	0.1%	1.6, 2.4	3
2	283.5	12.5	1.2	0.4%	11.7, 13.3	2	282.2	11.7	0.3	0.1%	11.4, 12.0	3
3	286.6	15.6	0.6	0.2%	15.2, 16.0	2	285.5	15.0	0.7	0.2%	14.4, 15.7	3
4	276.8	5.8	0.3	0.1%	5.5, 6.0	2	275.8	5.3	0.9	0.3%	4.5, 6.3	3
5	260.2	-10.8	0.5	0.2%	-11.2, -10.5	2	260.1	-10.3	0.4	0.1%	-10.6, -9.9	3
6	248.5	-22.5	0.4	0.2%	-22.8, -22.3	2	249.0	-21.4	1.6	0.6%	-23.2, -20.3	3
7	252.6	-18.4	1.5	0.6%	-19.4, -17.3	2	252.6	-17.9	1.9	0.7%	-20.0, -16.5	3
8	266.3	-4.7	1.1	0.4%	-5.4, -3.9	2	266.1	-4.4	1.2	0.4%	-5.7, -3.4	3
9	279.4	8.4	0.0	0.0%	8.4, 8.4	2	278.7	8.2	0.5	0.2%	7.7, 8.6	3
10	283.1	12.1	0.5	0.2%	11.7, 12.4	2	281.7	11.2	1.3	0.5%	10.0, 12.6	3
11	274.6	3.6	1.2	0.4%	2.8, 4.5	2	274.0	3.5	0.9	0.3%	2.9, 4.6	3
12	268.0	-3.1	1.0	0.4%	-3.8, -2.4	2	267.6	-2.9	0.3	0.1%	-3.1, -2.5	3

**Table 4.3.27:** Tropical (20°S-20°N) mean annual cycle data for CLWDN over all data sets, ERBE and CERES time periods. All values are for monthly mean anomalies from the overall annual average except for the overall monthly means listed in the first column. Relative standard deviations are computed with respect to the corresponding monthly mean. Annual means: ERBE period = 385.2 Wm<sup>-2</sup>, CERES period = 385.9 Wm<sup>-2</sup>.

Month	ERBE period						CERES period					
	Mean	Anom	St Dev	Rel StD	Range	N	Mean	Anom	St Dev	Rel StD	Range	N
1	382.4	-2.7	1.7	0.5%	-4.7, -1.4	3	382.4	-3.5	0.9	0.2%	-4.9, -3.0	4
2	383.5	-1.7	1.4	0.4%	-3.3, -0.9	3	384.5	-1.4	0.8	0.2%	-2.7, -0.9	4
3	388.0	2.8	0.4	0.1%	2.3, 3.1	3	387.2	1.3	1.3	0.3%	-0.6, 2.3	4
4	390.7	5.5	1.1	0.3%	4.4, 6.5	3	391.5	5.6	0.4	0.1%	5.2, 6.2	4
5	388.8	3.7	0.7	0.2%	2.9, 4.2	3	390.6	4.7	0.6	0.2%	4.2, 5.6	4
6	384.6	-0.5	0.5	0.1%	-0.9, 0.0	3	385.9	0.0	0.5	0.1%	-0.6, 0.5	4
7	381.4	-3.8	0.6	0.1%	-4.4, -3.4	3	383.2	-2.7	0.6	0.2%	-3.4, -2.1	4
8	382.7	-2.5	0.8	0.2%	-3.3, -1.6	3	383.5	-2.4	1.0	0.3%	-3.3, -1.1	4
9	384.9	-0.3	1.5	0.4%	-1.2, 1.4	3	384.7	-1.2	0.4	0.1%	-1.6, -0.7	4
10	385.9	0.7	1.6	0.4%	-0.5, 2.5	3	386.7	0.8	0.7	0.2%	0.1, 1.7	4
11	385.7	0.5	0.3	0.1%	0.2, 0.8	3	386.3	0.3	0.2	0.1%	0.0, 0.5	4
12	383.5	-1.7	1.2	0.3%	-3.0, -0.8	3	384.6	-1.3	0.3	0.1%	-1.7, -0.9	4

**Table 4.3.28:** Tropical (20°S-20°N) mean annual cycle data for CLWUP over all data sets, ERBE and CERES time periods. All values are for monthly mean anomalies from the overall annual average except for the overall monthly means listed in the first column. Relative standard deviations are computed with respect to the corresponding monthly mean. Annual means: ERBE period =  $459.2 \text{ Wm}^{-2}$ , CERES period =  $454.3 \text{ Wm}^{-2}$ .

Month	ERBE period							CERES period						
	Mean	Anom	St Dev	Rel StD	Range		N	Mean	Anom	St Dev	Rel StD	Range		N
1	454.2	-5.0	3.3	0.7%	-7.3, -2.6		2	452.0	-2.3	0.8	0.2%	-3.2, -1.8		3
2	458.2	-1.0	1.7	0.4%	-2.2, 0.2		2	453.8	-0.6	0.7	0.2%	-1.4, 0.0		3
3	462.6	3.5	0.6	0.1%	3.0, 3.9		2	455.4	1.0	1.1	0.2%	-0.0, 2.1		3
4	465.1	5.9	1.8	0.4%	4.7, 7.2		2	458.3	3.9	0.9	0.2%	3.0, 4.6		3
5	463.2	4.0	0.4	0.1%	3.7, 4.3		2	457.8	3.4	0.6	0.1%	2.9, 4.1		3
6	458.5	-0.7	0.1	0.0%	-0.7, -0.6		2	453.9	-0.4	0.7	0.1%	-0.9, 0.3		3
7	455.0	-4.2	0.8	0.2%	-4.8, -3.7		2	451.0	-3.3	1.5	0.3%	-4.9, -1.8		3
8	456.7	-2.4	0.8	0.2%	-3.0, -1.9		2	451.5	-2.8	1.0	0.2%	-3.6, -1.7		3
9	460.1	0.9	1.8	0.4%	-0.4, 2.2		2	452.9	-1.4	1.0	0.2%	-2.6, -0.7		3
10	460.3	1.1	0.4	0.1%	0.8, 1.4		2	456.8	2.4	2.6	0.6%	0.4, 5.4		3
11	459.9	0.7	0.7	0.2%	0.2, 1.3		2	455.2	0.8	1.4	0.3%	-0.1, 2.4		3
12	456.4	-2.8	0.9	0.2%	-3.4, -2.2		2	453.5	-0.8	0.8	0.2%	-1.5, 0.1		3

**Table 4.3.29:** Tropical (20°S-20°N) mean annual cycle data for CLWNET over all data sets, ERBE and CERES time periods. All values are for monthly mean anomalies from the overall annual average except for the overall monthly means listed in the first column. Relative standard deviations are computed with respect to the corresponding monthly mean. Annual means: ERBE period =  $-75.3 \text{ Wm}^{-2}$ , CERES period =  $-69.5 \text{ Wm}^{-2}$ .

Month	ERBE period							CERES period						
	Mean	Anom	St Dev	Rel StD	Range		N	Mean	Anom	St Dev	Rel StD	Range		N
1	-73.4	1.9	1.0	-1.4%	1.2, 2.6		2	-70.8	-1.3	0.3	-0.5%	-1.7, -1.1		3
2	-76.4	-1.1	0.0	0.0%	-1.1, -1.1		2	-70.5	-1.0	0.4	-0.6%	-1.3, -0.5		3
3	-76.1	-0.8	0.1	-0.1%	-0.8, -0.7		2	-69.6	-0.1	0.7	-1.0%	-0.6, 0.7		3
4	-75.8	-0.5	0.2	-0.3%	-0.6, -0.3		2	-68.0	1.5	1.0	-1.5%	0.9, 2.7		3
5	-75.9	-0.6	1.1	-1.5%	-1.4, 0.2		2	-68.2	1.3	0.3	-0.4%	1.0, 1.5		3
6	-75.1	0.2	0.7	-1.0%	-0.3, 0.8		2	-68.9	0.6	1.0	-1.4%	-0.5, 1.3		3
7	-74.6	0.8	0.6	-0.8%	0.3, 1.2		2	-68.7	0.8	2.0	-2.9%	-1.2, 2.8		3
8	-75.0	0.4	0.2	-0.3%	0.2, 0.5		2	-68.9	0.7	1.9	-2.8%	-1.3, 2.6		3
9	-76.1	-0.8	0.1	-0.1%	-0.8, -0.7		2	-69.4	0.2	1.5	-2.2%	-0.9, 1.9		3
10	-75.4	-0.1	1.7	-2.3%	-1.3, 1.1		2	-71.2	-1.7	1.9	-2.7%	-3.7, 0.1		3
11	-75.6	-0.3	0.4	-0.6%	-0.6, -0.0		2	-70.0	-0.5	1.2	-1.8%	-1.9, 0.6		3
12	-74.5	0.9	0.7	-0.9%	0.4, 1.3		2	-70.0	-0.5	1.1	-1.6%	-1.8, 0.2		3

**Table 4.3.30:** Tropical (20°S-20°N) mean annual cycle data for CTOTNET over all data sets, ERBE and CERES time periods. All values are for monthly mean anomalies from the overall annual average except for the overall monthly means listed in the first column. Relative standard deviations are computed with respect to the corresponding monthly mean. Annual means: ERBE period =  $195.7 \text{ Wm}^{-2}$ , CERES period =  $200.9 \text{ Wm}^{-2}$ .

Month	ERBE period						CERES period					
	Mean	Anom	St Dev	Rel StD	Range	N	Mean	Anom	St Dev	Rel StD	Range	N
1	199.1	3.4	2.3	1.2%	1.8, 5.1	2	201.6	0.7	0.1	0.1%	0.5, 0.8	3
2	207.1	11.4	1.1	0.6%	10.6, 12.2	2	211.6	10.7	0.2	0.1%	10.5, 10.8	3
3	210.5	14.8	0.7	0.3%	14.4, 15.3	2	215.9	14.9	0.4	0.2%	14.5, 15.1	3
4	201.0	5.3	0.1	0.0%	5.2, 5.4	2	207.7	6.8	0.7	0.3%	6.0, 7.2	3
5	184.2	-11.4	0.7	0.4%	-11.9, -11.0	2	191.9	-9.0	0.1	0.0%	-9.1, -9.0	3
6	173.4	-22.3	1.1	0.7%	-23.1, -21.5	2	180.1	-20.8	1.1	0.6%	-21.9, -19.7	3
7	178.1	-17.6	0.9	0.5%	-18.2, -17.0	2	183.9	-17.1	0.7	0.4%	-17.7, -16.3	3
8	191.4	-4.3	1.3	0.7%	-5.2, -3.4	2	197.2	-3.8	0.8	0.4%	-4.7, -3.1	3
9	203.3	7.6	0.1	0.0%	7.6, 7.7	2	209.3	8.4	1.7	0.8%	7.2, 10.3	3
10	207.6	11.9	2.2	1.1%	10.4, 13.5	2	210.4	9.5	0.6	0.3%	8.8, 10.1	3
11	199.0	3.3	0.8	0.4%	2.8, 3.9	2	204.0	3.0	0.4	0.2%	2.8, 3.5	3
12	193.5	-2.2	0.3	0.2%	-2.4, -2.0	2	197.6	-3.3	0.9	0.4%	-4.3, -2.7	3

## Appendix C4.5 for Chapter 4.5:

# Supplementary Figures

E. Raschke, S. Kinne

In this *Appendix C4.5* we provide with only small comments further details on the radiation fluxes at the surface as computed within the data projects ISCCP, SRB and CERES.

1. Time series of monthly zonal averages and of annual regional averages
2. Seasonal averages of solar (shortwave) radiation fluxes
3. Seasonal averages of infrared (longwave) radiation fluxes
4. Seasonal averages of the total net radiation
5. Seasonal averages of the total net radiation compared to IPSS median model data.

Short explanations are added to relate special features to the findings explained in the main sections of this report.

**Note:**

**All results shown below are not based on in-situ measurements. They have been computed from various ancillary data on the radiative transfer properties of the atmosphere and of the surface, which had been derived from various data sources!**

### C4.5.1. Time series of monthly zonal averages and of annual regional averages

#### 1.1: Cloud radiative effect on solar transmittance, surface reflectance, and on downward longwave radiation fluxes at the surface

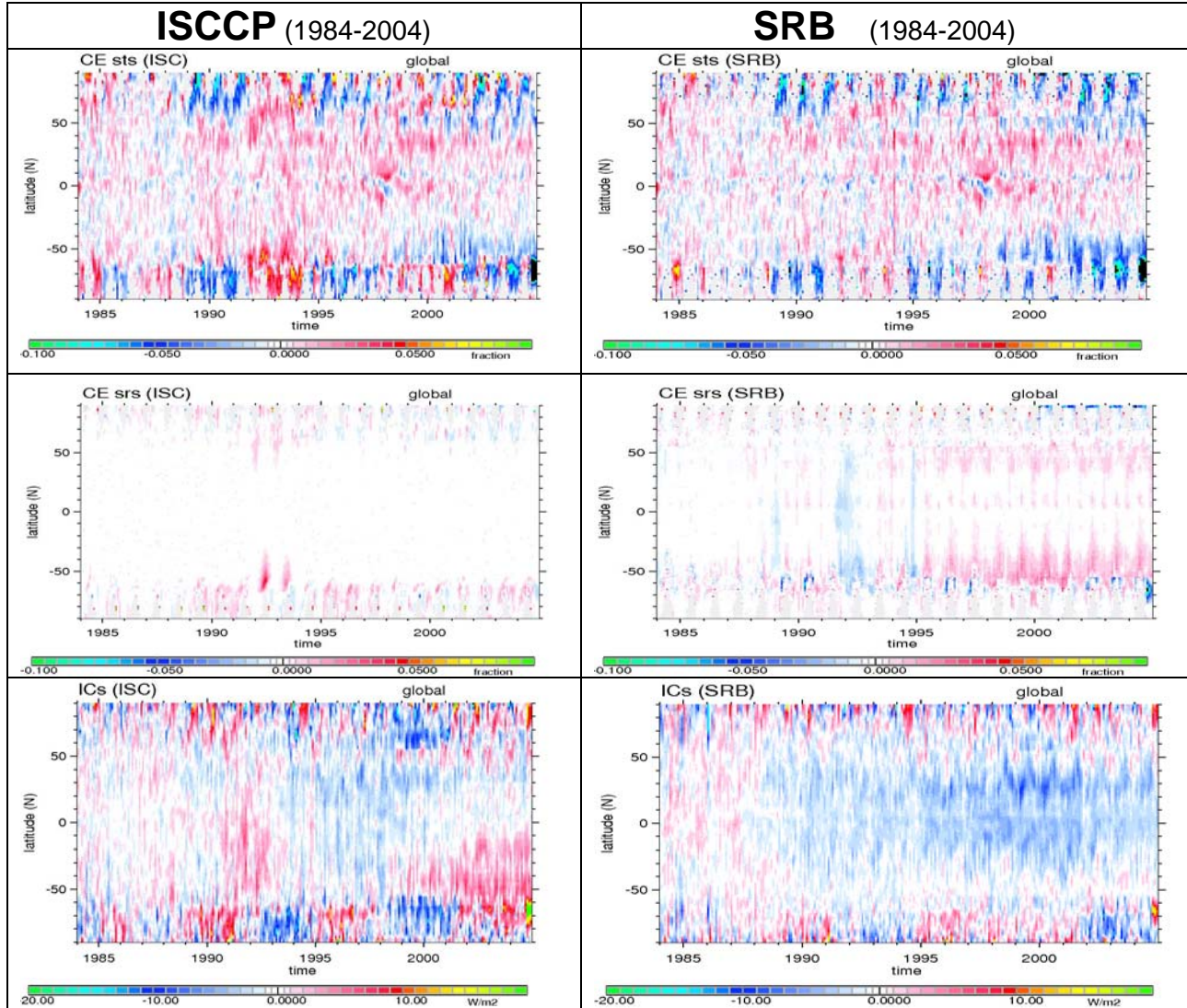


**Figure 1:** Monthly zonal deseasonalised anomalies of the **cloud radiative effects** on the solar atmospheric transmission (in fraction, *srs* in top row), on the solar surface reflectance (in fraction, *srs* in center row) and on the downward longwave fluxes to the surface (in  $Wm^{-2}$ , *ICs* in bottom row) for the satellite data climatologies of ISCCP (left) and SRB (right). Anomalies are in reference to the 1985-1988 time-period. Some abrupt changes may be linked to platform changes.

**Comment:** Particular interesting are interpretations of cloud effect features with the presence of enhanced stratospheric aerosol between 1991 and 1994 as it slowly moved from the tropics to Polar Regions. ISCCP and SRB suggest at mid-latitudes and Polar Regions more solar transmissions (thus weaker cloud optical depths) but differ in impacts on the solar surface albedo, which is stronger in ISCCP but weaker in SRB. The weaker cloud optical depth at higher latitudes is consistent with relative weak cloud-impacts on longwave downward radiative fluxes. Effective values of the surface albedo show small changes, which might be a result of computational errors.

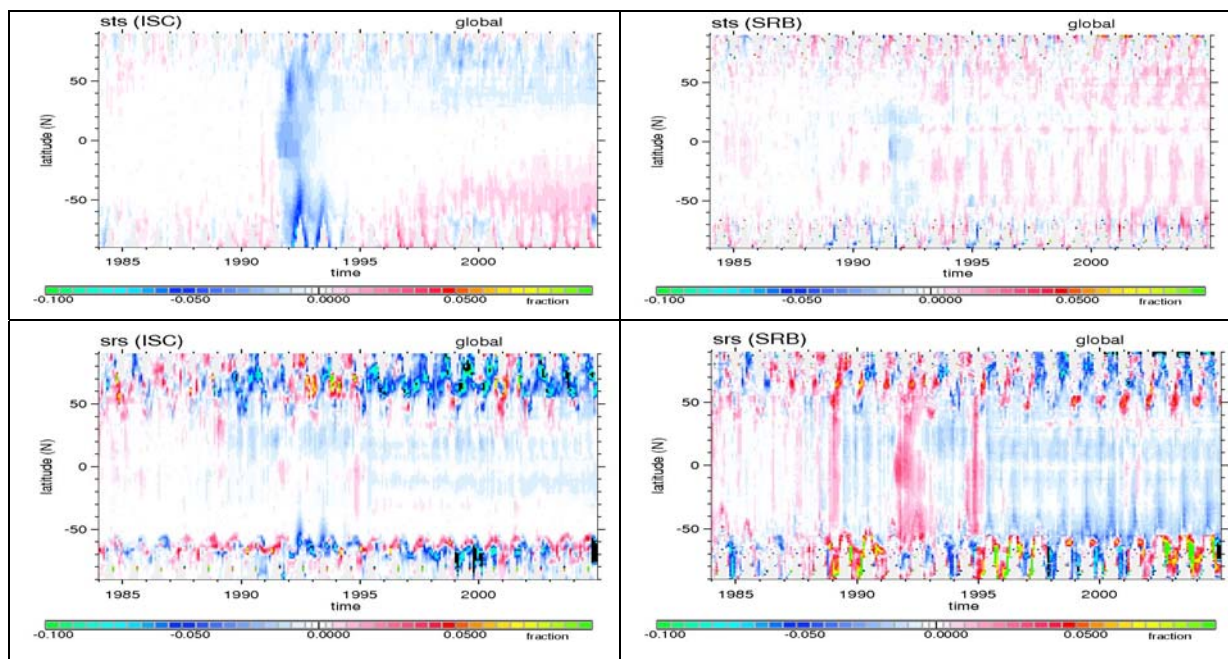


**Figure 1a:** Clear-sky transmittance (top) of the atmosphere and reflectance (bottom line) of the surface. Note the small decrease of srs with time, which in SRB data is interrupted by three positive anomalies.

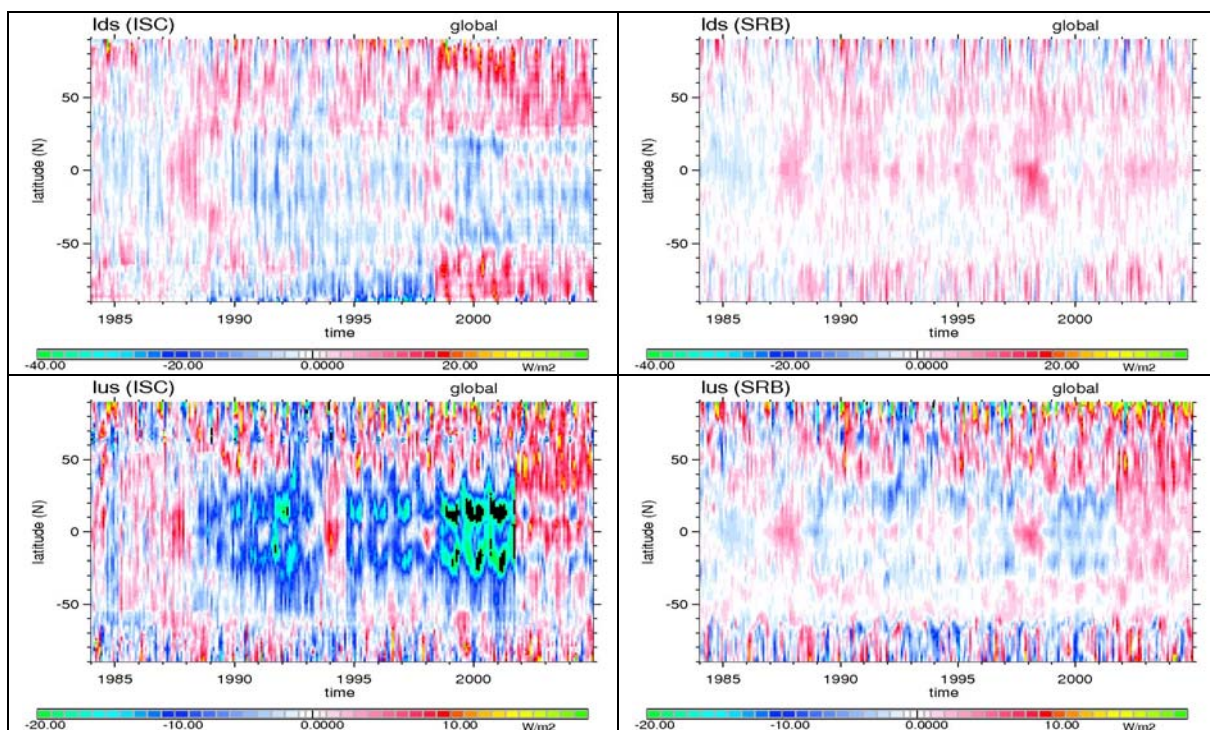


**Figure 1b:** Clear-sky downward longwave radiation at the surface (lds: top row) and upward longwave radiation at the surface (lus: bottom row). Note the strong anomalies of higher emissions (related to El-Nino events) in the equatorial zone, which are partly masked by the general decrease until Sept. 2001, a consequence of erroneous temperature analyses.

**1.2: Inter-annual variations of clear-sky ancillary data (top line) and of the cloud impact (bottom line) on the downward infrared radiation flux to the surface**

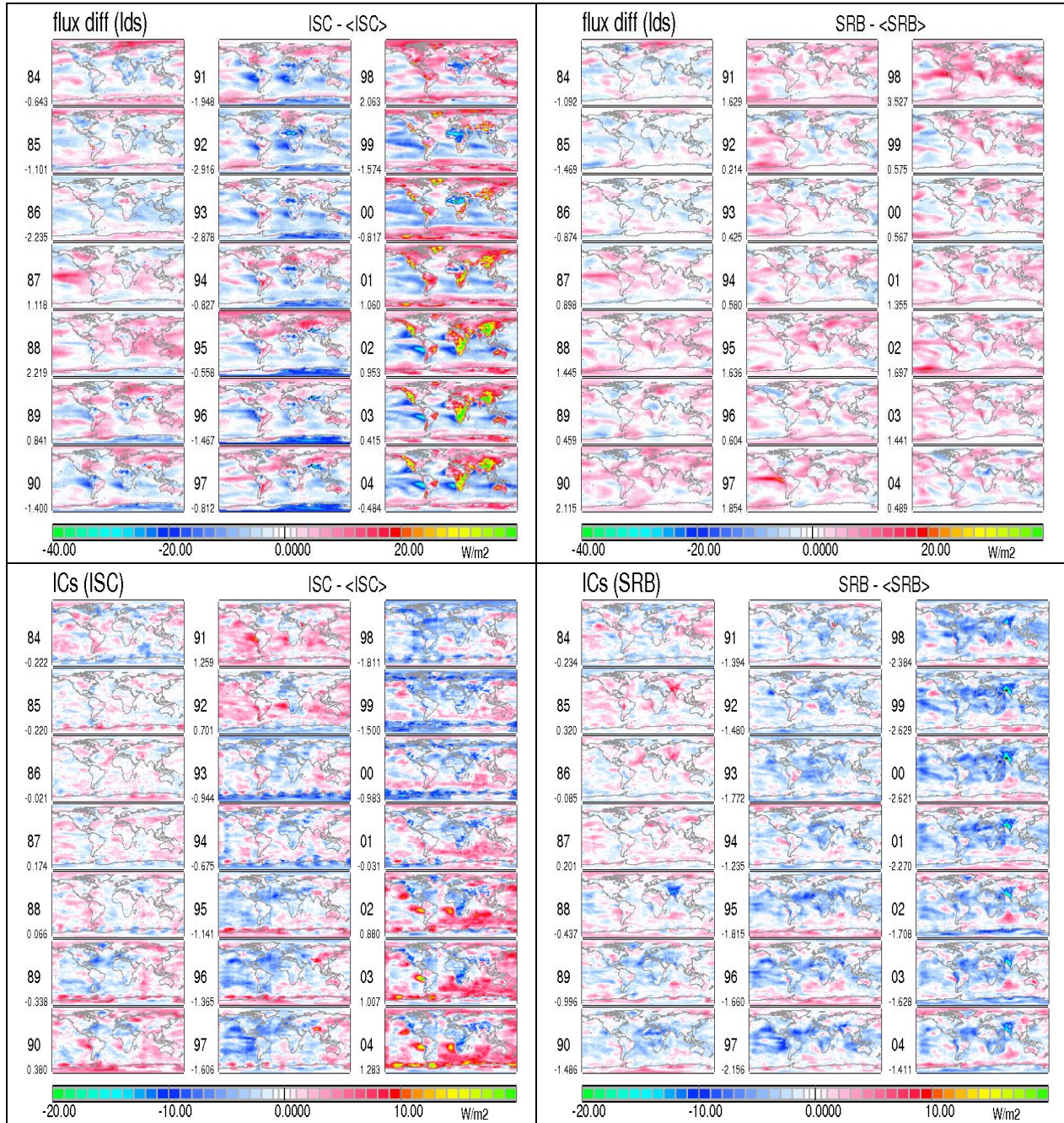


**Figure 2:** Anomalies of annual averages (in  $Wm^{-2}$ ) for the longwave downward fluxes to the surface at clear-sky conditions (upper row) and the cloud radiative effects on longwave downward fluxes (lower row) for ISCCP (left) and SRB (right) with respect to the 1985-1988 reference period.

**Comment:** The Interannual variability, as visible in these maps, is due to both the natural variability of ancillary information and also several errors in ancillary data. One dominant feature in the maps after 2001 is due to the errors in the temperature values entering the ISCCP analyses. The two different anomaly sources are at times of opposite in sign, so that errors may go unnoticed in all-sky data comparisons.

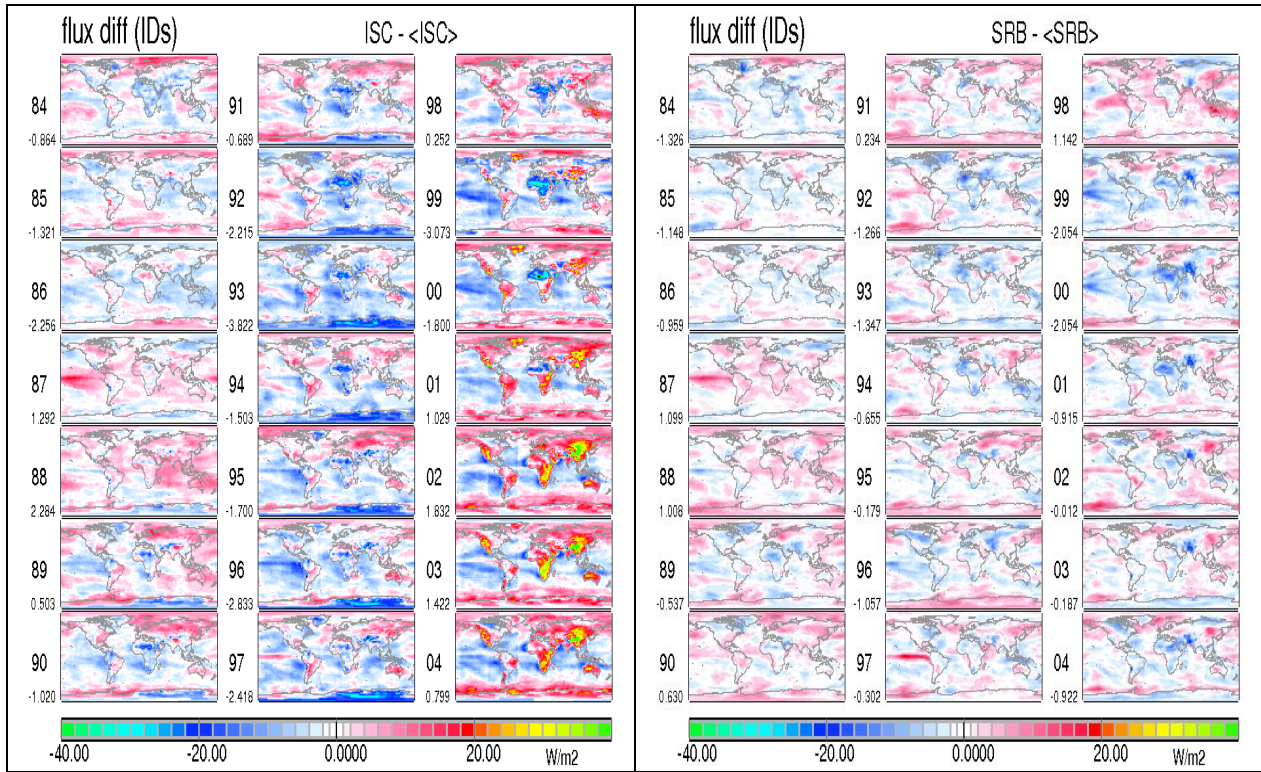


**Figure 2a:** Anomalies of annual averages of the *all-sky downward longwave radiation* at the surface. The pattern of Interannual variations is dominated by related variations of cloud fields.

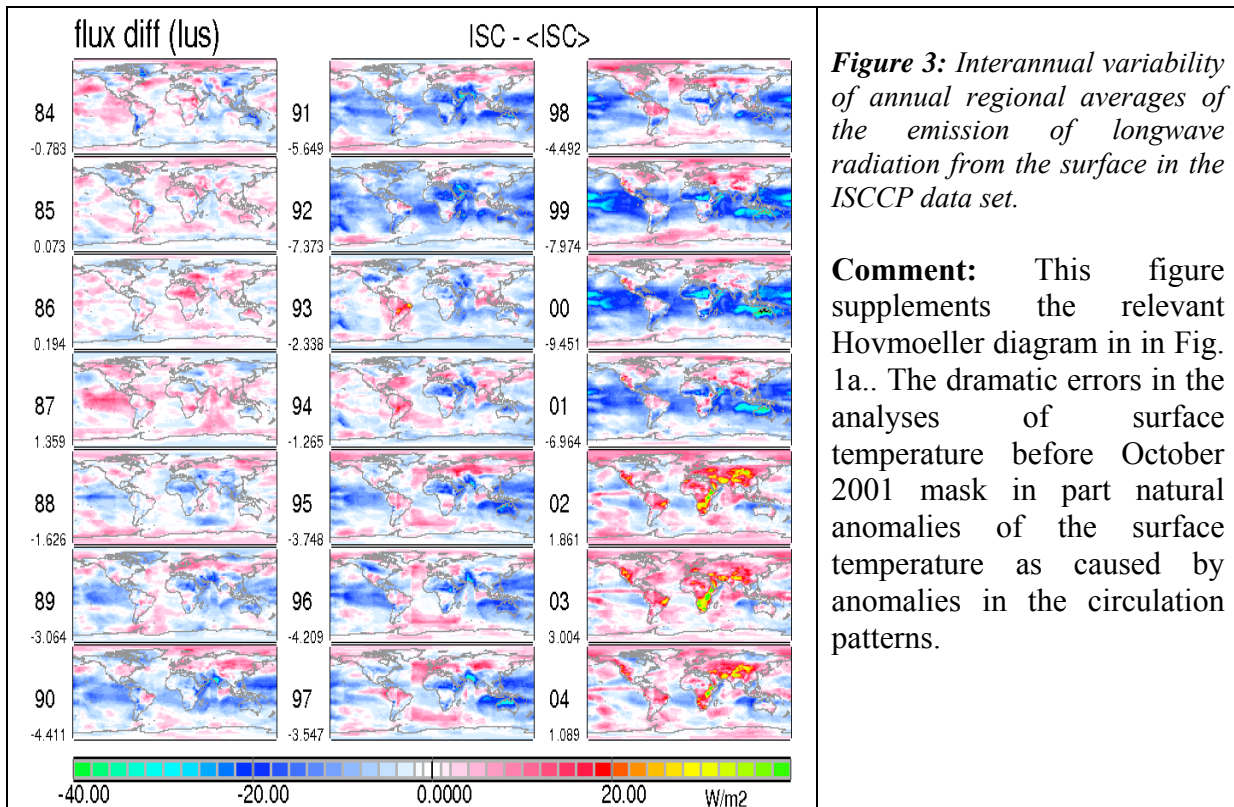


**Figure 3:** Interannual variability of annual regional averages of the emission of longwave radiation from the surface in the ISCCP data set.

**Comment:** This figure supplements the relevant Hovmoeller diagram in in Fig. 1a.. The dramatic errors in the analyses of surface temperature before October 2001 mask in part natural anomalies of the surface temperature as caused by anomalies in the circulation patterns.

## C4.5.2. Seasonal averages of solar (shortwave) radiation fluxes

**2.1:** Effective transmission of the **all-sky atmosphere** in CERES data and of the differences between ISCCP and CERES and SRB and CERES data sets **for solar radiation**

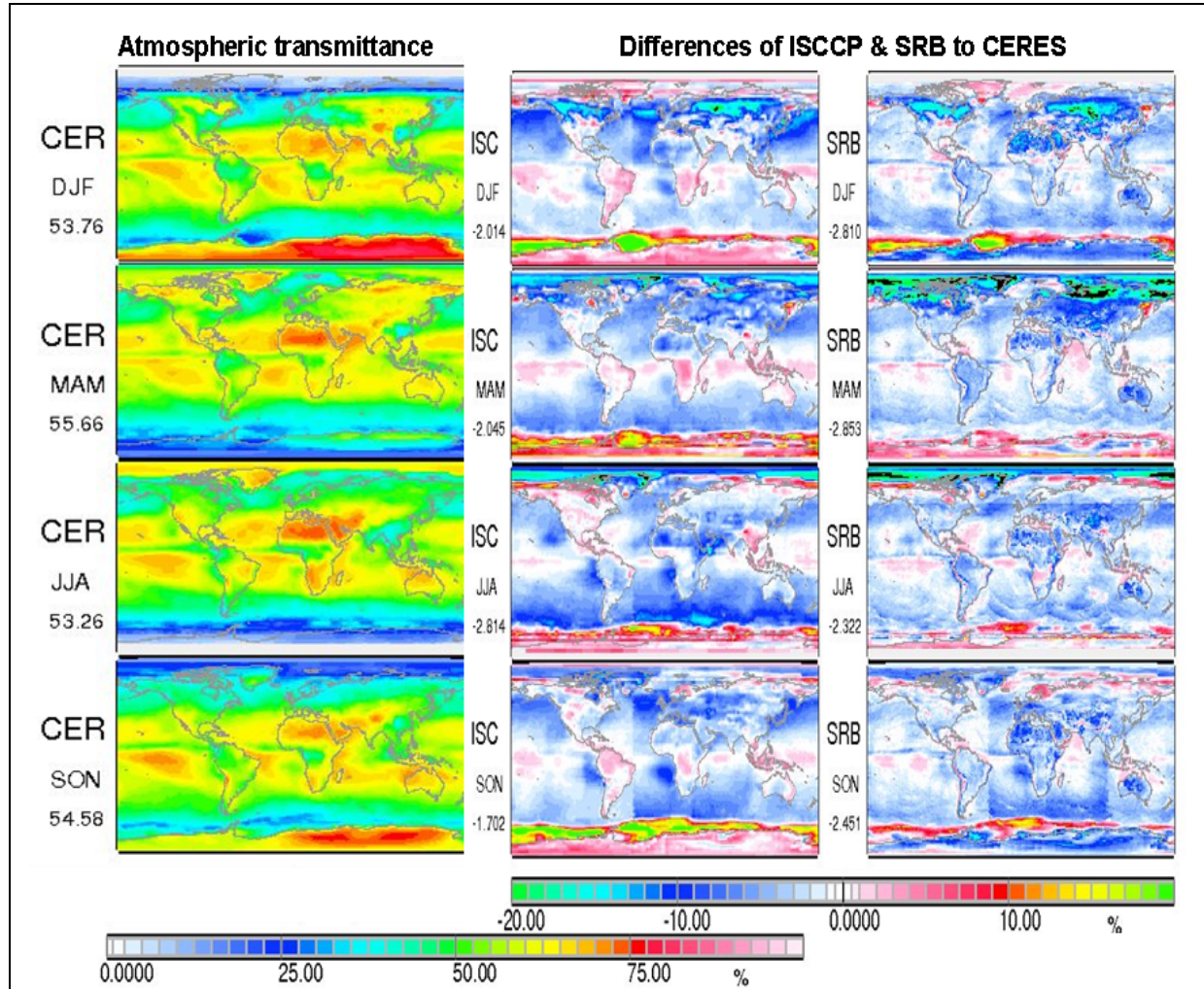


**Figure 4:** Seasonal averages of the *effective all-sky solar atmospheric transmittance* (in %) of CERES (left), and (absolute %) differences of ISCCP minus CERES (center) and SRB minus CERES (right). ISCCP and SRB data refer to 1984-1995 and CERES data to Mar2000-Feb2004 time-periods. Values below labels indicate global means.

**Comment:** The effective transmittance is the ratio of the downward solar radiation at the surface to the incoming radiation at the top of the atmosphere (TOA). Compared to the clear-sky transmission (presented in the main text), this solar transmission is strongly influenced (in addition to aerosol, trace-gases and molecular scattering) by the representation of clouds, which varies strongly among the three data-sets. Note the artifacts in the difference panels.

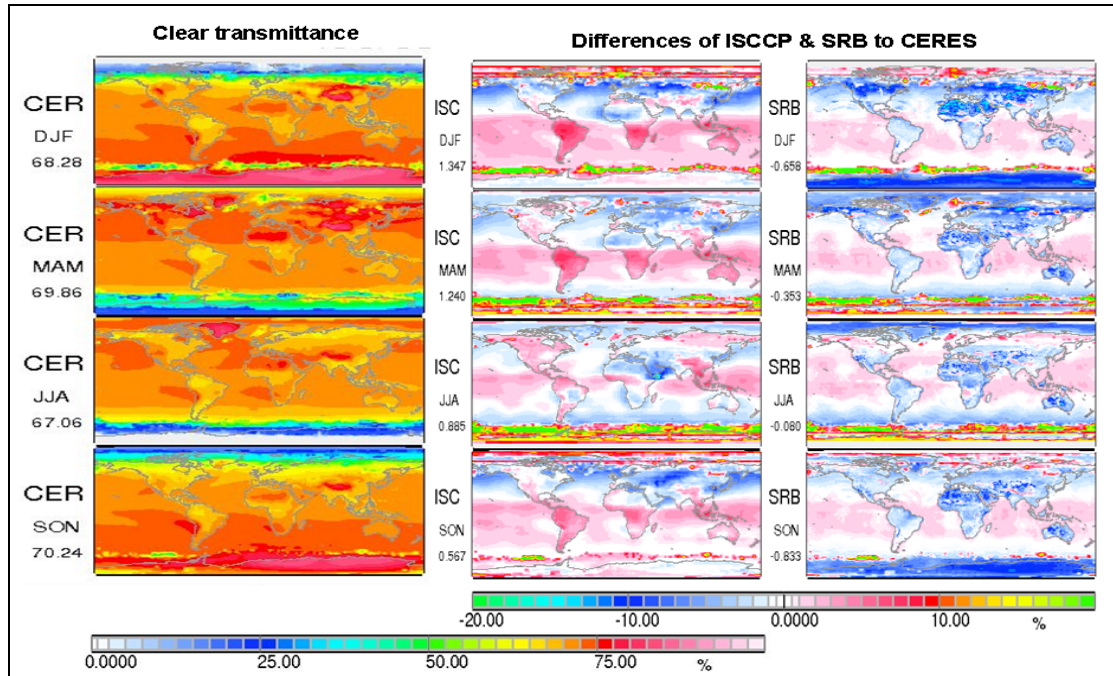


**Figure 4a:** Effective *clear-sky* transmittance of the atmosphere for solar radiation ISCCP and SRB data refer to 1984-1995 and CERES data to Mar2000-Feb2004 time-periods. Values below labels indicate global means. Anomaly pattern shows traces of known cloud fields.

**2.2: Effective all-sky surface albedo of CERES and the differences of ISCCP and SRB to CERES**

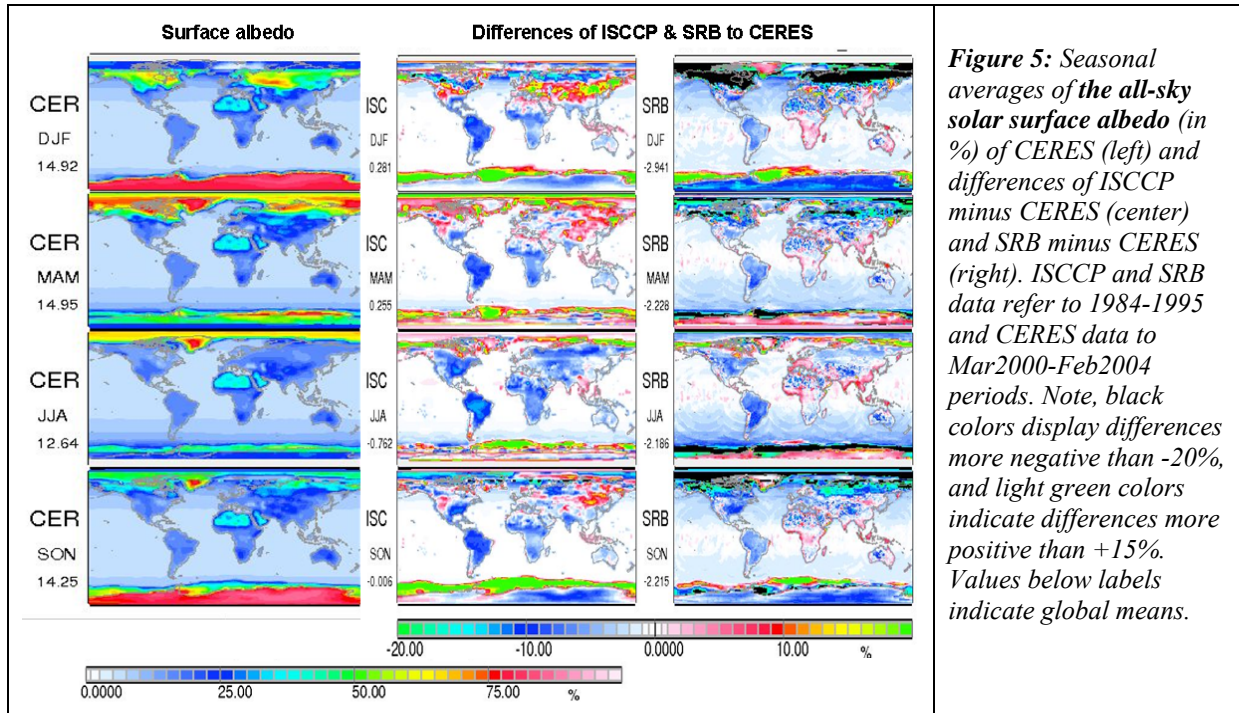


**Figure 5:** Seasonal averages of the *all-sky* solar surface albedo (in %) of CERES (left) and differences of ISCCP minus CERES (center) and SRB minus CERES (right). ISCCP and SRB data refer to 1984-1995 and CERES data to Mar2000-Feb2004 periods. Note, black colors display differences more negative than -20%, and light green colors indicate differences more positive than +15%. Values below labels indicate global means.

**Comment:** All-sky surface albedoes are expected to be almost identical to clear-sky solar surface albedos (presented in the main text). However, there are differences, because multiple scattering via clouds and surface are usually expected to increase solar surface albedo data. There are also differences caused by the incomplete cloud screening. However, due to the reduced solar radiative energy exchanges below clouds, these solar surface albedo differences are less important.

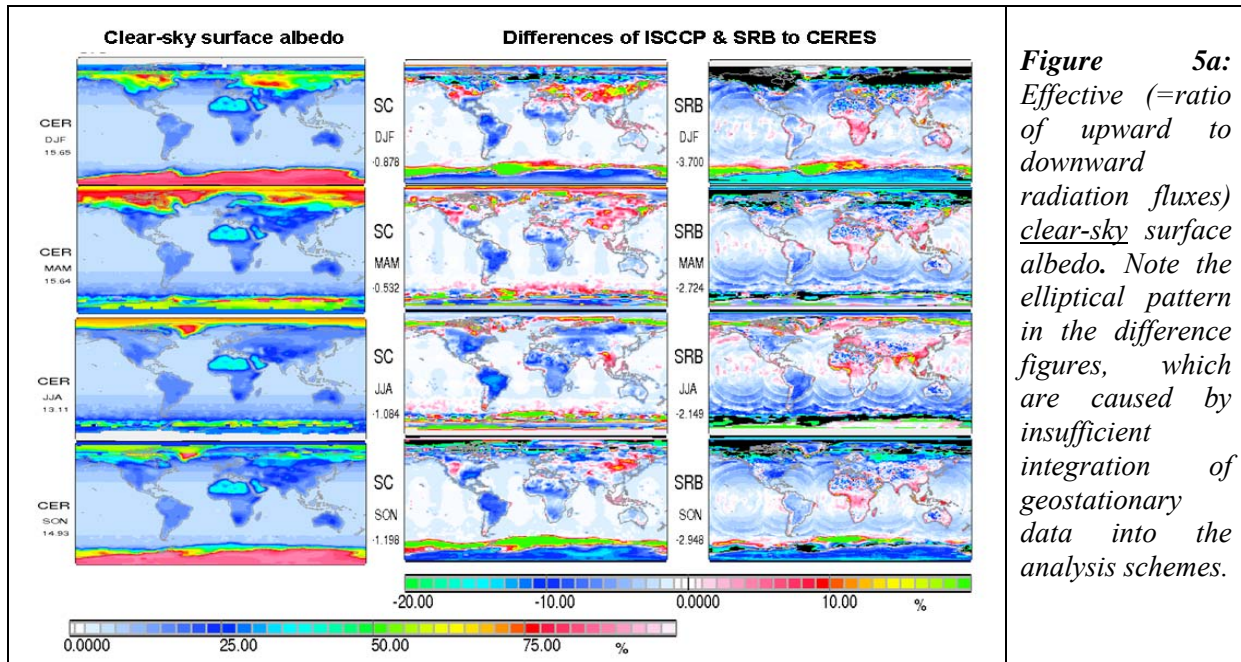


**Figure 5a:** Effective (=ratio of upward to downward radiation fluxes) clear-sky surface albedo. Note the elliptical pattern in the difference figures, which are caused by insufficient integration of geostationary data into the analysis schemes.

**Comments:** Note the quite large differences between the three data sets over most continental surfaces.

**Cloud-radiative effect on the effective surface albedo for CERES and differences of ISCCP and SRB.**

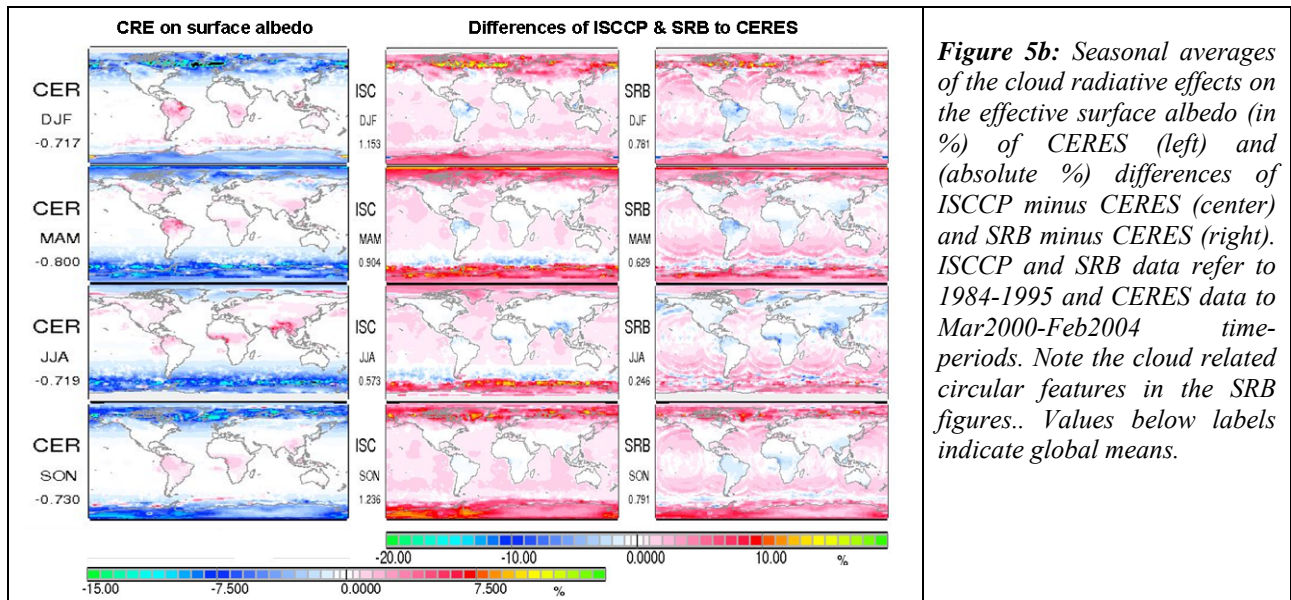


**Figure 5b:** Seasonal averages of the cloud radiative effects on the effective surface albedo (in %) of CERES (left) and (absolute %) differences of ISCCP minus CERES (center) and SRB minus CERES (right). ISCCP and SRB data refer to 1984-1995 and CERES data to Mar2000-Feb2004 time-periods. Note the cloud related circular features in the SRB figures.. Values below labels indicate global means.

**Comments:** It may be expected that with the presence of clouds the effective surface albedo is raised due to multiple scattering between clouds and surface. For CERES the cloud effects in both Sub-polar Regions, however, look rather strange and as a consequence also strange features occur for the ISCCP minus CERES and SRB minus CERES differences. With CERES clouds albedo increases are noticed over aerosol strong continental regions. These unusual features are not observed in ISCCP and SRB. In those data-sets clouds weakly brighten the solar surface albedo mainly over ocean regions with low cloud cover.

2.3: Downward fluxes of the solar radiation at the surface for CERES, ISCCP and SRB

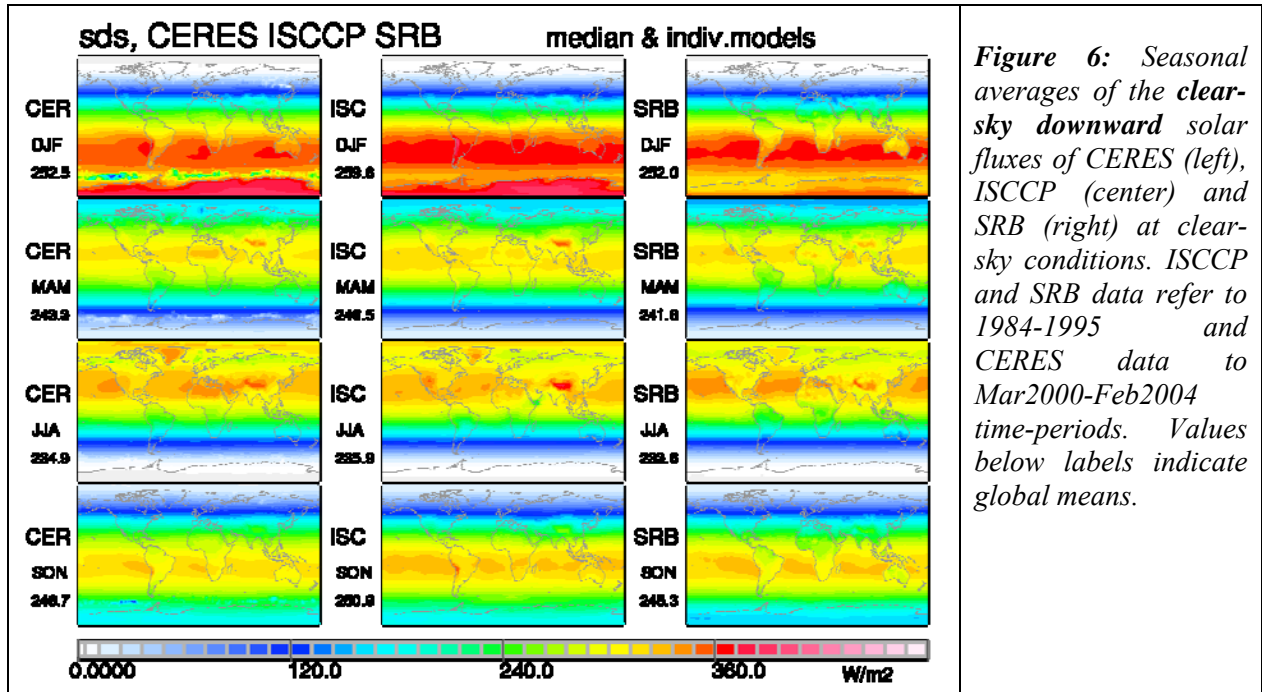


Figure 6: Seasonal averages of the clear-sky downward solar fluxes of CERES (left), ISCCP (center) and SRB (right) at clear-sky conditions. ISCCP and SRB data refer to 1984-1995 and CERES data to Mar2000-Feb2004 time-periods. Values below labels indicate global means.

Comment: The clear-sky solar downward fluxes are strongest in ISCCP, with larger clear-sky solar transmissions occurring over the (continental) tropics and southern hemispheric mid-latitudes.

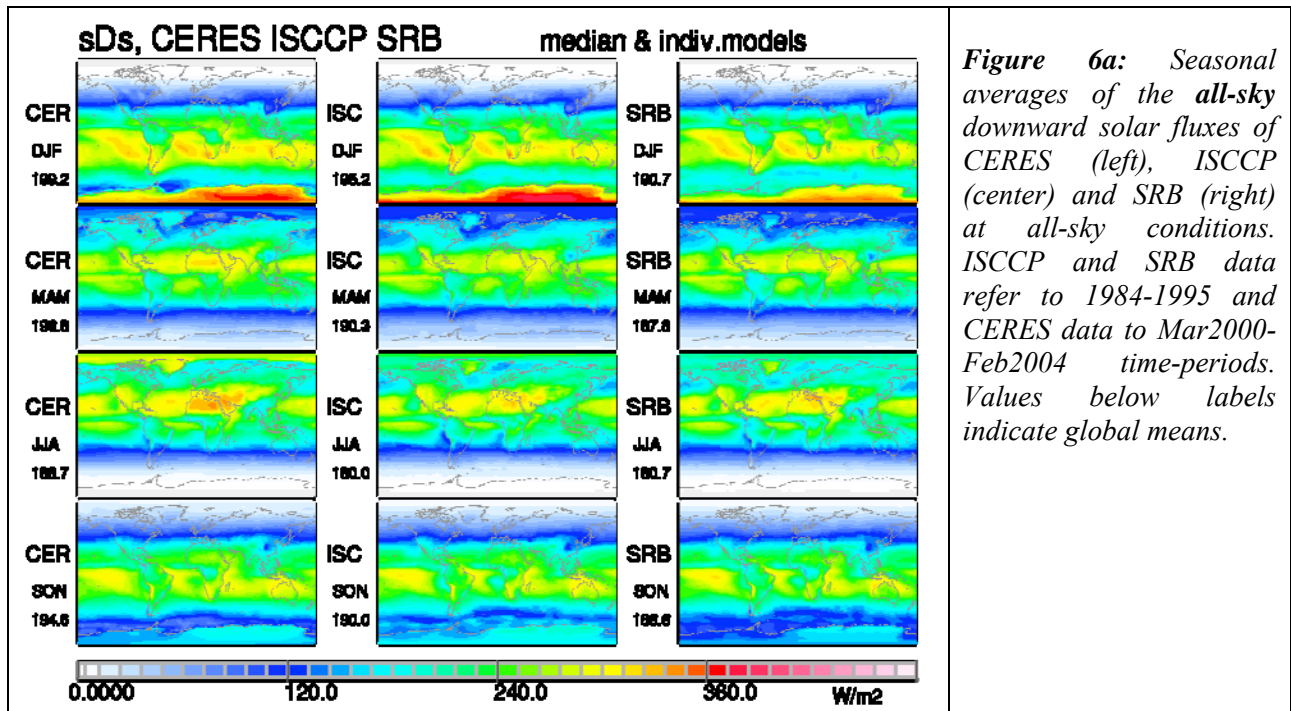
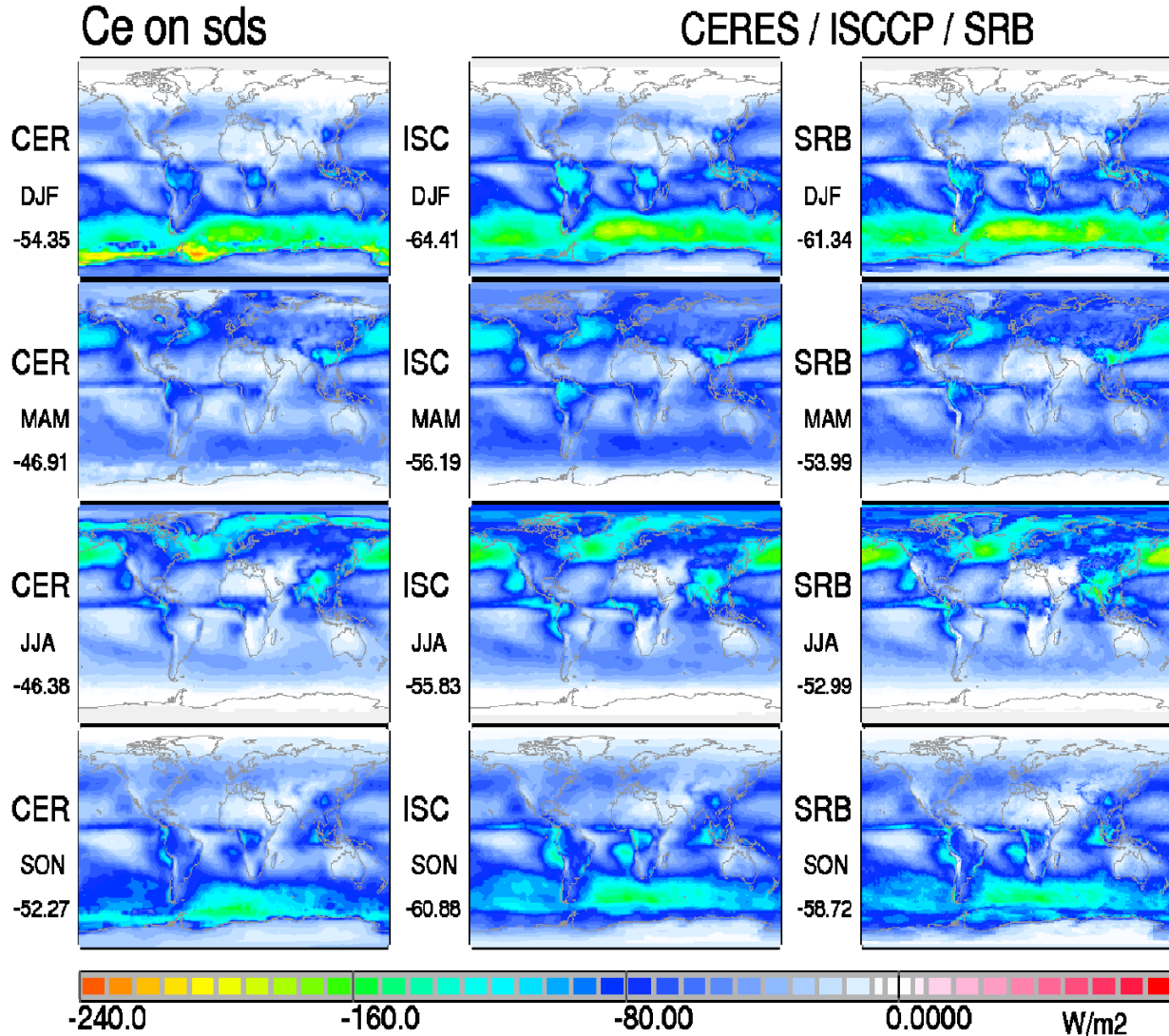


Figure 6a: Seasonal averages of the all-sky downward solar fluxes of CERES (left), ISCCP (center) and SRB (right) at all-sky conditions. ISCCP and SRB data refer to 1984-1995 and CERES data to Mar2000-Feb2004 time-periods. Values below labels indicate global means.

Comment: The all-sky solar downward fluxes are strongest in CERES, with larger all-sky solar transmissions occurring over desert regions. This indicates that the assumed cloud optical depths are relatively weak compared to ISCCP and SRB.

Cloud radiative effect on downward solar radiation fluxes at the surface for CERES, ISCCP and SRB



**Figure 6b:** Seasonal averages for cloud radiative effects on downward solar radiation fluxes for CERES (left), ISCCP (center) and SRB (right). ISCCP and SRB data refer to 1984-1995 and CERES data to Mar2000-Feb2004 time-periods. Values below labels indicate global means.

**Comment:** Clouds reduce everywhere the solar radiation reaching the surface. Overall cloud effects are weakest in CERES (despite larger values east of the Palmer pen-insula during the SH summer), with weaker cloud impacts are found in the central tropics and during mid-latitude summers. This is a bit surprising, since due to the difference clear-sky definition, the CERES cloud effect also include a water vapor effect, especially in regions of low cloud cover. Thus, CERES cloud radiative effects were expected to be larger. However, comparisons of the reductions of solar transmission by clouds had shown that the assumed cloud optical depths in CERES data is relatively low compared to ISCCP and SRB.

### C4.5.3: Seasonal averages of infrared (longwave) radiation fluxes

#### 3.1: Upward all-sky longwave radiation at the surface for CERES and differences of ISCCP and SRB

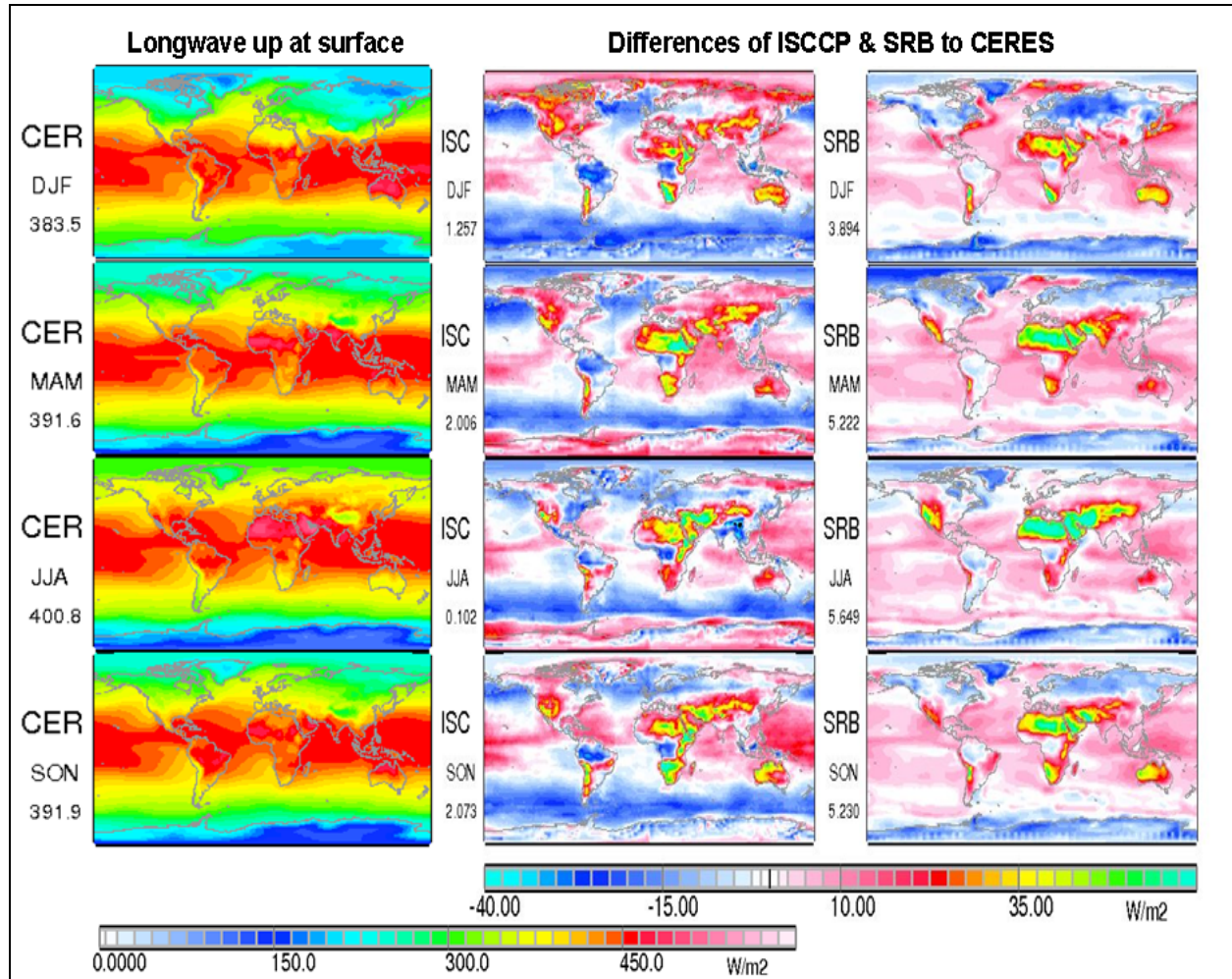


**Figure 7:** Seasonal averages of *all-sky upward longwave radiation fluxes* from the surface for CERES (left) and differences of ISCCP minus CERES (center) and of SRB minus and CERES (right). ISCCP and SRB data refer to 1984-1995 and CERES data to Mar2000-Feb2004 time-periods. Values below the labels are global averages.

**Comment:** All-sky upward radiation fluxes from the surface are expected to be almost identical to upward fluxes under clear-sky conditions (presented in the main text). The incomplete cloud-screening however causes features in the different data-sets that slightly modify upward IR radiative fluxes. There further large differences in the data sets of ISCCP and SRB over both Sub-polar regions.

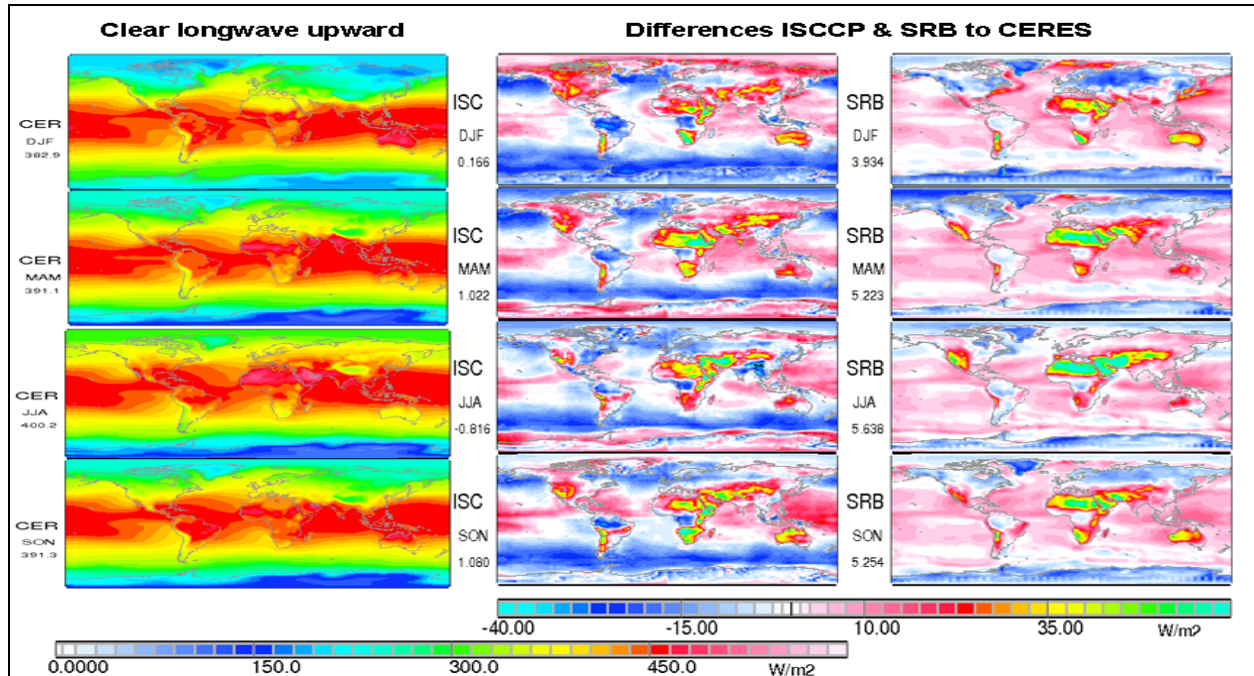


**Figure 7a:** Seasonal averages of *clear-sky upward longwave radiation fluxes* from the surface for CERES (left) and differences of ISCCP minus CERES (center) and of SRB minus and CERES (right). ISCCP and SRB data refer to 1984-1995 and CERES data to Mar2000-Feb2004 time-periods. Values below the labels are global averages.

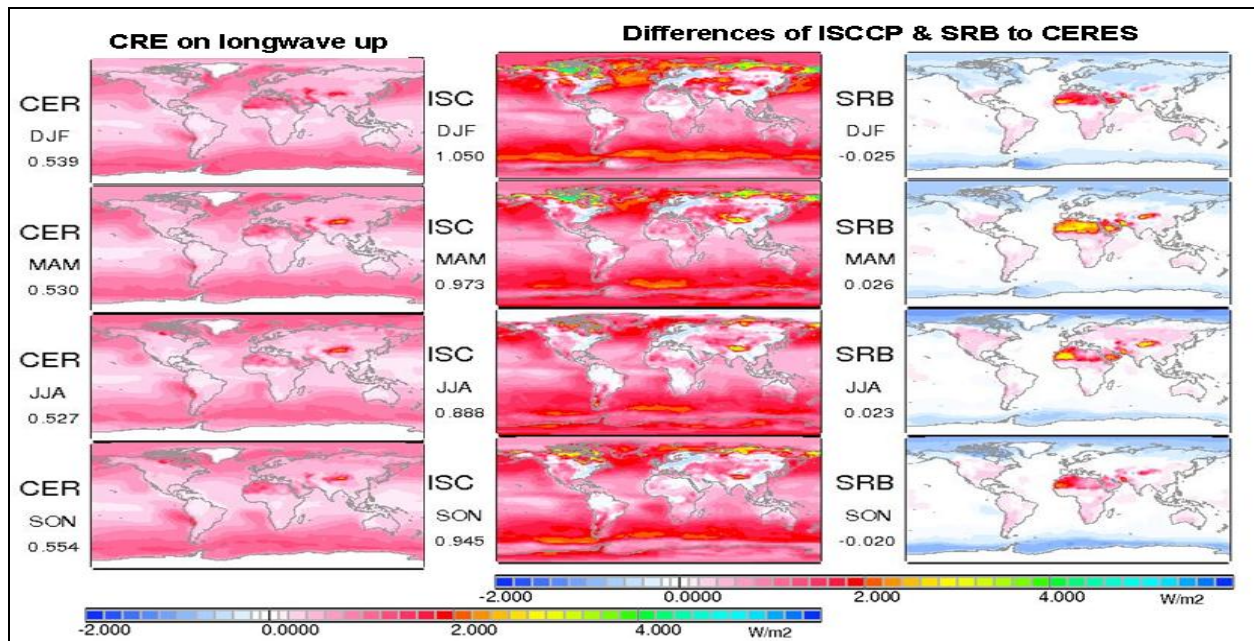


**Figure 7b:** Seasonal averages of cloud radiative effects (CRE) on the *upward longwave (IR) fluxes* from the surface at cloud-free conditions. Maps are presented for absolute values by CERES (left) and differences of ISCCP minus CERES (center) and SRB minus and CERES (right). Values below labels indicate global means.

**Comments:** The impact of clouds on the IR fluxes displays an unexpected small increase by up to  $4 Wm^{-2}$ , The values though are relatively small and by far strongest for ISCCP. Relative strong ISCCP impacts occur over snow or ice (of Polar regions) and relative strong SRB impacts occur over desert regions, where assumed SRB surface emissivity is apparently higher than in CERES or ISCCP.

### 3.2: Downward longwave radiation fluxes at the surface for CERES, ISCCP and SRB

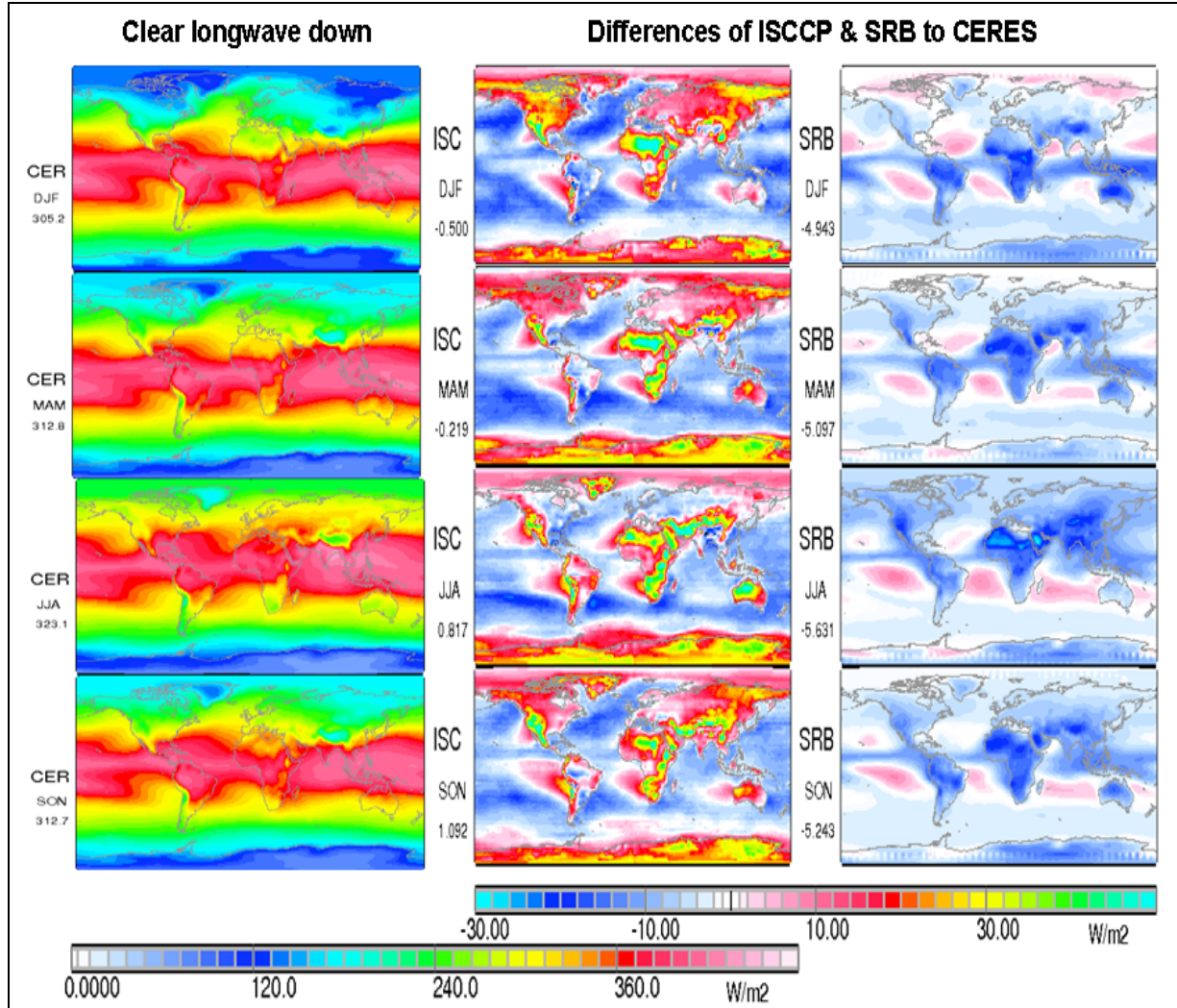


**Figure 8:** Seasonal averages of *clear-sky* downward longwave fluxes of CERES (left), ISCCP (center) and SRB (right) at *clear-sky* conditions. ISCCP and SRB data refer to 1984-1995 and CERES data to Mar2000-Feb2004 time-periods. Values below labels indicate global means.

**Comment:** Longwave downward clear-sky radiative fluxes to the surface are caused by sub-spectral absorption and subsequent emission by atmospheric aerosol and by trace-gases. The downward IR fluxes are strongly correlated to atmospheric near-surface temperatures, thus fluxes are smaller at higher altitudes and higher latitudes (and vice versa). CERES data are biased low in regions with larger low level cloud cover, because CERES data (by being based on clear-sky observations) miss the increased water vapor effect near clouds. Differences between ISCCP and CERES are positive over most continental areas while those between SRB and CERES are negative and More “perturbed” by cloud features.

All-sky downward longwave radiation fluxes to the surface for CERES, ISCCP and SRB

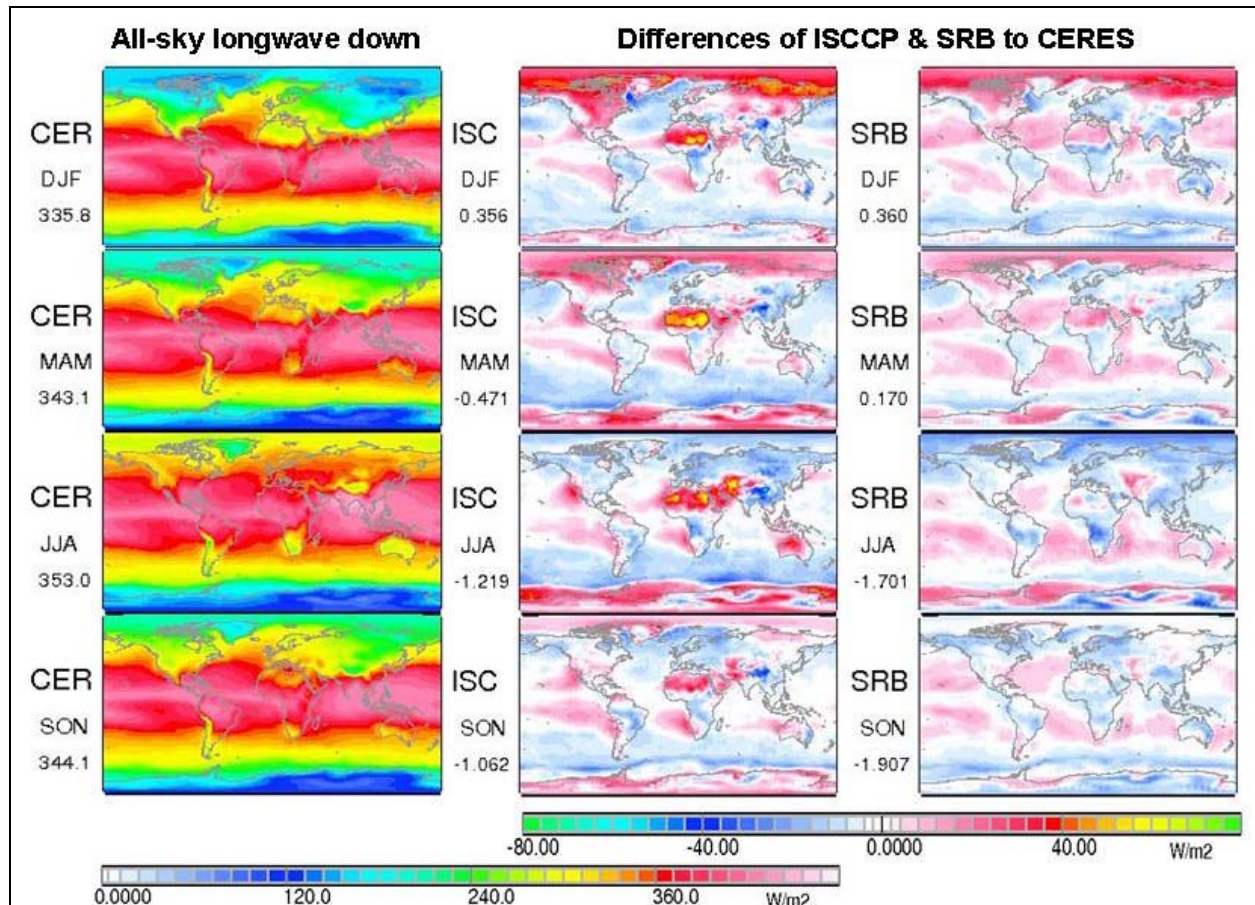


**Figure 8a:** Seasonal averages for all-sky downward longwave fluxes of CERES (left), ISCCP (center) and SRB (right) at all-sky conditions. ISCCP and SRB data refer to 1984-1995 and CERES data to Mar2000-Feb2004 time-periods. Values below labels indicate global means.

**Comment:** Longwave downward all-sky radiative fluxes to the surface are larger than corresponding clear-sky fluxes due to additional contributions by clouds. Compare with Figure 10, Cloud impact increases also with their vicinity to the surface, as with a lower cloud-base emissions occur usually at warmer temperatures. Regional values range between about 100 Wm<sup>-2</sup> over the polar areas to about 440 Wm<sup>-2</sup> over the equatorial regions.

Cloud-effect on downward IR fluxes to the surface for CERES, ISCCP and SRB

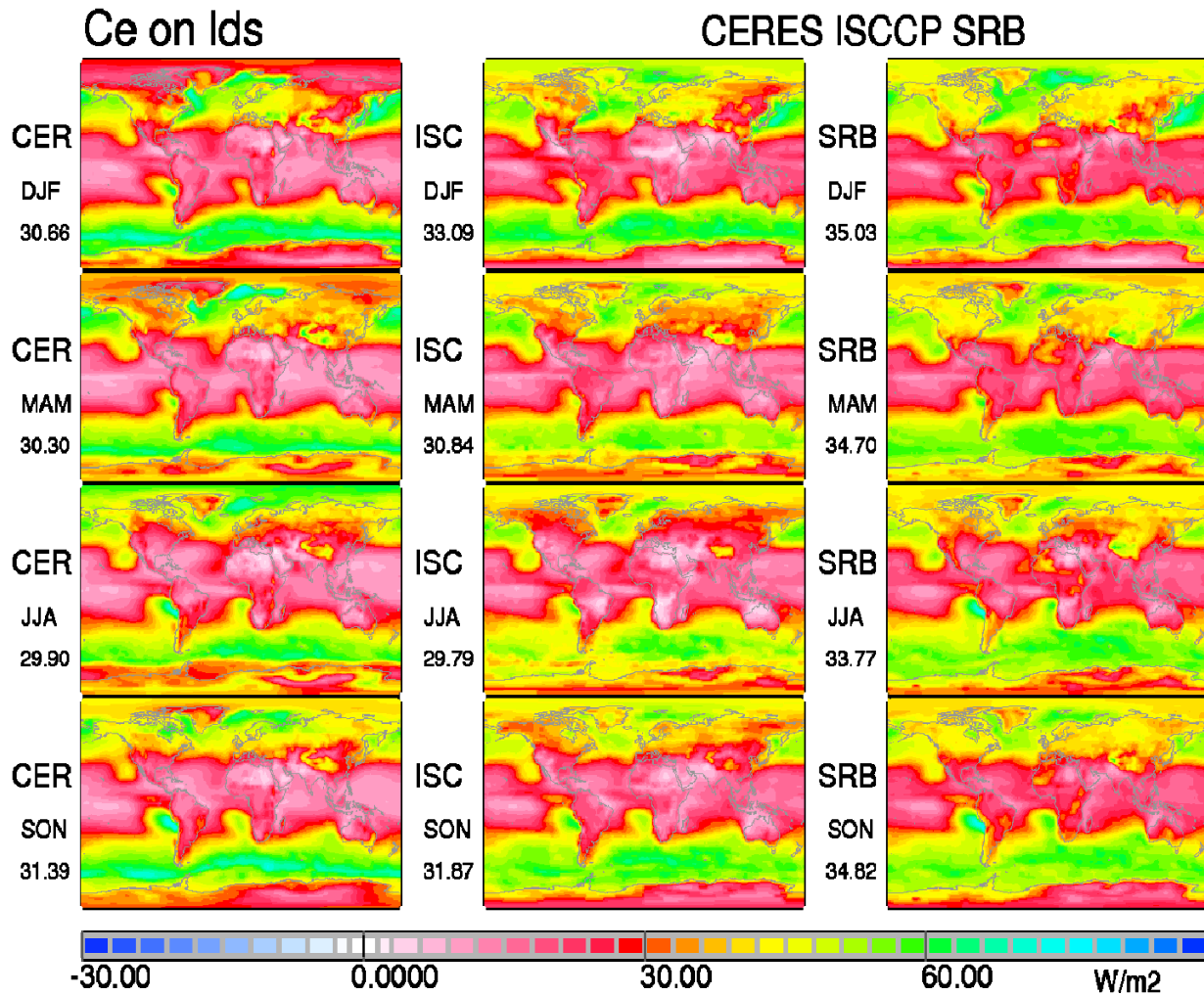


**Figure 8b:** Seasonal averages of the cloud radiative effects on downward longwave fluxes of CERES (left), ISCCP (center) and SRB (right). ISCCP and SRB data refer to 1984-1995 and CERES data to Mar2000-Feb2004 time-periods. Values below labels indicate global means. This figure has been produced in addition to the same, but with difference fluxes, in the main report, chapter 4.5.

**Comment:** Cloud contributions increase downward longwave fluxes to surface. Thus, only positive values are displayed. While the potential for cloud effects is largest over warm regions, the largest cloud impacts occur in regions with higher low-level cloud cover, as over storm tracks of the mid-latitudes and over off-coastal stratocumulus decks.

### C4.5.4: Seasonal averages of the total net radiation

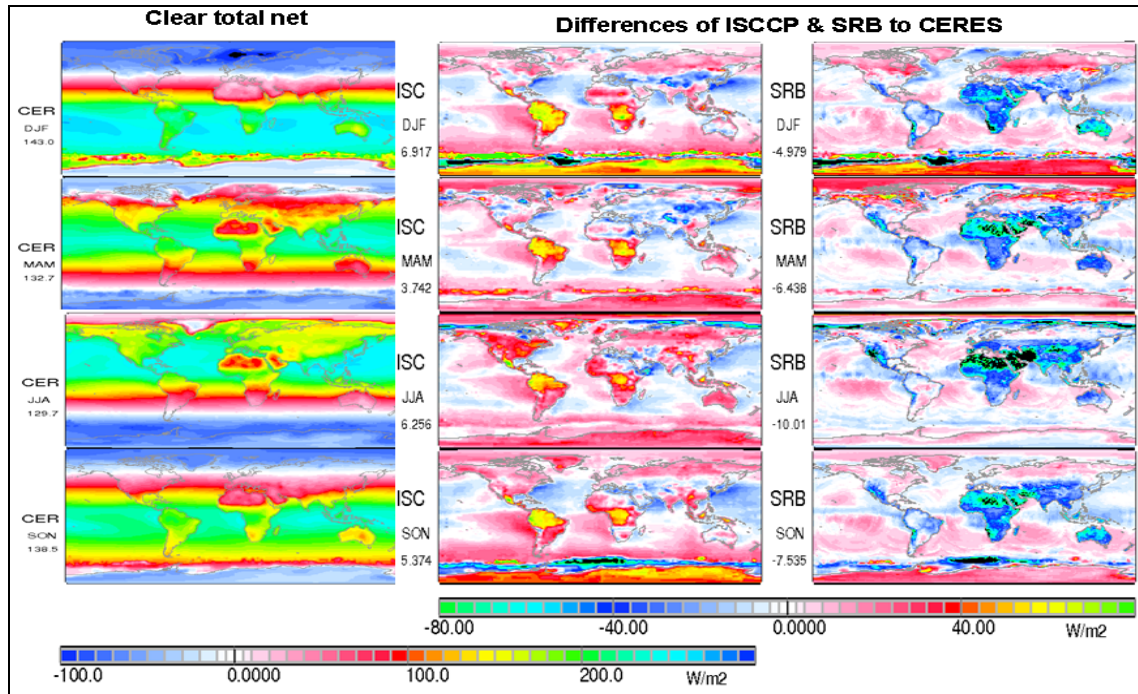


**Figure 9a:** Seasonal averages of the *clear-sky net radiation fluxes* at the surface of CERES (left), and the differences of ISCCP (center) and SRB (right) to CERES. ISCCP and SRB data refer to 1984-1995 and CERES data to Mar2000-Feb2004 time-periods. Values below labels indicate global means.

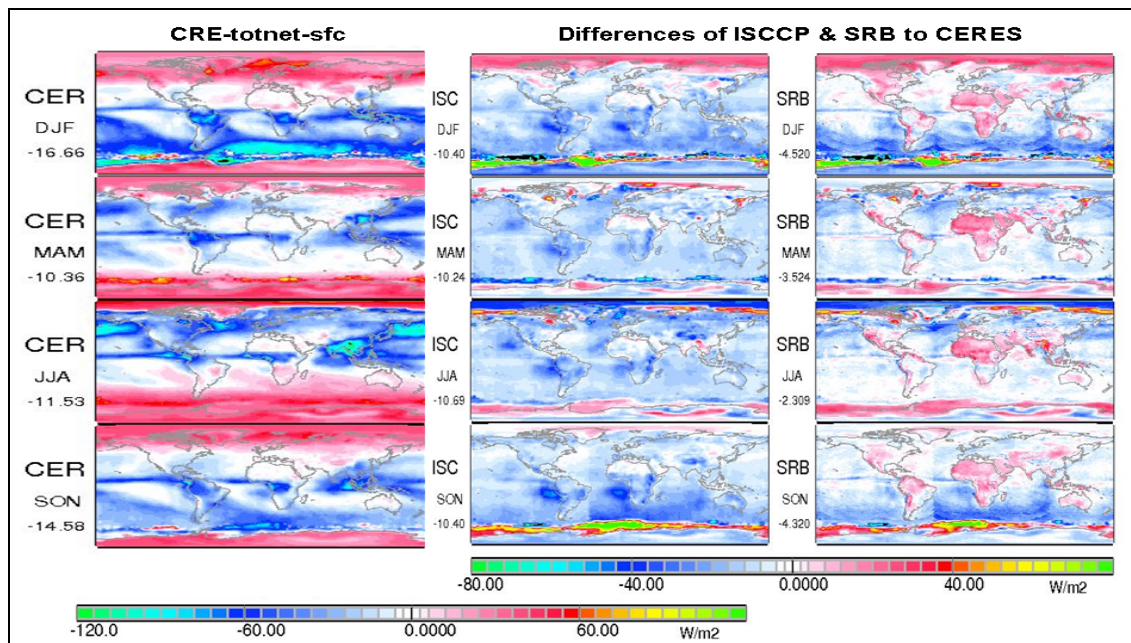


**Figure 9b:** Seasonal averages of the *cloud radiative effects on net radiation fluxes* at the surface of CERES (left), and the differences between ISCCP (center) and SRB (right) to CERES. ISCCP and SRB data refer to 1984-1995 and CERES data to Mar2000-Feb2004 time-periods. Values below labels indicate global means.

### C4.5.5: Seasonal averages of the total net radiation compared to the IPCC median results

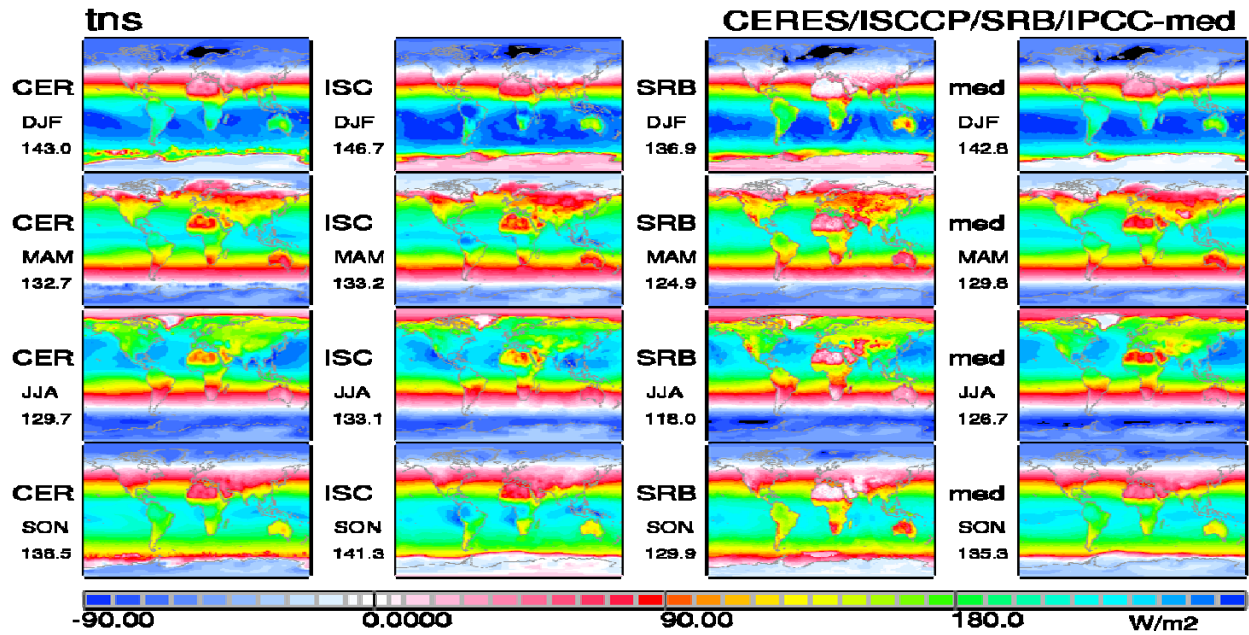


**Figure 10:** Seasonal averages of spectrally combined (solar and IR) radiative net-flux at the surface at clear-sky (no cloud) conditions between CERES (1.column, 3/2000-2/2004), ISCCP (2.column, 1984-1995), SRB (3.column, 1984-1995) and the median of models participating in the IPCC 4<sup>th</sup> assessment model. Values below labels indicate global means.

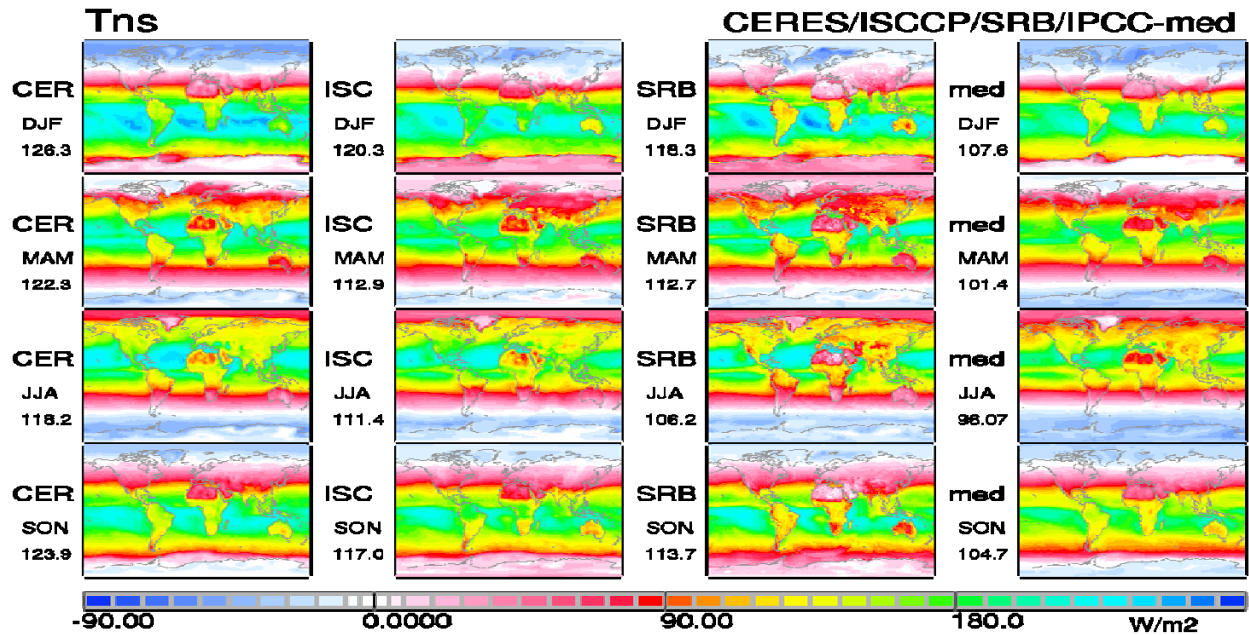


**Figure 10a:** Seasonal averages of spectrally combined (solar and IR) radiative net-flux at the surface at all-sky (with clouds) conditions between CERES (1.column, 3/2000-2/2004), ISCCP (2.column, 1984-1995), SRB (3.column, 1984-1995) and the median of models participating in the IPCC 4<sup>th</sup> assessment model. Values below labels indicate global means.

# Appendix C.7.1 for Chapter 7.1:

## Vertical Radiative Flux Divergence

E. Raschke and Y.-C. Zhang

In all cases the reference period covers 4 years (1985 to 1988). Main results have been summarized in *Chapter 7* of the report.

### C7.1.1: Deseasonalised anomalies and interannual variability of absorbed solar radiation.

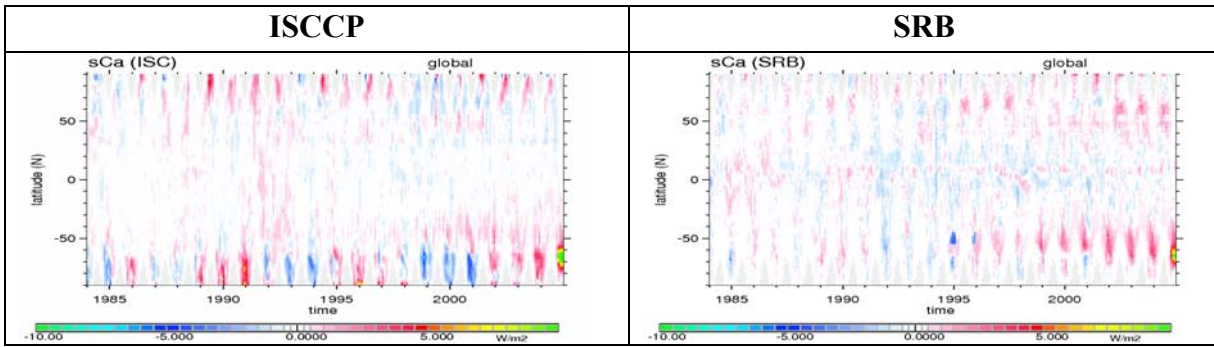


**Figure 1:** Monthly zonal deseasonalised anomalies of the cloud radiative effect (CRE) on the absorption of solar radiation during the period January 1984 to December 2004. The reference period covers 4 years: January 1985 to December 1988. Units are  $\text{Wm}^{-2}$ . Major anomalies at lower latitude are linked to the Pinatubo dust (1992-93) or to errors in temperature data (2001).

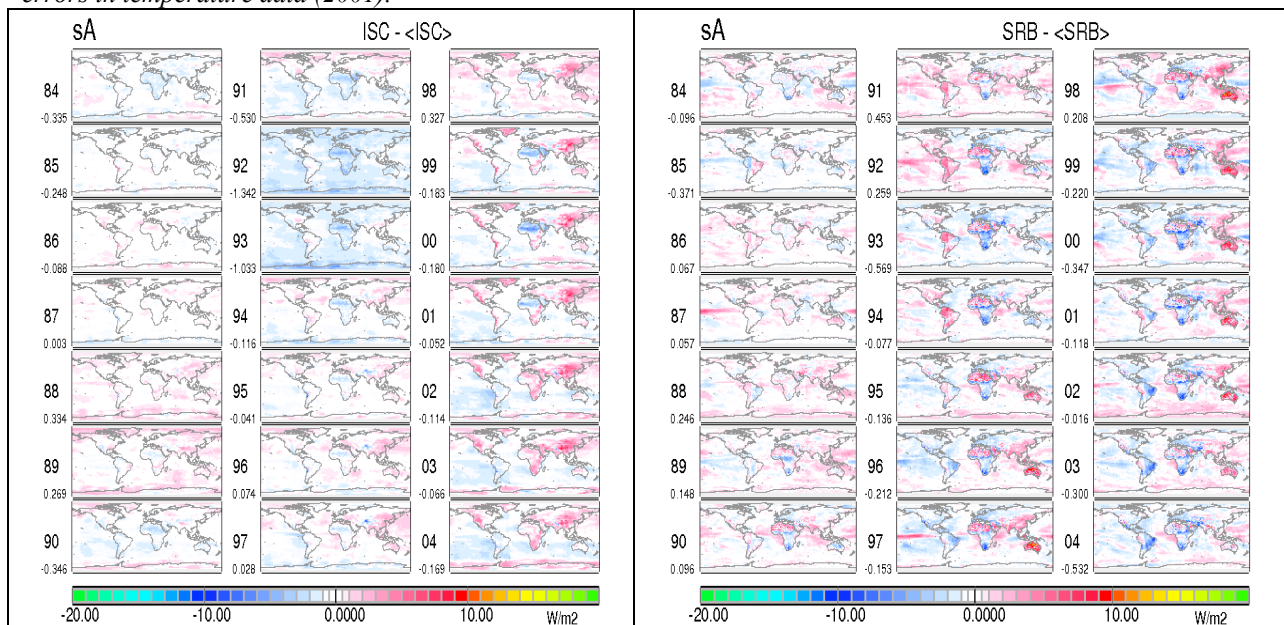


**Figure 2:** Interannual variability of annual averages of the anomalies (with respect to 1985 to 1988 averages) of the absorbed solar radiation in the all-sky atmosphere: ISCCP and SRB datasets. SRB data show a persistent minimum over South Africa.

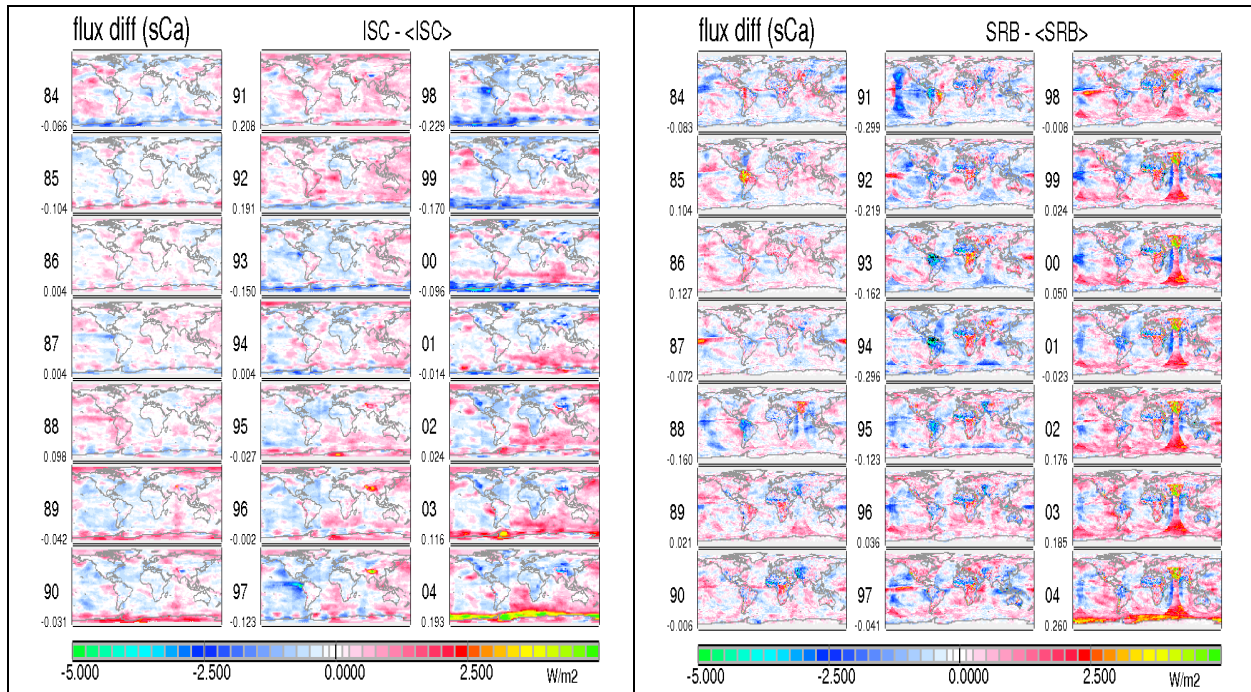


**Figure 3:** Interannual variability of annual averages of the anomalies of the cloud radiative effects on solar radiation absorbed in the atmosphere: ISCCP and SRB data sets.

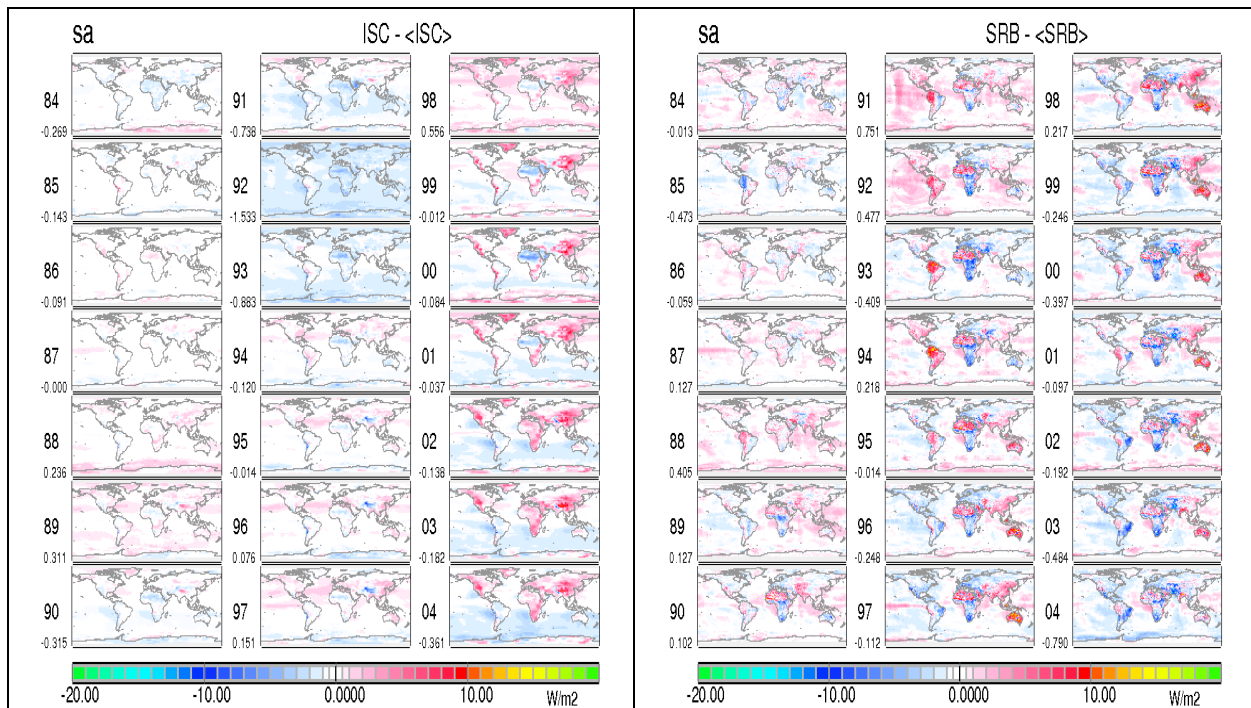


**Figure 4:** Interannual variability of annual averages of the absorbed solar radiation in the cloud-free atmosphere: ISCCP and SRB data sets

**Comments:** The solar absorption (here: negative convergence) describes the radiative atmospheric heating.

## 7.1.2: Interannual variability of the divergence of longwave radiation

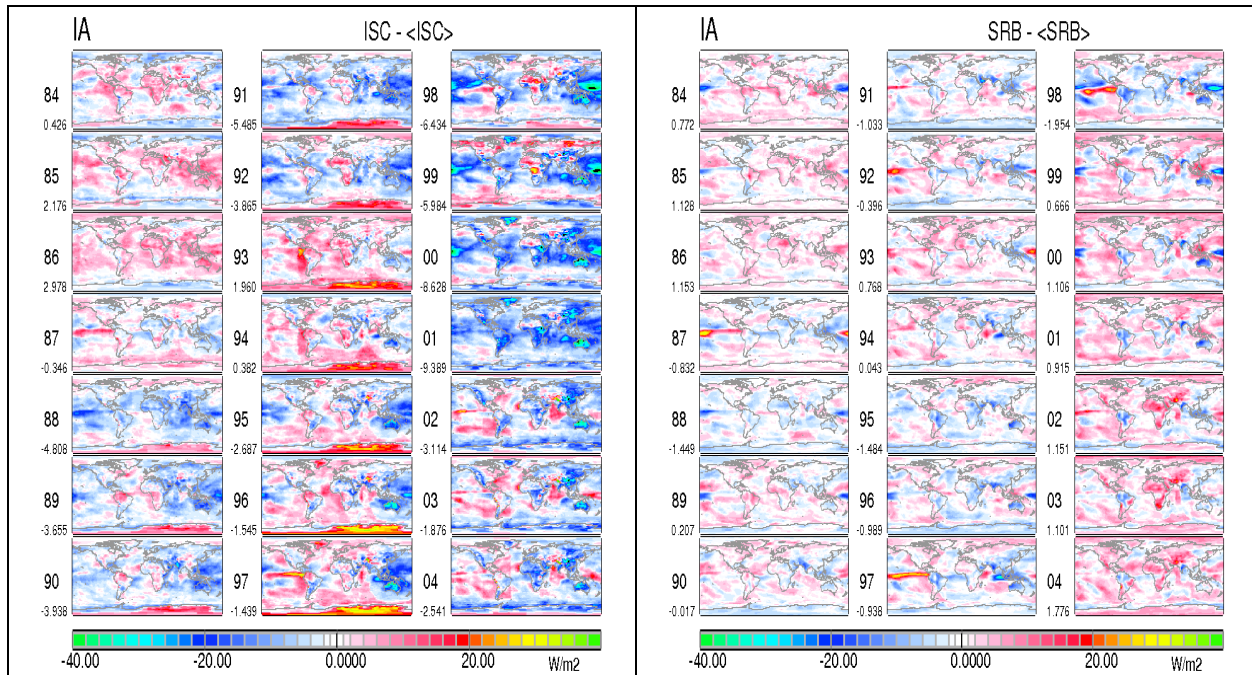


**Figure 5:** Interannual variability of annual averages of the longwave radiative divergence in the all-sky atmosphere: ISCCP and SRB

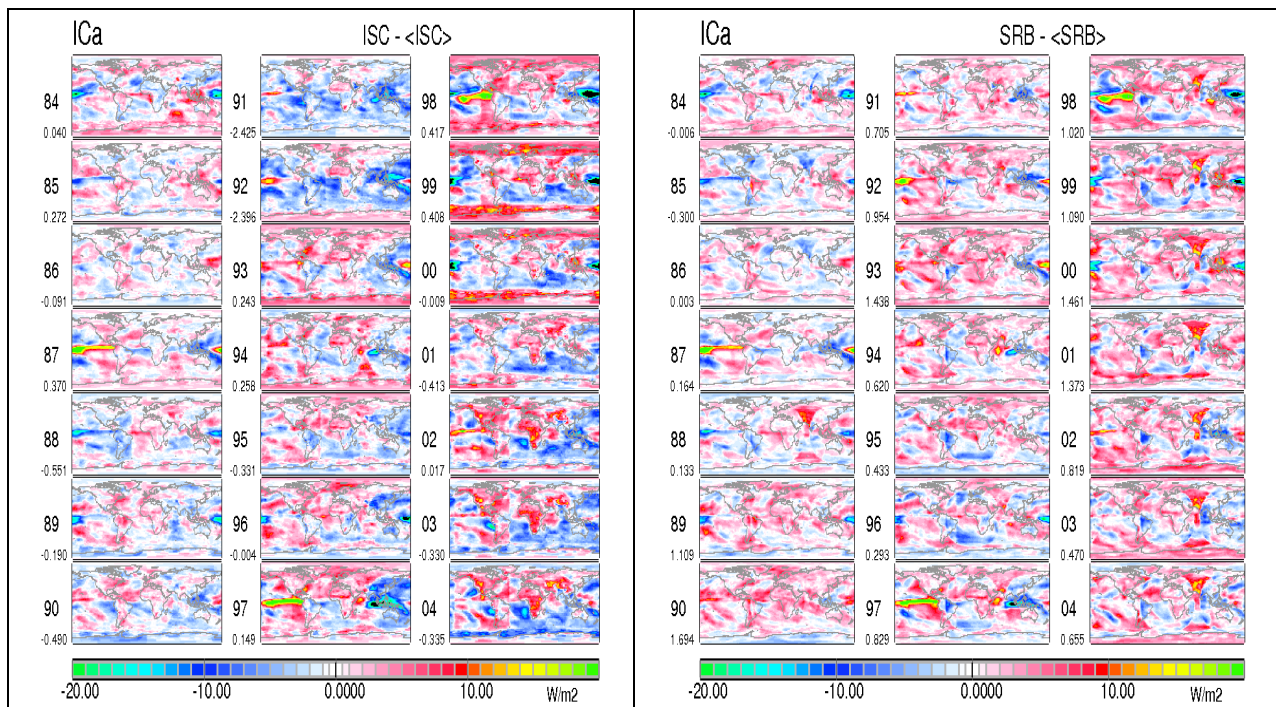


**Figure 6:** Interannual variability of annual averages of the CRE on longwave radiation flux divergence in the atmosphere: ISCCP and SRB data sets.

**Comments:** The longwave divergence describes the atmospheric **cooling** by radiation only.

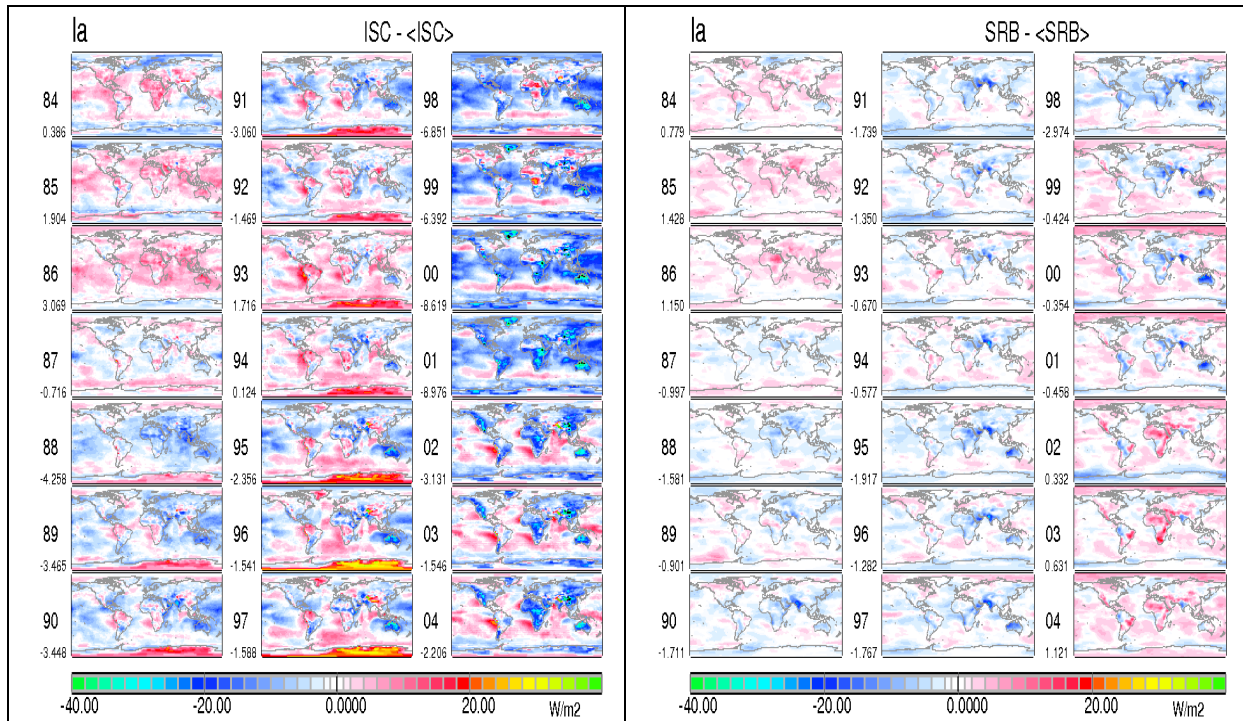


**Figure 7:** Interannual variability of annual averages of the divergence of longwave radiation in the cloud-free atmosphere: ISCCP and SRB datasets

**Comments:** Spatial variability is strongly linked to that of cloud field characteristics. Variations of the atmospheric gases and temperature should dominate the pattern in Figure 7, where we also see some structures due to incomplete cloud removal (de-clouding).

### 7.1.3: Seasonal averages of CERES results of the period March 2000 to February 2004

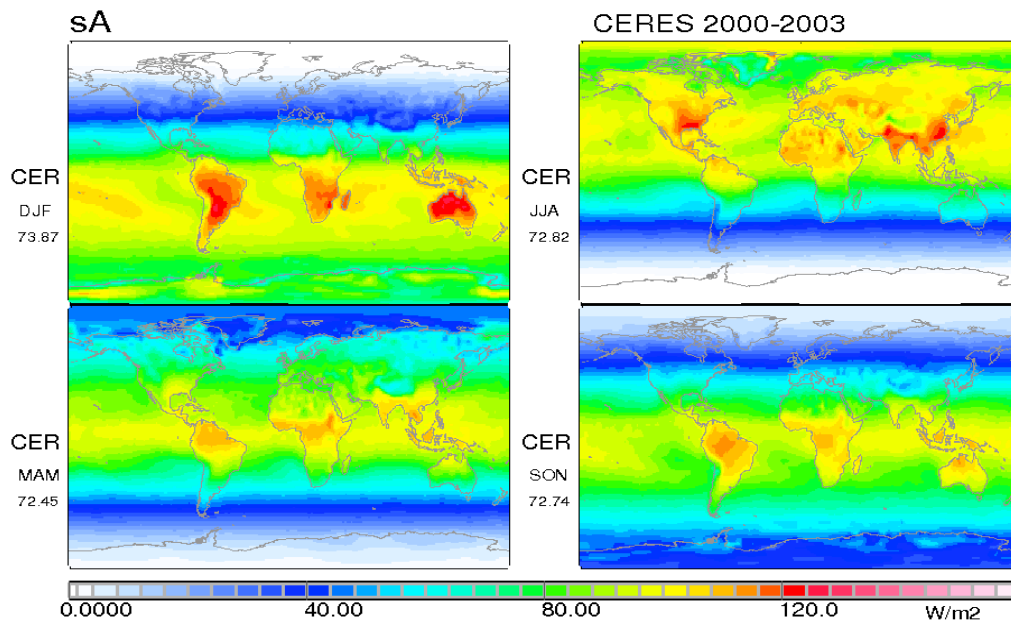


*Figure 8: CERES: Seasonal anomalies of the absorption of solar radiation in the all-sky atmosphere*

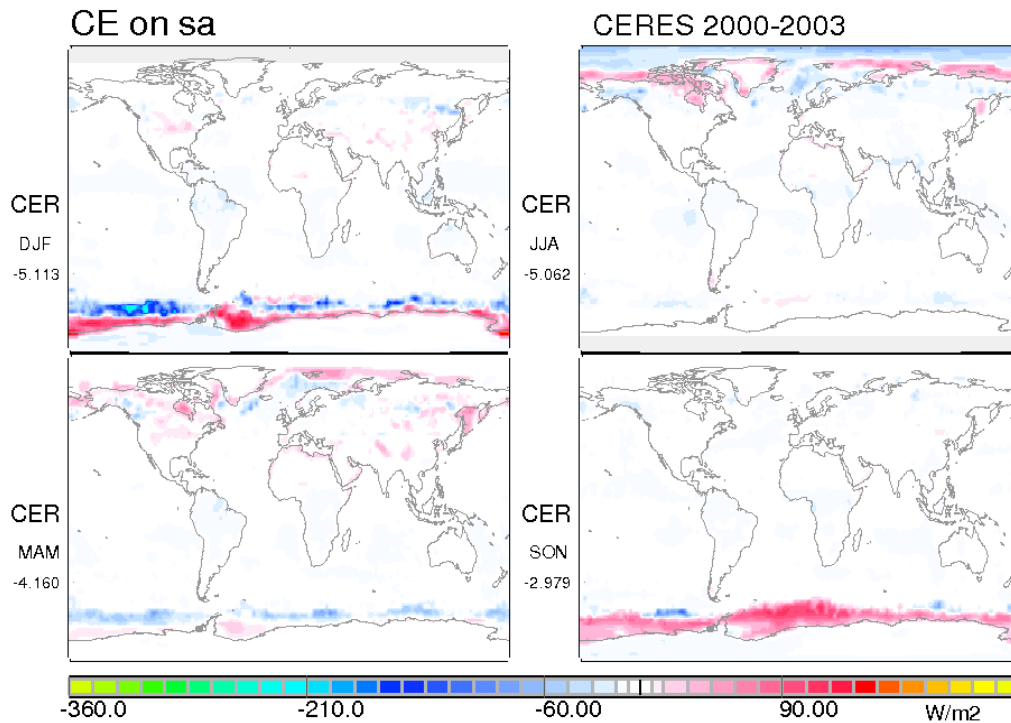


*Figure 9: CERES: Seasonal anomalies of the cloud radiative effect on the absorption of solar radiation*

**Comments:** The Sub-polar zones are notorious sources of errors due to errors in the identification of clouds and sea ice.

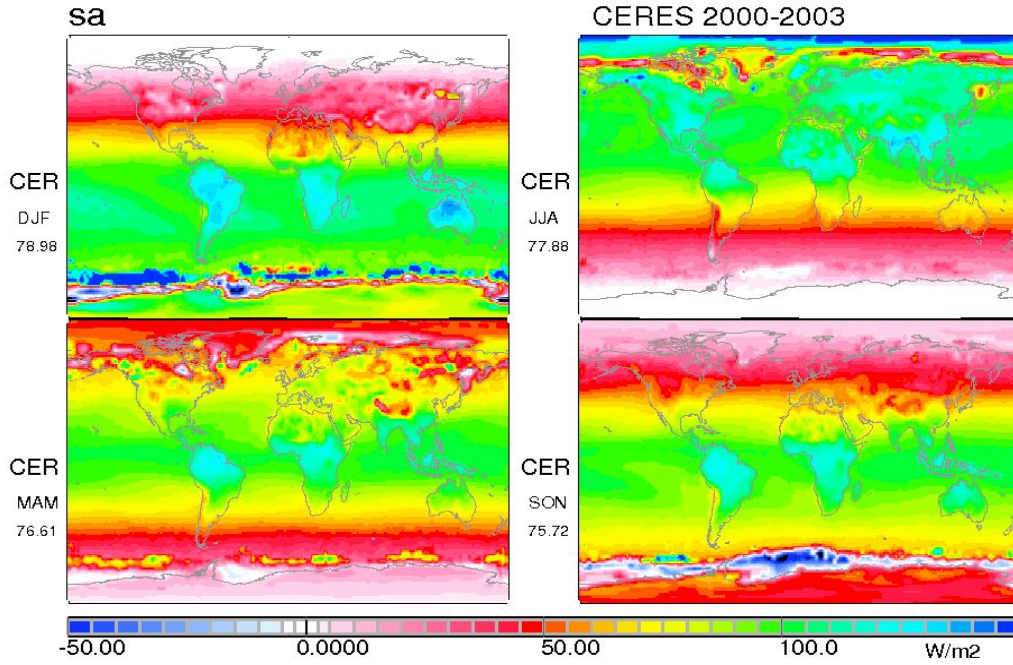


*Figure 10: CERES: Seasonal anomalies of the absorption of solar radiation in the cloud-free atmosphere*

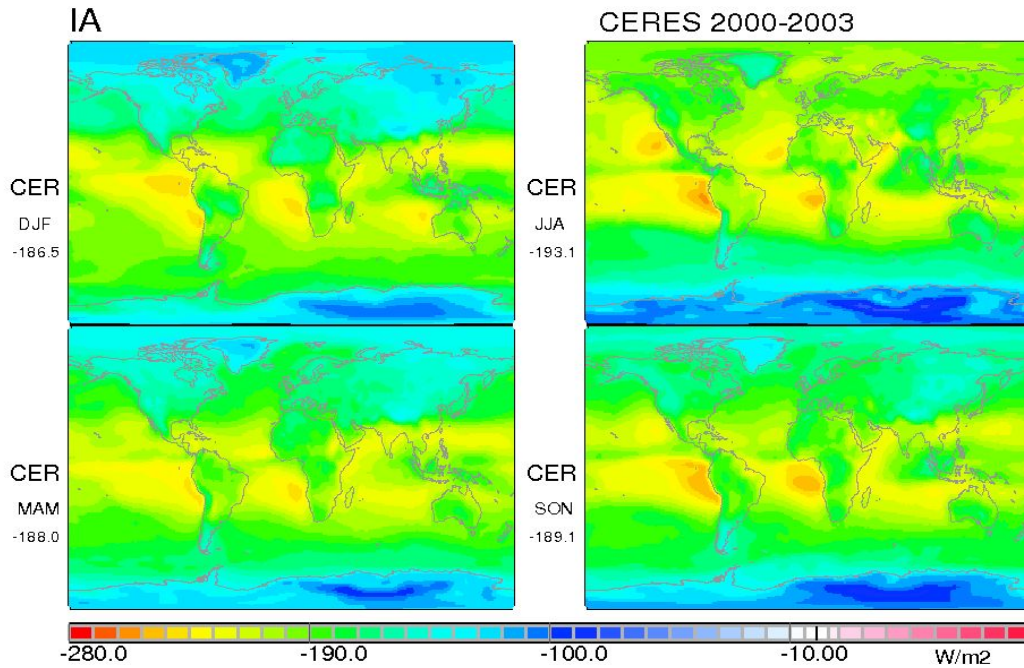


*Figure 11: CERES: Seasonal anomalies of the divergence of infrared radiation in the all-sky atmosphere*

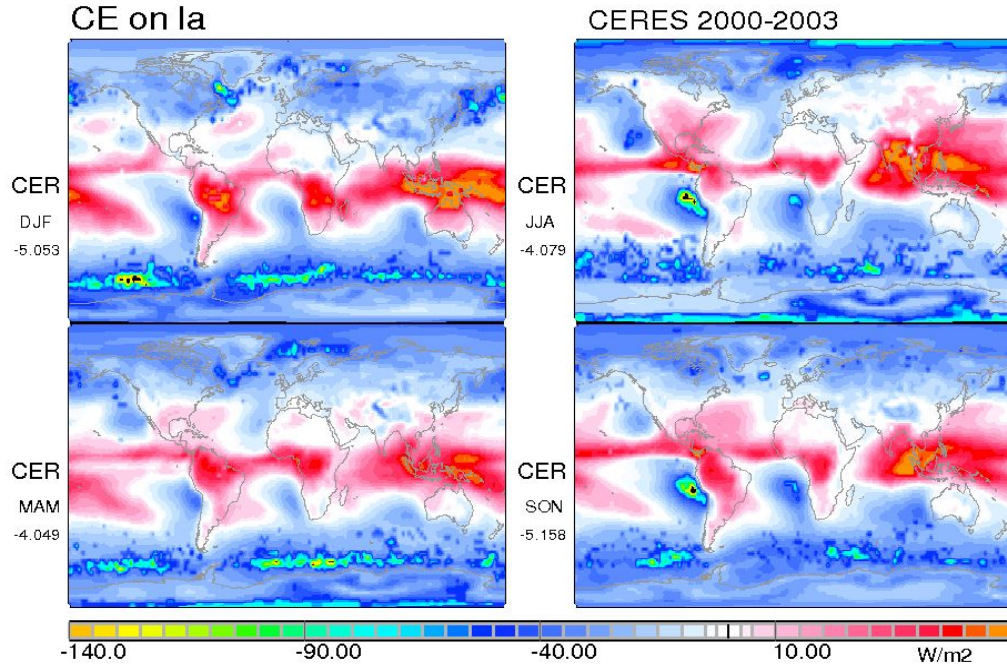


**Figure 12: CERES: Seasonal anomalies of the cloud radiative effect (CRE) on the divergence of infrared radiation in the atmosphere. Reddish/blueish areas describe the reduction/enhancement by clouds.**

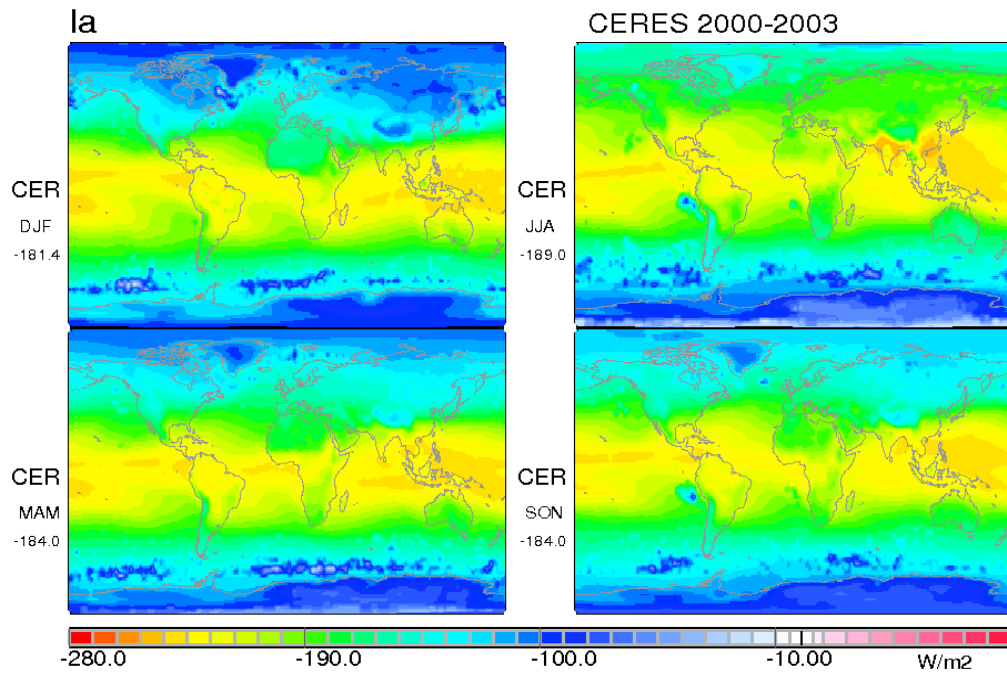


**Figure 13: CERES: Seasonal anomalies of the divergence of long-wave radiation in the cloud-free atmosphere**

**7.1.4: Differences between ISCCP/SRB to CERES results on seasonal averages of the period March 2000 to February 2004**

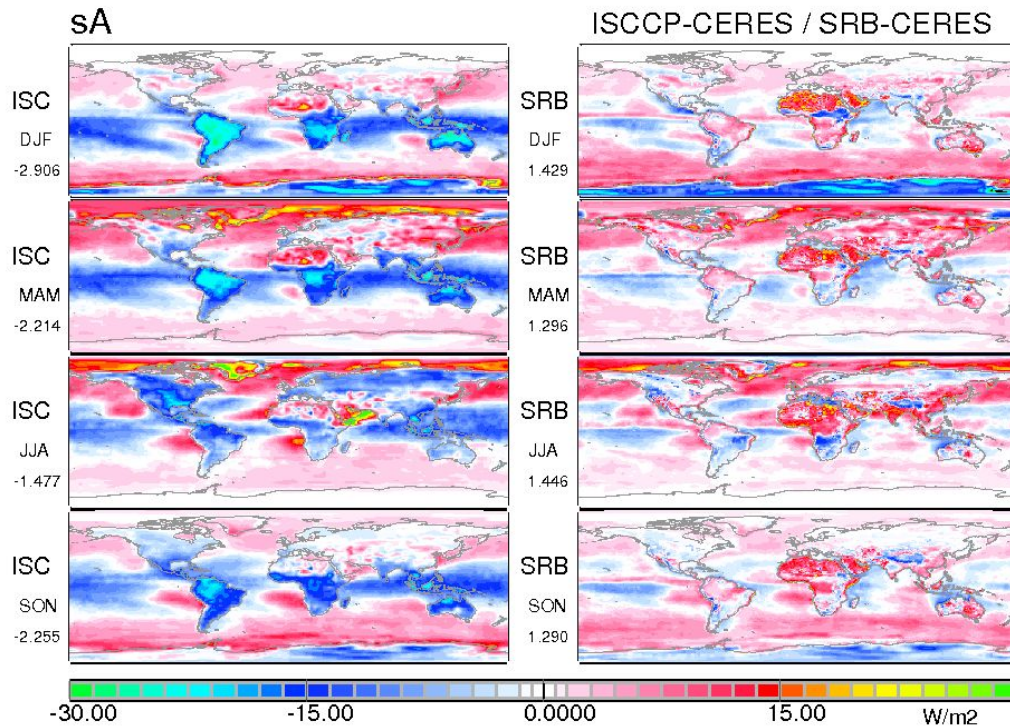


*Figure 14: ISCCP/SRB - CERES: Seasonal anomalies of the absorption of solar radiation in the all-sky atmosphere*

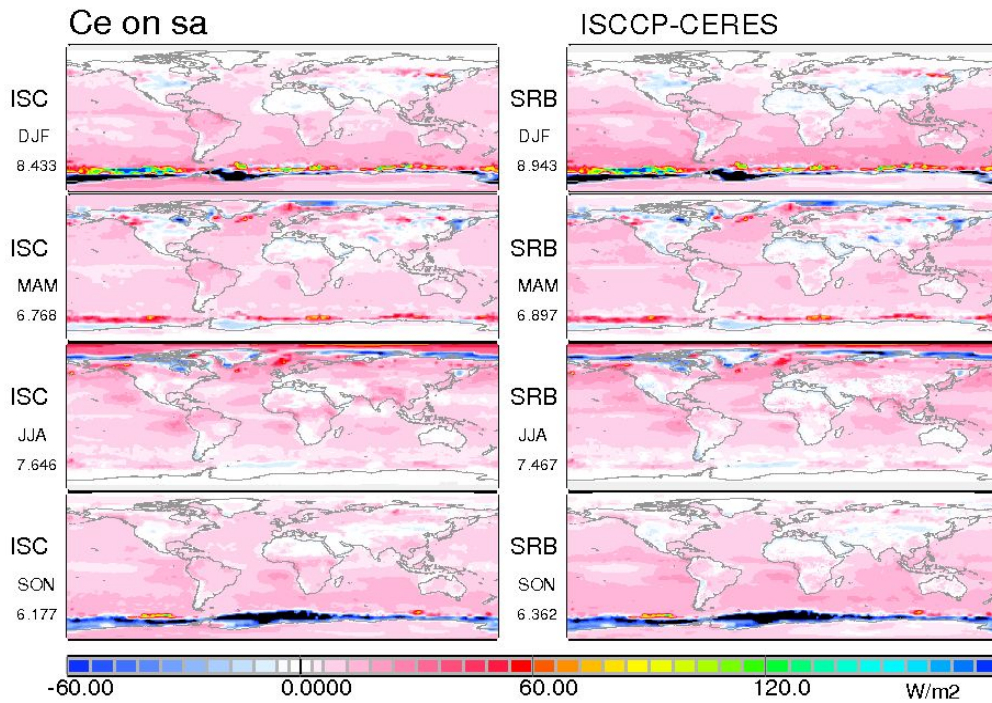


*Figure 15: Seasonal anomalies of the Cloud Radiative Effect on the absorption of solar radiation in the atmosphere. Reddish colors mean: absorption in ISCCP clouds is higher than in CERES clouds.*

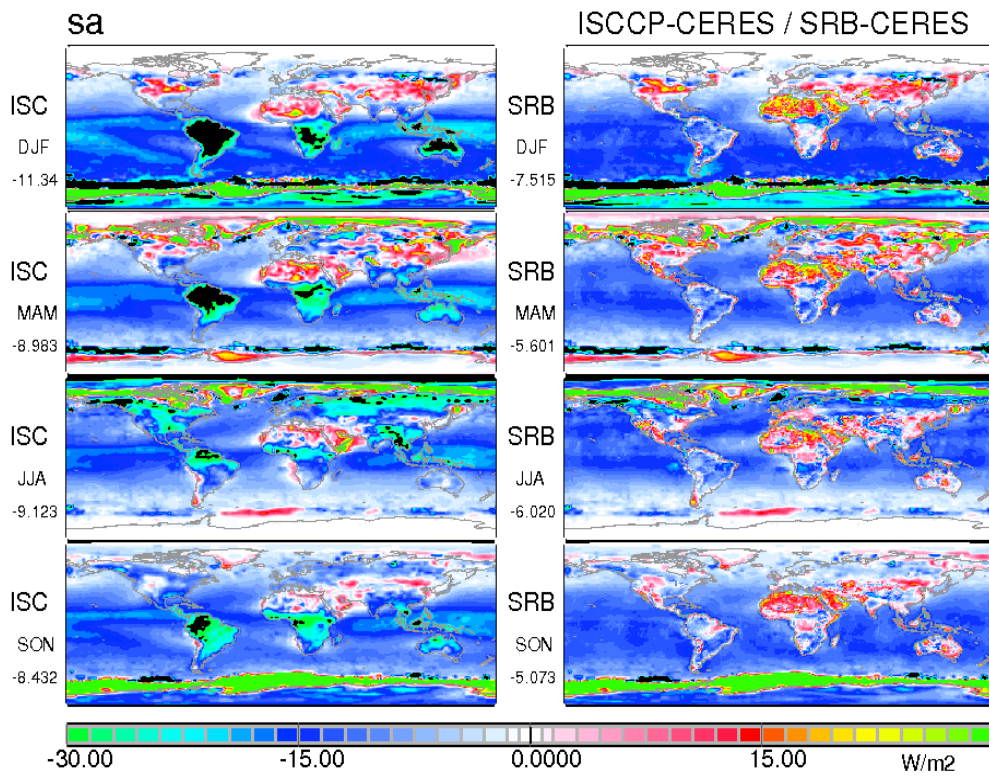


Figure 16: Seasonal anomalies of the absorption of solar radiation in the cloud-free atmosphere

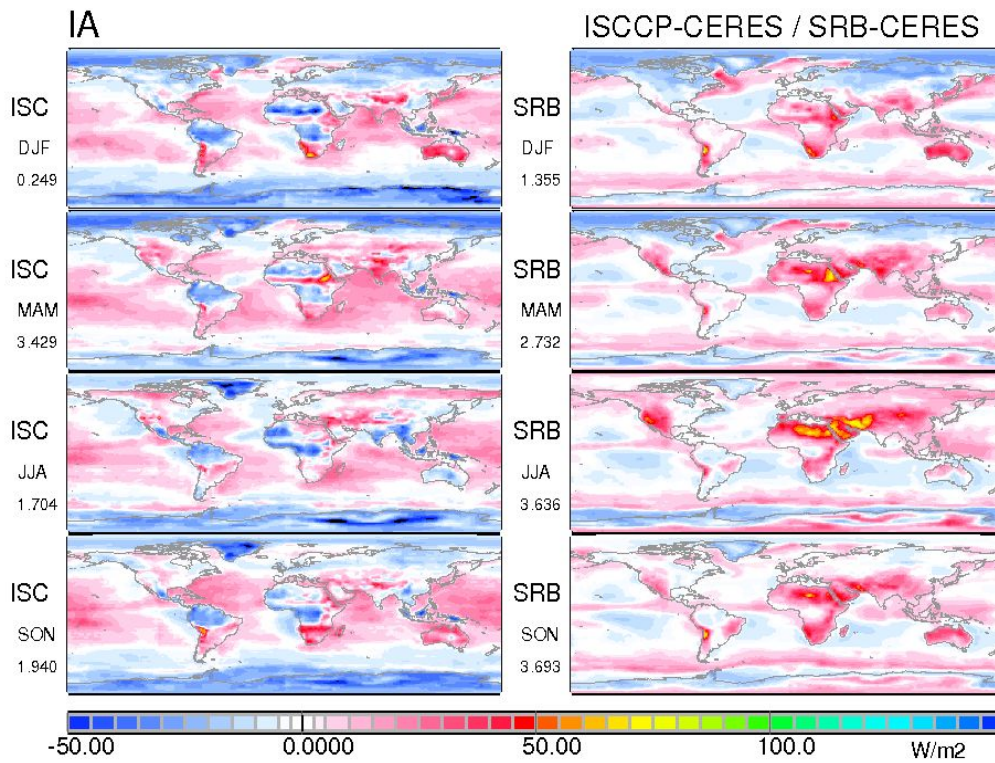
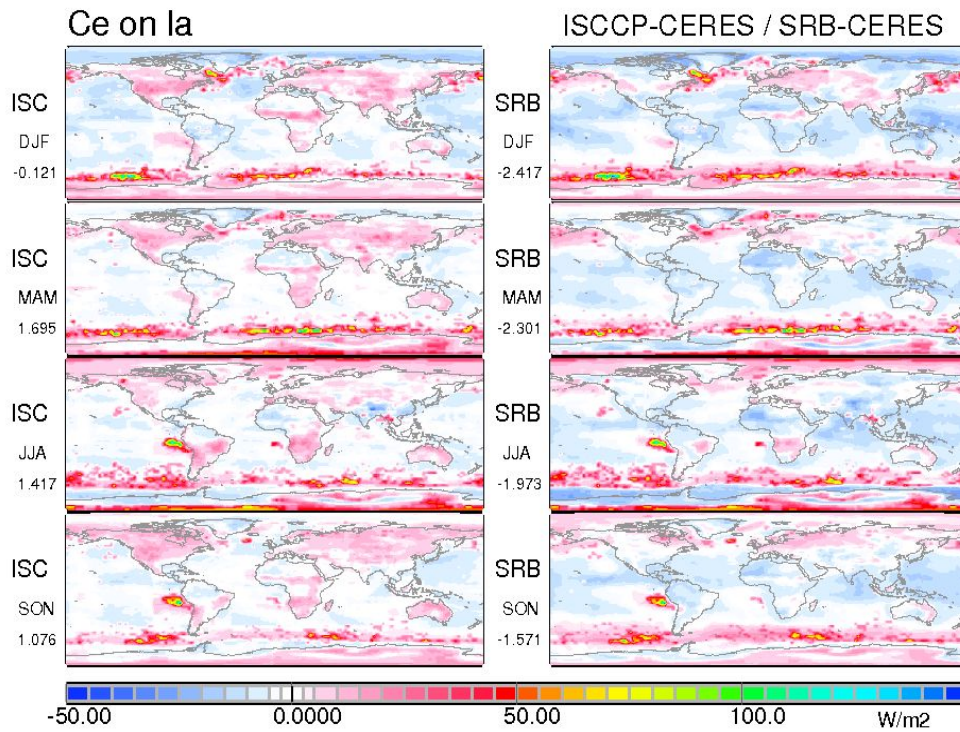
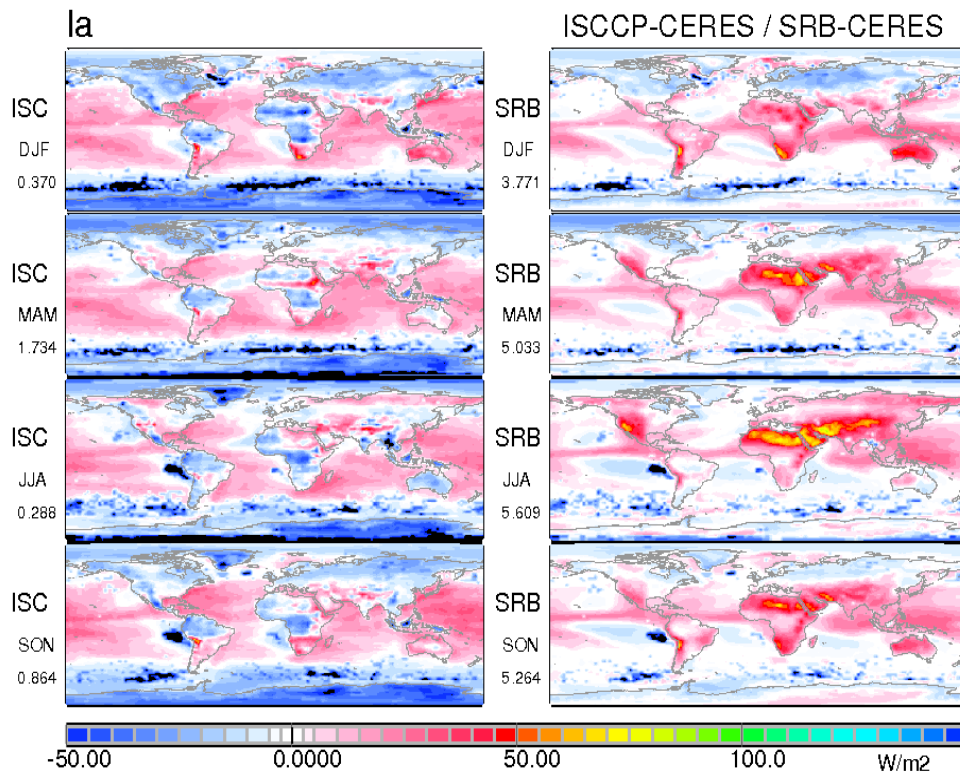


Figure 17: Seasonal anomalies of the divergence of infrared radiation in the all-sky atmosphere



**Figure 18:** Seasonal anomalies of the **cloud radiative effect** on the divergence of infrared radiation of the atmosphere. Reddish/bluish colors mean an enhancement/reduction of the cooling.



**Figure 19:** Seasonal anomalies of the divergence of infrared radiation in the cloud-free atmosphere

### Additional supporting information:

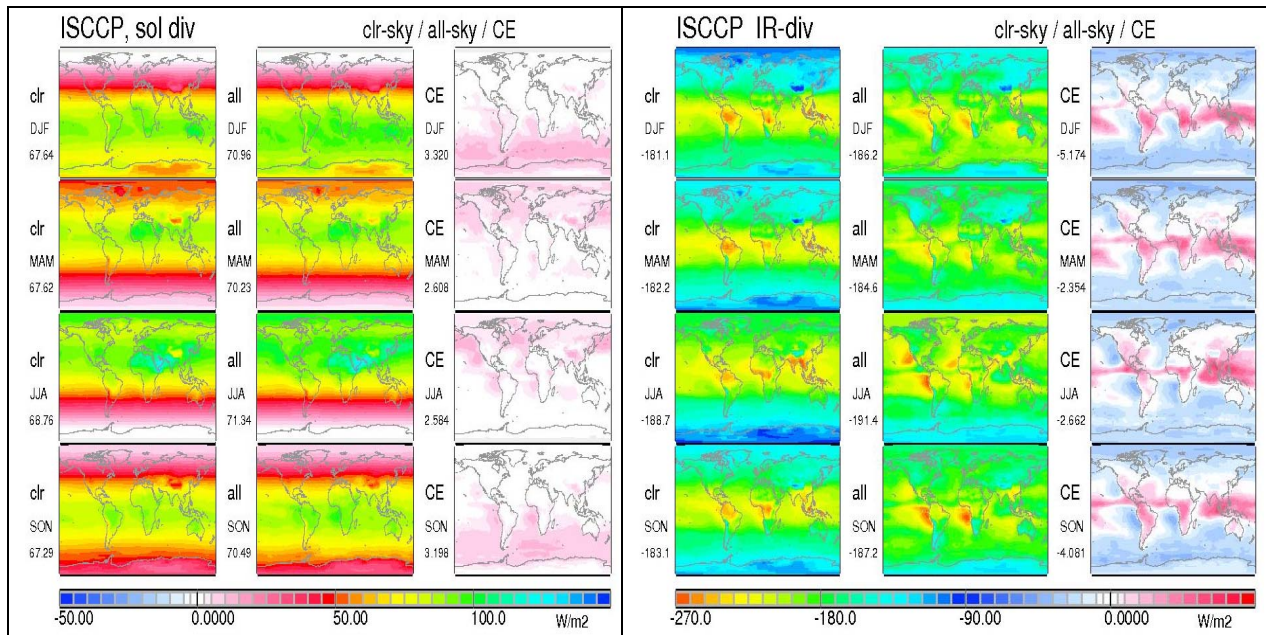


**Figure 20:** Seasonal pattern of total solar and terrestrial radiation divergences computed for clear sky (in each panel left column), all sky (middle column), and the cloud radiative effect (right) of ISCCP data. The pattern in solar data is less continental than in CERES and SRB data sets. Clouds add here to the absorption of solar radiation. In the infrared the pattern in CRE is similar to the other data sets, but the amount of atmospheric cooling appears to be slightly higher over the fields of maritime strato-cumulus fields.

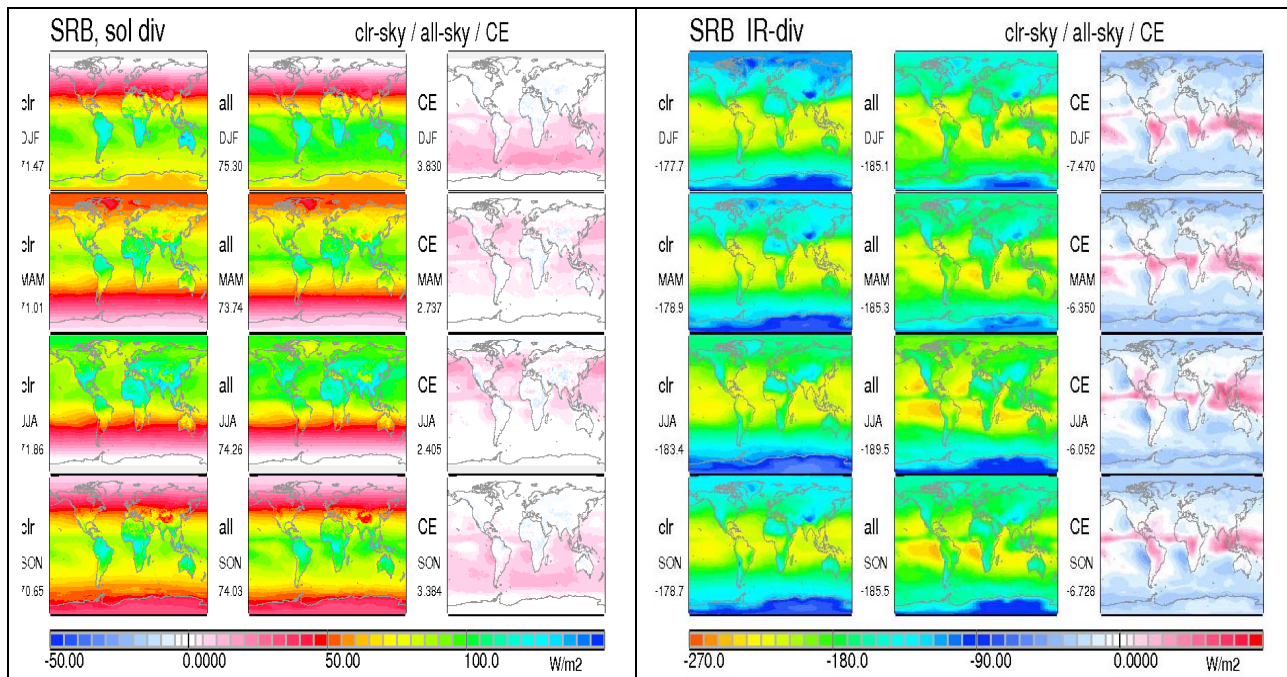


**Figure 21:** Seasonal pattern of total solar and terrestrial radiation flux divergences computed for clear sky (in each panel left column), all sky (middle column), and the cloud radiative effect (right) of SRB data. Note the small negative CRE here for solar radiation over some areas! In the SRB data on solar radiation the areal pattern indicates much smaller values over the oceans than in ISCCP data. In the infrared the radiative cooling of clear and cloudy atmosphere is smaller than in the ISCCP data sets, but their differences (= CRE) areal most the same.

# Appendix C.9.1 for Chapter 9.1:

## The IPCC median model

S. Kinne and E. Raschke

To recall, the median model picks the central local value given by different models for the same time (month) and location (1x1 lat/long) and combines the data to global maps. However, never all 21 models that participated in the IPCC 4<sup>th</sup> assessment contributed to those median maps. Some models failed to report relevant radiative fluxes (e.g. fluxes at clear-sky conditions or fluxes at the surface) and in some cases it seemed inappropriate to consider different versions of essentially the same model.

*Table C.9.1: List of the individual IPCC 4AR model outputs (the total is indicated under ‘#’) that contributed to median values of the IPCC median model for the properties of Table C.9.2.*

label	#	B C C	C C C	C C S	C C c	C C s	C N R	C S I	D N M	G F D	G I 1	G I 2	G I 3	G I S	I A P	I P S	M P I	M R I	N C A	P C M	U B O	U K M	
sdt	18	x	x	x	x	x	x	x		x	x			x	x	x	x	x	x	x	x	x	
sds	14		x	x	x	x	x		x	x	x				x	x	x		x			x	x
sDs	19	x	x	x	x	x	x	x	x	x	x				x	x	x	x	x	x	x	x	x
Csds	6			x	x												x		x			x	x
sut	14		x	x	x	x	x		x	x	x				x	x		x	x			x	x
sUt	18	x	x	x	x	x	x	x	x	x	x				x	x	x	x	x	x		x	x
Csut	6			x	x												x		x			x	x
lus	19	x	x	x	x	x	x	x	x	x	x				x	x	x	x	x	x	x	x	x
IUs	16	x	x	x	x	x	x	x	x	x					x	x	x	x				x	x
Clus	0																						
Iut	17		x	x	x	x	x	x	x	x	x	x			x	x	x	x	x			x	x
IUt	19	x	x	x	x	x	x	x	x	x	x	x			x	x	x	x	x	x		x	x
Clut	17		x	x	x	x	x	x	x	x	x	x			x	x	x	x	x			x	x
lds	14		x	x	x	x	x		x	x	x	x			x	x	x	x	x	x	x	x	x
IDs	18	x	x	x	x	x		x	x	x					x	x	x	x	x	x	x	x	x
Clds	14		x	x	x	x	x	x	x	x							x	x	x	x		x	x
sts	12				x	x	x		x	x			x		x	x	x		x			x	x
sTs	12				x	x	x		x	x			x		x	x	x		x			x	x
Csts	12				x	x	x		x	x			x		x	x	x		x			x	x
tnt	12				x	x	x		x	x			x		x	x	x		x			x	x
tNt	16	x			x	x	x	x	x	x			x	x	x	x	x	x	x			x	x
Ctnt	13				x	x	x	x	x	x			x		x	x	x		x			x	x
sa	12				x	x	x		x	x			x		x	x	x		x			x	x
sA	13				x	x	x		x	x			x		x	x	x	x	x			x	x
Csa	12				x	x	x		x	x			x		x	x	x		x			x	x
la	10				x	x	x	x	x	x							x	x				x	x
IA	10				x	x	x	x	x	x							x	x				x	x
ClA	10				x	x	x	x	x	x							x	x				x	x
snt	10				x	x	x		x	x			x				x	x				x	x
sNt	11				x	x	x	x	x	x					x	x	x					x	x
Csnt	8				x	x	x			x							x	x				x	x
srs	14		x	x	x	x	x		x	x	x				x	x	x		x			x	x
sRs	14		x	x	x	x	x		x	x	x				x	x	x		x			x	x
Csrs	11				x	x			x	x			x		x	x	x		x			x	x
srt	12				x	x	x		x	x			x		x	x	x		x			x	x
sRt	12				x	x	x		x	x			x		x	x	x		x			x	x
Csrt	13				x	x	x	x	x	x			x		x	x	x		x			x	x

Table C.9.1 lists for each of the 37 investigated radiative property of Table C.9.2 those individual models that contributed in the creation of the IPCC model median maps. As indicated in the second column usually more than 10 different models contributed.

### C9.1.2: Flux maps of ISCCP and SRB climatologies

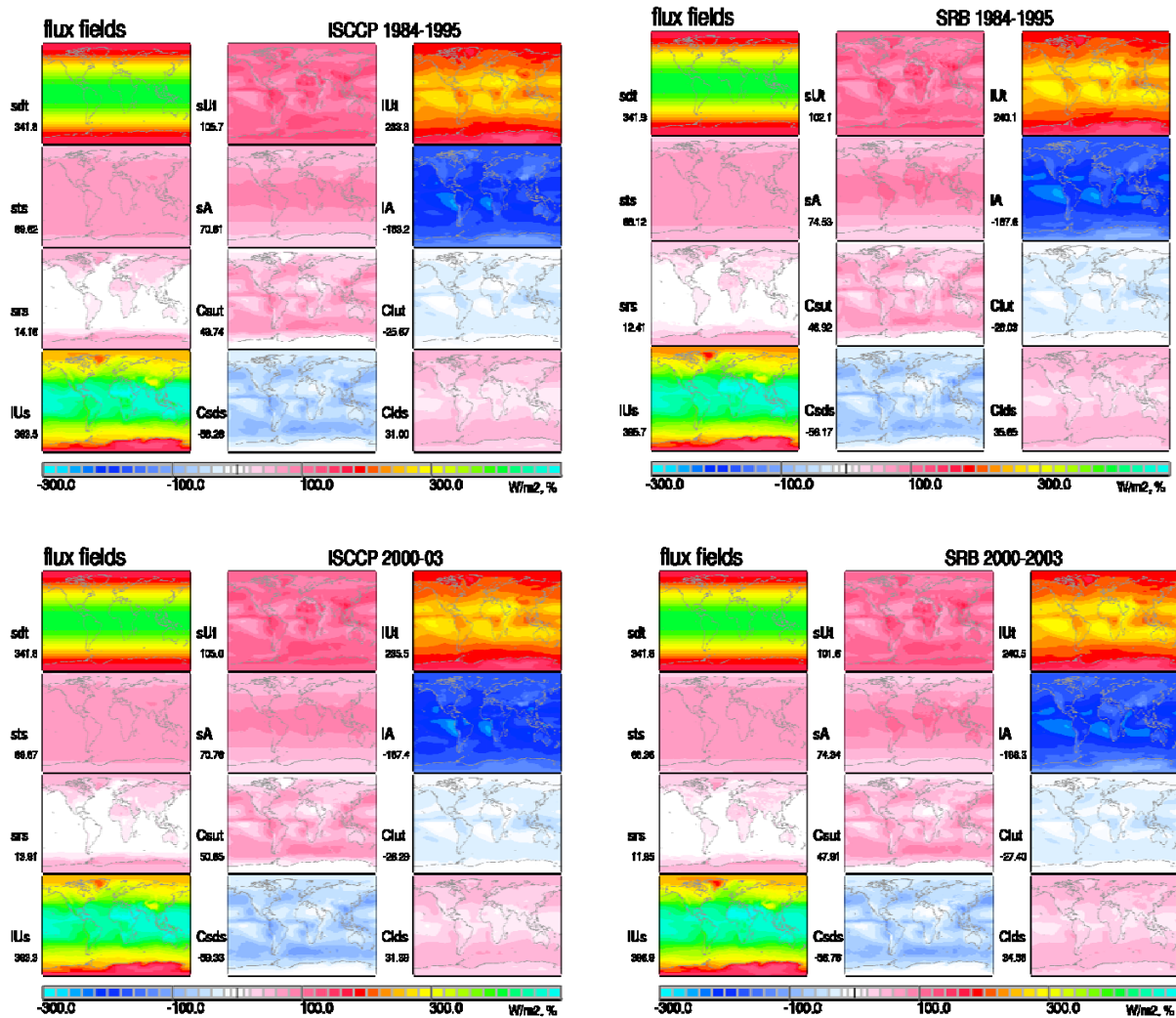


**Figure C.9.1:** Selected annual broadband flux fields and broadband cloud radiative effects (in  $W/m^2$ ) of the ISCCP (left) and SRB (right). Satellite climatology products averaged over two different time periods, 1994-1995 and 2000-2003. The labels are explained in Figure 9.1.1 and in Table 9.1.2 and the values below the labels indicate global (multi-)annual surface area weighted averages. The center column displays solar fluxes and the right column displays IR fluxes, hereby including cloud radiative effects (as fluxes change from 'clear-sky' to 'all-sky' conditions) to upward fluxes at ToA (C.ut) and to downward fluxes at the surface (C.ds). In addition, the left column presents ancillary data for the solar irradiance at the ToA often termed TSI (sdt), for the 'clear-sky' solar atmospheric transmittance (sts in %), for the solar surface reflectance (srs in %) and for IR surface upward fluxes.

This section provides supplementary information on flux fields of cloud climatologies for ISCCP and SRB. For two different time-periods (1984-1995, 2000-2003) selected flux fields and ancillary data are presented, corresponding in style to plots provided for the IPCC-median (*Figure C.9.1.*) and for the CERES (data) reference (*Figure C.9.5*).

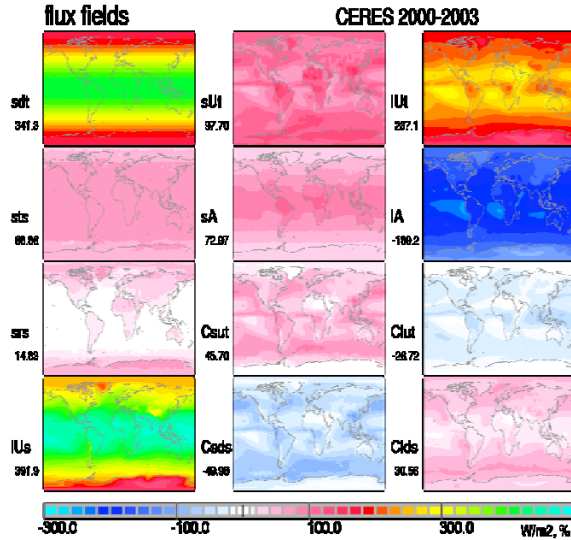


Figure C.9.2: CERES for comparison

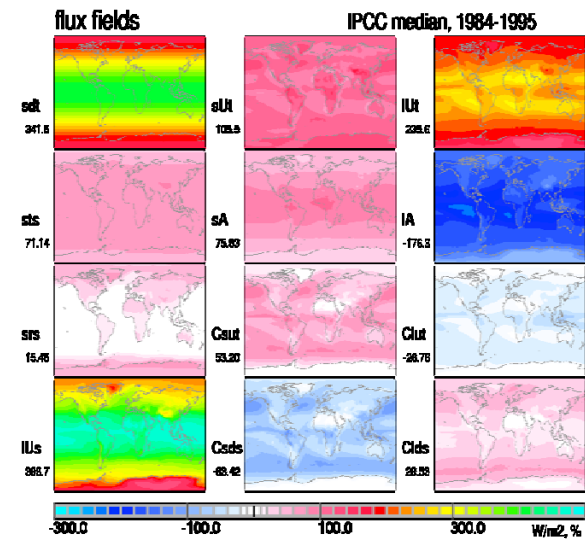


Figure C.9.3: IPCC-median for comparison

The flux products are explained in *Figure 9.1.1* below.

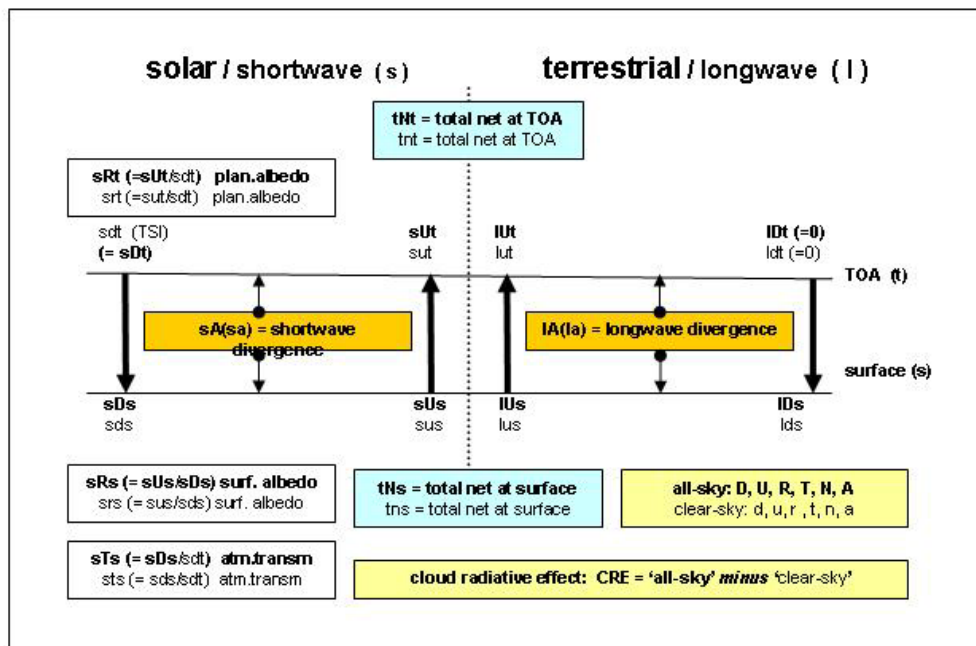


Figure 9.1.1: Logic of symbols used to identify radiation products in subsequent diagrams of this chapter. First column letters indicate the associated spectral range (e.g. 's' for shortwave, 'l' for longwave (or IR) and 't' for the shortwave and longwave total). Second column letters refer to the flux direction (e.g. 'u' for upward, 'd' for downward, 'n' for net). Here, note that lower-case (second column) letters indicate 'clear-sky' conditions and that capital-case letters refer to 'all-sky' conditions. Third column letters indicate the location ('t' for TOA and 's' for surface).

### C9.1.3: Global annual maps by individual IPCC models

In comparisons to satellite reference data, Chapter 9.1 only examined the IPCC median model. Although the model diversity was indicated by the standard deviation (*Figure 9.1.4*) and its ratio to the median value (*Figure 9.1.5*), there is certainly interest as to how individual models performed. This IPCC median model is usually much better behaved than individual models, which at times can display rather extreme features, even for multi-annual averages. This is illustrated in subsequent plots, where flux products of individual models (*Table 9.1.1*) are compared to those of the IPCC model median and to those of satellite climatologies, most prominently to CERES multi-annual data (Mar/2000-Feb/2004). Aside from comparisons from selected flux products or ancillary data, also difference plots to CERES are provided in order to highlight the differences. Although the model-output of the IPCC-4AR simulations are for a different time-period (1984-1995) than the CERES reference, no significant impact is expected given the length of the averaging periods. Specifically compared are

- all-sky net-fluxes at the ToA (*Figure C.9.2*)
- all-sky net-fluxes at the surface (*Figure C.9.3*)
- all-sky solar downward flux at the surface (*Figure C.9.4*)
- all-sky IR downward flux at the surface (*Figure C.9.5*)
- all-sky solar atmospheric divergence (*Figure C.9.6*)
- all-sky IR atmospheric divergence (*Figure C.9.7*)

In addition, also some important ancillary data maps are explored, in order to illustrate potential biases introduced by assumptions to aerosol and surface properties. Their impacts are revealed in flux data for

- clear sky solar transmittance ('aerosol') (*Figure C.9.8*)
- all-sky solar surface albedo ('ice/snow') (*Figure C.9.9*)
- all-sky upward IR flux at the surface ('T') (*Figure C.9.10*)

In all figures, individual models are identified according to the labels listed in *Table 9.1.1*. In the all figures only (multi-) annual maps and (multi-) annual difference maps to CERES are presented and hereby only for those individual models which contributed to the IPCC median model for that property. For comparison also the IPCC median model is always displayed. Selected highlights of these comparisons are:

- 'all-sky' net-fluxes at the top of the atmosphere (ToA) are usually balanced on a global annual basis in global modeling (see *Table C.9.2*) – which is a required for global models. However, on a regional basis there significant differences, which often involve the representation of low-level clouds.
- overall differences to the CERES reference are smallest for the IPCC median, indicating that in general the IPCC median model – similar to model ensembles – has more skill than any individual model.
- differences among models and to CERES for clear-sky solar transmission and for solar divergence can be traced to diverse assumptions for aerosol amount and absorption. Usually 'clear sky' aerosol deficiencies are compensated by adjustments to the cloud effects for acceptable 'all-sky' fluxes thereby introducing clouds to cloud-effects.
- differences among models and to CERES for the solar surface albedo illustrate diversity in snow and sea-ice cover, which propagates into many flux-products

- CERES by applying MODIS sensor retrieved microphysics simulates about  $20 \text{ Wm}^{-2}$  more downward fluxes to the surface than in most global models.

*Table C.9.2.: Global annual averages of radiation products. Model identifiers are given in Table 9.1.1.*

	All-sky solar reflac.	clear solar diver.	all-sky solar diver.	CRE solar diver.	clear OLR	all-sky OLR	CRE OLR	loss to space	ToA net (flux)	ToA n minus CERES	surf net (flux)	surf n minus CERES
<b>CERES</b>	<b>97.7</b>	<b>77.3</b>	<b>73.0</b>	<b>-4.3</b>	<b>262.6</b>	<b>237.1</b>	<b>-26.7</b>	<b>334.8</b>	<b>6.5</b>		<b>122.7</b>	
<b>ISCCP</b>	<b>107.4</b>	<b>67.7</b>	<b>70.6</b>	<b>3.0</b>	<b>258.9</b>	<b>233.3</b>	<b>-25.7</b>	<b>340.7</b>	<b>2.8</b>	<b>-3.7</b>	<b>115.4</b>	<b>-7.3</b>
<b>SRB</b>	<b>104.3</b>	<b>71.6</b>	<b>74.5</b>	<b>2.9</b>	<b>268.1</b>	<b>240.1</b>	<b>-28.0</b>	<b>344.4</b>	<b>-0.4</b>	<b>-6.9</b>	<b>112.7</b>	<b>-10.0</b>
<b>median</b>	<b>105.5</b>	<b>69.3</b>	<b>75.8</b>	<b>6.3</b>	<b>263.2</b>	<b>235.6</b>	<b>-26.7</b>	<b>341.1</b>	<b>3.4</b>	<b>-3.0</b>	<b>102.4</b>	<b>-20.3</b>
<b>BCC</b>	106.5					233.5		340.0	1.8	-4.7		
<b>CCC</b>	106.0				264.6	237.5	-27.1	343.5	-0.4		95.2	-27.4
<b>CCc</b>	106.2	65.2	71.7	6.5	264.2	236.8	-27.4	343.0	0.1	-6.3	96.1	-26.6
<b>CCS</b>	107.4	64.6	77.8	13.2	260.4	233.3	-27.1	340.7	1.2		97.2	-25.5
<b>CCs</b>	102.3	63.6	73.9	10.4	265.4	238.7	-26.7	341.0	0.9	-5.5	105.0	-17.7
<b>CNR</b>	111.5	82.0	84.0	2.0	266.2	232.5	-33.7	344.0	0.7	-5.8	108.2	-14.5
<b>CSI</b>	106.4				268.4	234.1	-34.0	340.5	1.2	-5.3	97.4	-25.3
<b>DNM</b>	105.5	74.6	77.3	2.7	261.1	233.1	-28.0	338.6	5.3	-1.1	108.6	-14.1
<b>GFD</b>	108.1	71.6	75.3	3.7	258.6	234.0	-24.6	342.1	1.2	-5.2	100.9	-21.8
<b>Gi1</b>	102.2				265.7	240.6	-25.1	342.8	0.4			
<b>Gi2</b>					265.7	240.6	-25.1		0.6			
<b>Gi3</b>		58.3	72.4	14.1					0.7			
<b>GIS</b>	109.3					230.8		340.1	3.5	-2.9	118.5	-4.2
<b>IAP</b>	107.5	63.4	70.0	6.7	259.7	231.6	-28.1	339.1	4.5	-2.0	101.6	-21.1
<b>IPS</b>	104.8	64.2	68.1	3.9	269.2	237.6	-31.7	342.4	0.7	-5.8	103.4	-19.3
<b>MPI</b>	108.0	73.4	76.6	3.1	260.6	232.6	-28.0	340.6	1.2	-5.2	102.6	-20.1
<b>MRI</b>	104.1		74.4		256.7	235.0	-21.7	339.1	3.6	-2.9	105.0	-17.7
<b>NCA</b>	107.6	71.9	76.8	5.0	264.4	234.3	-30.1	341.9	1.7	-4.8		
<b>UBO</b>	104.0	71.9	88.6	16.7	261.3	233.6	-27.6	337.6	3.4	-3.1	94.7	-28.0
<b>UKM</b>	103.4	70.9	76.2	5.3	260.8	239.5	-21.3	342.9	0.2	-6.2	102.4	-20.3

- ‘CCC’ and ‘CCS’ models also provided for at higher resolution: ‘CCc’ and ‘CCs’ (see *Table 9.1.1*)
- ‘GI1’ and ‘GI2’ refer to two GISS-ER realizations coupled to the Russell ocean model, ‘GI3’ refers to a GISS-EH realization coupled to a higher resolution HYCOM ocean model and ‘GIS’ is a separate developmental offshoot (<http://data.giss.nasa.gov/modelE/ar4/>)
- for CERES, the negative cloud effect for solar absorption surprises. It is unclear to what degree this is related to the low water vapor bias in CERES cloudy scenes or if CERES clouds are placed too high in the atmosphere
- for surface fluxes CERES is just another model and has limited capabilities to serve as reference

Although the focus in this Appendix C is on local diversity, also comparisons of global annual averages among different flux products are of interest. *Table A.9.2* lists global (multi-) annual averages of selected fluxes and flux-differences. Global (multi-) annual averages are provided for different satellite climatologies as well as for individual model simulations of the IPCC 4<sup>th</sup> assessment.

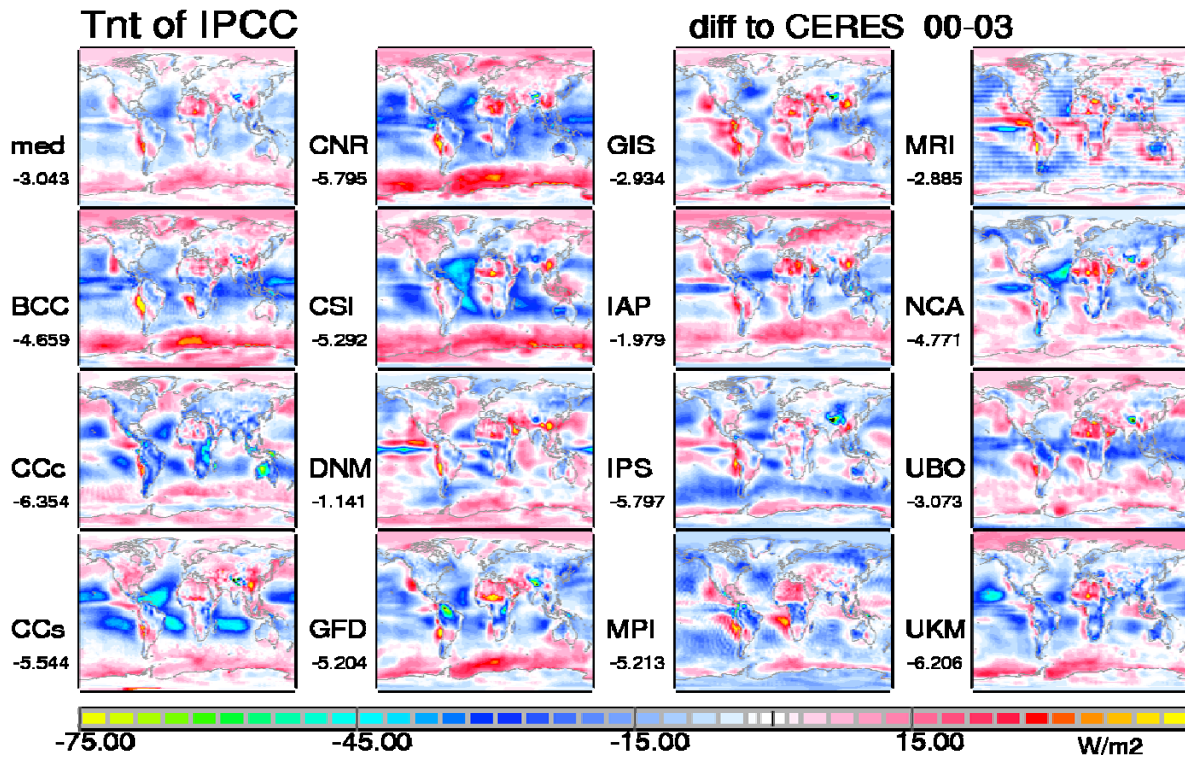
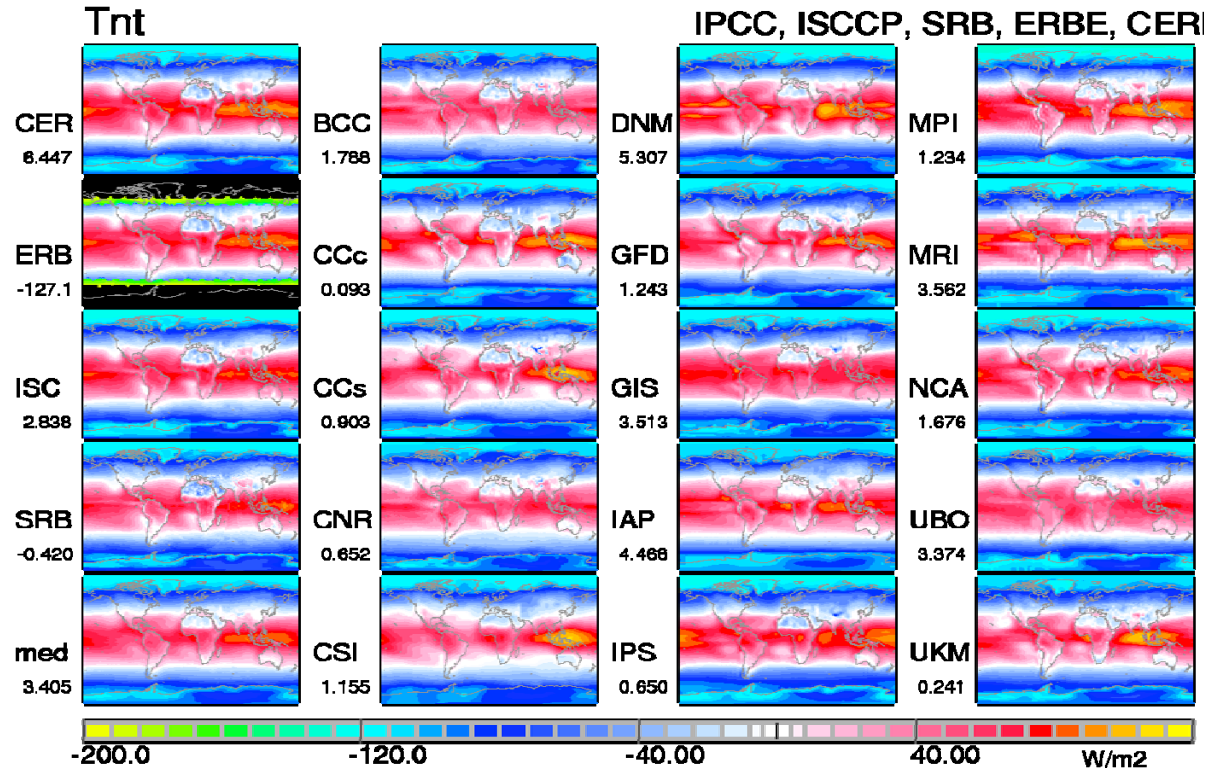


*Figure C.9.3: Radiative energy balance at the top of the atmosphere (ToA). Multi-annual (1984-1995) average maps of the IPCC median (med) and individual IPCC-4AR models of Table 9.1.1 are compared to each other and to satellite data-sets (upper set of panels) and in addition flux differences of these models with respect to CERES 2000-2003 reference data are given (lower set of panels)*

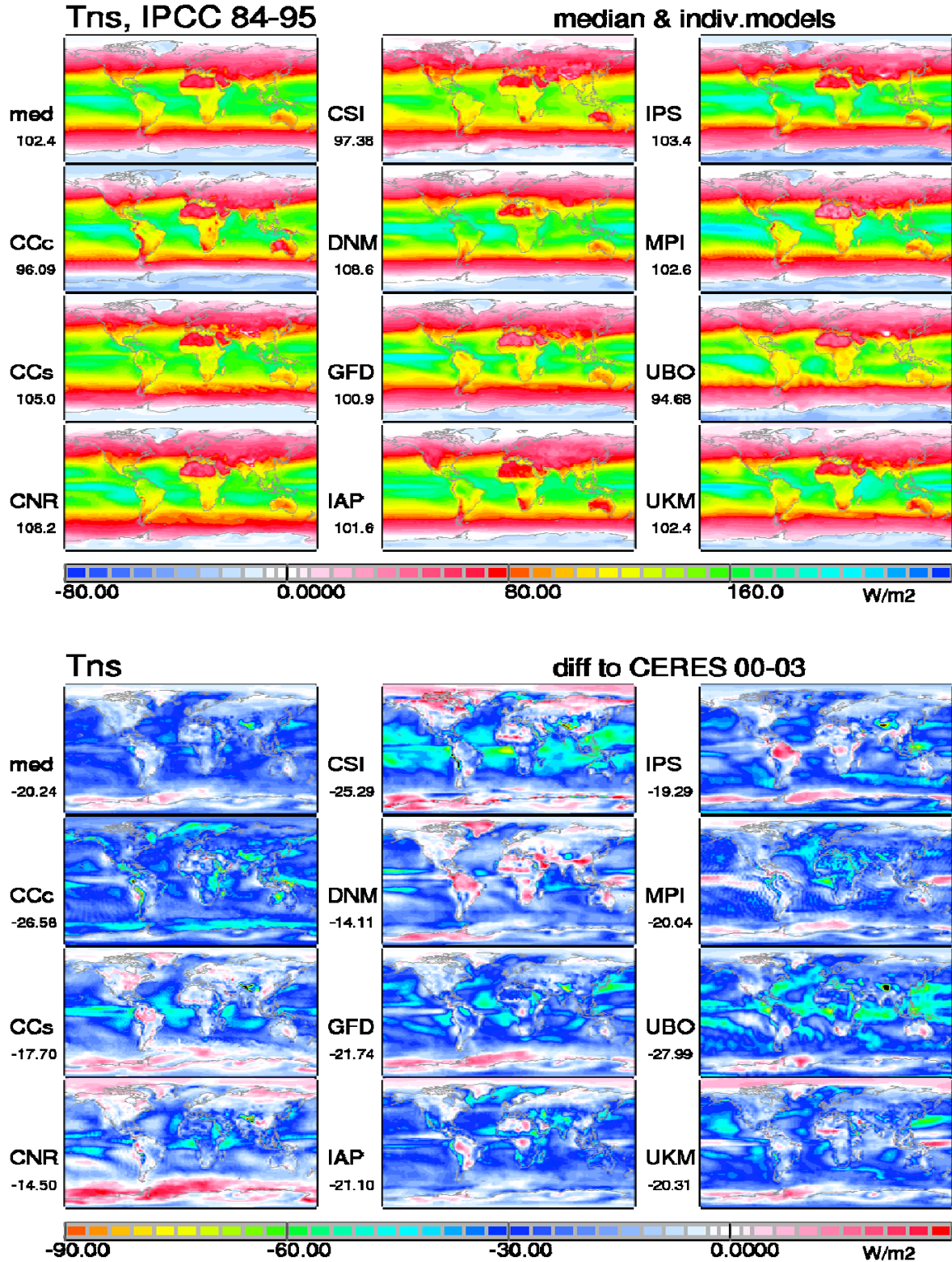


*Figure C.9.4: Total net radiative energy balance at the surface for all-sky conditions. Multi-annual (1984-1995) average maps of the IPCC median (med) and individual IPCC-4AR models of Table 9.1.1 are compared to each other (upper set of panels) and in addition flux differences of these models with respect to CERES 2000-2003 reference data are provided (lower set of panels)*

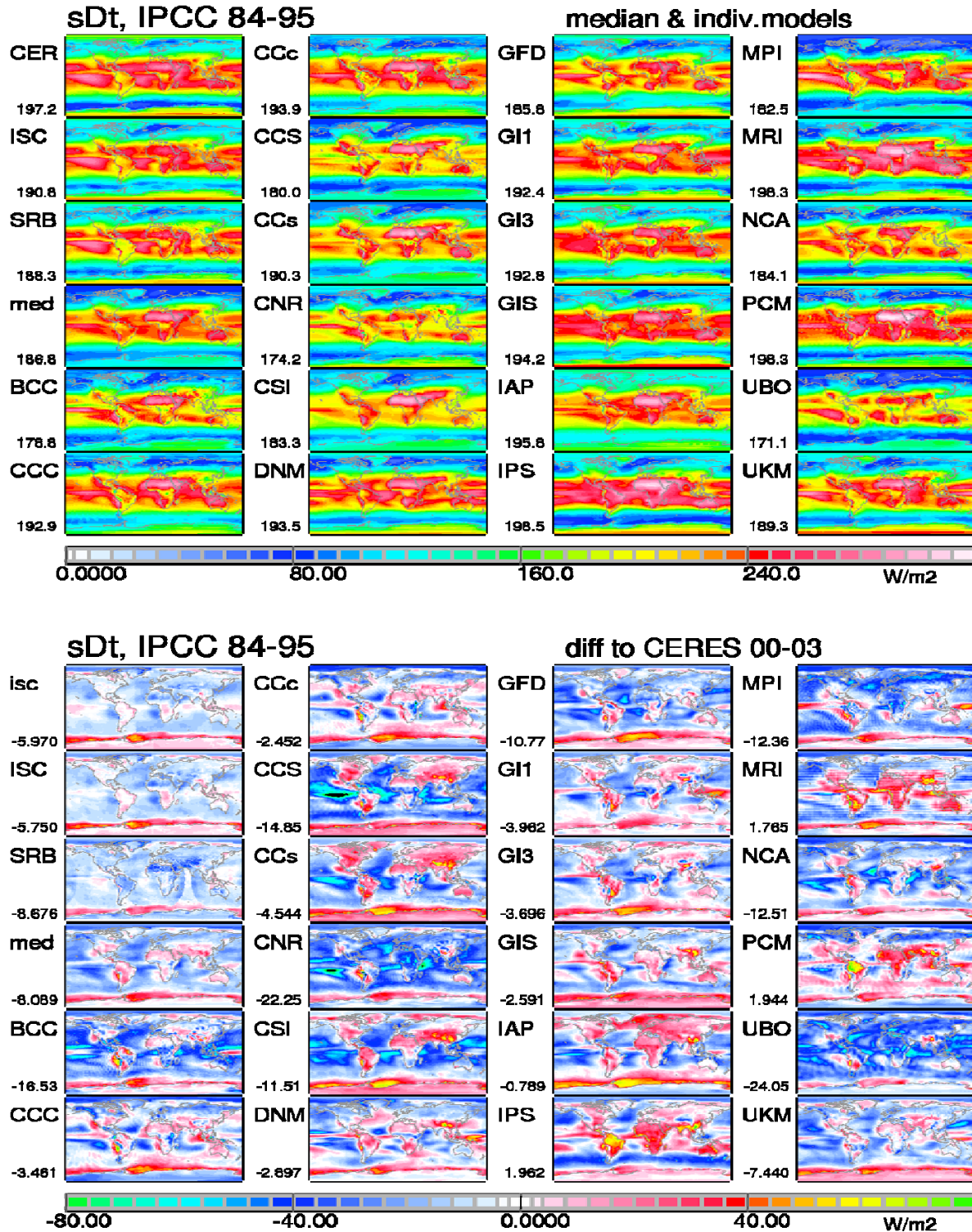


*Figure C.9.5: Downward solar flux to the surface at all-sky conditions. Multi-annual (1984-1995) average maps of the IPCC median (med) and individual IPCC-4AR models of Table 9.1.1 are compared to each other (upper set of panels) and in addition flux differences of these models with respect to CERES 2000-2003 reference data are provided (lower set of panels)*

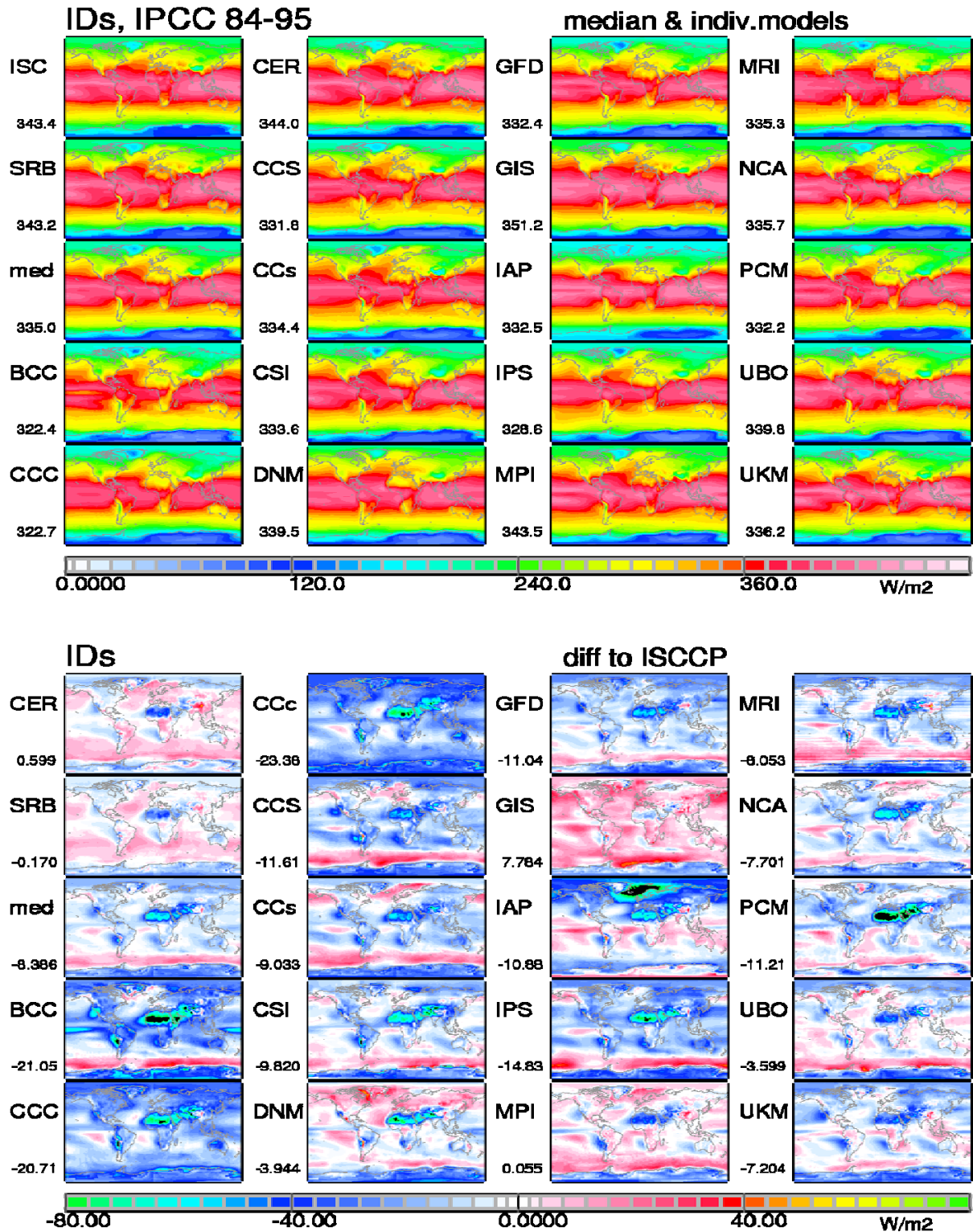


*Figure C.9.6: Downward longwave flux to the surface at all-sky conditions. Multi-annual (1984-1995) average maps of the IPCC median (med) and individual IPCC-4AR models of Table 9.1.1 are compared to each other (upper set of panels) and in addition flux differences of these models with respect to CERES 2000-2003 reference data are provided (lower set of panels)*

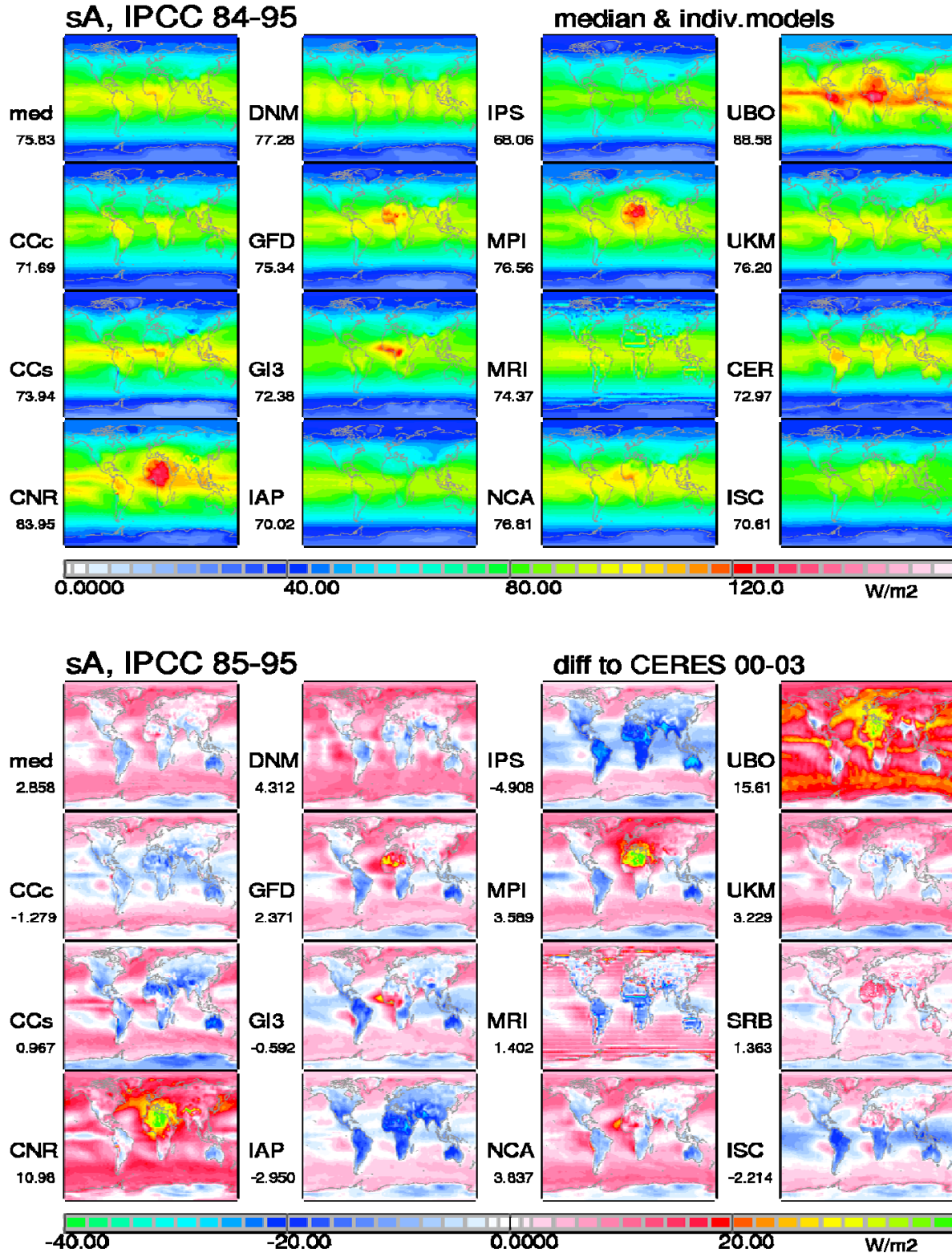


*Figure C.9.7: Solar atmospheric divergence (or solar atmospheric absorption) at all-sky conditions. Multi-annual (1984-1995) average maps of the IPCC median (med) and individual IPCC-4AR models of Table 9.1.1 are compared to each other (upper set of panels) and in addition flux differences of these models with respect to CERES 2000-2003 reference data are given (lower set of panels)*

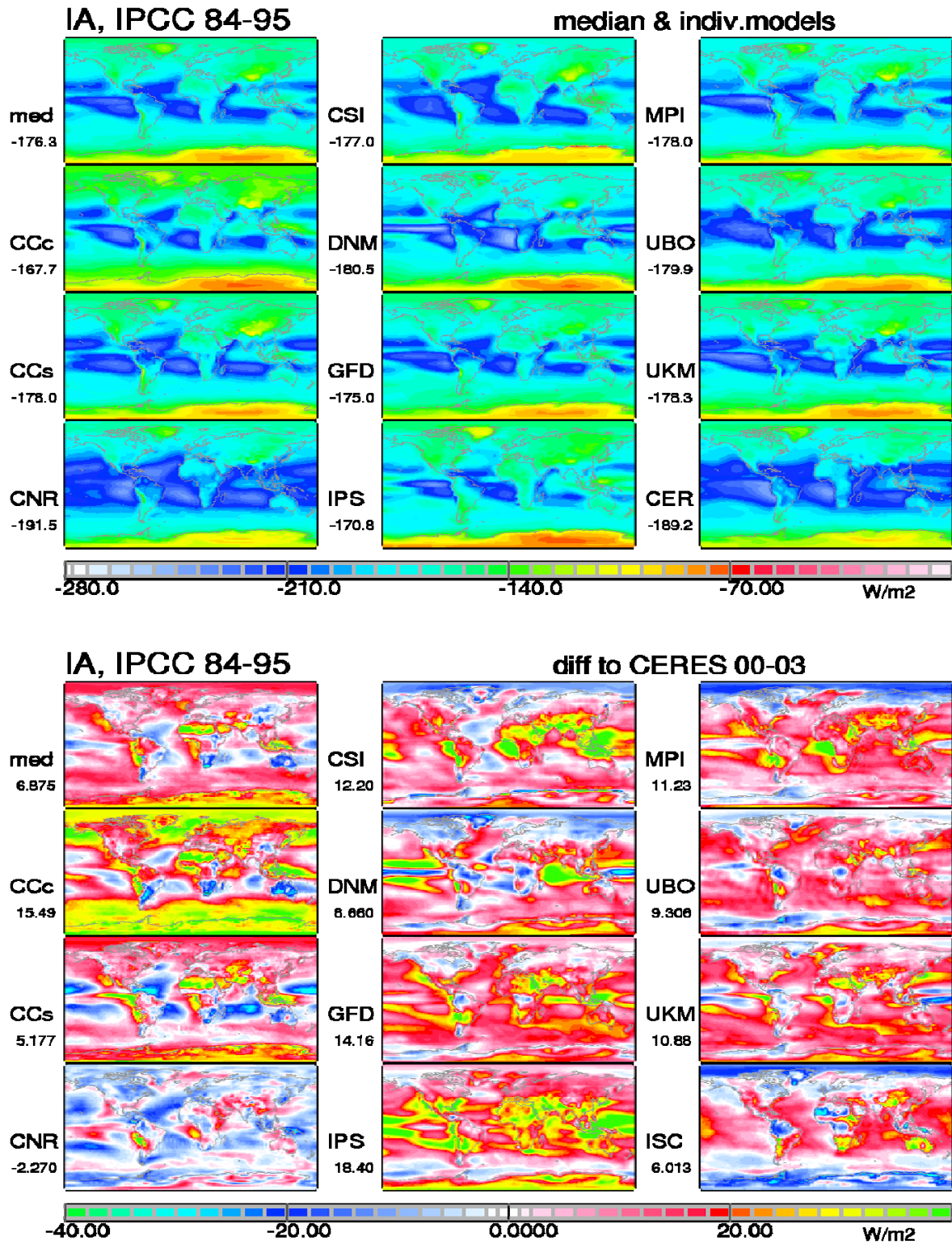


*Figure C.9.8: Annual longwave (or IR) atmospheric divergence at all-sky conditions. Multi-annual (1984-1995) average maps of individual models of Table 9.1.1 are compared to each other and to satellite data-sets (upper set of panels) and in addition flux differences with respect to the CERES 2000-2003 data are given (lower set of panels).*

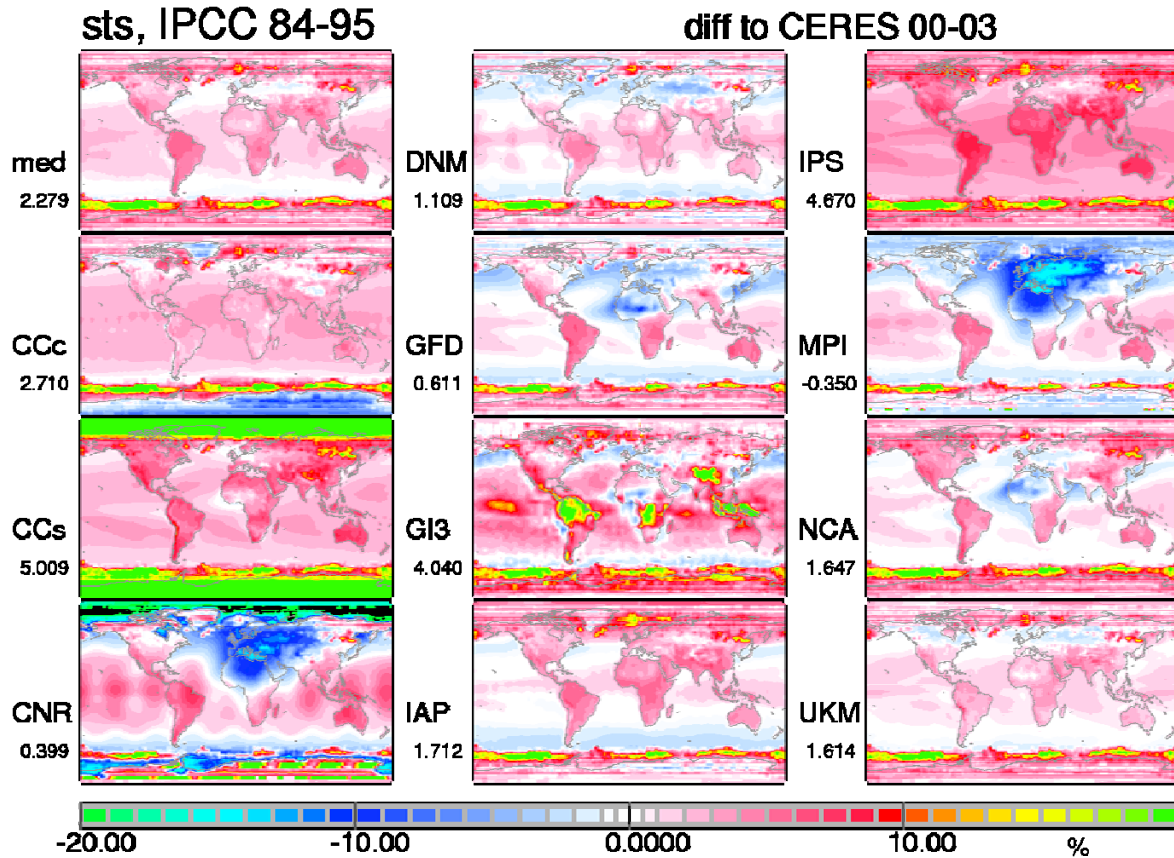


**Figure C.9.9:** Differences in solar atmospheric transmittance (based on the down-surface/down-ToA flux ratio under *clear-sky* conditions) between multi-annual (1984-1995) average maps of the IPCC median or individual IPCC-4AR models of Table 9.1.1 and CERES 2000-2003.

The maps in *Figure C.9.9* illustrate differences for the solar transmittance for a cloud-free atmosphere compared to CERES. These differences document the influence of the trace-gas absorption treatment and of the representation of atmospheric aerosol. Almost all models compute a larger atmospheric solar transmission, indicating that aerosol effects are underestimated. This is in sharp contrast to the overall smaller solar transmission under all-sky conditions. This means that clouds (over-) compensate for aerosol errors. There are three models (CNR, MPI, GFD), however, which show a smaller transmission over the greater Saharan region. These models apply a simplified aerosol climatology with too absorbing dust over the Sahara region. The associated strong aerosol absorption for this aerosol climatology is also responsible for the large (clear-sky and all-sky) solar divergence over the Sahara region in these models (see *Figure C.9.7*).

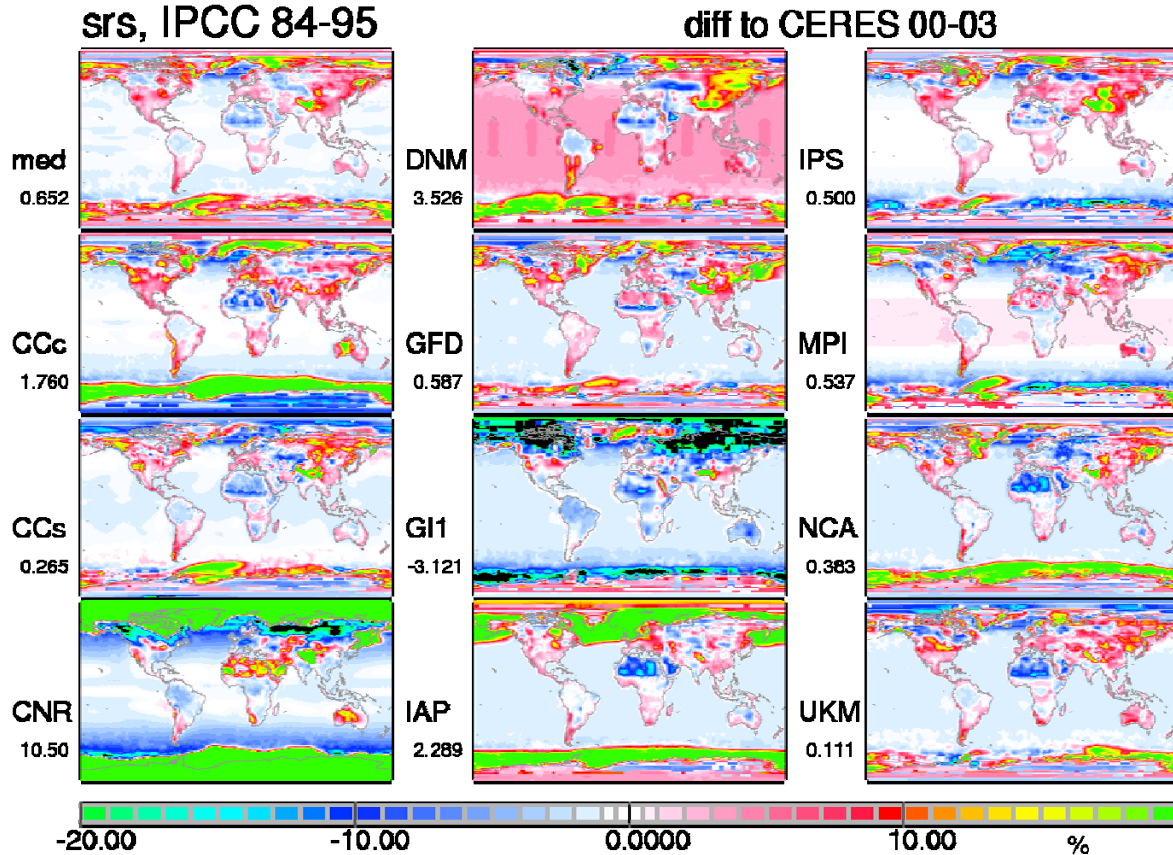


**Figure C.9.10:** Differences in solar surface albedo (based on the up/dn solar surface flux ratio under clear-sky conditions) between multi-annual (1984-1995) average maps of the IPCC median or individual IPCC-4AR models of Table 9.1.1 and CERES 2000-2003. Black colors indicate deviations more negative than -20% and green colors indicate deviations more positive than 20%.

The maps in *Figure C.9.10* illustrate differences for the solar surface reflection under cloud-free conditions compared to assumptions in the CERES modeling effort. By picking CERES as reference, this does not mean that the CERES assumptions for solar surface are correct. Global modeling, when examining difference to the IPCC-median, has larger issues over land. The surface reflectance in modeling over continents is usually larger (than CERES) over deserts but at times significant smaller (than CERES) over E and NE Asia and over the US. Still, there not all models have those ‘average’ tendencies in these regions. The largest regional diversity (not only in modeling) for solar surface albedo occurs in areas affected by of snow and ice-cover (at higher and polar latitudes). Here, deviations in some models even exceed the selected  $\pm 20\%$  scale. These larger deviations are a concern, because these (solar surface albedo) differences propagate into other flux products, including the planetary albedo.

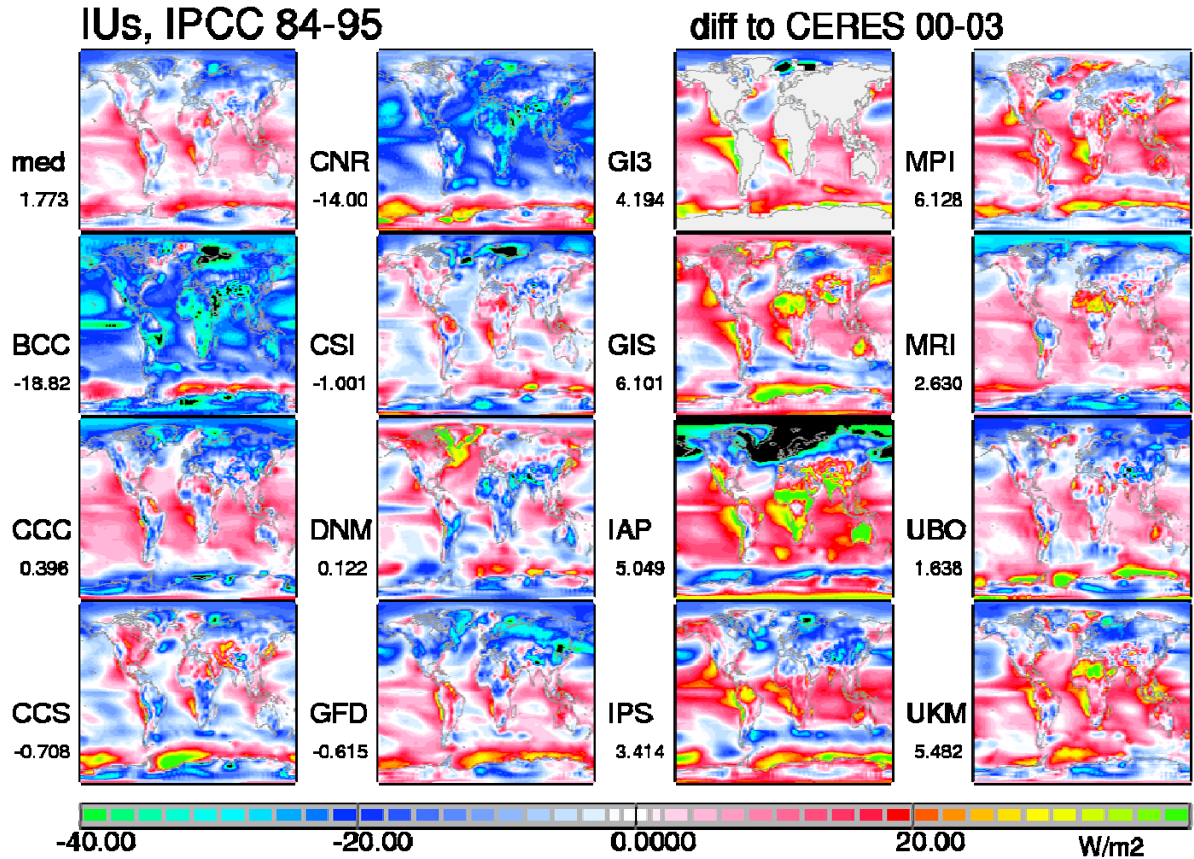


**Figure C.9.11:** Differences in all-sky longwave upward fluxes from the surface between multi-annual (1984-1995) average maps of the IPCC median and individual IPCC-4AR models of Table 9.1.1 to those suggested by CERES (2000-2003).

The maps in *Figure A.9.10* illustrate differences for IR upward surface emission fluxes compared to CERES. Unfortunately, the data for individual IPCC models were only available for ‘all-sky’ conditions, so that differences are also influenced by the representation of clouds. Still, the upward IR radiative fluxes from the surface are primarily determined by the surface temperature and also by assumptions to the surface emissivity. This emissivity is usually near 1.0, but can be less in the IR window regions over deserts, where indeed significant diversity in modeling is noticed. Still, the largest diversity, which often exceeds the selected range of  $\pm 40$  W/m<sup>2</sup>, is found in other regions. These include regions affected by snow and ice cover (e.g. upward IR fluxes from the surface are much larger over (warmer,) open oceans than over areas covered by sea-ice).

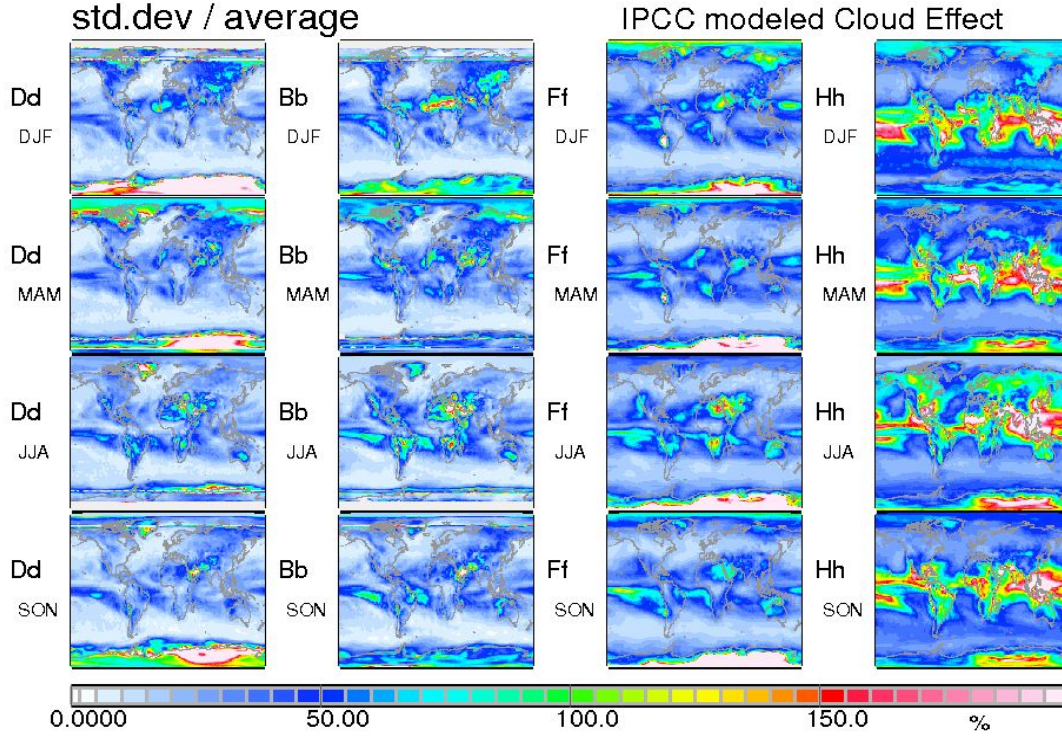


**Figure C.9.12:** Seasonal averages of the relative standard deviations of the modelled Cloud Radiative Effects (CRE) in the IPCC models at (from left) TOA, surface, TOA and surface. The abbreviations mean: Dd = upward solar flux at TOA, Bb = downward solar flux at surface, Ff = upward longwave flux at TOA, Hh = downward longwave flux at surface.

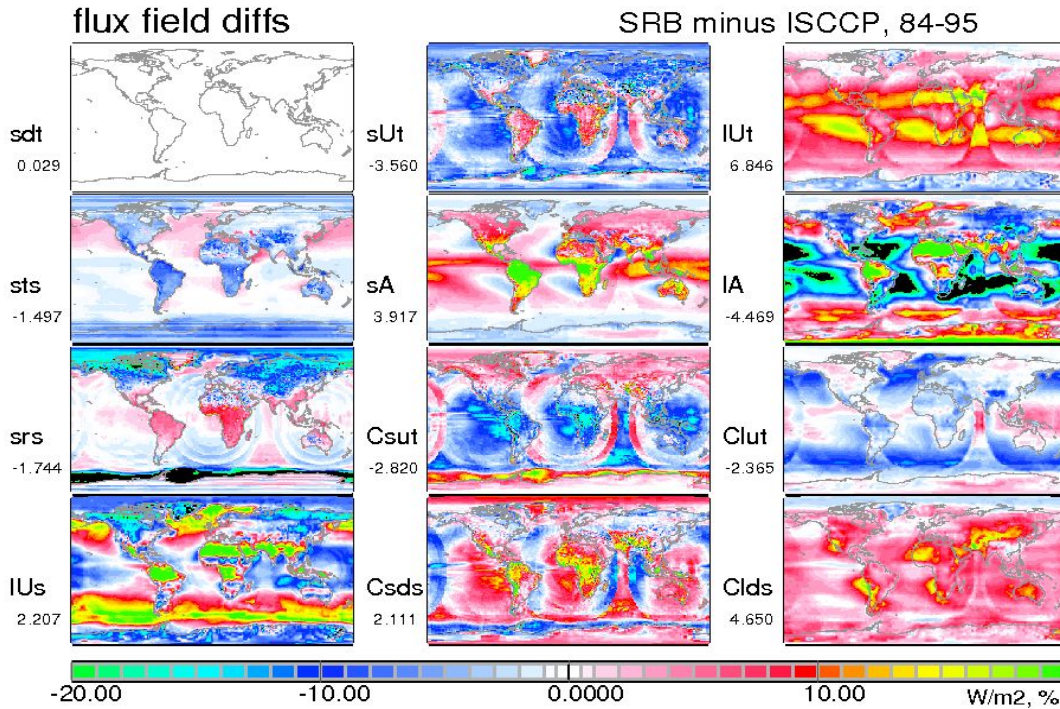


**Figure C.9.14:** Differences to ISCCP of SRB annual flux fields during the 12-year period 1984 to 1995. Note the perturbing artifacts in the difference figures. Quantities are explained in Figure 9.1.1.

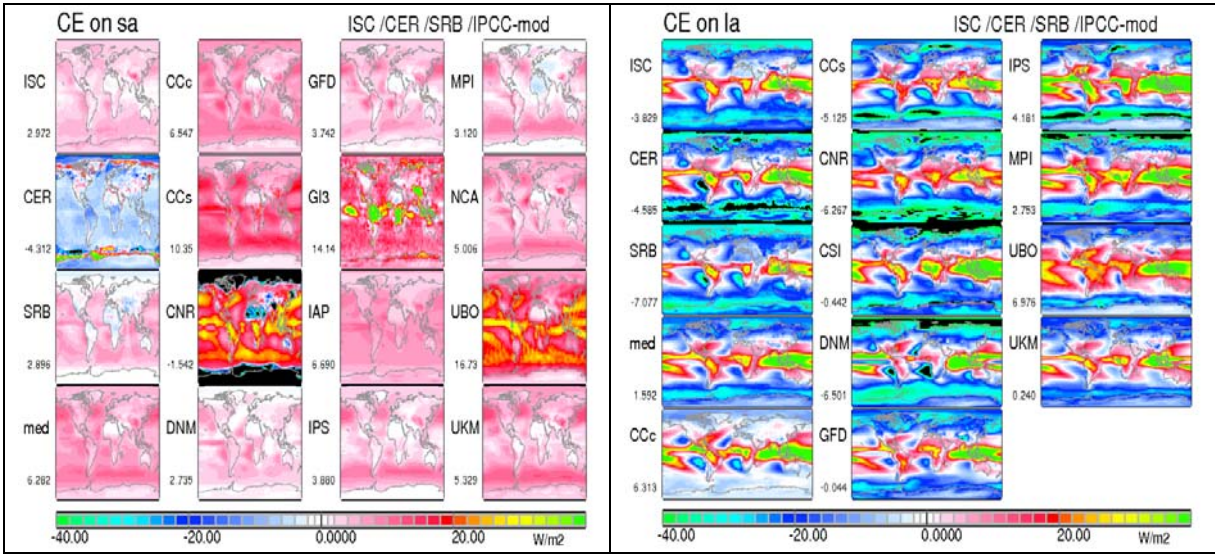


**Figure C.9.15:** Results of individual models and of the 3 climate data sets on the cloud radiative effects (CRE) on the solar absorption and longwave divergence.

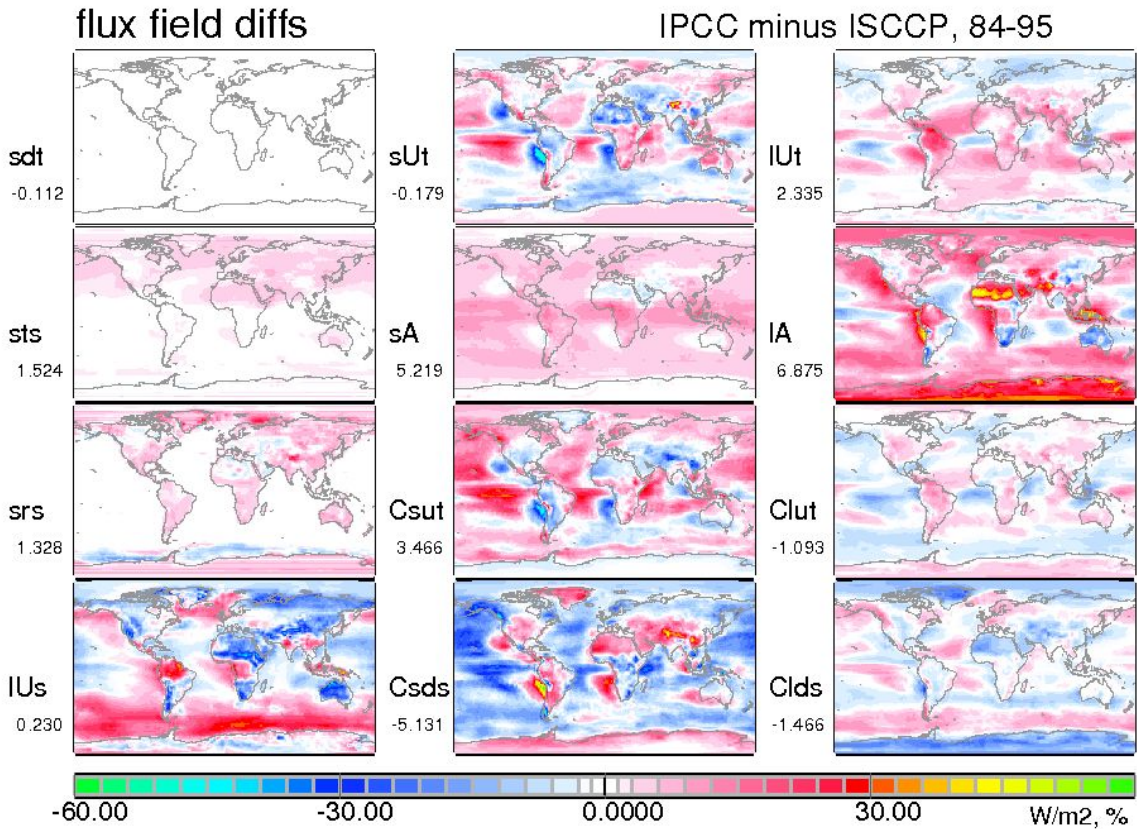


**Figure C.9.16:** Differences of flux fields between results of the IPCC median and the ISCCP. Symbols are explained in Figure 9.1.1.

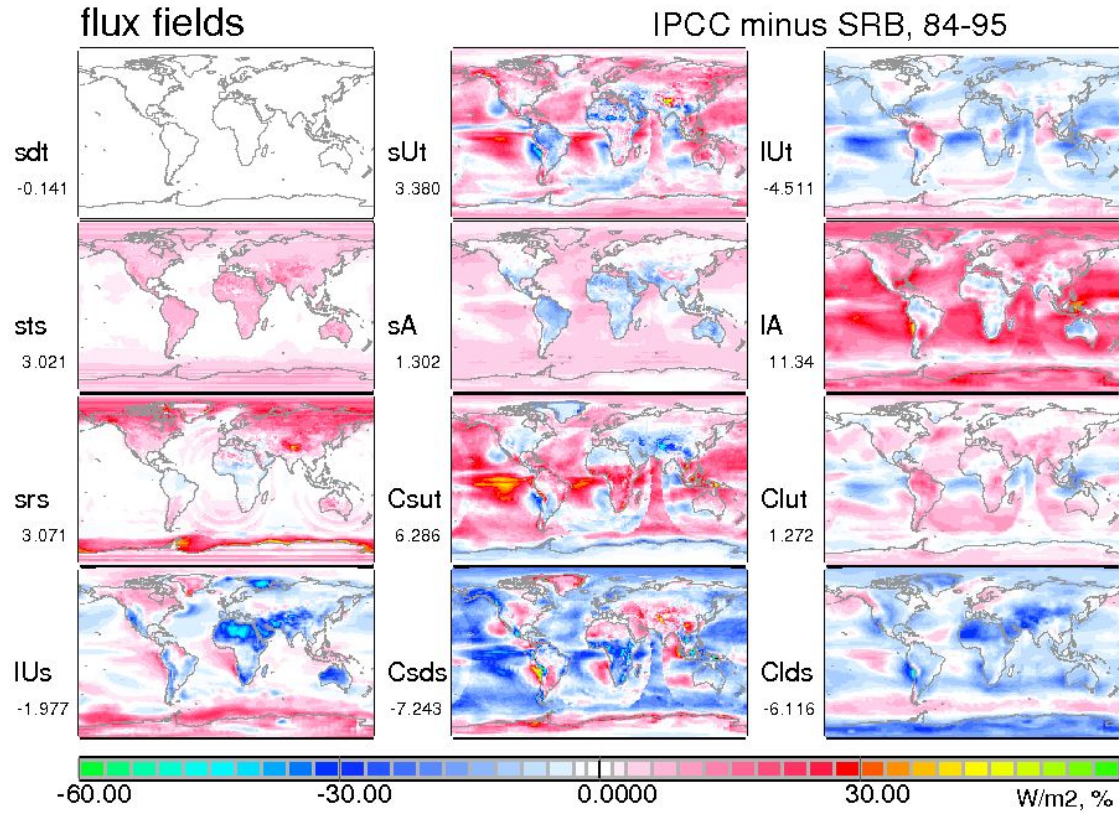


*Figure C.9.16: Differences of flux fields between results of the IPCC median and the SRB. Symbols are explained in Figure 9.1.1.*

# Appendix D:

## Lessons learned

**L. Hinkelman, L. Chambers**

### **D.1: Project scope**

The Assessment goals were established via participant meetings early in the project. The range of analyses desired was very large, running over multiple temporal and spatial scales and many parameters. More than 15 different satellite products, 4 different model/reanalysis data sets, and 6 different sets of surface observations were contributed to the Assessment, with a total of more than 30 different possible radiative variables. Performing the range of comparisons originally envisioned proved to require more time than the volunteer participants were able or willing to allot. In addition, reporting on such extensive analyses would have required a much longer report. In the end, many of the desired analyses were deferred to potential future assessments. While many of these analyses would have been valuable, the conclusion was that a more limited set of goals is necessary for a volunteer effort to be accomplished in a reasonable period of time.

### **D.2: Timeliness**

This Assessment began in 2004 and was completed in 2012, much later than originally planned. Many factors (lack of funding, scope of project, outside obligations, etc.) contributed to this delay. Potential solutions to these particular obstacles are outlined in the sections below. However, the slow progress could have been addressed more directly. Although schedules were established at several points during the Assessment, there was no mechanism to ensure participant accountability. Incentive for progress might have been increased by holding additional meetings at which analysis results were presented to the entire Assessment group for comments and further guidance. This, of course, would have required sufficient travel funding for all participants.

### **D.3: Participation**

The level of interest in this project from community members was high; nevertheless, it proved difficult to complete the Assessment. This was due in part to the lack of direct financial support for the project and the scientists' commitments to other activities. Most participants worked on the analysis and writing for the Assessment alongside their funded projects and could not make this effort a priority. Accordingly, the process moved slowly, which reduced the engagement of participants. A number of team members also changed job positions during the project period, preventing them from following through on promised tasks or providing ideas and information from a needed perspective.

The same problems affected the leadership of the assessment. Strong leadership was necessary because the Assessment team and the planned project scope were large. The project

began with an executive committee of five, but one member retired almost immediately and another moved on to a different project after two years. This left a void in the group vision and expertise and placed responsibility for the progress of the Assessment on the shoulders of a reduced number who had the extensive time demands typical of senior scientists. This leadership void was never adequately filled. In the end, much of the organizing and editing was performed by a committee member. It is possible that this situation could have been improved by direct funding of the remaining executive committee members, who would then have been obligated and able to spend time on the project.

#### **D.4: Funding**

As can be seen from the comments above, lack of specific funding for this project proved to be a major stumbling block. Without such funding, most of the scientists involved effectively participated in the Assessment in their “spare time.” Some funding for the support staff (paying the NASA Langley Atmospheric Science Data Center to build and support the data archive and some of the work of the local organizing committee) was obtained through NASA. However, securing this single year of funding required writing two proposals to open proposal calls.

It is our belief that this type of assessment is important to the general Earth science community, particularly the satellite and climate analysis communities. As such, it should be financially supported by the appropriate agencies, possibly with some international coordination. Dedicated funding would have allowed the Assessment to be completed much sooner and more thoroughly, making it more relevant and up to date. It is therefore recommended that funding commitments from national or international agencies be sought before such a project is undertaken in the future.

#### **D.5: Administration**

One organizational aspect that worked well was the formation of the local organizing committee. Because two of the executive committee members were at the NASA Langley Research Center, a support team was assembled there. This committee collaborated with the Langley Atmospheric Science Data Center to establish the data archive, assisted data providers in formatting and uploading data to the archive, organized Assessment workshops, and coordinated the writing and storage of the Assessment report during the first half of the project. After this, the committee effectively disbanded as its members moved on to other projects and institutions. During its existence, however, this team helped the Assessment move forward, since it removed the burden of focusing on practical details and answering queries from the executive committee.

In general, the skill mix for an effective and timely assessment activity should be carefully considered. Some key skills and activities are required that scientists may not be well positioned to provide, such as attention to schedules, organization of materials and events, or the details of editing and layout. It should be pointed out that, relative to other professional activities, service on assessment committees, particularly performing administrative functions, will not yield the highest recognition for a scientist. This is a disincentive to devoting significant efforts to supporting such an undertaking that should be considered when organizing the activity. This stands in contrast to the recognition that will be accorded the authors of the report, which will likely be cited many times by members of the user community.

#### **D.6: Division of labor**

In a project such as this, the question arises as to whether it is more beneficial to have a single person perform the analysis than a group. In this case, we divided the labor among several participants. This allowed individuals to focus on parts of the analysis where they were most knowledgeable and reduced the efforts of any individual. However, the fact that many people performed parts of the analysis meant that different analysis techniques were sometimes used in different parts of the report that would have better been made parallel. In addition, figures were in different formats with inconsistent representation of the different data sets. This was not corrected in the editing process because it would have required a substantial effort.

A possible solution to this problem would be to hire a dedicated programmer/analyst to perform all computational aspects of the Assessment under the guidance of the Assessment working group. Optimally, this person would also write a draft of the evaluation results, assist with the data archive, and provide coordination among the various team members. Here we note that this approach requires specific funding to support the analyst.

#### **D.7: Report preparation**

The effort required to generate a complete report document was underestimated. Given that there were approximately a dozen authors from multiple countries with multiple native languages who submitted report sections in the format of their choosing and the fact that the final length of the report was **XX** pages, the job of editing and assembling the report was a substantial one. Assistance from a professional editor would have greatly facilitated this process. Establishing a common document format early in the process would also have expedited compilation of the report.

#### **D.8: Electronic data storage and communication issues**

1) An important goal of this project was to produce a database of the data used in the analysis. This database was expected to fulfill two purposes. The first was to supply all of the contributed data sets to the team members performing the analysis for the Assessment. This could easily have been accomplished by establishing an ftp site. However, the second goal was to make the data used in the project available to the entire community in an easily accessible format. Meeting this goal proved to require a substantial effort involving the following tasks:

- a) Establishment of a common data format, including file structure, temporal and spatial resolution of satellite and model data, variable definitions, bad data/“fill” values. A separate file structure was also created for surface measurement data, which has high temporal sampling but is local in nature
- b) Specification of metadata and documentation requirements
- c) Establishment of procedures for data submission
- d) Development of an internal database structure and file serving procedures that included search functions to find the desired file types
- e) Development of two web sites, one to provide general information about the Assessment and the other to provide an interface for data file ordering.

Accomplishment of these tasks was only possible through close collaboration with computer and database experts. The services of the NASA Langley Atmospheric Science Data Center were called upon to meet these challenges.

2) Numerous web tools that can be used to facilitate communication among project team members spread over multiple locations are now available. During the course of this project, several such tools were employed. These included:

- a) A “forum” on the main Assessment web page.
- b) A Google group.
- c) A file server for upload, download, and storage of report chapters as they were composed and edited.
- d) A project web site controlled by the local organizing committee to provide general information, project updates, etc.

Of these, the file server proved the most useful. Early in the Assessment process, draft report sections were collected and stored by the Langley local organizing committee, which meant that they were not directly accessible by the group. Later, the same process was used but the files were linked to a restricted web site from which they could be downloaded. However, the site was not always kept up to date and was sometimes difficult to organize in a logical way. The file server, on the other hand, allowed all files to be uploaded or downloaded by all approved users at any time.

We believe that the other tools were less successful because most of the team members did not grow up in the Internet era, and so were not fully comfortable with these approaches. Tools of this type will probably be more useful in future projects. An additional factor in the lack of use of these tools was that only a few team members were involved in analyzing data and summarizing the results for each of the separate report sections. This meant that personal e-mails sufficed for most communications among these individuals.